NUMERICAL INVESTIGATIONS OF FLUID FLOW AND HEAT TRANSFER PROCESSES IN THE INTERNAL STRUCTURES OF THERMOACOUSTIC DEVICES

Thesis submitted for the degree of

Doctor of Philosophy

at the University of Leicester

by

Fatimah Al Zahrah Mohd Saat

Department of Engineering

University of Leicester

December 2013

Fatimah Al Zahrah Mohd Saat

Numerical investigations of fluid flow and heat transfer processes in the internal structures of thermoacoustic devices

Abstract

Thermoacoustic devices are built based on interactions between sound wave and a solid boundary, within a well-controlled environment, to produce either power or cooling effect. Recent studies on two important internal structures, namely regenerator and heat exchangers, are reviewed. Furthermore, the need for detailed investigations on a pressure drop condition in the flow through the regenerator and heat transfer condition in heat exchangers working in a thermoacoustic environment is also addressed.

A two-dimensional porous medium model is developed based on the pressure drop measurement of a regenerator working in a well-controlled travelling-wave time-phasing, wherein the pressure and velocity of the oscillatory flow across the regenerator are controlled to be in-phase. A friction correlation is proposed based on Darcy's law. The model is developed in a commercial software ANSYS FLUENT to determine a permeability coefficient for the model. The findings suggest that a steady-state correlation is applicable provided that the travelling-wave time-phasing is met. Otherwise, a phase-shift effect should be considered and the steady-state approximation may no longer hold true.

A pair of adjacent plate heat exchangers in the oscillatory flow is studied. It is shown that the application of the temperature difference between "cold" and "hot" plates leads to interesting asymmetries within the flow field. Also a need for a turbulence model at a drive ratio lower than suggested in current literature is discovered and discussed. It is found that the heat absorbed by the cold plate is lower than the heat supplied by the hot plate and heat accumulation is observed in the system. The vortex structures and viscous dissipation change with operating conditions. The combined effect of flow amplitude, natural convection and the "annular effect" of velocity profiles near the channel wall on the flow are discussed. A good agreement with experimental results obtained previously is shown.

Acknowledgements

To my first and former supervisor Professor Artur J. Jaworski for his support, ideas, guidance and encouragement throughout my study;
to the recently appointed supervisor, Dr Aldo Rona for his valuable guidance and help toward the submission of the thesis;
to the staff of Thermofluid group, especially Dr. Xiaoan Mao for the technical support and invaluable discussions during the development of the thesis;
to my parents, siblings and in-laws for their inseparable support and prayers;
to my friends and fellow colleagues, especially the past and present member of the thermoacoustic research group under the supervision of Professor Artur J. Jaworski;
and finally, special acknowledgement for the invaluable support of my loving son, Muhammad Hairul Irwan Mohd Hasmi and my adopted daughter, Siti Aisyah Abdullah.

This study has been sponsored by the Ministry of Higher Education Malaysia and Universiti Teknikal Malaysia, Melaka.

List of Contents

List of Figures

List of Tables

Abbreviations

CFD	Computational Fluid Dynamics
CHX	Cold heat exchanger
DeltaEC	Design Environment for Low-Amplitude Thermoacoustic Energy Conversion
HHX	Hot heat exchanger
LES	Large Eddy Simulation
PISO	Pressure-Implicit with Splitting of Operators
PIV	Particle Image Velocimetry
PLIF	Planar Laser-Induced Fluorescence
RANS	Reynolds-averaged Navier-Stokes
RLC	Resistance, *R*, ineratance, *L*, compliance, *C*.
RSM	Reynolds stress model
SST	Shear Stress Transport
UDF	User-Defined Function

Chapter One: Introduction

This chapter provides an overview to the area of thermoacoustics. The background about thermoacoustics is presented in section 1.1 followed by problem definition in section 1.2. Section 1.3 touches upon the objectives of the current study. The significance of the study is highlighted in section 1.4. The structure of the thesis is outlined in section 1.5.

1.1 Background

A thermoacoustic system is a system based on the thermoacoustic effect, which generates energy, when an acoustic wave interacts with a solid boundary in the presence of a temperature gradient, and which produces cooling effects when appropriate acoustic power is supplied. Thermoacoustic systems have gained considerable attention due to their environmental friendliness by using inert gases as the working media. Another attractive feature is the lack of moving parts in the thermodynamic process, which makes them potentially simple, reliable and inexpensive.

The thermoacoustic phenomenon was discovered circa two centuries ago by Higgins who experimentally observed acoustic excitation when a hydrogen flame was placed correctly in a pipe (Putnam and Dennis, 1956). Similar phenomenon was observed by Rijke when a heated net was used instead of the hydrogen flame (Feldman, 1968).

A simple prototype of a thermoacoustic engine is the ‘Sondhauss tube’ in which a strong sound is emitted when a hot glass bulb is attached to a cool glass tubular stem. Internal structures such as stack of plates are introduced to the Sondhauss tube to improve the performance of the system. A significant refrigeration effect by means of thermoacoustic conversion was obtained by Gifford and Longsworth in 1966.

The mechanism of thermoacoustic phenomena was qualitatively described over hundred years ago, when Rayleigh realised that oscillatory thermal expansion and contraction of a gas could create acoustic power “if heat is given to the air at the moment of greatest condensation, or taken from it at the moment of greatest rarefaction”, and that the oscillatory thermal expansion and contraction could themselves be caused by the

acoustic wave under consideration, in a channel with a temperature gradient (Backhaus and Swift, 2002). Rayleigh's criterion of spontaneous thermoacoustic oscillation (that heat should flow into the gas while its density is high and out of the gas while its density is low) is met in two types of thermoacoustic engines: the standing-wave engine and travelling-wave engine. Pressure and velocity in travelling-wave devices are in-phase, meanwhile in standing-wave systems they are out-of-phase.

The quantitative description of the related mechanism of flow was described by Nicholas Rott through the introduction of the Linear Thermoacoustic Theory in 1969 (Rott, 1980). The theory describes acoustic oscillations in a gas in a small channel (with dimension of the order of the gas thermal penetration depth) with an axial temperature gradient. Following Rott's theory, Hoftler et al. (1988) proposed a standing-wave thermoacoustic refrigerator.

In the 19th century, the Stirling engine has been investigated and developed as a possible alternative technology to steam power. The discovery of a 'free-piston' Stirling engine opens the door to modern developments whereby the interaction between piston dynamics and gas dynamics replaces the similar mechanism offered by the crankshaft and connecting rods (Swift, 2004). Urieli and Berchowitz (1984) analysed these mechanisms by assuming sinusoidal time oscillations of all important variables and using complex numbers to account for amplitudes and time phases. Ceperley (1979, 1985) added an additional acoustic perspective to Stirling engines and refrigerators when he realised that the time phasing between pressure and motion oscillations in their regenerators is that of a travelling acoustic wave. In thermoacoustic devices the "free piston" is replaced by the oscillating gas itself.

Thermoacoustic technology has vast potential in application in areas such as domestic heat pumps, combined heat and power systems, cooling for microelectronic devices and solar powered electricity. One of the significant developments was the construction of a natural-gas-powered natural-gas liquefier using thermoacoustic principles, which essentially produced refrigeration from waste heat (Swift, 1997). Another interesting application is in the gas-mixture separation as discovered by Spoor (2000). The gas mixture is separated through a radially oscillating thermal diffusion and axially oscillating viscous motion in the gas along the length of a tube.

In the last two decades, the theoretical and experimental research in thermoacoustics has been led by Las Alamos National Laboratory in the United States (Swift, 2002). A one-dimensional numerical model known as 'Design Environment for Low-Amplitude Thermacoustic Energy Conversion' (DeltaEC) has been developed based on Rott's Linear Thermoacoustic equations for the design and analysis of low-amplitude thermoacoustic engines. Other numerical packages such as 'Regen 3.2' and 'Sage' sacrifice speed in order to improve accuracy by including transient analysis but are still limited to one-dimensional assumptions (Swift, 2002). Commercial Computational Fluid Dynamics (CFD) codes such as ANSYS FLUENT 13.0 (2010) provide comprehensive numerical algorithms for numerical integration of fully three-dimensional and time dependent models. This capability could allow a more detailed analysis of fluid and heat transfer phenomena especially in modelling specific parts of thermoacoustic systems.

1.2 Problem definition

Currently the calculations of hydrodynamic and heat transfer conditions for modelling and designing internal structures within thermoacoustic systems are carried out using correlations obtained from steady flow data. The necessity of using the steady flow assumptions is caused by the limited information and data pertaining to oscillatory flow. Therefore thorough investigation on oscillatory flow within the internal structures of thermoacoustic systems is required in order to comprehend the flow and heat transfer processes. Numerical modelling is a good tool for understanding the complex flow fields wherein analytical solution is difficult and experimental investigation is costly and very time consuming. Experimental studies often reveal signs of nonlinearities that are insufficiently addressed by linear model (Swift, 2002). Therefore CFD capabilities in the present thermoacoustic context need to be improved in order to help the design of future thermoacoustic systems.

1.3 Objectives of study

The study aims to develop a CFD model for investigation of oscillatory flow within the internal structures of thermoacoustic devices. The detailed objectives are as follows:

(i) To develop an axi-symmetrical time-dependent computational model for a regenerator working in a travelling-wave thermoacoustic system using commercial CFD software, ANSYS FLUENT 13.0 (2010).

(ii) To investigate the hydrodynamic condition of a regenerator modelled as a porous medium and validate the model using pressure drop data obtained from experiment.

(iii) To develop a CFD model, based on an existing experimental setup, for the investigation of low amplitude flow and corresponding heat transfer processes in a parallel-plate heat exchanger in a standing-wave thermoacoustic system.

(iv) To investigate the effect of the heat exchanger wall temperature on the flow and heat transfer within the parallel-plate heat exchangers.

(v) To investigate the effect of thermoacoustic device orientation on the flow and heat transfer within the parallel-plate heat exchangers.

(vi) To investigate flow and heat transfer at higher amplitude of flow by increasing the drive ratio and validate with existing experimental data.

(vii) To investigate flow and heat transfer at varied thermoacoustic flow conditions. These include the change in operating frequency, mean pressure and geometrical dimensions of the plates and their spacing.

1.4 Significance of study

The key to a better development of a good thermoacoustic system lies within the understanding of the flow and heat transfer within the internal structures in oscillatory flow conditions. Through this work, the author hopes to contribute to a better fundamental understanding of such processes. The study is expected to reveal the behaviour of a particular reciprocating oscillatory flow (with a zero mean flow) working within a strict context of time-phasing condition as defined in the classification of thermoacoustic systems. It is hoped that a clear understanding of the behaviour and working condition will eventually help boosting the efficiency of the future practical systems.

1.5 Thesis Structure

The thesis is organised into seven chapters in the following manner:

Chapter two – begins with a brief introduction that presents the important features of thermoacoutics. Current literature related to the internal structures of thermoacoustic systems with emphasis on regenerators and heat exchangers together with relevant computational studies is reviewed.

Chapter three – reports the outcome of the current work in relation to pressure loss study of a porous structure known as 'regenerator' used in a travelling-wave thermoacoustic system. A numerical model developed based on the porous-medium theory will be presented. Details of the experimental measurement of the pressure drop are also reported. The results and discussion of the hydrodynamic condition of the regenerator are presented.

Chapter four – provides further discussion of a computational model of parallel-plate heat exchangers for a low-amplitude standing-wave thermoacoustic system. Validation of the model with available in-house experimental data is shown. Detailed discussion about the effect of heat exchanger walls temperature on flow and heat transfer condition across the heat exchanger is provided.

Chapter five – discusses the effect of the flow amplitude, known as drive ratio, on the flow and heat transfer around the parallel-plate heat exchangers. The chapter reveals the need to use intermittence and fully turbulent models to describe the condition of flow discovered in earlier experimental work.

Chapter six – is an extended study following the achievement of the model developed in chapters four and five. The effects of several operating conditions involving various resonance frequencies, mean pressures, and channel geometries on the flow and heat transfer in the parallel-plate heat exchanger are discussed. The heat transfer models for all cases are validated against results from studies published earlier.

Chapter seven – presents the conclusions of the current work and suggests research directions for future.

Appendices – There are three appendices. Appendix One shows the figures related to model validations for cases in chapter six which were not shown in the chapter to avoid repeating discussions. Appendix Two contains the user-defined codes developed for the investigations in this thesis. These codes would be helpful to the researchers carrying out any follow-on-work. Appendix Three shows the list of publications related to this thesis.

Chapter Two: Literature Review

The basic concepts of thermoacoustics are given in section 2.1. Section 2.2 follows with a review of numerical modelling of thermoacoustic phenomena. Recent studies on hydrodynamic condition of regenerator are reviewed in section 2.3. Section 2.4 gives a review related to the study of flow and heat transfer within a parallel-plate heat exchanger of a thermoacoustic system. Section 2.5 ends the chapter with a description of the current study in the context of existing literature.

2.1 Basic concepts of thermoacoustics

Thermoacoustic systems are usually divided into engines and refrigerators. The working principle of thermoacoustic refrigerator is illustrated with the aid of Figure 2.1.

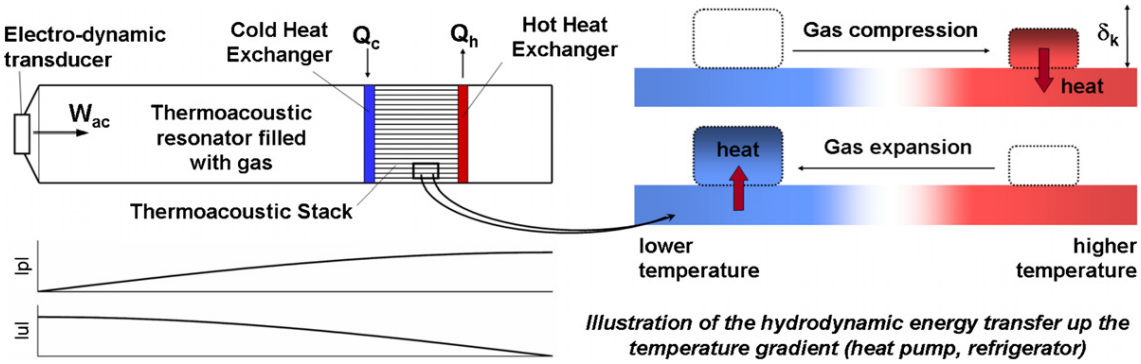

Figure 2.1: Schematic of a simple thermoacoustic cooler arrangement. The acoustically induced compression and expansion of fluid elements causes heat pumping effects along the stack (Mao and Jaworski, 2010b).

The acoustic driver at the left end of the resonator illustrated on the top left of Figure 2.1 supplies acoustic power, W_{ac}, to the working gas inside the resonator. The supplied acoustic power moves the gas parcels forward and backward. The standing wave inside the resonator is illustrated by the distribution of pressure amplitude, $|p|$, and velocity amplitude, $|u|$, as shown on the bottom left of the figure. Internal structures (heat exchangers, stack/regenerator) are commonly placed at a location where oscillating pressure and velocity are not zero. A small portion of the stack has been magnified and

shown on the right side of the figure. A parcel of gas undergoing an acoustic oscillation is shown. As the fluid oscillates back and forth within the portion of the plate, it undergoes changes in temperature due to the adiabatic compression and expansion resulting from the pressure variations which accompany the standing sound wave. The gas parcel is compressed as it moves to the right and the parcel temperature increases to be slightly higher than the plate temperature. Consequently heat is being transferred from the parcel to the plate. As the flow reverses, the gas parcel expands and the temperature drops slightly lower than the plate. As a result heat is being absorbed from the plate and the parcel returns to its original thermodynamic state. This completes thermodynamic cycle. The acoustic wave provides power that allows the heat to be pumped up the temperature gradient.

If we now consider the full length of the stack as shown in the upper portion on the left of Figure 2.1, the overall heat pumping process is analogous to a "bucket brigade" in which each set of gas parcels picks up heat from its “neighbour” to the left at a lower temperature and hands over the heat to its “neighbour” to the right at a higher temperature. Heat exchangers are placed at the ends of the stack to absorb the useful heat load at the left-end (cold) of the stack and remove the heat at the right-end (hot) of the stack. Conversely, if a high enough temperature gradient is imposed across the stack/regenerator, an acoustic power will be self-excited and useful energy will be produced (Swift, 2002). This in turn could be extracted by a linear alternator to produce electricity, or used to drive a coupled cooler.

Figure 2.2 illustrates series of processes occurring between solid wall and gas medium for an ideal system and the corresponding Stirling thermodynamic cycle is shown on a pressure-volume (PV) diagram (the outer loop in Figure 2.2(b)). In an ideal Stirling cycle, the compression and expansion of the working medium occur at adiabatic condition. Furthermore, the heat transfer is ideally an isochoric process. In real thermoacoustics application compression, expansion and heat transfer occurs simultaneously; hence creating irreversibilities to the system. Therefore, the actual cycle for thermoacoustic systems resembles an elliptical shape. The work required by the cycle to produce the necessary cooling effect is represented by the area inside the “loop” representing the cycle. In the case of an engine the same process will follow but in a reverse direction.

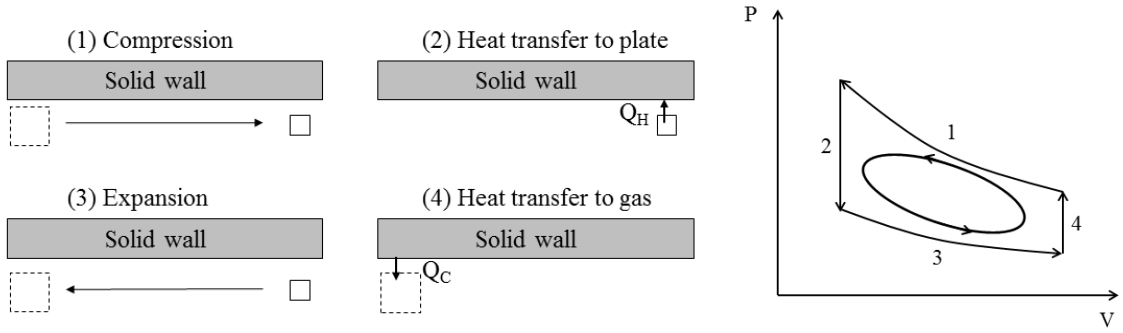

(a) (b)

Figure 2.2: (a) Sequence of ideal process between working medium and the solid structures and (b) Thermodynamic cycle executed by the working gas in a thermoacoustic cooler. The numbers 1-4 in (b) correspond to the sequence described in (a).

The thermoacoustic systems can work either in a standing or a travelling wave conditions. The difference between standing-wave and travelling-wave device is the time-phasing between pressure and gas motion. In the standing-wave device, pressure and velocity oscillation are 90° out of phase, whereas the pressure and velocity in the travelling-wave are in phase (Swift, 2002). The relationship between pressure and velocity for both modes is illustrated in Figure 2.3.

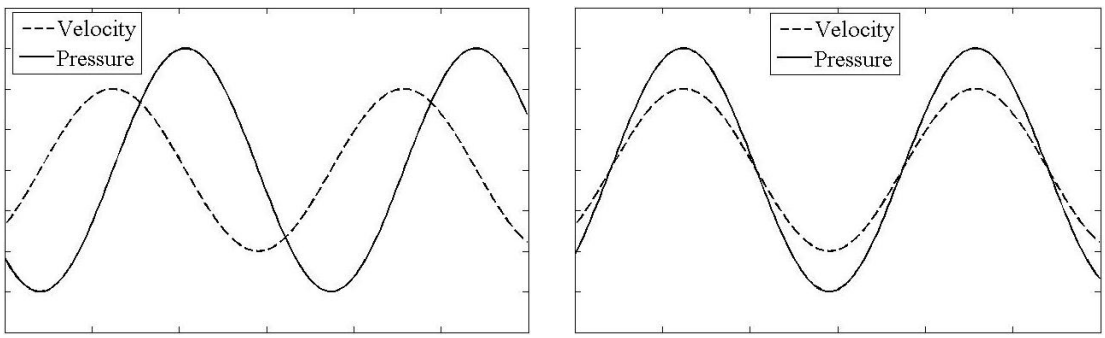

(a) (b)

Figure 2.3: A time-phasing between pressure, $p(t)$ and velocity, $u(t)$ at a point inside (a) standing-wave and (b) travelling-wave systems.

A standing-wave device has a stack of plates, referred to as ‘stack’, with gaps enough to create standing-wave time-phasing. The designed gap allows an imperfect thermal contact as the gas particle passes through the solid surface of the stack. The imperfect

thermal contact is important in order to introduce a significant time delay between gas motion and gas thermal expansion and contraction (Swift, 2002).

A very good thermal contact is required in a travelling-wave device. This is where the regenerator is needed. A regenerator is a fine wire mesh commonly made of stainless steel. In the most common practice, the mesh screen will be stacked randomly to form a very tortuous and porous structure which is capable of offering a huge surface contact area for heat transfer between the solid and the moving gas (Swift, 2002).

The efficiency of a standing-wave thermacoustic device is limited by the requirement of the imperfect thermal contact to sustain standing-wave time-phasing (Swift, 2002). Nonetheless, the simplicity offered by the standing-wave device still makes it an attractive option. The almost perfect thermal contact offered by the travelling-wave time-phasing is thermodynamically more favourable. The challenge lies in reducing losses primarily within the core of the travelling-wave system, where the regenerator is located. The pressure loss imposed by the structure may degrade the acoustic power produced or consumed (depending on engine or heat pump) within the regenerator (Swift, 2002).

2.2 Numerical modelling of thermoacoustic phenomena

Generally, three-dimensional fluid flow and heat transfer conditions can be physically modelled by a Navier-Stokes equation given as (Versteeg and Malalasekera, 2007):

$$\frac{\partial \rho}{\partial t} + \nabla(\rho \vec{v}) = S_c \tag{2.1}$$

$$\frac{\partial(\rho u)}{\partial t} + \nabla(\rho u \vec{v}) = -\nabla p + \frac{\partial \tau_{xx}}{\partial x} + \frac{\partial \tau_{yx}}{\partial y} + \frac{\partial \tau_{zx}}{\partial z} + S_{M_x} \tag{2.2a}$$

$$\frac{\partial(\rho v)}{\partial t} + \nabla(\rho v \vec{v}) = -\nabla p + \frac{\partial \tau_{xy}}{\partial x} + \frac{\partial \tau_{yy}}{\partial y} + \frac{\partial \tau_{zy}}{\partial z} + S_{M_y} \tag{2.2b}$$

$$\frac{\partial(\rho w)}{\partial t} + \nabla(\rho w \vec{v}) = -\nabla p + \frac{\partial \tau_{xz}}{\partial x} + \frac{\partial \tau_{yz}}{\partial y} + \frac{\partial \tau_{zz}}{\partial z} + S_{M_z} \tag{2.2c}$$

$$\begin{aligned} \rho c_p \frac{DT}{Dt} = {} & \frac{\partial}{\partial x}\left(k \frac{\partial T}{\partial x}\right) + \frac{\partial}{\partial y}\left(k \frac{\partial T}{\partial y}\right) + \frac{\partial}{\partial z}\left(k \frac{\partial T}{\partial z}\right) + \frac{Dp}{Dt} + \tau_{xx} \frac{\partial u}{\partial x} + \tau_{xy} \frac{\partial v}{\partial x} + \tau_{xz} \frac{\partial w}{\partial x} \\ & + \tau_{yx} \frac{\partial u}{\partial y} + \tau_{yy} \frac{\partial v}{\partial y} + \tau_{yz} \frac{\partial w}{\partial y} + \tau_{zx} \frac{\partial u}{\partial z} + \tau_{zy} \frac{\partial v}{\partial z} + \tau_{zz} \frac{\partial w}{\partial z} \end{aligned} \tag{2.3}$$

where

$$\tau_{xy} = \tau_{yx} = \mu\left(\frac{\partial v}{\partial x} + \frac{\partial u}{\partial y}\right); \tau_{xx} = -\frac{2}{3}\mu(\nabla \cdot \vec{v}) + 2\mu\frac{\partial u}{\partial x}; \tau_{yy} = -\frac{2}{3}\mu(\nabla \cdot \vec{v}) + 2\mu\frac{\partial v}{\partial y};$$

$$\tau_{zz} = -\frac{2}{3}\mu(\nabla \cdot \vec{v}) + 2\mu\frac{\partial w}{\partial z}; \tau_{xz} = \tau_{zx} = \mu\left(\frac{\partial u}{\partial z} + \frac{\partial w}{\partial x}\right); \tau_{yz} = \tau_{zy} = \mu\left(\frac{\partial w}{\partial y} + \frac{\partial v}{\partial z}\right) \quad (2.4)$$

Equations (2.1), (2.2) and (2.3) are the continuity, momentum and energy equations, respectively. The terms ρ, $\vec{v}$, t, μ, τ, p, k, and T represent the density, velocity vector, time, viscosity, stress tensor, pressure, thermal conductivity and temperature, respectively. The terms u, v, w correspond to the x, y and z components of velocity. The sources S_c, S_M, and S_E are the user-defined features as commonly available in commercial software such as ANSYS-FLUENT.

In thermoacoustics, there are a few important length scales commonly used in the analysis of thermoacoustic systems. In the direction of wavelength propagation, e.g. in the x-direction, the wavelength of sound is defined as (Swift, 2002):

$$\lambda = \frac{a}{f} \quad (2.5)$$

where a is the speed of sound and f is the frequency. Another important length scale in the direction of flow is the amplitude of gas displacement, δ. The gas displacement is defined as the velocity amplitude, $|u_1|$, divided by angular frequency, ω, $\delta = |u_1|/\omega$.

In the direction perpendicular to the main flow, two important parameters known as thermal penetration depth, δ_κ, and the viscous penetration depth, δ_υ, are usually used. These two characteristics are expressed as follows (Swift, 2002):

$$\delta_\kappa = \sqrt{\frac{2k}{\omega\rho c_p}} = \sqrt{\frac{2\kappa}{\omega}} \quad (2.6)$$

$$\delta_\upsilon = \sqrt{\frac{2\mu}{\omega\rho}} = \sqrt{\frac{2\upsilon}{\omega}} \quad (2.7)$$

where k and κ are the thermal conductivity and diffusivity of the gas, μ and υ are its dynamic and kinematic viscosities, and c_p is the isobaric specific heat per unit mass. In thermoacoustic system, the gas displacement, δ, is often much larger than the penetration depth, but still much smaller than the acoustic wavelength $\delta_\kappa, \delta_\upsilon << \delta << \lambda$ (Swift, 2002).

Equations (2.6) and (2.7) explain the heat and momentum diffusivity laterally during a time interval. In this way, the thermal and viscous dominancy can be expressed by its distance from the wall. At distances larger than the penetration depth, the thermal and viscous effect will not influence the gas flow very strongly.

Flow inside a typical thermoacoustic system is oscillatory in nature. The basic assumptions associated to the linear theory of thermoacoustics are presented by Rott (1980), and are commonly referred to as 'Rott's acoustic approximation'.

The time-dependent variables are assumed to be small so that first order Fourier series is sufficient to describe the dynamic properties of the flow. The density, ρ, temperature, T, pressure, p, and velocity , u, are expressed as (Swift, 2002):

$$\rho(x,y,z,t) = \rho_m(x) + \mathrm{Re}\left[\rho_1(x,y,z,)e^{i\omega t}\right] \tag{2.8}$$

$$T(x,y,z,t) = T_m(x) + \mathrm{Re}\left[T_1(x,y,z,)e^{i\omega t}\right] \tag{2.9}$$

$$p(x,y,z,t) = P_m + \mathrm{Re}\left[p_1(x)e^{i\omega t}\right] \tag{2.10}$$

$$u(x,y,z,t) = \mathrm{Re}\left[u_1(x,y,z)e^{i\omega t}\right] \tag{2.11}$$

The gradients of pressure in the y and z directions are small and negligible; hence the oscillating pressure is always written as a function of x only. The mean pressure, p_m, is a constant and independent of locations x, y or z – there is no acceleration caused by the mean pressure. Most other flow variables have the same form as ρ and T. The subscript m refers to the mean value while subscript 1 refers to the first order harmonic oscillation of the time-dependent variable. The time-dependent variables are assumed to be small in comparison to the mean value (i.e. $\rho_1 << \rho_m$, $T_1 << T_m$). The product of two time-

dependent variables is very small and therefore neglected. The mean values of T and ρ depends only on the direction of flow, x, which means that nothing but the oscillation can cause gradients perpendicular to the direction of flow. The working medium is assumed to be an ideal gas. The velocity in the direction of flow, u, is larger compared to the other components, v and w. Therefore the flow is assumed to be one-dimensional. Derivatives with respect to x tend to be of the order of $1/\lambda$ while derivatives perpendicular to x tend to be of the order of $1/\delta_\upsilon$ and $1/\delta_\kappa$. Hence x-derivatives can often be neglected in comparison to y and z derivatives.

Putting all the variables listed in equation (2.8) to (2.11) into the one-dimensional Navier-Stokes equation and following the assumptions given, the linear thermoacoustic theory is shown as (Swift, 2002);

$$i\omega\rho_1 + \rho_m \frac{\partial u_1}{\partial x} = 0 \tag{2.12}$$

$$i\omega\rho_m u_1 = -\frac{dp_1}{dx} + \mu\left[\frac{\partial^2 u_1}{\partial y^2} + \frac{\partial^2 u_1}{\partial z^2}\right] \tag{2.13}$$

$$\rho_m c_p\left(i\omega T_1 + u_1 \frac{dT_m}{dx}\right) - i\omega p_1 = k\left[\frac{\partial^2 T_1}{\partial y^2} + \frac{\partial^2 T_1}{\partial z^2}\right] \tag{2.14}$$

Applying Rott's assumptions to solve the equation of motion, it is assumed the oscillating flow to be steady, mono-frequency and one-dimensional. The higher order function is neglected due to the small contribution to the flow. Further improvements are made with an introduction of the averaged-shape-dependent function, f_υ and f_κ to capture the effect of the three-dimensional shape of internal structures used in thermoacoustic system into the one-dimensional transport equation. The shape-dependent functions for some basic shapes of stacks or regenerators can be found in Swift (2002).

Equations (2.12), (2.13) and (2.14) are the basic thermoacoustic equations used to calculate the pressure, velocity and temperature of the flow for further analysis such as the friction factor, the Nusselt number, acoustic power and total power produced within the selected area of interest.

The simplest form of the thermoacoustic theory is known as the lossless model. The lossless model neglects the effect of viscosity. The analytical solution of amplitude of pressure and velocity are given as (Swift, 2002):

$$p_1 = p_a \cos k_w(x - l) \tag{2.15}$$

$$u_1 = \frac{p_a}{ia\rho_m} \sin k_w(x - l) \tag{2.16}$$

The terms p_a and a refer to the pressure amplitude at the location of pressure antinode and the speed of sound, respectively. The term $k_w=2\pi/\lambda$ is the wave number. The lossless model provides a solution useful for a location where viscous effects are minimum and negligible, which is the case for locations where the flow is not disturbed by the presence of any structures.

The assumption that viscous effects are negligible might not hold true in most practical situations. Most gases have almost the same size of viscous and thermal penetration depths. Hence viscous effects are as significant as the thermal effect in the development of the thermoacoustic effect. This is an important fact that needs to be carefully considered especially within the area of the internal structures (stack/regenerator and heat exchangers) where the viscous effect is expected to be important.

A more general solution can be obtained from equations (2.12), (2.13) and (2.14). The loss occurred due to viscosity is captured by an introduction of a shape factor into the solution. The analytical solution for oscillatory velocity gained through the general thermoacoustic theory is given as (Swift, 2002);

$$u_1 = \frac{i}{\omega\rho_m}[1 - h_\upsilon(y,z)]\frac{\partial p_1}{\partial x} \tag{2.17}$$

where h_υ is a viscous shape factor which varies according to geometry of the internal structure involved in the system. The shape factor for parallel plate geometry is given as (Swift, 2002):

$$h_{\kappa,\upsilon} = \frac{\cosh\left[(1+i)y/\delta_{\kappa,\upsilon}\right]}{\cosh\left[(1+i)y_0/\delta\kappa,\upsilon\right]} \tag{2.18}$$

The shape factor defines the viscous, υ, or thermal, κ, effects depending on the definition of the penetration depths used. Equation (2.17) is useful for predicting velocity profiles within the internal structures. Equations (2.15) to (2.17) are used appropriately for developing and validating the numerical models to be presented in chapter three to chapter six.

The solution of oscillating temperature, $\langle T_1 \rangle$, form linear thermoacoustic theory is given as (Swift, 2002):

$$T_1 = \frac{1}{\rho_m c_p}(1-h_\kappa)p_1 - \frac{1}{i\omega A}\frac{dT_m}{dx}\frac{(1-h_\kappa)-\Pr(1-h_\upsilon)}{(1-f_\upsilon)(1-\Pr)}U_1 \tag{2.19}$$

and the space-averaged value is as follows:

$$\langle T_1 \rangle = \frac{1}{\rho_m c_p}(1-f_\kappa)p_1 - \frac{1}{i\omega A}\frac{dT_m}{dx}\frac{(1-f_\kappa)-\Pr(1-f_\upsilon)}{(1-f_\upsilon)(1-\Pr)}U_1 \tag{2.20}$$

The terms ρ_m, c_p, p_1, ω, A, T_m, x, and U_1 refer to mean density of the fluid, the heat capacity, oscillating pressure, angular velocity, cross sectional area of the flow, mean temperature, axial length, and volume flow rate, respectively. The spatial-averaged shape factors, f_κ and f_υ are defined as (Swift, 2002):

$$f_{\kappa,\upsilon} = \frac{\tanh\left[(1+i)y_0/\delta_{\kappa,\upsilon}\right]}{(1+i)y_0/\delta_{\kappa,\upsilon}} \tag{2.21}$$

The spatial-averaged function f for selected geometries is shown in Figure 2.4 (Swift, 2002). The shape factor represents the influence of fluid viscosity near the wall on the flow through f_υ and the influence of thermal contact between the wall and the fluid through f_κ. For example, if f_κ =1, the thermal contact between fluid and solid wall is

perfect. On the other extreme, if f_κ=0, there is no thermal contact between gas and solid. In the more general situation where the value falls in between these extremes, the oscillating motion of the gas along the temperature gradient leads to complex density oscillations.

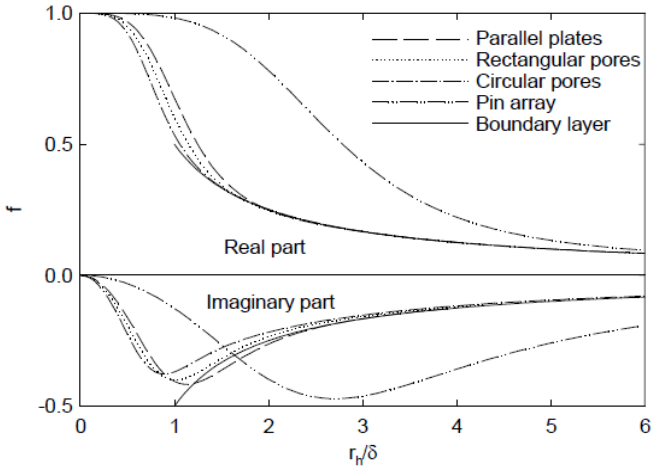

Figure 2.4: Spatial-averaged function f for selected geometries. Extracted from page 101 of Swift (2002).

2.3 Hydrodynamic condition of regenerator

As part of the requirement to achieve high performance, the regenerator is used in travelling-wave thermoacoustic device with an aim to provide sufficient thermal contact with the working medium but is also supposed to generate as small viscous losses as possible. Thermal contact is improved due to the large surface area of the porous and tortuous structure of the regenerator. But careful attention must be given to this tortuous structure as it might induce unwanted losses. It is very important to understand these losses as they will influence the performance of the whole system.

The friction factor is a dimensionless parameter used to represent the hydrodynamic condition of a flow across a structure. In a steady flow, a Fanning friction factor is commonly used to represent pressure losses and its definition is given as (Choi et al., 2004):

$$f_F = \frac{\Delta P d_h}{2\rho u^2 L_r} \tag{2.22}$$

The terms ΔP, d_h, ρ, u and L_r represent the pressure drop, hydraulic diameter, gas density, velocity and length of the regenerator, respectively. The definition has been adapted for application with oscillatory flows where the amplitude of pressure drop, $X_{\Delta p}$, and amplitude of velocity, X_{u_m} are used to replace the pressure drop and velocity of the steady flow. The term u_m is the mean value of velocity between two measured points. The adapted correlation is defined as (Choi et al., 2004):

$$f_{osc} = \frac{X_{\Delta p} d_h}{2\rho X_{u_m}^2 L_r} \tag{2.23}$$

The hydraulic diameter, d_h, is defined as (Choi et al., 2004):

$$d_h = \frac{\sigma}{1-\sigma} d_w \tag{2.24}$$

The value of porosity, σ, and the wire diameter, d_w, are usually supplied by the manufacturer. The experimentally measured pressure drop and velocity are used to calculate the friction factor. The results calculated through equation (2.23) may be fitted with suitable correlation to represent the hydrodynamic condition of the flow investigated. A few models of correlations are discussed here.

The basic form of friction factor correlation is given by the standard two-parameter Ergun equation (Gedeon and Wood, 1996):

$$f = \frac{a_1}{\mathrm{Re}} + a_2 \tag{2.25}$$

where a_1 and a_2 are constants that fit the condition tested. Swift and Ward (1996) showed that the two constants of equation (2.25) can be represented by an equation for porosity defined as:

$$a_1 = 1268 - 3545\sigma + 2544\sigma^2 \tag{2.26}$$

$$a_2 = -2.82 + 10.7\sigma - 8.6\sigma^2 \tag{2.27}$$

In their correlation, Swift and Ward (1996) defined the Reynolds number by taking into consideration the simple harmonic oscillation in regenerator and expressed it as the first order amplitude of complex Reynolds number, Re, given by:

$$\mathrm{Re} = \frac{4\langle u_1 \rangle r_h \rho_m}{\mu} \tag{2.28}$$

where $\langle u_1 \rangle$, r_h, ρ_m and μ are the first order spatial average velocity, hydraulic radius, mean density and viscosity, respectively. Assuming a simple harmonic oscillation in the regenerator, their correlation based on equations (2.25), (2.26) and (2.27) is reported to fit well to the steady experimental data of Kays and London (1964). This equation had been widely used in thermoacoustic community in conjunction with DeltaEC, a design software for thermoacoustic devices (Ward and Swift, 1994). The suitability of Swift and Ward's equation for use in an oscillatory flow is however questionable because it is fitted to steady flow data.

Gedeon and Wood (1996) investigate experimentally the pressure loss of the regenerator placed in an oscillatory environment. They introduced a minor modification to correlation (2.25) to better fit their experimental data obtained within an oscillating flow test rig. The modified form is called the three-parameter-Ergun form (Gedeon and Wood, 1996):

$$f = \frac{a_1}{\mathrm{Re}} + a_2\,\mathrm{Re}^{a_3} \tag{2.29}$$

The underlying idea of this correlation is to keep unknown a_3 negative and small so that the friction factor at low Re still agrees with the original two-parameter Ergun equation. Gedeon and Wood (1996) also report an attempt to introduce porosity in their other correlation of four-parameter Ergun equation. Unfortunately, the four-parameter correlation fails to agree with their experimental data.

Ju et al. (1998) carried out experimental study of the correlation equation for the friction factor for regenerator used in a 50 Hz pulse-tube-cooler and showed that the experimental data are well fitted by:

$$f = \frac{1}{X_d}\left(1.10\times10^4 + \frac{3.78\times10^5}{\mathrm{Re}}\right) \tag{2.30}$$

with X_d introduced as dimensionless distance expressed as:

$$X_d = \frac{1}{2}\frac{u_{\max}}{d_h\omega} \tag{2.31}$$

The friction correlation of equation (2.30) has the same form as the standard Ergun equation (2.25), but is multiplied by a factor of inverse dimensionless distance. The phase control mechanism available in the experimental rig is not used to set the experimental condition to a specific time phasing. Instead, it is used to record experimental results at three different valve openings. Additional correlation is proposed relating the resulting phase shift between pressure and velocity to the Reynolds number.

Another modification of the friction factor correlation is also proposed by Nam and Jeong (2005). This time, the multiplying factor is a newly defined breathing factor, *B*, introduced as:

$$B = \frac{X_{\Delta\dot{m}} R T_m}{L_r A_g \omega X_{p_m}} \tag{2.32}$$

$$f = \frac{1}{B}\left(\frac{65.78}{\mathrm{Re}_l} - 0.14\right) \qquad \left(5 \le Re_l \le 100\right) \tag{2.33}$$

Nam and Jeong (2005) include the breathing factor in their correlation for precise estimation of the phase angle of the pressure drop and the mass flow rate in regenerators. In equation (2.32), X represents the amplitude; R is the gas constant; T_m is the mean temperature; A_g is the free flow cross sectional area of regenerator; $\dot{m}$ is the

mass flow rate; ω is the angular frequency and p_m is the mean value of pressures between the warm and cold ends of the regenerator.

In a separate research paper, Nam and Jeong (2006) further investigate the validity of equation (2.33) at cryogenic operating temperature. At cryogenic conditions, when the temperature is extremely low, changes of the fluid properties affect the hydrodynamic condition of the regenerator. The friction factor and pressure drop tend to differ from the normal ambient condition. A new friction factor correlation is suggested to include the Valensi number, $Va = \rho\omega d_h^2 / \mu$, and expansion parameter, $\varepsilon = (\mathrm{Re} \cdot d_h)/(Va \cdot L_r)$. The Valensi number and Reynolds numbers are found to change dramatically at cryogenic conditions. The new correlation is presented as (Nam and Jeong, 2006):

$$f_{osc} = \frac{1}{Va^{0.65}}\left(\frac{0.045}{\varepsilon_1} + 0.096\right) \tag{2.34}$$

These reviews show that additional terms may be introduced to the conventional friction correlation to better fit the results obtained from the oscillatory flow experimentation. This indicates a presence of at least one additional feature distinguishing the oscillatory flow from a steady flow.

Another important criterion of an oscillatory flow is called impedance. Impedance is defined as a ratio between pressure and velocity of a flow. Impedance relates the pressure and velocity of an oscillating flow not only in magnitude but also in phase difference between them (Yu and Jaworski, 2010). In most of the papers discussed above, the phase difference between pressure and velocity is not set experimentally to a specific value. This may introduce an additional unknown effect. There is yet no clear explanation as to how this affects the friction losses of the whole system. It is found, however, that several situations have been reported in the literature where the friction factor is misleading when the phase difference is present.

Hsu (2005) showed that when a phase difference exists, setting the amplitude alone is not sufficient to predict the hydrodynamics of flow in the porous medium. The experimental detail is reported by Hsu et al. (1999). The coefficients a_1 and a_2 of the

friction correlation (2.25) are presented in Hsu's study as a Darcy and a Forchheimer coefficient. The friction factor gained from experimental results is discussed from a theoretical point of view. The theoretical explanation involves Stokes drag force, C_s, frictional force due to boundary layer, C_B, and Inviscid form drag, C_I, first defined in Hsu et al. (1990) and further developed theoretically in Hsu (2005). The theoretical prediction in that study is in good agreement with experimental result when the effect of phase difference is considered. In this thesis, the phase difference between pressure and velocity will be named as "phase shifting" for brevity.

The findings of Hsu may be related to the phase shifting phenomena reported by Ju et al. (1998) and the breathing factor, *B*, introduced by Nam and Jeong (2005). The phase shift effect is also observed in the experimental study of Zhao and Cheng (1996) when the kinetic Reynolds number increases according to frequency. Clearly the phase-shifting between pressure and velocity has an effect on friction losses reported in many oscillating flow investigations. There is a possibility that these phenomena occur as a result of the experimental conditions not being set to a particular time-phasing between pressure and velocity. Yet, no attention is given to the possibility of controlling the time-phase between pressure and velocity in the experimentation for determination of hydrodynamic condition of oscillating flow through a regenerator. This is crucial in thermoacoustic application because the regenerator should works in a well-controlled travelling-wave time-phasing.

The porous and tortuous structure of the regenerator is difficult and computationally very expensive to model using CFD if the full original structure is to be replicated. The economic way of modelling such a structure is through the use of the porous medium theory.

The porous medium theory models a porous structure through the use of additional parameters in the transport equation that represent the flow resistivity. Flow resistivity is modelled through the knowledge of pressure drop caused by the structure. According to the Darcy-Forchheimer model, the pressure gradient, ∇p, is defined as (Bejan et al., 2004):

$$\nabla p = -\frac{\mu}{K} v - FK^{-1/2} \rho |v| v \tag{2.35}$$

where μ, ρ, and v are the gas dynamic viscosity, density and velocity, respectively. The terms K and F represent the additional parameters of flow resistivity known as permeability coefficient and Forchheimer inertial coefficient, respectively. In the simplest case, the flow across the porous medium can be represented by Darcy's law. Darcy's law simply neglects the second term on the right hand side of equation (2.35) leaving only the term with permeability coefficient, K, to represent the resistance to the flow. This law is valid only when the Reynolds number, defined by the average flow velocity, is an order of magnitude smaller than one. When the velocity is high, the Forchheimer modified equation should be considered to account for the inertial losses in the porous medium. In this condition, equation (2.35) should be applied in full. In a highly viscous flow, a further modification is suggested where the second term on the right hand side of equation (2.35) is replaced with the Brinkmann number, $\mathrm{Br}=K\nabla^{2}\upsilon$.

Darcy's permeability, K, and Forchheimer inertial coefficients, F, are empirical constants. As empirical constants, both permeability and inertial coefficients are uniquely dependent on the porosity and tortuousity of the porous structure (regenerator). The values will determine the momentum losses occurring in the porous media. In experimental practice, the momentum loss can be obtained from the pressure drop measured across the regenerator. On the other hand, to model a system with regenerator, one will need to determine the permeability, K, and Forchheimer inertial coefficient, F, beforehand. This becomes a challenge especially due to the lack of friction factor correlations suitable for oscillating flow in porous media.

Cha et al. (2008) reported a CFD-assisted method for determining the permeability and inertial coefficient of a porous regenerator in an oscillating flow. The regenerator in their study, limited to a few sizes of mesh screens, is tested in a small sized device where the inertial effect could be significant. The oscillating flow friction factor is shown to deviate from the steady flow data of Clearman et al. (2008) when the permeability Reynolds number, $\mathrm{Re}_K = \rho u K^{1/2}/\mu$, is greater than 0.1. Landrum et al. (2010) followed the same CFD procedure in establishing the hydrodynamic property of the regenerator in an oscillating flow but with small mesh fillers suitable for miniature cryocoolers. In a different study, the porous medium coefficients are also derived by Tao et al. (2009). In the derivation, an oscillating flow friction factor reported by Nam and Jeong (2006) is used. The pressure drop gained from their simulation is reasonably

matched to the experimental result of Nam and Jeong (2006) but with some deviation. The reason for this is not reported. Moreover, the derived equation is inappropriate for general use as the friction factor applied in defining the pressure drop is the equation specifically built for cryogenic conditions.

2.4 Flow and heat transfer within heat exchanger

The heat exchanger has been one of the most important parts in any energy transfer system. The flow and heat transfer within heat exchanger working in an oscillatory flow is not well understood. The following subsections will try to focus on selected aspects of these processes. However, admittedly, it is often very difficult to split complex works of others into such a structure.

2.4.1 Flow structure

A study of velocity and temperature profile inside the stack located between cold and hot heat exchangers was undertaken by Mao et al. (2007). The temperature variations are discussed and thermal boundary layer is observed to be thicker in comparison to the calculated thermal penetration depth. Temperature overshoot phenomenon (a profile with temperature maximum occurring near – but not at – the wall) is also reported and suggested to be the effect of thermal relaxation of the stack wall. Comparison between experimental results and calculation based on theoretical work of Arnott et al. (1991) suggests that the temperature values within the temperature profile may be overestimated when calculated analytically.

The effect of temperature on the flow structure within parallel-plate heat exchanger is studied experimentally by Shi et al. (2010a). The velocity profiles are shown to be affected by temperature. Hence, the presence of imposed temperature field resulted in a broken symmetry of time-dependent velocity profiles over the cycle.

A natural convection effect is also observed near the hot heat exchanger as a result of temperature gradient in the area (Shi et al., 2010b). This is shown in Figure 2.5. Natural convection and asymmetry of flow are signs of non-linearity, which may not be represented by the linear thermoacoustic theory.

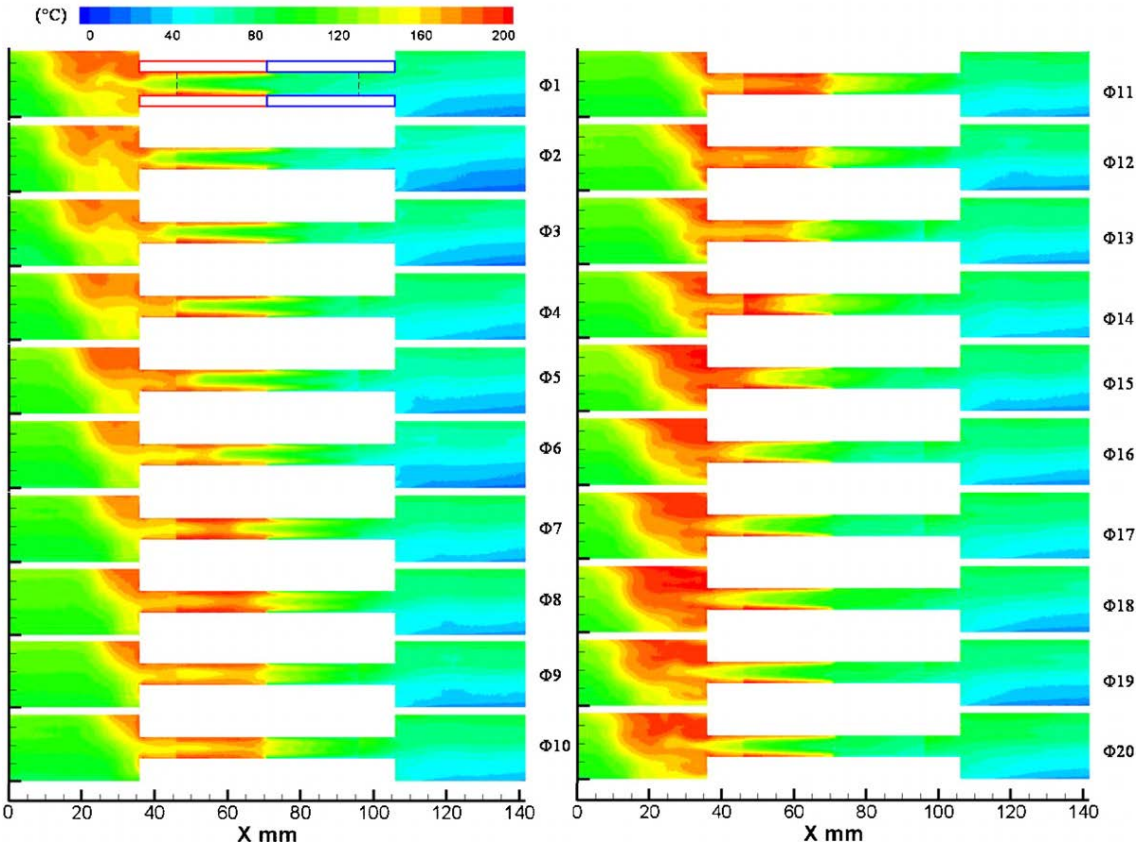

Figure 2.5: Temperature contours for 20 phases (ϕ1-ϕ20) of a flow cycle recorded using Planar-Laser-Induced-Fluorescence (PLIF) showing a natural convection effect at the hot end (left end of picture for each phase) (Shi et al., 2010b).

There are also losses related to viscous dissipation and there are many reasons for these within the heat exchanger area. One of the possible contributors are the flow structures at the end of heat exchanger plates. Any object/structure within a flow will create an obstruction/disturbance to the flow depending on the strength and nature of the flow. For structures within thermoacoustic systems the oscillatory nature of the flow makes the disturbance travel in a reciprocal manner into and out of the flow channels and changes with time. This type of disturbance is illustrated in the experimental observation reported by Mao et al. (2008), as shown in Figure 2.6.

The variation of the vortex pattern at the end of the stack is observed for different sizes of plate thickness and gap between them (Mao et al., 2008). The structure is expected to influence the flow and possibly induce losses of energy that may affect the efficiency of thermoacoustic systems. The formation of vortex structures at the end of the plates are

further discussed and illustrated with the help of dimensionless parameters identified through a similarity analysis (Mao and Jaworski, 2010).

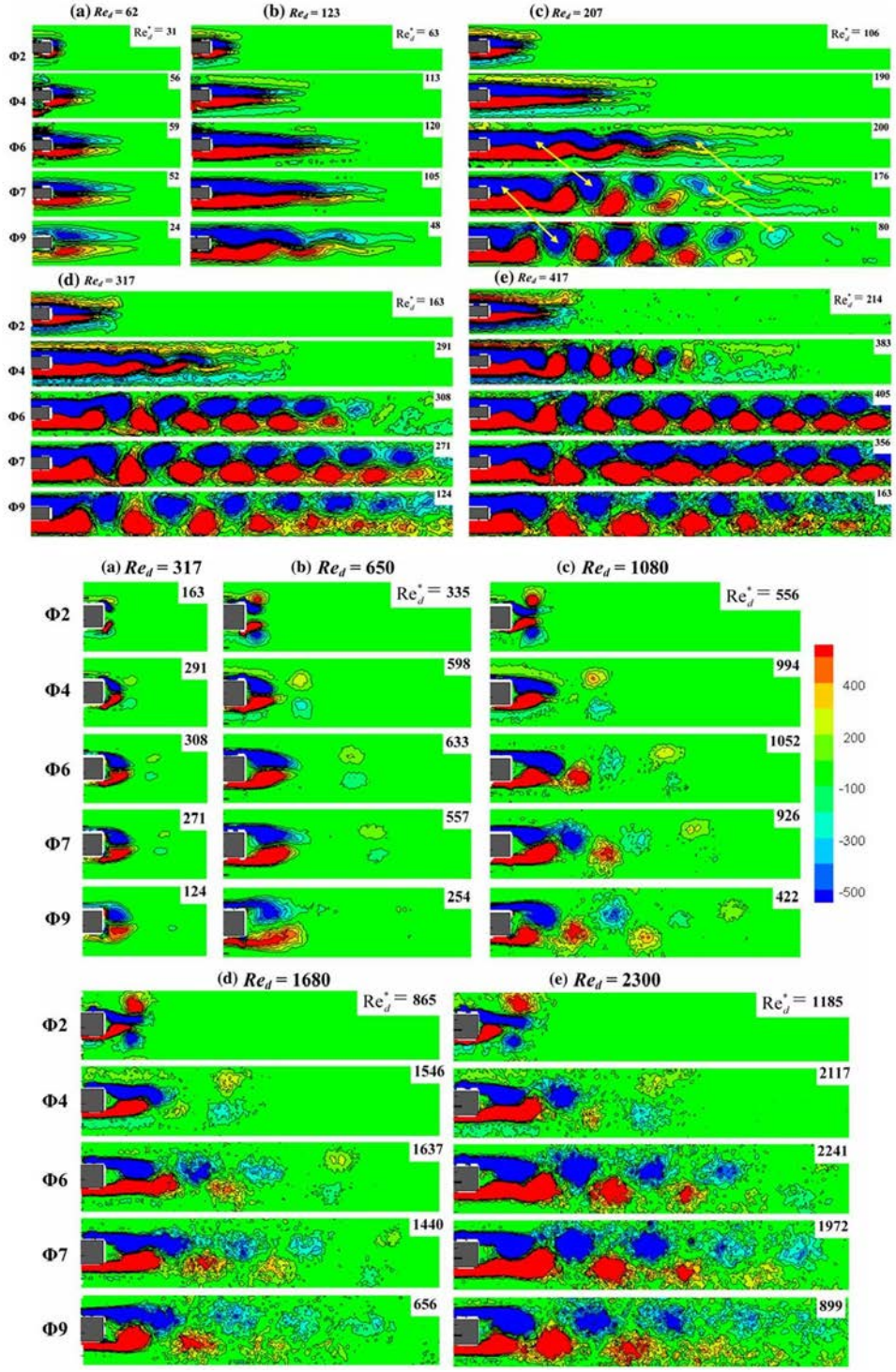

Figure 2.6: The formation of vortex structures at the end of plates observed through Particle-Image-Velocimetry (PIV) at various amplitude of flow. Top: the stack with 1.1 mm plate thickness and 5 mm spacing. Bottom: the stack with 5 mm plate thickness and 10 mm spacing (Mao et al., 2008).

The changes in the character of the vortex structures is shown and described to relate to the plate length, gap between plates, as well as the velocity amplitude of the flow. The similarity approach presented shows an attempt in understanding the vortex behaviour investigated experimentally in conjunction with the detail flow visualisation presented in Mao et al. (2008).

The effect of vortex structures on the flow characteristics within the neighbourhood of the parallel plate stack was investigated by Worlikar and Knio (1996). They looked at the streamlines and viscous dissipation within the plates in comparison to the open area next to the plates. The investigation is carried out numerically using a simplified periodic computational domain covering some length of the open area next to the plates. Streamlines and viscous dissipation discussed are related to the mechanical energy losses within the model. It is shown that the viscous dissipation increases with an increase of Stokes layer thickness and length but has not been affected by blockage ratio (gap between plates). The study also suggests that the dissipation is higher when the structure is located at the velocity antinode and reduced as it moves further from the antinode. This is very much related to the difference in the magnitude of velocity at different locations. It is acknowledged that selecting a suitable length between the end of the plates and the boundary of computational domain is very important in this study so that the vortex shedding developed at the end of plates does not interfere with the imposed boundary conditions; too short a length can cause computational error due to the travel of vortices across the boundary.

The group has made several improvements to the model investigated (Worlikar and Knio, 1998, Besnoin and Knio, 2001, Besnoin and Knio, 2004). These involve adiabatic stacks and heat exchangers, all working in a thermoacoustic standing wave environment. In all the models, a simplified periodic configuration is used covering the area between the plates and some extension to the open area next to the plates to include possible contribution from the vortex shedding phenomenon. The adiabatic stack investigation focuses on the flow structures while the heat exchanger investigations mainly discuss the temperature field between plates, energy flux and the effect of operating condition and geometry on the cooling load. The temperature differences involved are small (a maximum of 18 K is reported) and the drive ratio achieved is within an average to high value (some up to 8%), therefore natural convection is

assumed to be very small in comparison to the oscillatory flow magnitude, and hence is neglected.

It is important to highlight that most numerical modelling work presented in this review applies a simplified model whereby a thin plate or a pair of adjacent plates with an implementation of periodic boundary condition to replicate the array of plates is considered. In modelling, a periodic boundary condition means that the flows at the matching periodic boundary are linked so that flow conditions are shared at this boundary. As a result the flow will be duplicated for all other channels in a periodic manner (ANSYS FLUENT 13.0, 2010). Whilst this has advantages in terms of computational cost, it must be carefully applied as it might give misleading information pertaining to the flow structure. An example of this has previously been reported by Guillaume and LaRue (2001) whereby an experimental comparison of the vortex shedding behaviour is carried out between a structure of a single plate and an array of plates. The results show that, for a structure with an array of plates, the flow structures at the end and in the middle of plates are influenced by the adjacent plates. The Strouhal number (the ratio of product of a characteristic length and the frequency of the vortex shedding to a reference velocity) is reported to have changed in magnitude when comparison is made between the two arrangements. The investigations are carried out in steady flow and might not be directly applicable to the oscillatory condition but it does give an idea of possible sources of discrepancy if investigations of array of plates are carried out using single plate approximation.

Their experimental result of flow around a plate array is later compared to numerical model developed using a commercial software, Fluent (Guillaume and LaRue, 2002). The model is developed using a number of plates similar to experiment. The computational results obtained are consistent with the experimental findings, hence it is concluded that numerical model should consider the whole array so that the vortex structures at the end of each plate behave in a similar way as observed in the experiment.

The observation of asymmetry and non-periodic development of vortex structure at the end of plate array is also reported by Mao et al. (2008). This suggests that periodic physical structure (array of plates) does not guarantee that the flow structures are

periodic. Hence modelling a single plate may not be adequate to describe the physics of flow around a structure with an array of plates.

Even on a single plate, the flow structure at one end may not be the same to the other end when the flow reciprocates. Most investigations related to flow structures (c.f. Mao and Jaworski, 2008, Worlikar and Knio, 1998, Guillaume and LaRue, 2002) assumed that flows at the two ends of a plate are symmetrical. Therefore the analysis is mainly focussed at one end of the plate. This is true for investigations that do not involve a temperature gradient, which is the case for adiabatic stack. However, the presence of a temperature gradient on solid boundaries is necessary for the thermoacoustic effect to take place. Previous experimental results show that the symmetry of the velocity profile is broken due to the presence of temperature effects (Shi et al., 2010a). This indicates that the flow structures at the opposite ends might not be identical. The natural convection, as observed by Shi et al. (2010b) may also alter the flow at both ends.

The effect of natural convection in an oscillatory flow has been previously tested in an experiment involving heated wire located in an empty resonator (Mozurkerwich, 1995). The heat transfer due to the imposed acoustic wave and natural convection is found to fall under three regimes, namely, the small acoustic velocity regime, the transition regime, and the high acoustic velocity regime. The natural convection dominated the flow under small velocity regime but when the velocity is high enough, the natural convection is reported to be negligible. It is thought that the heat transfer at high velocity regime can be predicted by its time averaged steady-flow equivalent. Between these two extreme regimes lies the transition regime which is reported to take place at a streaming Reynolds number, $Re_s=u_1^2/\ \omega\upsilon$, of 88. Here, u_1, ω and υ are the acoustic velocity, angular velocity and viscosity respectively. The transition regime is a region when a “bottleneck” is observed during the heat transfer process as a result of streaming in an oscillatory flow. The start of the regime is also reported to move towards larger Reynolds number as the frequency increases. The results of the study are not very conclusive because the temperature difference investigated is not widely varied. Furthermore, it is speculated that the presence of additional structures such as stack and heat exchanger may alter the influence of the natural convection effect on the flow. Although the geometry investigated is not at all similar to the heat exchangers or stack

structures within the thermoacoustic applications, the results still serve as a basic starting point for understanding the natural convection in an oscillatory flow.

A related topic to the flow structures is the occurrence of turbulence. Theoretical (Swift, 2002, and Arnott et al., 1991) and numerical works (c.f. Worlikar and Knio, 1996, and Piccolo, 2011) related to thermoacoustic processes, typically assume a laminar flow (limited to very low drive ratios). The critical Reynolds numbers for transition to turbulence in an oscillatory flow are reviewed by Ohmi et al. (1982). The experimental results of Ohmi et al. (1982) agree with the critical Reynolds number, $\mathrm{Re}_c=2u_m/(\upsilon 2\pi f)^{1/2}=400$, suggested by Merkli and Thomann (1975), with u_m, υ and f representing the velocity magnitude at the center of pipe, kinematic viscosity and frequency, respectively. The flow regions are categorised as laminar, transitional and turbulent. However, oscillatory flows of Re_c higher than 400 are shown experimentally by Akhavan et al. (1991) to experience a stage of relaminarisation where the velocity profiles match the laminar prediction during the initial stage of the acceleration phase and change to turbulent-like profiles at the later phase, before turning back to laminar.

An additional complication in the transition/relaminarisation processes lies within the appearance of temperature dependencies in fluid properties, compressibility effects, or additional forces such as gravity (Narasimha and Sreenivasan, 1979). Experimental work, as reported in Shi et al. (2010b), has shown the evidence of flow asymmetry and temperature-driven flow due to natural convection. The presence of temperature has proven to change the structure of flow and heat transfer in an unpredicted way. Therefore necessary precautions need to be exercised in the course of modeling such flow. In addition, a possibility of turbulence especially at an increasing drive ratio should be considered.

2.4.2 Heat transfer condition

A common way of presenting flow and heat transfer problems is carried out through the application of appropriate dimensionless numbers (Schlichting, 1987). Dimensionless numbers can be recognised in several ways, but the most common way of recognition is through normalising the transport equation (i.e Mao and Jaworski, 2010, Olson and Swift, 1993, Schlichting, 1987,) or through the Buckingham π-theorem (c.f. Olson and Swift, 1993, Incropera and DeWitt, 1996). A dimensionless number allows the result to

be presented in such a way that it can be easily compared with other sets of experimental or numerical data. The Nusselt number, Nu=hd/k (where h, d and k are the heat transfer coefficient, characteristic length and thermal conductivity, respectively) is the dimensionless number commonly used to represent heat transfer. A general heat transfer correlation normally relates the Nusselt number to another dimensionless number depending on the flow condition. For example, in steady flow, most heat transfer correlations relate the Nusselt number to the Reynolds number. The Prandtl number, Pr=$\mu c_p/k$ (μ, c_p and k are the viscosity, heat capacity and thermal conductivity, respectively) is sometimes included to take into account the variety of working media involved. When natural convection is involved, the correlation may also include the Grashof number, Gr=$g\beta(T-T_\infty)d^3/\upsilon^2$ (where g, β, $(T-T_\infty)$, d, and υ are the gravity, fluid thermal expansion coefficient, temperature difference, characteristic length and viscosity, respectively).

The Nusselt number is a relationship relating the heat transfer coefficient of the working medium to its thermal conductivity. Heat transfer coefficient depends on the temperature difference between the solid medium and the fluid temperature. In oscillatory flow, the fluid temperature changes in time and location due to the forward and backward movement of the gas particles. Heat transfer coefficients are typically defined for steady flow and may not strictly be appropriate for oscillating flow. Thus far no general guideline has been developed to articulate the manner in which the heat transfer coefficients can best represent the oscillatory nature of reciprocating flow. The changes of velocity in a periodic pattern result in a special flow characteristic and its corresponding heat transfer performance achieved is as yet unpredictable. Hence, to understand the heat transfer phenomenon, it is always useful to investigate the fundamental feature of the velocity and temperature that shows the behaviour of flow and how it changes the heat transfer across the plates.

Mozurkerwich (2001) investigated experimentally three configurations of heat exchangers separated by a stack working in a standing wave thermoacoustic system. The three configurations involve tubes of heat exchangers (cold and hot heat exchanger) installed perpendicular to the direction of flow with stack located between them. The measurement is done at the hot heat exchanger to avoid any possible uncertainty due to acoustic streaming between cold heat exchanger and the loudspeaker. The investigation

is focussed on the identification of heat transfer correlation with natural convection effect omitted. The correlation mainly relates the Nusselt number, Nu, to the product of Reynolds number and Prandtl number, $Nu=CRe^{m}Pr^{n}$, with different values of multiplying constant and power constant of the Reynolds and Prandtl numbers. This is a standard way of obtaining an empirical equation for the Nusselt number (Incropera and DeWitt, 1996). The results, subjected to limitations of the flow investigated, suggested a range of constants *m* and *n*. These constants of the correlation vary according to the configuration and operating condition of the case investigated.

Brewster et al. (1997) carried out experimental investigations of temperature discontinuities between a stack and heat exchanger and heat transfer coefficient of the heat exchanger. The heat transfer coefficient is calculated based on the heat flux at the hot heat exchanger and the difference of temperature between the hot heat exchanger and that of the hot end of the stack. The experimental results show that the heat transfer coefficient for flow at low amplitudes is within 20% of the theoretical prediction. The difference becomes more significant at higher amplitude with experimental value much lower than the theoretical prediction. No heat transfer correlation is proposed but useful insight into the temperature discontinuities between the stack and heat exchanger is presented.

Wakeland and Keolian (2004a) investigate experimentally the heat transfer condition of heat exchangers placed in an oscillatory flow. Their experimental results are discussed and compared to the calculation using the thermoacoustic design software, DeltaE (the earlier version of DeltaEC). The effects of geometrical configurations and operating conditions on the heat transfer performance are discussed. The heat exchanger built with a big spacing, ($y_0/\delta_k \geq 1$), gives heat transfer performances that agree with predictions from DeltaE. However, when the space becomes smaller, $y_0/\delta_k \leq 1$, the predictions become incorrect. Their results also suggest that the conventional practice of setting the heat exchanger length to be approximately the same as the length of the gas displacement is not necessary. The length can be made shorter without affecting the performance of the heat exchanger. The effect of frequency on the heat transfer also varies depending on the velocity amplitude. Generally, within the limit of low

frequency investigated, it is suggested that heat transfer estimation from DeltaE may be incorrect.

In addition, it is notable that the experimental arrangement of Wakeland and Keolian (2004a) is neither standing-wave nor travelling-wave. The phase between pressure and velocity is not controlled by any specific mechanism. Furthermore, the experimental setup induces oscillatory flow by using two shakers working in phase. Therefore the influence of pressure gradient is absent. In another paper, Wakelin and Keolian (2004b) show numerically that the pressure-gradient may completely alter the heat transfer condition within the heat exchanger, making the conclusion they made from their experimental results less definitive.

Paek et al. (2005) carried out an experimental investigation into heat transfer correlations to characterise the heat transfer coefficient for a micro-channel heat exchanger in a thermoacoustic cooler prototype. The heat transfer coefficient is calculated based on measurements made at cold heat exchanger. Their experimental results suggest that prediction of heat transfer coefficient by the boundary layer conduction model, which is normally adopted for thermoacoustic calculation, will lead to incorrect results. A modification is suggested by introducing a correction factor that correlates the oscillatory Reynolds number and the steady Reynolds number, taking into account the difference of particle velocity between the positive and negative direction of the flow. The modified Reynolds number is applied to a steady flow correlation and the resulting Colburn j-factor, $j_c=\mathrm{Nu}/\mathrm{RePr}^{1/3}$, is then compared to the experimental result. A good agreement was achieved. Based on the experimental results, it is concluded that the heat transfer prediction from DeltaEC may give an error as big as twice the real value.

Nsofor et al. (2007) have also conducted experimental investigation to study heat transfer correlation for the heat exchanger of a thermoacoustic refrigeration system. A classic correlation of Nusselt number in the form $\mathrm{Nu}=C\mathrm{Re}^m\mathrm{Pr}^n$ is used. Within the Reynolds number investigated, the oscillatory Nusselt number obtained is reported to be lower in comparison to the published data for a steady case. The Reynolds number investigated (calculated using root-mean-square velocity) is reported to be within the range of 15 to 55.

A time-averaged numerical investigation of temperature and heat flux for parallel plate thermoacoustic heat exchangers in standing wave oscillatory flow is presented by Piccolo (2011). The model is developed based on the one-dimensional linear thermoacoustic theory incorporating the two-dimensional energy balanced. The physical domain involves an arrangement similar to Mao and Jaworski (2007); a stack and pair of heat exchangers. The numerical work involves various parametric investigations at different sizes of the heat exchanger plate and several flow conditions. The study involves a very small temperature differential (3 K) between the heat exchangers and therefore natural convection is neglected. The resulted heat transfer coefficient is predicted with errors in the range between 36% and 56% when compared to experiments. Several important characteristics that influence the performance of the parallel-plate heat exchanger are discussed. Assuming symmetry for flow and geometry, the physical computational domain selected for the study is simplified considerably into half of the plate thickness and half of the gap between the plates. The simplified domain together with the time-averaged approach saves substantial amount of computational effort in solving the problem. The simplification provides the advantage of delivering quick results. However, simplification could overlook the details which might influence the real performance of the system when put into practice.

The heat exchanger arrangement of Shi et al. (2010b) was recently modelled using a numerical model developed by Piccolo (2011). A comparison is made between results from the numerical model and experiment (Jaworski and Piccolo, 2012). The model is limited only to the area within the plates of the heat exchanger and neglects the effect of gravity. The natural convection effect observed in the experiment is assumed to occur as a result of heat leaks and hence modelled as heat loss where a fictitious heat sink and heat source are introduced next to the heat exchangers. This approach provides a general idea about the magnitude of heat losses occurring in the experiment. However, detailed investigation needs to be carried out in order to identify the mechanism that contributes to these losses.

A common pitfall highlighted in most of the literature is the lack of knowledge related to oscillatory nature of the flow in thermoacoustics. The situation is even worse when there are nonlinear effects such as significant changes in working medium properties

due to the change in temperature. Most thermoacoustic systems work under relatively high temperature gradients. Swift (2002) concluded that under such circumstances, the temperature obtained through linear thermoacoustic theory can be significantly under-predicted compared to the experiment. The above non-linear effects may be a possible reason for this, as they are not considered in the linear theory.

The non-linear effects found in thermoacoustic applications are also reported to be caused by factors such as the gravity related phenomena. Gravity-driven convection is one form of time-dependent mass-flux that could be superimposed on the main oscillation. A simplified analytical model shows that gravity affects the streaming flow pattern and streaming induced heat convection in thermal buffer tubes (Matveev et al., 2006). From the thermoacoustic perspective, streaming is defined as an additional mass-flux or velocity occurring in the system apart from the main acoustic oscillation induced in the system. The additional flux or streaming is normally small compared to the main flux. Even so, streaming is a mechanism of convective heat transfer that can either produce an undesirable loss to the system or may also assist the heat-transfer process.

Zhao and Cheng (1998) summarise their findings related to flow and heat transfer characteristics of oscillatory flows. The flow and heat transfer characteristics are presented in a form of temperature profile, velocity profile and Nusselt number. The flow and heat transfer is reported to be affected by two factors; the amplitude of flow and the kinetic Reynolds number, $Re_\omega=\omega d^2/\upsilon$ (where ω, d and υ are the angular velocity, characteristic dimension and the fluid viscosity, respectively). The amplitude of flow depends on the gas displacement that is also related to the velocity of the gas particle. The kinetic Reynolds number represents the effect of frequency on the flow. These two factors are identified as the determining factors for the heat transfer performance of a system with an oscillatory flow.

Generally, the thickness of the thermal boundary layer decreases with an increase of frequency. Therefore, Zhao and Cheng (1998) speculated that the heat transfer rate may be enhanced with an increase of frequency due to a higher transverse temperature gradient. However, the speculation may not hold true for all situations; some investigations, particularly related to pulsatile flow, show an inverse trend. This is related to the velocity amplitude of the pulsatile flow which becomes smaller as the

frequency increases. Hence the convective term in the energy equation becomes less significant even though the thermal layer is thinner. This is expected to cause the reduction of heat transfer as the frequency increases. A recent investigation by Nsofor (2007) also shows a possible degradation of heat transfer when the frequency increases above the resonance frequency. There is still no definite understanding how frequency changes the heat transfer condition of an oscillatory flow.

2.5 Current study in the context of existing literature

The current study focuses on numerical modelling of flow across two internal structures of thermoacoustic systems; a regenerator and a parallel-plate heat exchanger. For the regenerator study, the literature review indicates that time-phasing is an important controlled parameter that may influence flow resistance of the regenerator used in thermoacoustic systems. Yet, the friction correlations proposed in the literature review comes from experimental data where time-phasing is not properly defined. There is a need to define a friction correlation suitable for oscillatory flow working in travelling-wave time-phasing.

The present study of flow across the regenerator focuses on two aspects. First, the regenerators tested in the present study are subjected to the travelling-wave conditions. Second, a resistive parameter representing the porous structure is determined by modelling the structure as a porous medium. The condition of flow resistance defined in this way is hoped to provide better correlation that represents the regenerator of a thermoacoustic system. Eventually, the identified resistive parameter may be useful for correct modelling of the regenerator in future CFD modelling of the system.

For the study of flow across parallel-plate heat exchanger, the review shows that temperature effects should be carefully considered when modelling a heat exchanger to account for additional phenomena such as temperature-driven buoyancy effects (Mozurkewich, 1996, and Shi et al., 2010b) and non-linear effects that could affect the flow structure (Swift, 2002, and Matveev et al., 2006). Following earlier experimental findings of Shi et al. (2010b), the current study focuses on developing a CFD model aimed at detailed investigation of flow and heat transfer around parallel-plate heat exchangers. Realising the application of thermoacoustic technology in a broader context (e.g. tilted-angle solar powered systems (Shen et al., 2009), space applications), the

scope of the investigation is extended to include gravity effects and effects of the device orientation on the flow structure in the interest of understanding its implications on the flow and heat transfer across the heat exchanger plates.

Various experimental and numerical investigations reviewed show that the flow structure at the end of plates had an impact on the flow within the plates. In oscillatory flow the flow moves in positive and negative directions into and out of the plates from both ends. With this cyclical movement, the vortex structure created at the end of the plates will exert a certain degree of interference on the incoming or outgoing flow. Disturbances have been observed from investigations using an adiabatic stack as reported in Mao et al. (2008). Hence, it is interesting to investigate the structures of flow in the presence of temperature. This insight could provide useful information about the oscillatory flow behaviour within parallel plate heat exchanger under the influence of temperature.

In most papers related to oscillatory flow, the effect of frequency investigated is not necessarily at resonance. The experimental setup of Wakeland and Keolian (2004), Nsofor et al. (2007) and Zhao and Cheng (1996), for example, fix the length of their experimental apparatus and then vary the frequency without concern about whether it is resonant or not. The results describe the heat transfer performance at varying frequency but may not be very helpful in comparing performance between two modes of thermoacoustic systems working at resonance frequency. In fact, the oscillatory flow investigated by them is not set to a particular wave-mode (standing-wave or travelling-wave). Nsofor (2007) shows that heat transfer may be enhanced or degraded if frequency is not set to resonance. It may be costly and time-consuming to experimentally investigate the effect of resonance frequency because it will involve changing the length of apparatus. The computational model developed in this study will be used to investigate the changes of flow and heat transfer when the resonance frequency changes.

In addition to frequency, some geometrical configurations are studied. The model is built upon in-house experimental findings at a mean pressure of 1 bar. In the interest of improving performance, most practical thermoaocustic systems are now built at high mean pressure (Swift, 2002). Hence extending the investigation to a higher mean

pressure is of interest. The results are discussed with an aim to uncover the flow and heat transfer processes at the operating conditions tested through studying the velocity and temperature profiles. Understanding the changes of flow and temperature field and its influence on heat transfer will be the target of the study. It is anticipated that the discussion will provide a better insight into the physics of oscillatory flow and how it responds to operating conditions in the context of thermoacoustics.

Chapter Three: Friction losses within a regenerator

This chapter investigates friction losses within a porous structure of a regenerator working in a travelling-wave thermoacoustic system. Section 3.1 reports the experiments in which a pressure drop within the regenerator was measured. Section 3.2 presents the flow chart of numerical work applicable to the models developed in the current and consecutive chapters. Experimental data is used as boundary conditions for numerical modelling developed in section 3.3. The derivation of friction factor correlation that is applicable to the porous structure of the regenerator and associated discussions are given in section 3.4. The phase shift between pressure and velocity seen within the regenerator fabricated using a coarse mesh is discussed in section 3.5. The role of hydrodynamic condition (pressure drop) of the regenerator in thermoacoustic system is illustrated in section 3.6 followed by a summary in section 3.7.

3.1 Experimental condition for regenerator study

A regenerator is placed in a travelling-wave cooler and the resulting pressure drop is measured. The schematic diagram of the travelling-wave test rig is shown in Figure 3.1. The rig consists of a linear motor, resonator, hot and cold heat exchanger, regenerator and a set of components known as resistance, *R*, inertance, *L*, compliance, *C* (RLC network). The network is a combination of suitable valves, a 1.6 m long tube with a diameter of 8 mm and a buffer volume of 2.5×10^{-3} m^3. The frequency of the acoustic wave is set using an acoustic driver connected to a linear motor. The linear motor is enclosed in a specially designed highly-pressurised cylinder with a glass window to allow laser displacement measurement of the motor piston. The laser displacement sensor (Keyence LK-G152) sensed the piston displacement, δ. The amplitude of the velocity at that location, defined as V_1, is then calculated as $V_1=\omega\delta$.

The resonator has the inner diameter of 55 mm. Hot heat exchanger, regenerator and cold heat exchanger are made to fit into the resonator. Their lengths are 185 mm, 25 mm, 50 mm and 27 mm respectively. The regenerator is built using stainless steel mesh screens stacked on top of one another to fill up the 50 mm length. The supplied acoustic wave created a temperature gradient along the regenerator. The development of the temperature gradient is controlled to concentrate only on the hydrodynamic condition.

This is carried out through the cold heat exchanger located at the bottom end of the regenerator. The cold heat exchanger is connected to a reservoir that supplies water at room temperature so as it is kept at room temperature. The temperatures, at locations T1, T2, T3 and T4, are measured by type-K thermocouples.

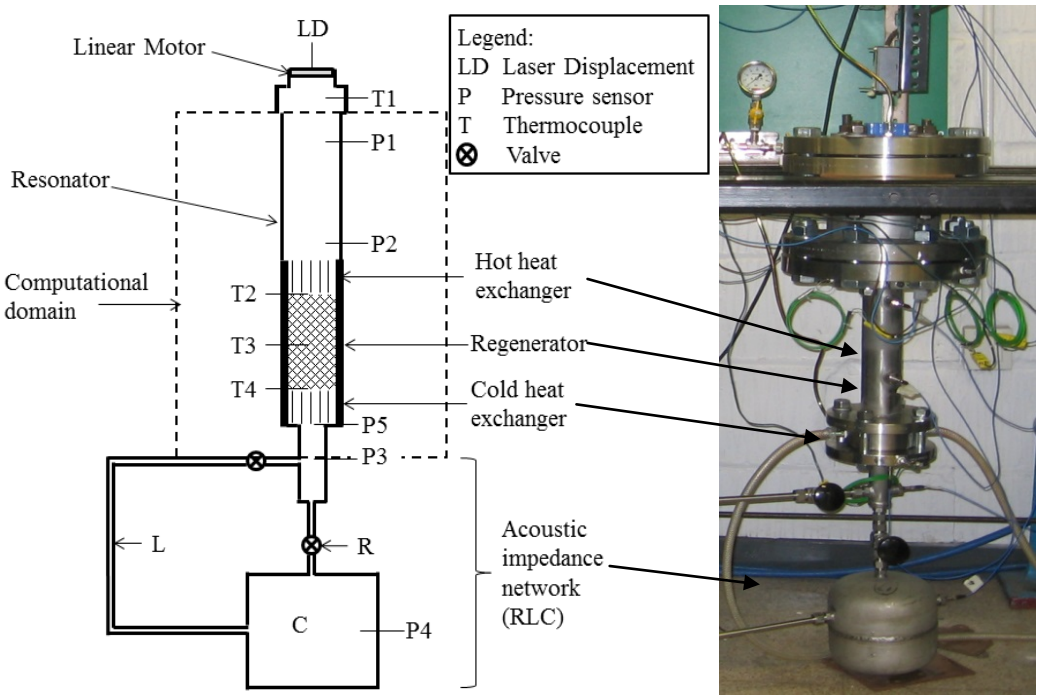

Figure 3.1: Schematic representation of the experimental rig and the selected computational domain.

3.1.1 Data collection and reduction

The travelling-wave time phasing is controlled via the RLC network as shown in Figure 3.1. The valve is adjusted accordingly until the travelling-wave phasing is achieved. The phase is observed by monitoring the impedance at location 5, Z_5:

$$Z_5 = \frac{P_5}{u_5} = |Z_5|(\cos\phi_z + i\sin\phi_z) \tag{3.1}$$

The terms P_5, u_5, and ϕ_z represent the pressure, velocity and the phase differences between pressure and velocity, respectively, at location 5. The travelling-wave phasing is achieved when the impedance becomes zero. This is done by carefully adjusting the opening of the valve on the RLC acoustic network. Pressures are measured in the

experiment. The velocity at location 5, u_5, is determined using a Transfer Matrix Method.

The Transfer Matrix Method is originally used to measure the acoustical properties of components such as the porous medium in the study by Song and Bolton (2000) and Ueda et al. (2009). Ueda et al. (2009) apply a linear thermoacoustic to estimate acoustic characteristics of a regenerator. In the current study, the method is used to theoretically provide information of variables not measured in the experiment. Lossless thermoacoustic model is used to relate pressure and velocity at two locations. This is shown in a matrix form as follows:

$$\begin{pmatrix} \frac{\partial P}{\partial x} \\ \frac{\partial u}{\partial x} \end{pmatrix} = \begin{pmatrix} 0 & -i\omega\rho_m \\ \frac{i\omega}{\gamma p_m} & 0 \end{pmatrix} \begin{pmatrix} P \\ u \end{pmatrix} \tag{3.2}$$

These lossless equations are based on assumptions that the flow is adiabatic and inviscid. The assumptions are considered valid between points 3 and 5 due to a short distance between them and the absence of the influence of temperature within the area. The solutions of equation (3.2) may be shown in a matrix form as:

$$\begin{pmatrix} P_5 \\ u_5 \end{pmatrix} = \begin{pmatrix} m_{11} & m_{12} \\ m_{21} & m_{22} \end{pmatrix} \begin{pmatrix} P_3 \\ u_3 \end{pmatrix} \tag{3.3}$$

Four equations are needed to solve for the four unknowns. Two equations are obtained from the lossless thermoacoustic model with analytical solutions given in equations (2.15) and (2.16). These solutions casted into the matrix form of equation (3.3) to represent m_{11} and m_{21} are shown as follows:

$$m_{11} = \cos(kx) \tag{3.4}$$

$$m_{21} = \frac{i}{\rho a}\sin(kx) \tag{3.5}$$

Two more equations are obtained through the wave characteristics following the analysis of Song and Bolton (2000). The flow is reciprocal and the area of interest is symmetrical. For symmetrical system, m_{11} equals m_{22}. The reciprocity of the flow requires that the determinant of the transfer matrix be unity. These two characteristics are shown as follows:

$$m_{11} = m_{22} \tag{3.6}$$

$$m_{11}m_{22} - m_{12}m_{21} = 1 \tag{3.7}$$

The transfer matrix method used in the experiment is finally shown as:

$$\begin{pmatrix} P_5 \\ u_5 \end{pmatrix} = \begin{pmatrix} \cos(kx) & i\rho a \sin(kx) \\ \frac{i}{\rho a}\sin(kx) & \cos(kx) \end{pmatrix} \begin{pmatrix} P_3 \\ u_3 \end{pmatrix} \tag{3.8}$$

The terms ω, ρ, and a are the angular velocity, density and sound speed, respectively. The velocity at location 3, u_3, is calculated using the lumped element method with the equation given by Swift (2002):

$$u_3 = \frac{i\omega V_c P_4}{S\gamma P_m} \tag{3.9}$$

In the lumped element method, the velocity is calculated using information gained from the compliance. The volume of the compliance, V_c, and its cross-sectional area, S, are measured manually, while pressure, P_4, is measured by the pressure transducer located at the compliance. P_m is the mean pressure set for the experiment.

Four differential pressure transducers (PCB#112A21), connected to a signal conditioner (PCB Piezotronics 48OB21), are used to measure the amplitude of the oscillating pressure at locations P1, P2, P3, P4 and P5 (refer Figure 1). Data is collected using a PC-based data acquisition board. The time phasing is monitored for each test condition to ensure that a near travelling-wave phasing is achieved in every test.

The experimental results are used to calculate a friction factor using equation (2.23). The velocity used for calculating the friction correlation of equation (2.23) is an averaged value calculated as:

$$u_m = \frac{u_1 + u_5}{\sigma} \tag{3.10}$$

where u_1 and u_5 are the velocities at locations 1 and 5, respectively. The velocity, u_m, represents the actual velocity amplitude in the regenerator. All the regenerator samples are tested at a frequency of 30 Hz and a mean pressure of 25 bar.

3.1.2 Properties of gas and dimensions of solid matrix

Four different sizes of mesh screens were tested. The dimensions and parameters of each regenerator mesh screen are listed in Table 3.1.

Table 3.1: Geometric dimension of regenerator tested.

Mesh screen regenerator (material: stainless steel)				
Regenerator	Mesh number	Wire diameter (mm)	Porosity (%)	Hydraulic radius (μm)
1	180	0.058	67.5	30.31
2	200	0.041	74.8	30.27
3	30	0.28	72.7	195
4	94	0.089	74.2	63.79

Table 3.2: Properties of helium gas and stainless steel solid matrix

Properties	**Helium**	**Stainless steel**
Ratio of heat coefficient, γ	1.6667	-
Speed of sound, a (m/s)	1019.2	-
Density, ρ (kg/m^3)	4.0115	7918.1
Specific heat, c_p (J/kg.K)	5193.4	453.84
Gas expansion, β (1/K)	3.3333×10^{-3}	-
Thermal conductivity, k (W/m.K)	0.15243	14.388
Viscosity, μ (kg/m.s)	1.9938×10^{-5}	-

The working medium is helium. Helium is commonly used in thermoacoustic applications because of its good thermal conductivity and specific heat. This allows producing large temperature gradients for a better heat pumping effect. The mesh screen

is made of stainless steel. The properties of both the gas and solid material are shown in Table 3.2. These properties are obtained at a temperature of 300K.

3.2 Flow chart of numerical solutions

The workflow involved in current numerical investigations is shown in a flow chart in Figure 3.2. This workflow describes the steps required for numerical solutions in a very general way. The same philosophy is applied for investigations from chapter three to chapter six although the detailed modelling will differ.

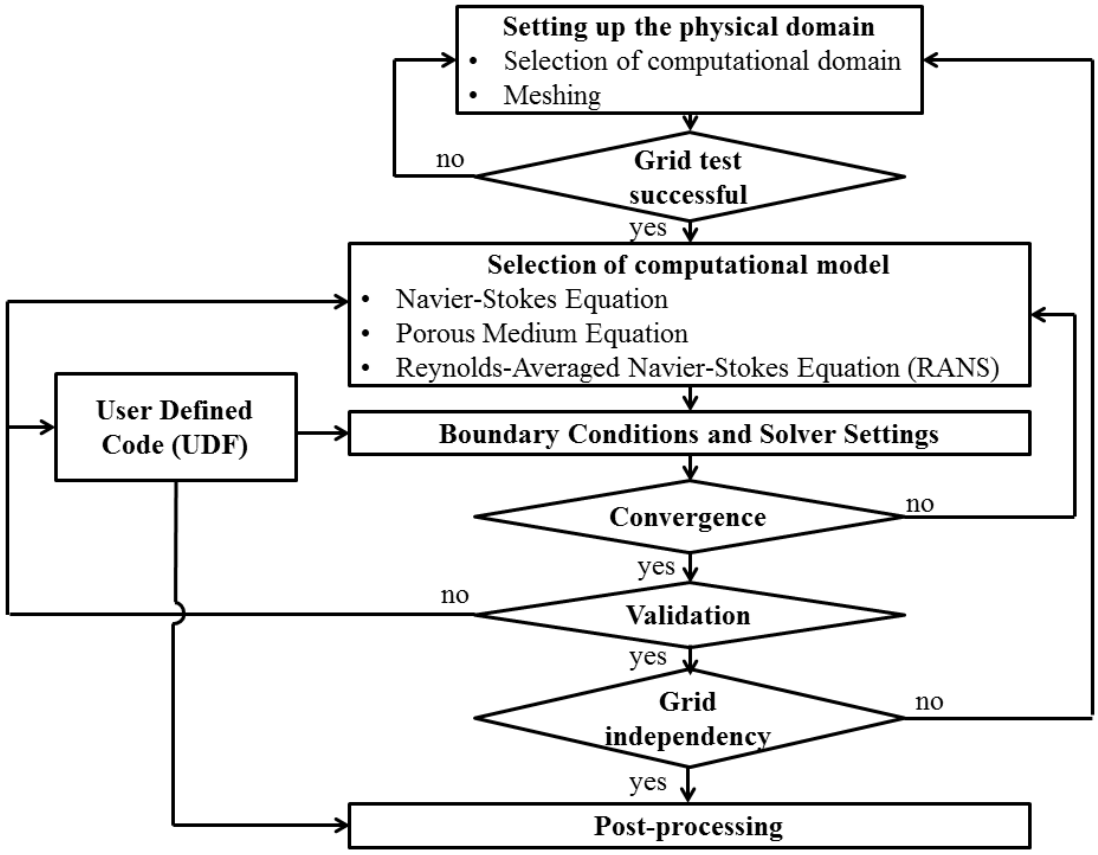

Figure 3.2: Flow chart describing the workflow of the numerical calculations.

The series of boxes on the right side of the flow chart represents the main work flow carried out within ANSYS FLUENT 13.0 (2010). The single box on the left of the flow chart represents the step where the user-defined-code (UDF) is developed via C programming language. These codes will then hooked into and compiled within ANSYS FLUENT 13.0 (2010). The codes were developed for use in several stages during the setting up of the model and post-processing of the numerical data. Appendix

Two shows all the codes developed in C and compiled via UDF function available in ANSYS FLUENT 13.0 (2010).

The main numerical procedure (series of boxes on the right side of the chart) starts with defining a suitable computational domain. The domain is discretised with a suitable mesh and tested for grid errors. An appropriate transport equation is then assigned to the domain depending on the type of internal structure and flow investigated. The boundary conditions are set up with suitable equations developed via user-defined-code (UDF). An appropriate solver is set.

The models developed in this study involve solving unsteady flow field (transient). Calculations start at an assigned size of a time step. The time step for each case is set during "setting up of the solver" so that the best convergence can be achieved for each model. If divergence is reported, the model will be revised based on the type of divergence. The correction may involve a change in the boundary condition or solver setting. If the solution converges, the model will be validated by comparing the results obtained with the experiment or analytical solutions. A modification on the solver setting or user-defined-code that defines the boundary conditions may be needed until reliable results are obtained. Once validated, the model is tested for grid independency. The mesh density is increased until the solution is insensitive to the grid density. The validated grid independent solution is then ready for post-processing and thorough analysis is conducted. A set of user-defined-code was developed during this stage to obtain data required for the relevant flow and heat transfer analysis. Data processing involved software such as MATLAB 2011b, Techplot 360 and Microsoft Excel Office 2007.

3.3 Computational model of the regenerator

The regenerator is modelled using a porous medium theory. A two-dimensional Darcy-Forchheimer porous medium equations are expressed as follows (Hsu, 2005):

$$\sigma \frac{\partial \rho}{\partial t} + \nabla \cdot \left(\rho \vec{v} \right) = 0 \tag{3.11}$$

$$\frac{\partial(\rho\vec{v})}{\partial t}+\nabla\cdot(\rho\vec{v}\vec{v})+\nabla p-\nabla\cdot(\tau)=\left(\frac{\mu\sigma}{K}\cdot\vec{v}+\frac{F\sigma^2\rho}{\sqrt{K}}\cdot|\vec{v}|\vec{v}\right) \tag{3.12}$$

The terms σ, ρ, t, $\vec{v}$, p, τ, μ, K and F represent the porosity, fluid density, time, velocity vector, pressure, stress tensor, fluid kinematic viscosity, permeability coefficient and Forchheimer inertial coefficient, respectively. For a homogeneous porous medium with local thermal equilibrium assumption, the one-dimensional energy equation for this porous region is given as (Bejan et al., 2002):

$$\begin{aligned}\left[\left(\sigma k_f+(1-\sigma)k_s\right)\nabla T+(1-\sigma)q_s'''+\vec{v}\left(-\frac{\partial P}{\partial x}+\rho_f g\right)\right]\\ =\left(\sigma\rho_f c_{p\,f}+(1-\sigma)\rho_s c_s\right)\frac{\partial T}{\partial t}+\rho_f c_{p\,f}\vec{v}\frac{\partial T}{\partial x}\end{aligned} \tag{3.13}$$

where q''' refers to the heat generation rate and T is the temperature. The term c_p is the isobaric specific heat and c is the specific heat. The subscripts f and s refer to fluid and solid constituents, respectively. Assuming local thermal equilibrium, the temperature of the gas and solid structure is the same at any time and spatial location due to the condition of perfect thermal contact of the regenerator.

In ANSYS-FLUENT, the porous medium is solved using equations given as:

$$\frac{\partial(\sigma\rho)}{\partial t}+\nabla\cdot(\sigma\rho\vec{v})=0 \tag{3.14}$$

$$\frac{\partial(\sigma\rho\vec{v})}{\partial t}+\nabla\cdot(\sigma\rho\vec{v}\vec{v})+\sigma\nabla p-\nabla\cdot(\sigma\tau)=\sigma B_f-\left(D\mu+\frac{C\rho}{2}|\vec{v}|\right)\vec{v} \tag{3.15}$$

$$\frac{\partial}{\partial t}\left(\sigma\rho_f E_f+(1-\sigma)\rho_s E_s\right)+\nabla\cdot\left(\vec{v}\left(\rho_f E_f+p\right)\right)=\nabla\cdot\left[k_{eff}\nabla T-(\tau\cdot\vec{v})\right] \tag{3.16}$$

The term $E=c_pT-P/\rho+\vec{v}^2/2$ is the energy of the fluid and $k_{eff}=\sigma k_f+(1-\sigma)k_s$ is the effective thermal conductivity within the porous regions. Note that the velocity vector $\vec{v}$ in ANSYS FLUENT 13.0 (2010) is the superficial value. The real value of velocity within the porous region is the superficial value divided by the porosity of the region,

σ. Relationships between the coefficients (D_x and C_x) used in ANSYS-FLUENT and the coefficients of the standard porous medium theory (permeability coefficient, K, and Forchheimer inertial coefficient, F) may be obtained by dividing equation (3.15) by σ and then compared to equation (3.12). Note that the viscous dissipation represented by the stress tensor, τ, and the body force, B_f, in equation (3.15) is neglected. The relationships obtained are shown as follows:

$$K = \frac{\sigma^2}{D_x} \tag{3.17}$$

$$F = \frac{C_x \sqrt{K}}{2\sigma^3} \tag{3.18}$$

These coefficients characterise the hydrodynamic condition of a porous medium that represent momentum sink (pressure drop) caused by the presence of the medium. As reviewed earlier, the Darcy model suggested that the permeability coefficient alone is enough to represent the pressure drop in a low speed flow. As the speed increases, an inertial effect takes place and the Forchheimer coefficient becomes important to improve the flow model.

3.3.1 Computational domain

The computational model in Figure 3.3 is a two-dimensional axi-symmetrical model. Flow in the domain occupied by the regenerator is solved using the porous medium theory. Elsewhere, the flow and energy transfer is solved using standard Navier-Stokes equation available in ANSYS FLUENT 13.0 (2010).

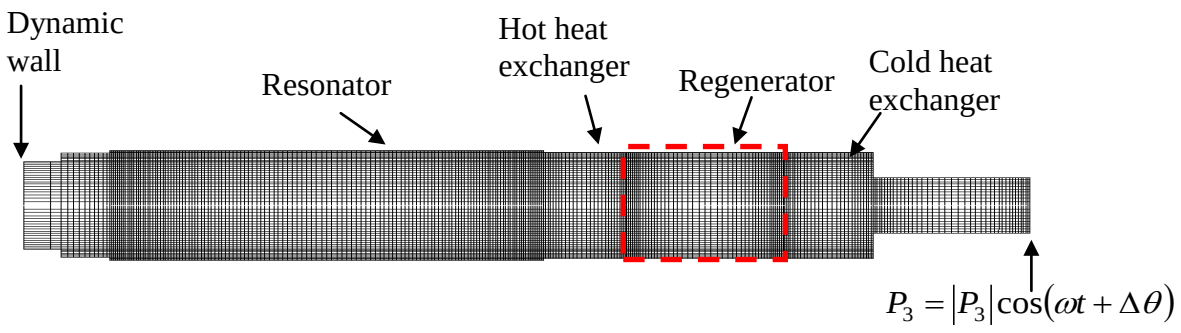

Figure 3.3: Computational domain for the regenerator study. The red-dashed box shows the regenerator domain (porous medium).

A local thermal equilibrium is assumed for the energy equation. Hydrodynamic losses may be attributed to the viscous shear (skin friction) due to the presence of the wall, and a pressure force (form drag) due to the presence of a solid body (Kays and London, 1964). Generally, both effects are considered as a package that contributes to resistance losses. However, ANSYS FLUENT 13.0 (2010) defines body forces as separate from the momentum sink that represents the porous medium. Structures investigated in this study have a relatively high porosity. Furthermore, the flow investigated is limited to a low speed. For the conditions of the current study, it is found that the highest pressure drop due to the body force of the porous structure investigated is less than 0.1%, and hence is neglected.

In this study, the porous medium is treated as isotropic. The losses in the direction other than the main flow direction are assumed small and negligible. The inertial effect is neglected because of the low speed of the flow. Pressure and velocity are expressed in terms of mean components and first order fluctuating components (except that the mean velocity is zero). The simple harmonic equations (c.f. equations (2.10) and (2.11)) are applied in defining the boundary conditions of the computational domain.

A dynamic mesh is imposed as the inlet boundary condition to replicate the movement of the piston of the linear motor. The dynamic mesh area and the resonator are separated by a short tube (15 mm in length and 50 mm in diameter). The computational domain excluded the RLC network, but imposed the phase control using a user-defined-function (UDF) at the inlet wall and the exit pressure at location P3 (refer to Figure 3.1). The last region after the cold heat exchanger is 75.5 mm long and has a diameter of 27.17 mm. The working gas is treated as a compressible ideal gas. The model is solved using an unsteady pressure-based implicit solver with the first order implicit scheme for the discretisation of time. Pressure-velocity coupling is solved using PISO algorithm available in ANSYS FLUENT 13.0 (2010). All variables (pressure, density, momentum and energy) are discretised using second-order upwind method.

The operating pressure is set at 25 bar. Temperatures at the location of the hot and cold heat exchangers are set as a constant with values following the measured temperatures

in the experiment. The temperature developed reflects the result of the thermoacoustic effect occurring at the regenerator when the travelling-wave time phasing is set.

The contribution of pressure loss from the heat exchanger is calculated using the pressure drop prediction for a compact heat exchanger as presented in Kays and London (1964):

$$\frac{\Delta p}{p_1} = \frac{v_1^2/2g}{p_1/\rho_1}\left[\left(K_c + 1 - \sigma^2\right) + 2\left(\frac{1}{\rho} - 1\right) + f\,\frac{L}{r_h}\rho - \frac{1}{\rho}\left(1 - \sigma^2 - K_e\right)\right] \qquad (3.19)$$

The subscript 1 refers to parameters obtained at the inlet of the heat exchanger. The terms p, v, ρ, g, σ, and r_h refer to pressure, velocity, fluid density, gravity, porosity and hydraulic radius, respectively. The parameter K_c, K_e and f are the entrance losses, exit losses and Fanning friction losses respectively, as given in Kays and London (1964). The calculation shows that the contribution of cold heat exchanger losses is within 1%-5% of the whole pressure drop measured between location P2 and P5. The loss varies according to the range of velocity and pressure drop achieved in the experiment. The overall contribution of losses is small because of the low speed of flow. The calculated loss is deducted from the total pressure measured in the experiment. The hydrodynamic condition of the regenerator for CFD modelling is gained by determining the permeability coefficient that gives a pressure drop similar to the experimentally measured value.

3.3.2 Grid independency

The mesh is defined to be denser near the wall and at the interfaces between the rig components inside the resonator. The mesh near the dynamic wall is made coarser to allow for the movement of the wall. The grid independency test is carried out by increasing the number of mesh points by a factor of 1.3. The grid structure remains unchanged with only the mesh density being increased. The resulting pressure drop obtained for grids of different sizes is shown in Figure 3.4. A grid size with a total number of nodes of 9192 is shown to be sufficient to provide a solution that is independent of the grid and therefore selected for this investigation. The model is also run in both single and double precision solver in readiness to test for round-off error. It

appears that the single precision is sufficient to solve this two-dimensional axis-symmetrical model.

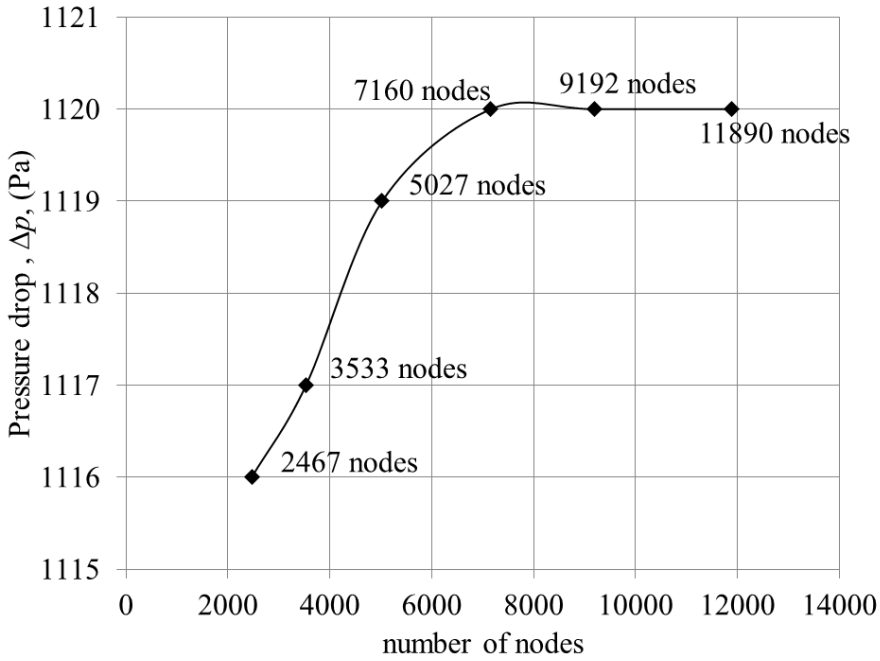

Figure 3.4: Grid independency test for pressure drop in regenerator made of mesh screen #200.

3.3.3 CFD model validation

The model is pre-validated for boundary conditions and then the porous coefficients C_x and D_x are set followed by the final validation of the porous model. In the pre-validation stage, only the velocity and pressure at the location before the porous medium (locations P1 and P2 in Figure 3.1) are compared to the experiment. A good agreement is found as shown in Figure 3.5. Once the model has been pre-validated, the permeability coefficient, *K*, of the regenerator is then predicted by carefully increasing the ANSYS FLUENT's permeability value until the pressure drop matches the experimental value. As soon as the pressure drop matches, the validation is finalised by comparing the inlet velocity, calculated from the measured displacement of linear motor's piston (V1 in Figure 3.5), and pressures at location P2 and P5 (definition of location is given in Figure 3.1). The same procedure is repeated for each case until a good agreement with the experiment is obtained for all samples tested. Figure 3.6 shows the results for pressure at locations P2 and P5 after the permeability tensor set matched the pressure drop measured in the experiment.

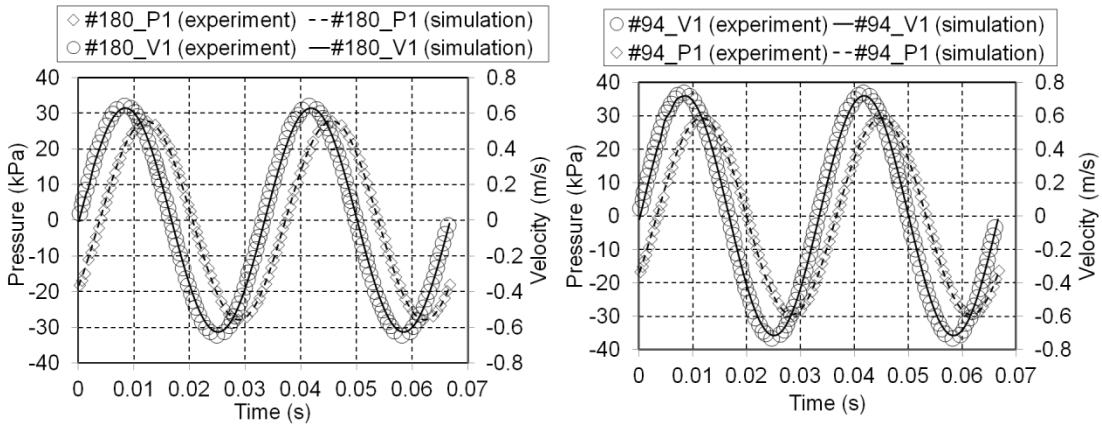

Figure 3.5: Instantaneous pressure at P1 and velocity at the piston.

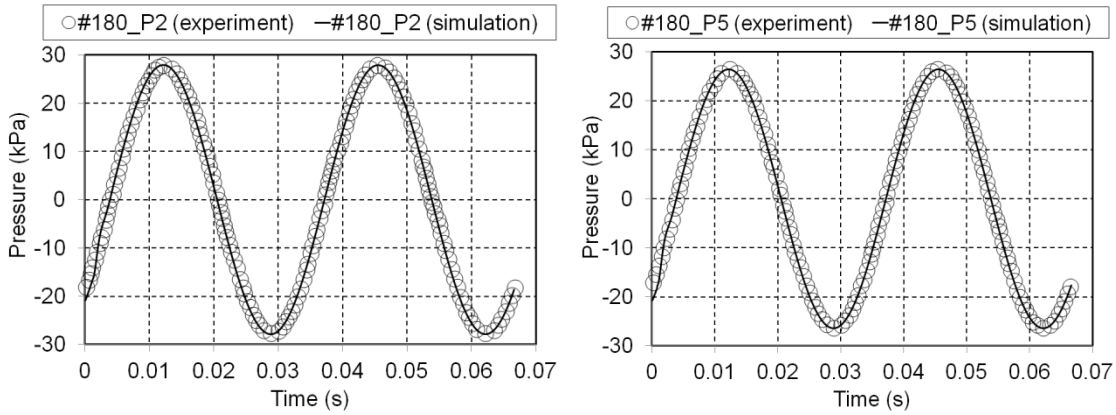

(a)

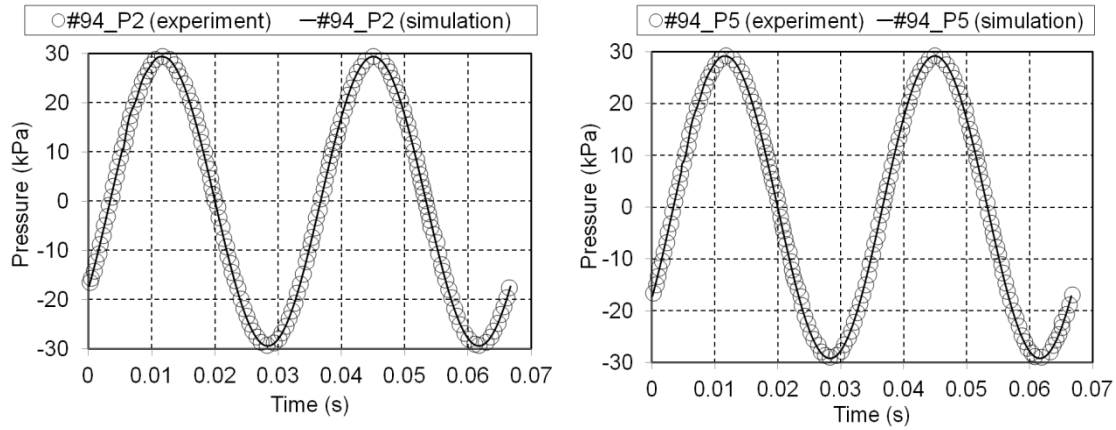

(b)

Figure 3.6: Validation of instantaneous pressures at location P2 and P5 for (a)#180 and (b)#94.

3.4 Friction factor correlation

In the porous medium theory, the friction factor of most porous media is presented by the permeability Reynolds number, $\mathrm{Re}_K = \rho u K^{1/2}/\mu$. The pressure drop characteristic of the porous medium is related to the permeability Reynolds number as given by Bejan et al. (2004):

$$-\nabla P = \frac{1}{2}\frac{f\rho u^2}{\sqrt{K}} \tag{3.20}$$

The pressure gradient can also be represented by the Darcy-Forchheimer model as in equation (2.35). The following formula can be derived from equation (2.35) and equation (3.20):

$$f = \frac{2\sqrt{K}}{\rho u^2}\left[\frac{\mu}{K}u + \frac{F\rho}{\sqrt{K}}u^2\right] \tag{3.21}$$

Further modification of equation (3.21) can be made to include the hydraulic diameter as follows:

$$f = \frac{2\sqrt{K}}{\rho u^2}\cdot\frac{d_h}{d_h}\left[\frac{A_1\mu}{K}u + \frac{A_2 F\rho}{\sqrt{K}}u^2\right] \tag{3.22}$$

$$f = \frac{2d_h}{\sqrt{K}}\cdot\frac{A_1}{\mathrm{Re}_h} + 2A_2F \tag{3.23}$$

The permeability coefficient, K, has a unit $(\text{length})^2$ and the Forchheimer inertial coefficient, F, is dimensionless. Parameters A_1 and A_2 are constants introduced to correlate the equation to fit the experimental result. Simple dimensional analysis shows that equation (3.23) is dimensionless. The derived correlation agrees with the well-known Ergun form presented in equation (2.25). From this derived friction factor, the coefficients a_1 and a_2 in the Ergun equation are defined as:

$$a_1 = \frac{2A_1 d_h}{\sqrt{K}} \tag{3.24}$$

$$a_2 = 2A_2F \tag{3.25}$$

In the simplest Darcy model, when the velocity is small, the inertia effect is neglected and the friction factor is left with:

$$f = \frac{2d_h}{\sqrt{K}} \cdot \frac{A_1}{\mathrm{Re}_h} \tag{3.26}$$

Finally, with this correlation the porous coefficient predicted through CFD model is used to predict the friction factor of the porous medium and then compared to the experimentally calculated friction factor for the actual sample. The friction factor correlation presented in equation (3.26) is derived from the Darcy correlation. Hence comparing the simulation results to experiment requires the friction factor predicted by simulation model to be divided by four. In this study, all comparisons are carried out in line with the Fanning-based correlation. The Fanning-based correlation for computational models is given as:

$$f = \frac{d_h}{2\sqrt{K}} \cdot \frac{A_1}{\mathrm{Re}_h} \tag{3.27}$$

Permeability is an empirical constant used in the porous medium community to characterize the blockage occurring due to the presence of porous media. The permeability coefficients for the regenerator samples investigated, obtained from the CFD-assisted method, are tabulated in Table 3.3.

Table 3.3: CFD-predicted permeability for regenerator investigated.

Regenerator mesh numbers	#200	#180	#94	#30
Permeability, K (m^2)	1.1505×10^{-10}	0.99012×10^{-10}	0.105715×10^{-10}	0.04129×10^{-10}

A higher regenerator mesh number refers to a finer mesh. This is portrayed in the value of the wire diameter of each sample as listed in Table 3.1. The permeability is high at a mesh number #30 and decreases as the mesh number increases to #200. The permeability coefficient in Table 3.3 is used to calculate the friction factor using

equation (3.27). Several cases of measurement/numerical prediction were considered for each sample. These corresponded to different level of excitation produced by the linear motor, and result in different values of Reynolds number, Re_d, as defined in equation (2.28). The results are plotted in Figure 3.7.

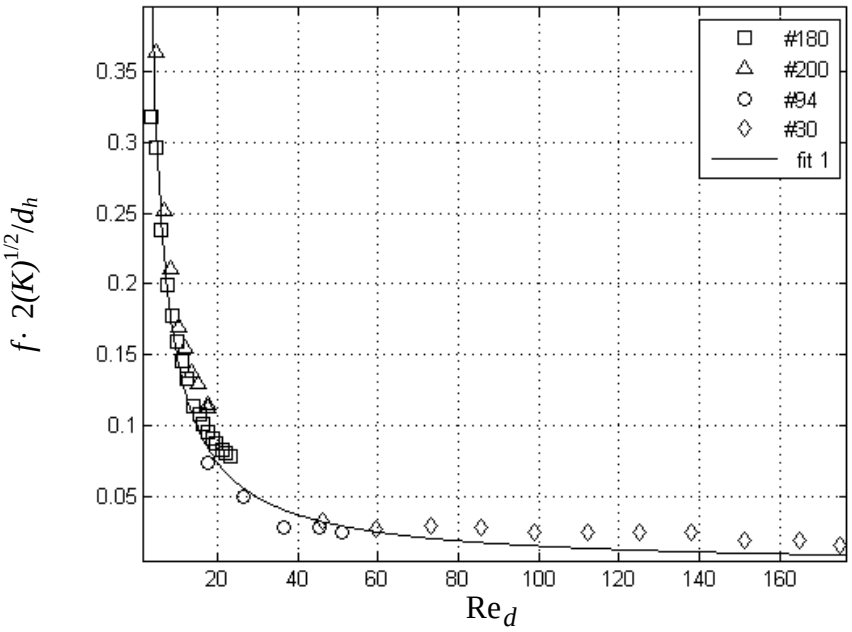

Figure 3.7: Correlation of friction factor in terms of d_h, K and Re_d.

In Figure 3.7 there are 17 square, 9 triangular, 6 circle and 11 diamond symbols that represent tests of samples #180, #200, #94 and #30, respectively. A fit can be obtained for all the cases as shown by the line in the figure. The friction data obtained from the numerical model fitted the following correlation:

$$f = \frac{d_h}{2\sqrt{K}} \cdot \frac{1.48}{\mathrm{Re}_d} \tag{3.28}$$

The correlation is obtained based on the least-square fit with a confidence level of 95%. The correlation represents a friction loss of all the four mesh screens tested. The correlation best represents the hydrodynamic losses of high mesh numbers and slightly under predicts the losses occurring at low mesh numbers. The maximum difference between the correlation and the friction value of low mesh number are 30% and 50 % for #94 and #30 respectively. The diamond symbols for Re_d larger than 60 are clearly

deviating from the line. This may be due to the fact that for large Reybolds number and a very coarse size of regenerator mesh screens the Forchheimer inertial coefficient may become significant and equation (3.23) may apply. The constant 2 in the denominator of equation (3.28) is the result of the conversion from Darcy-based correlation to Fanning-based correlation and left for clarity on purpose.

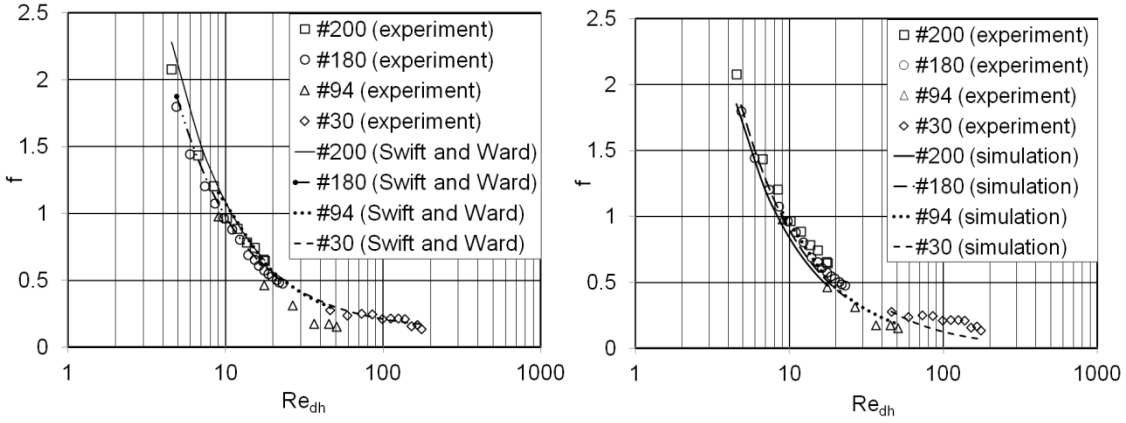

(a) (b)

Figure 3.8: Comparison between friction factor from experiment; (a) Swift and Ward (1996) correlation and; (b) current CFD-assisted correlation.

Figure 3.8 shows that the numerical results represented by correlation (3.28) and the results calculated using Swift and Ward (1996) correlation (equations (2.25) to (2.27)) both qualitatively agree with experimental measurement. Swift and Ward (1996) defined their friction correlation based on the Darcy-based correlation, and therefore the results calculated through equations (2.25) to (2.27) need to be divided by 4 for the purpose of comparison. The results indicate that the assumption used by Swift and Ward (1996) is acceptable. The assumption states that pressure drop and velocity relates in a similar way as in steady flows (Swift and Ward, 1996). There are arguments found in the literature that claimed that a pressure drop condition in oscillatory flow deviated from predictions of steady flow. An explanation to that situation could relate to the influence of phase-shifting between pressure and velocity. Further discussion of this is provided in section 3.5 for low mesh number regenerators. Current results have shown that a pressure drop condition for an oscillatory flow with travelling-wave time-phasing does not deviate much from the Swift and Ward's correlation, especially when the mesh number is high.

3.5 Analysis of phase shift

Time phasing between pressure and velocity is important in determining the hydrodynamic condition of porous media such as the regenerators. If the pressure and velocity are not in phase, the maximum pressure occurs at a certain phase lag compared to maximum velocity. Then, the amplitude data may not be accurate enough to represent the friction factor according to equation (2.23).

In other studies (Ju et al., 1998, Zhao and Cheng, 1996, and Cha et al., 2008), the phase shift between pressures at location before and after the regenerator is observed when the operating frequency increases. The phase shift effect is observed even at a frequency as low as 5 Hz in the results presented in Cha et al. (2008). Zhao and Cheng (1996) reported that the phase shift between pressure and velocity in their experimental investigation appeared at a very low kinetic Reynolds number (calculated to be equivalent to 2.5Hz).

In the current experiment it is not possible to measure the pressure drop and velocity amplitude within the regenerator. However, the numerical model is validated for several points within the rig. So it is reasonable to expect that it will reliably predict the pressure drop and velocity within the regenerator.

Figure 3.9 shows the pressure drop and velocity within the regenerator. For coarse regenerator mesh screens (#200 and #180), the pressure drop is in phase with the velocity within the regenerator. When the mesh screen is coarser (#30 and #94), the pressure drop becomes slightly out of phase from the velocity within the regenerator. The instantaneous pressure drop tends to lead the instantaneous velocity further as the mesh becomes coarser. Theoretically, bigger pore size results in slower velocity of flow within the porous region, if set at a similar level of excitation. The shear stress and form drag is likely to be smaller too. However, due to the limitation of the experimental setup, data for coarse mesh number are only available for a relatively high Reynolds number. Similarly, data for fine mesh are only available for the low Reynolds number region. Therefore, it is possible that the phase shift between pressure and velocity seen within the coarse mesh is due to the relatively high velocity excited by the linear motor. This could be the reason for the time delay between pressure drop and velocity. It is

likely that the phase shift between pressure and velocity is the feature of the inertial effect described by the Forchheimer model.

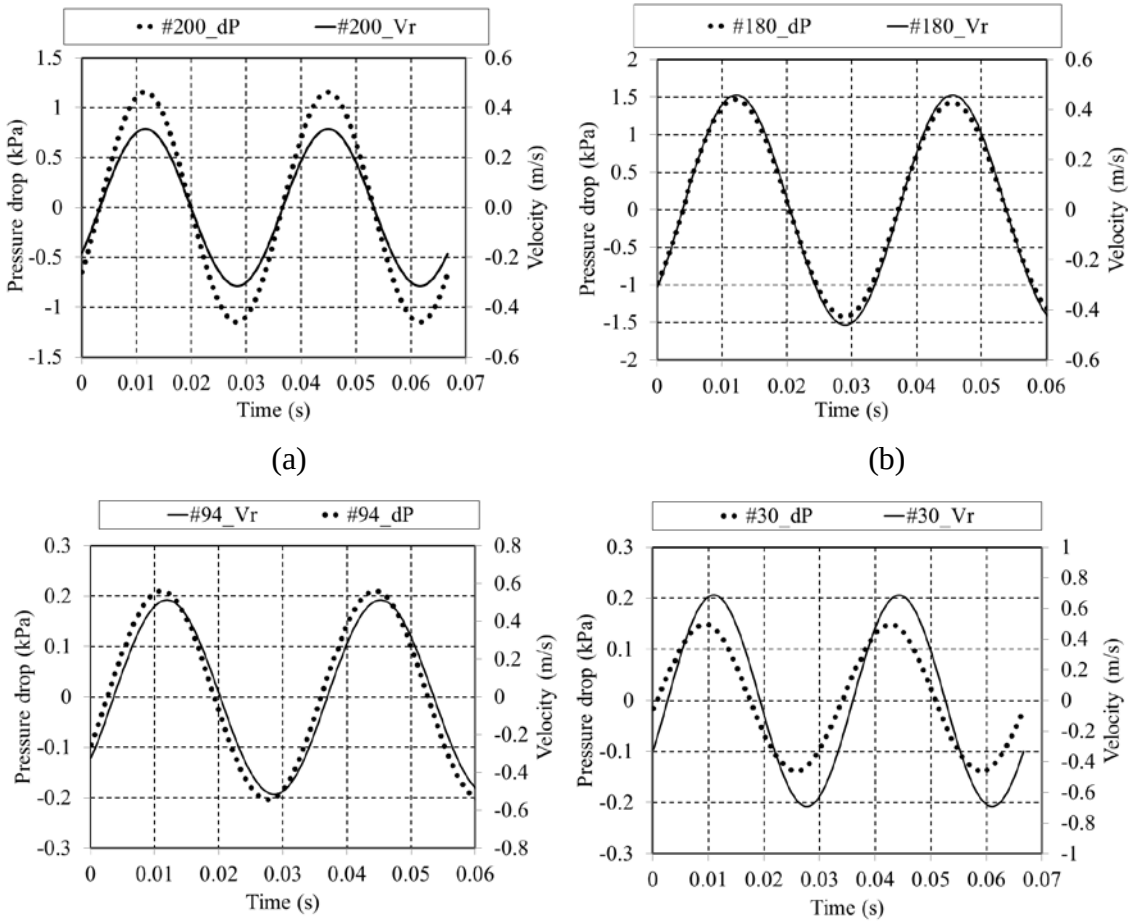

Figure 3.9: Pressure drop (dP) and velocity at regenerator (Vr) for (a)#200 (b)#180 (c)#94 (d)#30.

3.6 The role of hydrodynamic condition of the regenerator in thermoacoustic applications

The flow resistance is represented in thermoacoustic theory as viscous resistance, r_v, defined by Yu and Jaworski (2010) as:

$$r_v = \frac{\mu_m}{r_h^2 \sigma A}\left(\frac{a_1}{8} + \frac{a_2 \,\mathrm{Re}}{3\pi}\right) \tag{3.29}$$

In current thermoacoustic practice, constants a_1 and a_2 refer to coefficients of Swift and Ward (1996) correlation as given in equations (2.26) and (2.27), respectively. In the CFD modelling described in the literature, information on porosity alone is insufficient because the resistance is modelled using permeability and when necessary the Forchheimer inertial coefficients are needed. The correlation developed in this study, which agrees with Swift and Ward (1996) correlation, takes into account the permeability coefficient of the porous medium only. Nevertheless, the correlation developed allows further analysis of flow resistance of thermoacoustic systems using CFD methods such as ANSYS FLUENT 13.0 (2010).

Clearly, equation (3.29) requires both a_1 and a_2. Since inertial effects are neglected, coefficient a_2 is assumed to be zero. Assuming a Darcy flow, the viscous resistance in equation (3.29) can now be analysed in terms of the permeability coefficient and rewritten as:

$$r_v = \frac{\mu_m}{r_h^2 \sigma A}\left(\frac{0.74 d_h}{8\sqrt{K}}\right) \tag{3.30}$$

The role of hydrodynamic losses in the regenerator and how it impacts the performance of a thermoacoustic system is illustrated here by examining the regenerator's power output capacity of a thermoacoustic engine, ψ_p, defined by Yu and Jaworski (2010) as:

$$\begin{aligned}\psi_p = &-\frac{\pi \,\mathrm{Pr}}{2n^2}\frac{\delta_k}{r_h}\left(\frac{a_1}{8}+\frac{a_2\,\mathrm{Re}}{3\pi}\right)-\pi(\gamma-1)\,\mathrm{Im}\left(\frac{\varepsilon_s+(g_c+g_v)\varepsilon_h}{1+\varepsilon_s+\left(g_c+e^{2i\theta_T}g_v\right)\varepsilon_h}\right)\\ &+\frac{1}{2n}\,\mathrm{Re}\left(1-\frac{\varepsilon_s+(g_c+g_v)\varepsilon_h}{1+\varepsilon_s+\left(g_c+e^{2i\theta_T}g_v\right)\varepsilon_h}\right)\Theta_{\nabla T}\end{aligned} \tag{3.31}$$

In equation (3.31), a_1 and a_2 are the coefficients from the friction factor correlations. Pr is the Prandtl number, $\delta_k=(2k/\omega\rho c_p)^{1/2}$ is the thermal penetration depth with k, ρ and c_p represents the working fluid property of thermal conductivity, density and specific heat, respectively. The term n is the impedance factor defined as $Z/\rho a$ (a is the sound speed). Im( ) and Re( ) represents the imaginary and real part of the term in brackets. ε_s and ε_h are defined as $\varepsilon_s=\sigma\rho_m c_p,m/(1-\sigma)$. $\rho_{s,m}c_{s,m}$ (s represents solid) and $\varepsilon_h=8ir_h^2/b(\sigma)\mathrm{Pr}^{1/3}\delta_k^2$.

Parameter $b(\sigma)$, g_c(Re) and g_v(Re) are factors resulting from the fitting of heat transfer data of Kays and London (1964). Further details on the description of the variables are available in Swift and Ward (1996).

The first and the second terms in the first bracket on the right hand side of equation (3.31) represent the hydrodynamic impact on the performance of the regenerator. Meanwhile, the second and the third terms on the right hand side of the equation is the effect of heat transfer on the performance of the regenerator. It is clear that the hydrodynamic characteristics, commonly defined by friction factor correlation, have an impact on the overall performance of the regenerator. In the thermoacoustic engine application, the regenerator acts as a power amplifier that stores and supplies heat to the working medium. The hydrodynamic resistance, according to equation (3.31), will degrade the performance of the entire system.

The central focus of this study is pressure drop. It is shown that a "coarse" structure provides a favourable low pressure drop. However the resulting heat transfer performance in the practical application may not be as attractive judging from the size of the pore and the thermal contact offered by it. The heat transfer contribution (the second and the third terms of equation (3.31)) is also a condition that needs to be considered when choosing an appropriate dimension of the porous medium structure for use in a thermoacoustic system, suggested as part of future investigations.

3.7 Summary

Modelling the full state of a regenerator may be very computationally demanding due to the very small size of pore and the tortuosity of the structure. Hence, in this chapter, an economic way of modelling a regenerator is developed. The structure is modelled as a porous medium. Modelling a porous medium requires a proper closure model to represent the momentum losses and thermal inertia of the flow due to the presence of the structure. In this study, the momentum losses are modelled with pressure drop data gained from the experiment conducted in a well-controlled travelling-wave time-phasing.

The literature shows that friction correlation in an oscillatory flow condition differs from the steady flow condition. This study, however, suggested that the difference in

friction correlation between oscillatory flow and steady flow is related to the phase shifting between pressure and velocity used in predicting the friction factor. For a travelling-wave system, when the pressure and velocity are in-phase, the pressure drop and velocity relate to each other in a similar way as in a steady flow. Results of this investigation shows that the size of the mesh screen used in a travelling-wave system should not be too big, otherwise it may result in difficulty in sustaining the travelling-wave time-phasing within the regenerator. If this happens the friction correlation may need to be revised to account for the effect of the phase-shifting phenomenon.

The illustration of the role of the hydrodynamic performance of a regenerator on a thermoacoustic system suggests that apart from the hydrodynamic condition, the thermal condition is also an important criterion to consider when selecting a regenerator. A regenerator with a coarse mesh screen may be favourable in that it provides a smaller pressure drop. Nevertheless, the thermal contact may not be as good as the fine mesh. Further investigation on this subject is strongly suggested to cover the whole range of the thermoacoustic phenomena, including the heat transfer within the regenerator.

Chapter Four: Heat exchanger: Flow and heat transfer at low amplitude oscillatory flow

In this chapter, the development of a computational model of flow and thermal performance of a heat exchanger working in a low amplitude standing-wave thermoacoustic system is presented and validated by earlier experimental results. This is covered in sections 4.1 to 4.3. The effect of initial fluid temperature on the flow and heat transfer is shown in section 4.4. The effect of the imposed temperature field on the oscillatory flow within the heat exchanger is discussed in section 4.5. Section 4.6 is devoted to the study of the flow and heat transfer at different thermoacoustic device orientations. Section 4.7 reports the dimensional analysis of the Navier Stokes equations for the identification of suitable dimensionless number to be used in this study. The effect of fluid temperature and device orientation on viscous dissipation is presented in section 4.8 followed by a summary in section 4.9.

4.1 The computational model

The computational model is developed based on the experimental set up of Shi et al. (2010a, b). A full two-dimensional model referred to as "long model", as shown by the red-dashed box in Figure 4.1(a), is created covering a rectangular area 0.132 m x 7.4 m of the quarter-wavelength resonator. The cold and hot plates of the heat exchangers had a thickness, d, of 3 mm and are arranged in a parallel configuration with a spacing, D, of 6 mm between them. The heat exchangers are located next to each other with a joint positioned at 0.17λ from the pressure antinode. The wavelength, λ, is defined in equation (2.5). The location of the pressure antinode for this quarter-wavelength rig with nitrogen as a working medium is at the end wall as shown in Figure 4.1. The heat exchanger plates are modelled exactly as they are arranged in the experiment together with five pairs of "dummies" treated as adiabatic plates. The dummies are used in the experiment to provide consistent porosities within the investigated area, as reported in detail by Shi et al. (2010b).

A two-dimensional "long model" extending over the whole height of the test section is used due to the asymmetrical flow characteristics observed experimentally in the rig

(Shi et al., 2010b). The use of symmetry or periodic flow boundary condition is inappropriate due to the presence of temperature-driven buoyancy effects. The intention was to replicate as closely as possible the phenomena taking place in the physical apparatus.

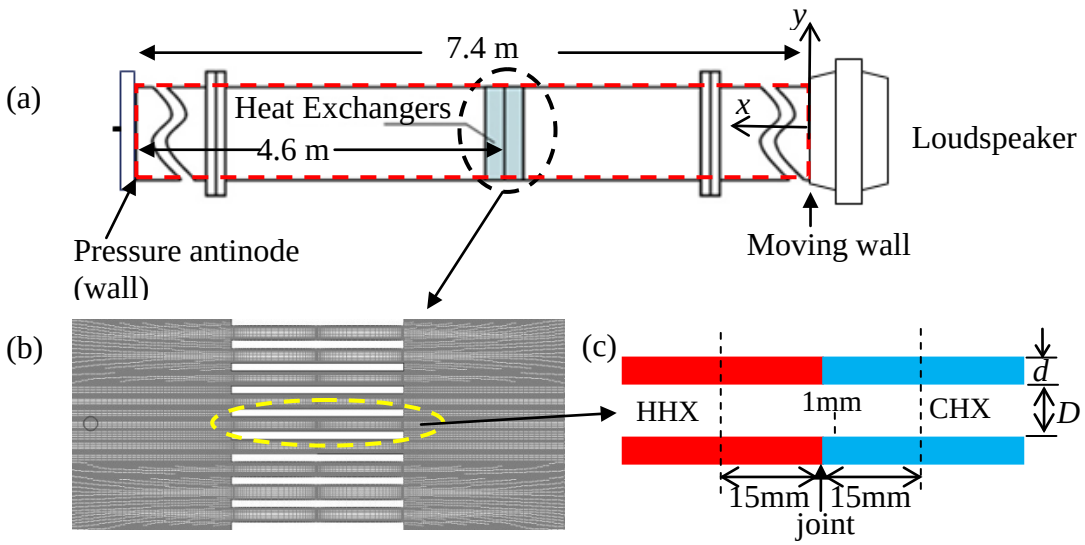

Figure 4.1: (a) The computational domain for "long model" (red dashed-box) shown on the schematic diagram of the experimental setup (b) fine mesh generated in the critical area of heat exchangers (c) designation/location used for analysis in this chapter.

Oscillatory flow past a heat exchanger assembly generates vortex structures that travel away from the edge and subsequently sucked back into the flow channels. The area needs to be large enough to prevent the flow structures from leaving the computational domain (Worlikar and Knio, 1996). In addition, the experimental data are based on phases determined by comparing the phase of velocity between the plates to the phase of pressure at the pressure antinode. Hence, a full two-dimensional "long model" is chosen to be the best model to represent the best match for the phases between the numerical and experimental results.

The mesh, as shown in Figure 4.1(b), is designed to be denser within the vicinity of the heat exchanger covering a length of 300 mm to the left and right from the ends of the heat exchangers. Elsewhere, a much coarser mesh is adopted as the problem consists of solving the governing equations for an empty resonator.

This methodology is tested numerically and verified by comparing the numerically predicted pressures and velocities to the theoretical predictions of linear thermoacoustic theory (Swift, 2002). It is found that, at a location of 300 mm away from the heat exchanger, the pressure and velocity follows the linear model as predicted. The use of a coarser mesh beyond this distance is thus justified. The boundary condition at the right end of the resonator is defined as a moving wall to replicate the acoustic displacement induced by the loudspeaker. The displacement is modelled as a wave displacement, δ, represented by:

$$\delta = \left[\frac{p_A}{\omega \rho_m a} \sin\left(k_w x_s\right) \right] \cos\left(\omega t\right) \tag{4.1}$$

In equation (4.1), ω, ρ_m, a, k_w and t are the angular velocity, mean density, speed of sound, wave number and time, respectively. The term p_A is the oscillating pressure at the location of pressure antinode and x_s is the distance from the joint to the pressure antinode (shown as 4.6 m in Figure 4.1(a)). The mean pressure, p_m, is 0.1 MPa. The drive ratio (p_A/p_m) of the low amplitude flow investigated throughout this chapter is 0.3%. The resonator wall is treated as adiabatic. The model is solved for two thermal conditions. In the first model, the wall of the heat exchangers is adiabatic. In the second model, two heat exchangers are assigned two different temperatures. The temperatures at cold and hot heat exchangers are modelled as a function of location. The profile of the wall temperature is assigned following a linear interpolation of the experimentally measured wall temperatures reported by Shi et al. (2010b) as shown in Figure 4.2.

The fluid used in this study is nitrogen modelled as a compressible gas with temperature-dependent properties. A seventh order polynomial model suggested by Abramenko et al. (1992) is selected to model temperature-dependent thermal conductivity while a power law model suggested by Swift (2002) is used for temperature-dependent viscosity. The flow is modelled in ANSYS-FLUENT13.0 (2010) with a two dimensional Navier-Stokes equation as described by equations (2.1), (2.2) and (2.3).

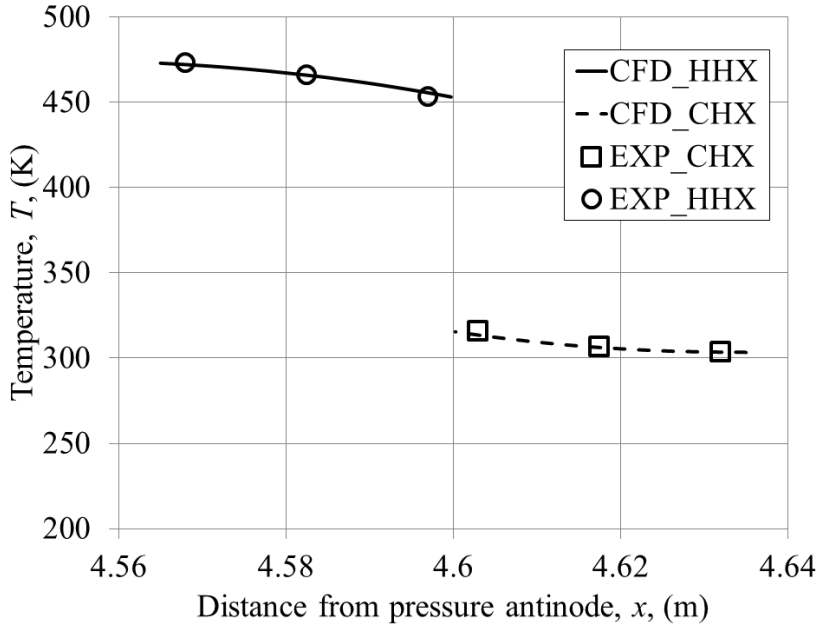

Figure 4.2: Heat exchangers wall temperature.

Viscous heating (the last nine terms on the right-hand-side of equation (2.3)) is taken into account in this model. This is included because of the presence of heat exchangers with large surface area. The flow is assumed laminar due to the small Reynolds number involved in the case investigated. The Pressure-Implicit with Splitting Operators (PISO) algorithm is selected for pressure-velocity coupling as the algorithm provides better solutions for transient cases (ANSYS FLUENT 13.0, 2010).

A first order scheme is used for the discretisation of time due to the presence of the moving wall (ANSYS FLUENT 13.0, 2010). The momentum and energy equations are discretised using a second order scheme with convergence set to 1×10^{-4} for the velocity and continuity equation, and 1×10^{-7} for energy equation. The density is calculated using the second order numerical scheme. The best time step for convergence is determined and set at 1200 steps per cycle. The area-weighted-average of pressure at the end wall, known as pressure antinode, is monitored until steady state oscillatory flow is attained. The steady oscillatory state is defined as the state when pressure, velocity and temperature do not change much during each cycle change. When the steady oscillatory state condition is reached, the model is validated and used for analysis. In this study, the development of flow within one oscillatory cycle is investigated following a time scales as defined in Figure 4.3.

Figure 4.3 illustrates the relationship between pressure, velocity and gas displacement for the 20 phases of a flow cycle. Phase ϕ1 is set for the maximum value of the oscillating pressure at the location of pressure antinode (rigid wall of resonator). The cycle is subdivided into twenty phases starting from the first phase, ϕ1. This definition of phases will be used for the rest of the investigation until chapter six.

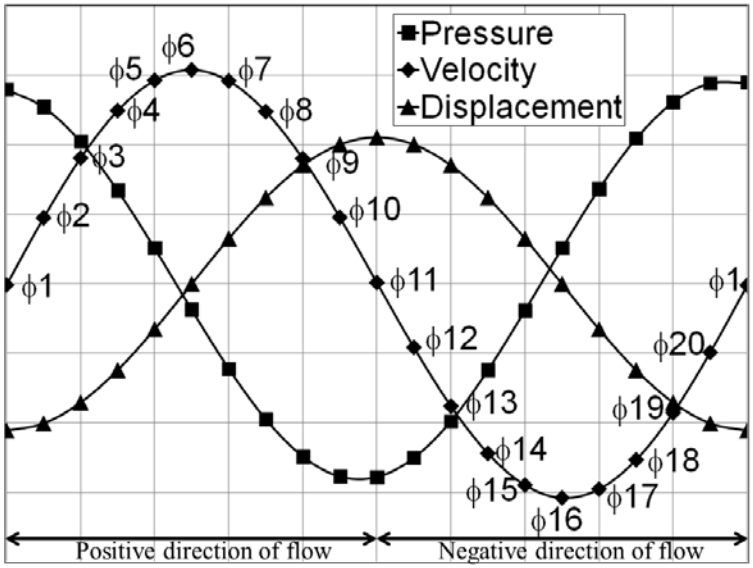

Figure 4.3: Pressure, velocity and displacement over 20 phases of a flow cycle.

4.2 Grid independency

A structured mesh is developed for the model. Three selections of mesh density are made in both *x* and *y*-directions of the computational domain. The description of mesh density is given in Table 4.1. The term y^+ indicates the location of the nearest nodes to the wall and serves as a reference for resolution of mesh near the wall, which will be relevant for the investigation of turbulence to be presented in chapter five.

Table 4.1: Description of mesh counts for grid independency study.

Case	**Total cells**	y^+
Grid 1	37260	1.22
Grid 2	45910	0.94
Grid 3	52830	0.78

The resulting velocity profiles are plotted for every case and comparisons for selected phases between profiles of different mesh density, to check for grid independency, are carried out. Figure 4.4 shows the effect of mesh density on the velocity profiles.

Generally, values of velocities for all locations and times do not differ between solutions obtained using grids 2 and 3.

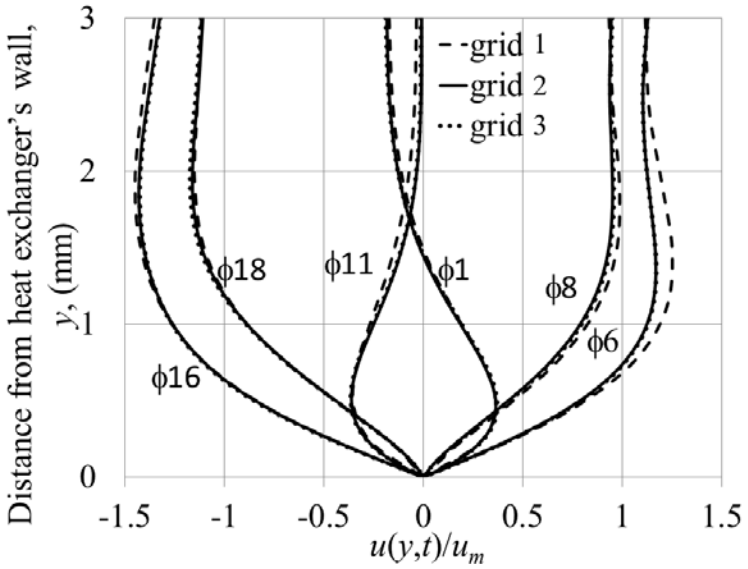

Figure 4.4: Grid independency test for velocity profiles within the flow channel.

At low mesh density, the velocity profile is slightly over predicted at all of the 6 phases shown. The velocity within the boundary layer appears the same for all cases because the mesh is always designed denser in that area. It is found that model with a total of 45910 cells is sufficient to provide a grid-independent solution.

4.3 Model validation

The velocity ampitude obtained from the converged model that reaches steady oscillatory state is then compared to the experimental result to validate the model. The validation is shown in Figure 4.5. The velocity amplitude shown is for the location at the centre of the gap between the plates of the heat exchanger, 1 mm away from the joint, for all the 20 phases of a flow cycle. The location is defined in Figure 4.1 (b). Referring to Figure 4.5(a) for the adiabatic condition, results from available theoretical solution (equation (2.17)) and the experimental results of Shi et al. (2010a) are compared to the current numerical results. The theoretical solution is calculated for the mean density taken at 300 K. A good match between the experiment, simulation and analytical solution is shown for the adiabatic flow. Referring to Figure 4.5(b) for the configuration with imposed temperature difference, the theoretical adiabatic solutions is plotted as a reference, together with experimental results and numerical solution.

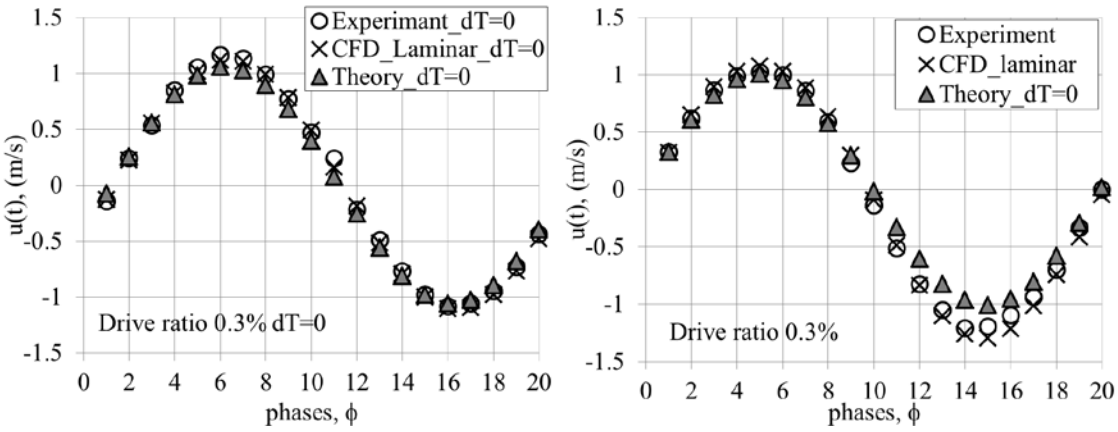

(a) (b)

Figure 4.5: Velocity amplitude from model with heat exchanger walls treated as (a) adiabatic and (b) constant temperature profile.

Experimental results and numerical solutions show that, when there is an influence of heat exchanger wall temperature, the flow in the second half of the cycle exhibits larger amplitude of velocity compared to the first half of the cycle. This is counterintuitive since one would expect that a hotter fluid would travel with higher velocity in the first half of the cycle, while cold fluid would flow with a lower velocity in the second half of the cycle. It is possible that there is a mean flow along the channels (streaming effect) due to the convective flows at the ends of the heat exchanger assembly. This is discussed later in section 4.5.3.

Figure 4.6 shows the validation of temperature profiles for a location 15 mm from the joint, (refer to Figure 4.1(c) for definition of location) above both the cold and hot plates. Good agreement between experimental and theoretical values at both locations is achieved. The largest disparity between the simulation results and experiment is 17 °C at the hot side and 18 °C at the cold side of the heat exchanger (2 °C higher than experimental uncertainty reported by Shi et al. (2010b)). Apart from the disparity stated, the trend of the temperature profiles agreed qualitatively well with experimental values. The disparity could be associated to the heat accumulated during the period of experimental data collection or may be an artefact of the physical three-dimensional experimental set up.

An investigation into the initial fluid temperature was then carried out to check for a possibility of bringing the temperature field within the computational domain closer to experiment. This is described in the next section.

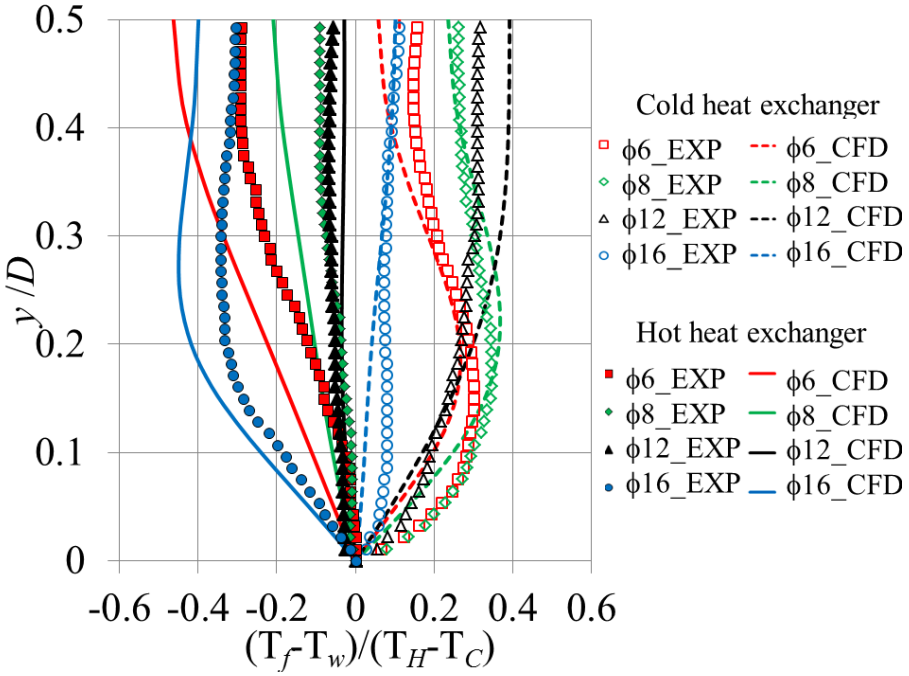

Figure 4.6: Temperature profiles for cold and hot heat exchangers-comparison between experimental (EXP) and computational (CFD) results.

4.4 Investigation of the effect of initial fluid temperature on flow and heat transfer

A computational model with temperature defined at the heat exchanger walls requires a longer time to reach steady oscillatory flow in comparison to the model with adiabatic wall. This is also reported by Worlikar and Knio (1998). Their stratified model requires double the computational time needed for adiabatic flow to reach steady oscillatory state. The study of Worlikar and Knio (1998) involves a very small temperature difference. In the current study, the model is developed based on the experimental measurement within the heat exchanger with a relatively high temperature gradient. It is difficult to numerically achieve a temperature field similar to that of experiment at the time experimental data are collected.

A possible way of bringing the temperature field of the computational model to a state similar to the experiment, within a reasonable computational time, is through setting an

appropriate initial fluid temperature to the model. Three approaches of initial temperature were investigated and are discussed in this section.

First, the model is initialised at 300 K. A comparison of the temperature contour for phase $\phi 1$, within the area similar to visualisation recorded in the experiment, is shown in Figure 4.7 (a) and (b). The model is iterated until it reaches 70 flow cycles which is equivalent to 5 seconds of real time. Figure 4.7(b) shows that the resulting temperature field is still dominated by the low temperature of the initial 300 K. On the other hand, the experimental data (c.f. Figure 4.7(a)) shows that the average fluid temperature is considerably higher due to the fact that the experimental data is collected after the flow is conveniently settled in the steady oscillatory state with an established thermal equilibrium. At that stage the heat has been accumulated in the system giving rise to the mean temperature of the flow. For the computational model with initial temperature of 300 K, a significant amount of computational time and effort will be required if a similar heat accumulation as in experiment is to be achieved.

A second attempt is made by initialising the model with a fluid mean temperature closer to the experimental temperature. The experimental results show a value of mean temperature around 360 K. This value is used as the initial temperature in this second attempt. The result is shown in Figure 4.7(c). Although the resulting mean temperature is visually shown to be closer to the experimental results, the effect of natural convection that has been experimentally observed at the open area next to the cold heat exchanger is not visible in the computational result. In addition, the temperature of the fluid within the channel of the cold heat exchanger reduces from the initial high temperature to a lower temperature due to the cooling effect at that location. The reason for the mismatch is not clear especially as the wall of the heat exchanger is already modelled following the temperature measured by the thermocouples as reported in the experimental work. However, it is possible that additional features need to be introduced into the model such as heat losses (the modelled resonator is adiabatic, in reality there are considerable heat losses); or three-dimensionality of the real flow versus a two-dimensional numerical solution. There may also be an uncertainty related to the experimental measurement as the calibration is reported to be only carried out at the area of the hot heat exchanger. Similarly, there is a possibility that the resolution of

the PLIF measurement for the experimental results obtained within the cold heat exchanger is compromised.

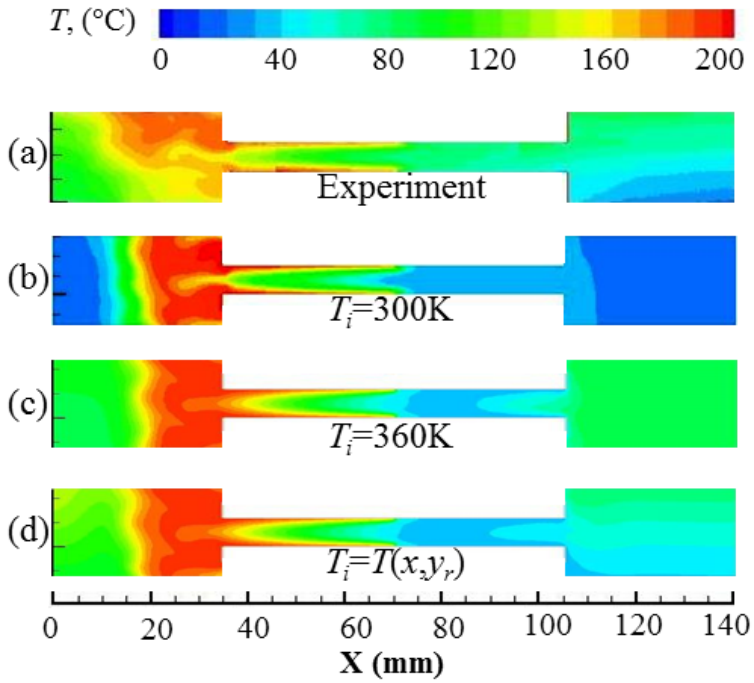

Figure 4.7: Temperature contours at phase ϕ1 from numerical models initialised at different constant temperature.

The third approach is an attempt to improve the model of natural convection observed experimentally at the end of the plates. This is undertaken by initialising the model with an approximate temperature field estimated from the experimental results (as given in Appendix Two). The resulting temperature contour from this model is shown in Figure 4.7(d). The effect of initialisation temperature is still seen dominating the temperature field especially at the open area next to the parallel-plate heat exchangers. In the area between the plates of the heat exchanger, the wall temperature seems to control the temperature within the area.

Figure 4.8 shows the effect of initial temperatures on the velocity amplitudes at 1 mm away from the joint above the cold plate. Evidently, a higher mean temperature of 360K results in a slightly higher amplitude of velocity especially during the second half of the cycle. This may suggest that the experimental temperature field is affected by the accumulation of heat within the investigated area since raising initial temperature from 300 K to 360 K brings the solution closer to experimental results. Nevertheless, the

resulting profiles of temperature for all models shown in Figure 4.6 exhibit similar trends to the experiment. Further studies pertaining to the temperature field would be required to provide the best agreement.

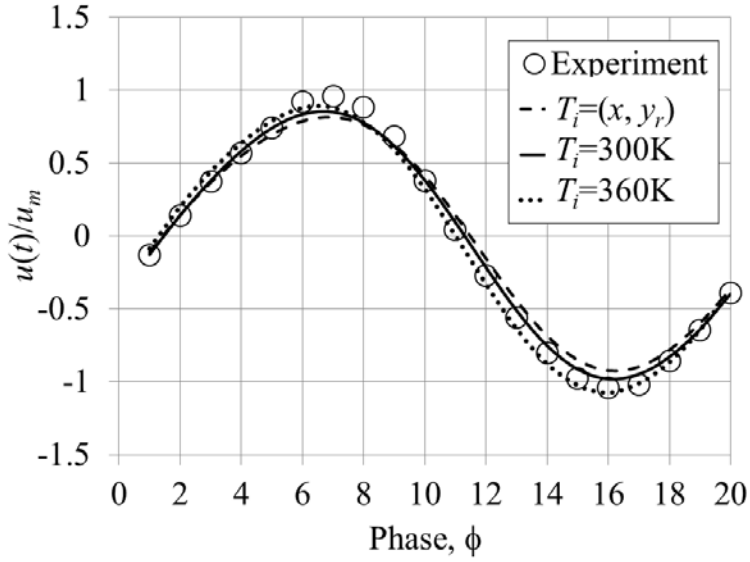

Figure 4.8: The effect of initial temperature on the velocity amplitude.

Finally, the effect of initial temperature on the heat flux is shown in Figure 4.9. Here, the heat flux is calculated in the same way as reported in Shi et al. (2010b). The heat flux is averaged over the length of the heat exchanger and is calculated as:

$$q_{h,c} = \frac{1}{l}\int_0^l -k\frac{dT}{dy}\bigg|_{wall} dx \tag{4.2}$$

The subscript *c* and *h* refers to cold and hot heat exchanger, respectively.

Figure 4.9 shows that the wall heat flux predicted by the model initialised at 360K is closer to experiment. At the cold heat exchanger, the wall heat flux fits perfectly to the experimental results, but some significant discrepancies still exist for that heat exchanger.

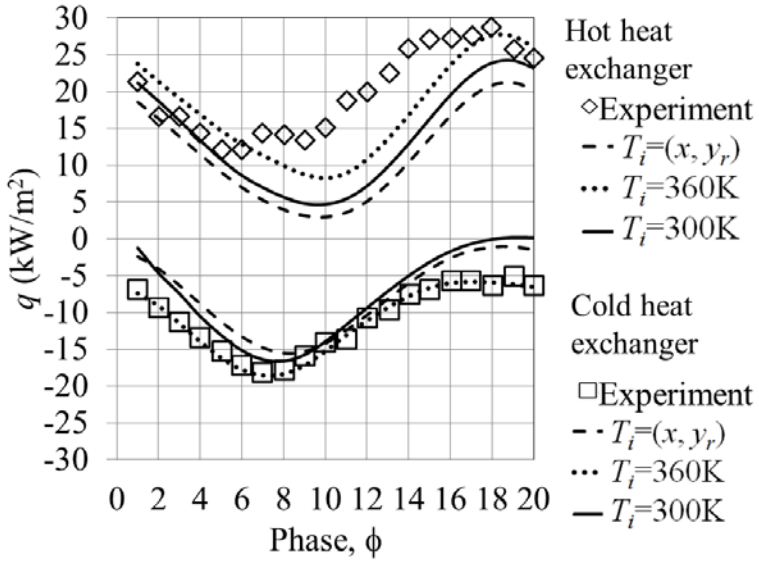

Figure 4.9: The effect of initial temperature on the wall heat flux of the heat exchangers.

Overall, the computationally predicted space-averaged wall heat fluxes are in-phase with experimental values at both heat exchangers as seen from Figure 4.9. However the magnitude of heat transfer differs noticeably at the hot heat exchanger, especially when the flow starts slowing down at ϕ6 and changes direction. The numerical space-time-averaged wall heat flux is calculated to be 30% lower than experimental values. The difference is within the range reported in other numerical investigations (Piccolo, 2011).

There are some concerns about the initialisation approaches. An incorrect initialisation temperature field may affect the flow field and introduce unwanted errors to the numerical results as Figure 4.10 may suggest. Figure 4.10 shows the temperature profile plotted at a location in the open area next to the cold and hot heat exchangers (40 mm from the cold end, and 38 mm from the hot end). The profiles show the variation of temperature along the vertical y_r-direction between the bottom and top wall of the resonator. The open areas are empty areas next to the heat exchangers where most of the natural convection effect is seen in the experiment. Clearly, initialising the temperature at 360 K (dotted lines) gives wrong values of temperature especially at the lower area of the domain. Natural convection is not properly modelled with this initial value. Setting the initial value as a temperature field distribution, $T=(x,y_r)$ (dashed lines), seems to give a closer match to the profile from experimental measurement at this particular area.

However, it seems that the natural convection effect at the cold end is still not modelled correctly due to a strong influence of the initial temperature distribution.

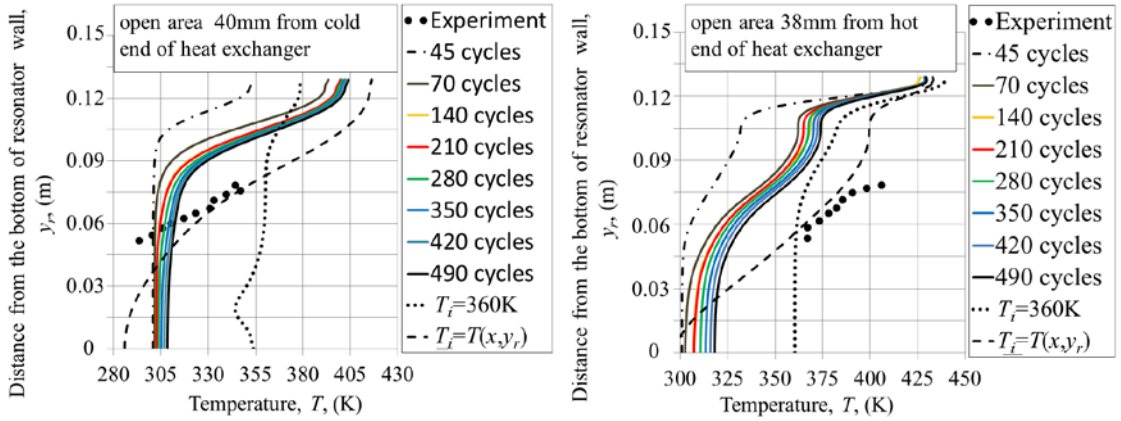

Figure 4.10: Temperature profiles at the open area next to the (a) cold and (b) hot ends of the heat exchanger assembly – comparison between experiment and numerical model with different approach of temperature initialisation.

The model initialised at 300 K is run for longer cycles to see the development of the temperature field over time. Temperatures for all the cycles are plotted in Figure 4.10 as coloured lines between dash-dotted black line (45 cycles) and solid black line (490 cycles). The temperature profiles change slowly and closely to the experimental values. However, the change becomes smaller and smaller and it is unlikely the numerical profile would match experimental data even for a much larger number of cycles (to reach a steady oscillatory state) steady starting at 70 cycles onward. After 70 cycles, the temperature increases very slowly and the shape of the profile remains similar. This stage is known as a steady oscillatory state.

Figure 4.11 shows the temperature field within and around the heat exchanger assembly. This illustrates the convective currents at both hot and cold end to supplement the information in Figure 4.10. The temperature contour shown is for a case initialised at 300 K and iterated for 490 cycles.

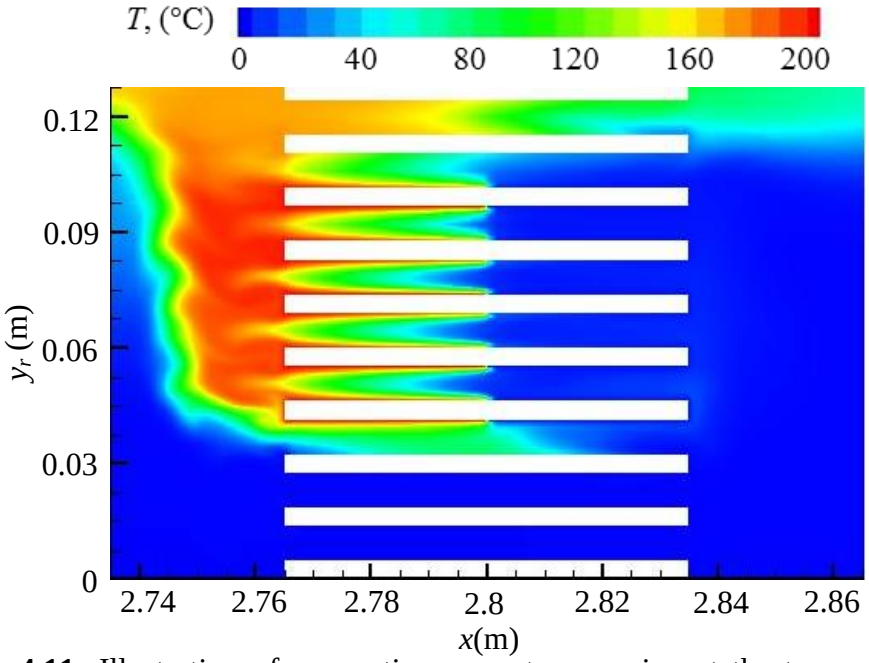

Figure 4.11: Illustration of convective currents occurring at the top area of the heat exchanger assembly.

As can be seen from Figure 4.10 (a) the temperature profile at the lower part of the open area next to the cold end is over predicted by the computational model where numerically calculated temperature values are shown higher than experimental ones. This indicates that there may be losses in the experiments, caused by the un-insulated resonator walls. The heat accumulation illustrated by the "hot plume" at the top creates a higher temperature at that area. In practice the accumulated heat would "leak" into the surroundings. This is not accounted for in the numerical model since the resonator walls are set to the adiabatic condition.

Figure 4.12 shows the temperature profiles plotted from the heat exchanger wall to the location $y=D/2$ at the centre between the plates at location 10 mm from the joint above both hot and cold plates. The development of temperature profiles within a flow cycle is shown for selected phases (ϕ6, ϕ8, ϕ12, ϕ16). The top four plots are the temperatures at the cold plate while the four plots at the bottom are taken at the hot plate. Evidently, the initial temperature has an effect on the temperature profiles. An initial temperature of 360 K leads to a profile with magnitudes bigger than the experiment. A use of temperature distribution, $T=(x,y_r)$, provided solutions almost similar to a model initialised at 300K. Both offer temperature profiles closer to experiment. However, an

initial temperature of 360 K is already shown to incorrectly model the natural convection effect at the open area next to the heat exchangers.

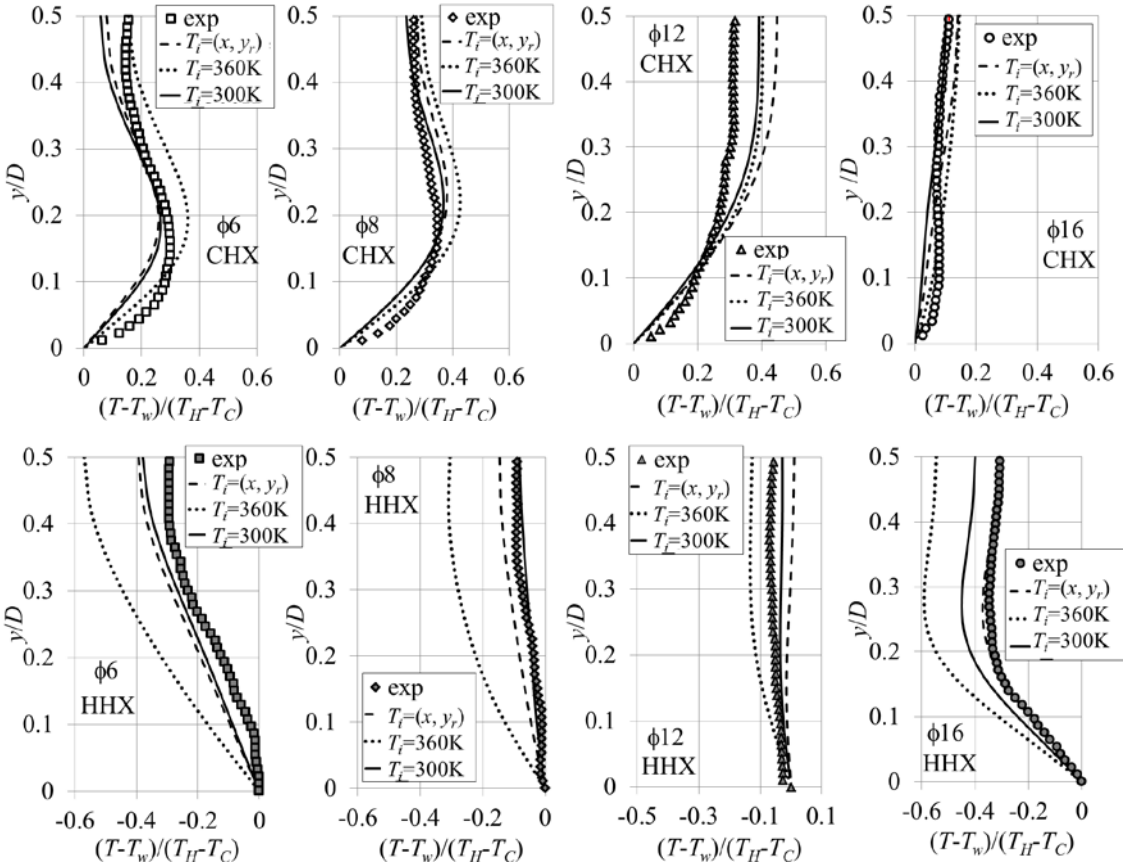

Figure 4.12: The effect of initial temperature on the temperature profiles between heat exchangers plates.

Another concern about the current initialisation attempts is that the initialisation temperature may not be applicable to all cases in later investigations when various operating parameters are investigated. It is difficult to predict the initial temperature in cases where experimental results are unavailable. Unsubstantiated guesses will lead to ambiguity in the results.

The investigation of initial temperature suggested that the model is best initialised with a temperature of 300K. Other attempts, although sometimes bringing the temperature at certain areas closer to experiment, seemed to cause false predictions of the temperature field within the rest of the domain. This may induce uncertainties as it may alter the flow field in unexpected ways. Although the attempt of mimicking the heat accumulation is considered to be “less” successful, the practice leads to a better

understanding of the result and provides confidence in selecting the initialisation temperature. All subsequent models developed in this study are initialised at 300 K.

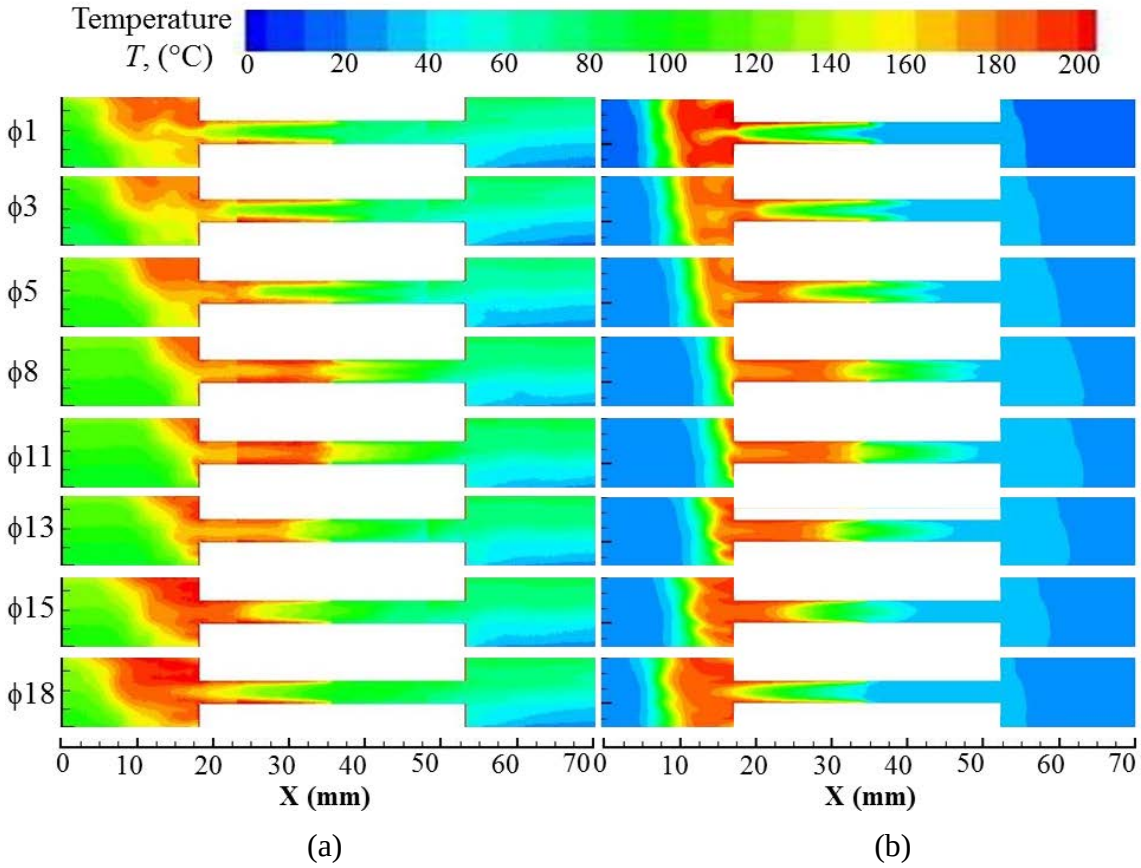

(a) (b)

Figure 4.13: Temperature contours for ϕ1-ϕ20 within the cold and hot channels covering the open area next to the heat exchanger assembly: (a) experimental measurement by Shi et al. (2010); and (b) current numerical model with fluid temperature initialised at 300 K.

Figure 4.13 shows the resulting temperature contours for all twenty phases of the cycle. The plots cover the area within the channel as well as the open area next to both the cold and hot channels, following the same choice of the viewing area as in the experiment. Results from the computational model show a natural convection occurring in the open area next to the hot heat exchanger but with a pattern slightly different than experiment. The effect is not seen in the area next to the cold heat exchanger possibly because the model has not yet reached the level of heat accumulation similar to the experiment in order to allow the gravity-driven flow to occur within the area. The temperature within the channel is bounded by the constant temperature profile set at the

cold plate. Therefore achieving higher temperature within the cold channel, as observed in the experiment, cannot be attained under current numerical time integration and modelling. The discrepancy between the computational result and the experimental data could be related to the essence of the three-dimensional feature of the temperature-driven buoyancy effect that could be under-predicted by the current two-dimensional computational model.

The gravity effect that is already considered in the model is shown to be weak so as insufficient to create the same plume as observed in the experiment possibly due to the losses occurring at the resonator wall. Judging from the nature of the hot plume, it is expected that the top resonator wall will be hotter than the bottom wall. This creates additional temperature gradient that encourages more strength of temperature-driven flow as experimentally observed in the open area next to the heat exchangers.

Despite the difficulties in matching the natural convection phenomenon in the open area next to heat exchangers, the temperature contours between the plates are shown in Figure 4.14 to have a pattern of profiles that match the experimental results. Hot fluid starts flowing into the channel during the first part of the cycle (ϕ1-ϕ10). As the flow reverses (ϕ11-ϕ20), the cold fluid starts flowing from the right end. The disagreement of values of temperature field within the cold channel has been discussed earlier. The differences observed may be an artefact of the three dimensional feature of the real flow that is not captured by the two dimensional model.

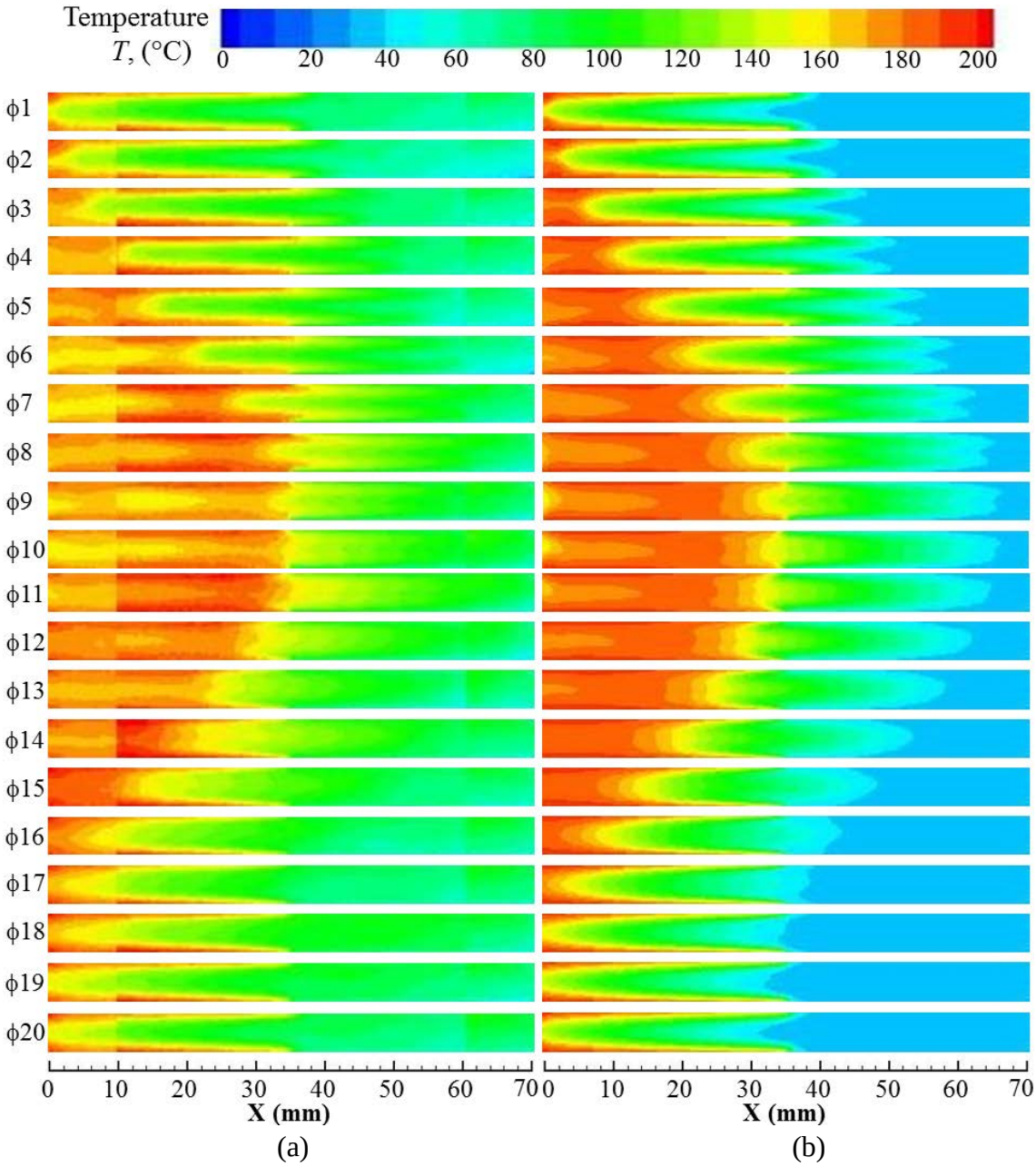

Figure 4.14: Temperature contours in the area bounded by heat exchanger's wall – comparison between (a) experiment and (b) simulation.

4.5 The effect of heat exchanger wall temperature on the flow field

4.5.1. Model description

The presence of temperature field introduces several changes (i.e. natural convection, and forced convection due to temperature change) to the flow structure within a system. It is interesting to learn more about the effect of temperature field into the flow structure. Different sets of boundary conditions for the heat exchanger walls were

applied in the model to investigate the effect of the wall temperature on the flow within the channel. The descriptions are presented in Table 4.2.

Table 4.2: Wall temperature condition of heat exchanger.

Drive ratio (%)	Working medium	Frequency (Hz)	Mean Pressure (bar)	Heat exchanger wall temperature (°C)	
				Hot	Cold
0.3	Nitrogen	13.1	1	Adiabatic	adiabatic
				200	30
				100	30
				300	30
				300	100

4.5.2. Study of the flow using adiabatic model.

The investigation of flow across the parallel plate structure starts with a model where the wall of the heat exchanger is treated as adiabatic. The resulting velocity profiles are shown in Figure 4.15 in comparison to the experimental results of Shi et al. (2010a). The velocity profiles are plotted at a location of 1mm from the joint above the cold plate. The resulting velocity profiles between the heat exchanger plates agree well with experimental data.

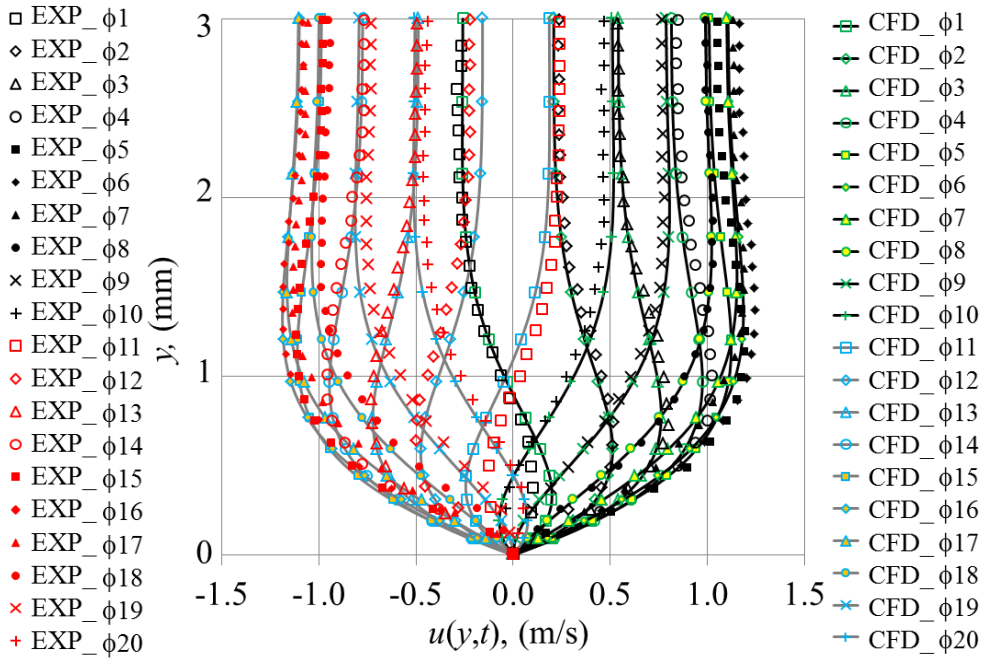

Figure 4.15: Velocity profiles from CFD (black and grey lines) and experiment (red and black symbol) for all the 20 phases of a flow cycle. The heat exchanger walls are adiabatic.

Figure 4.16 shows the vorticity contour plotted for selected phases of the oscillatory flow. The contours are plotted within the heat exchanger plates similar to the "viewing area" in the experiment (Shi et al., 2010), described in Figure 4.1.

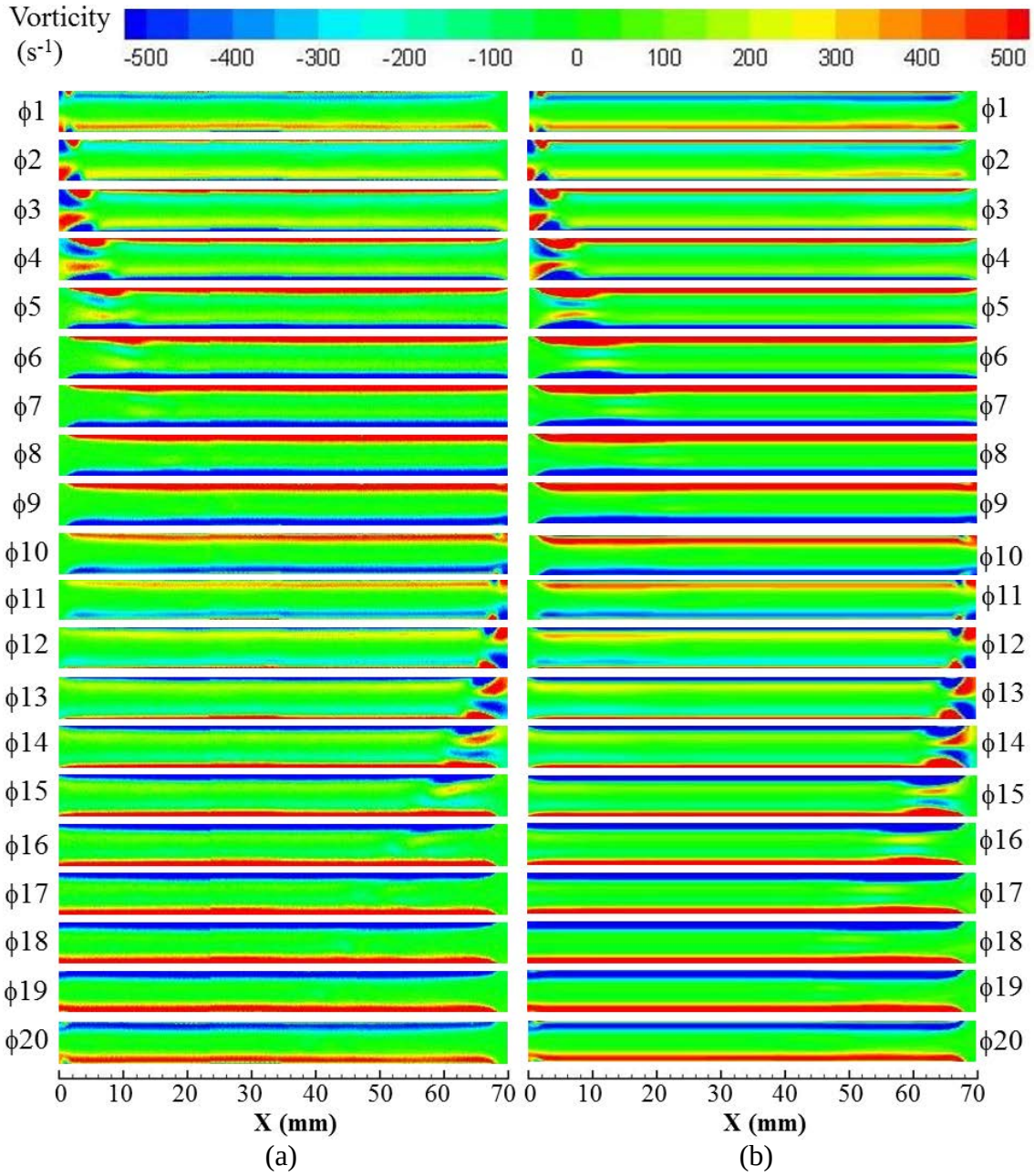

Figure 4.16: Vorticity contours within the channel with plates treated as adiabatic wall – comparison between results from (a) experiment of Shi et al. (2009) and (b) CFD.

From phases ϕ1 to ϕ10, the fluid is flowing into the channel from the left. The flow reverses during phases ϕ11 to ϕ20. The vorticity, ω_z, from the numerical model is

calculated as:

$$\omega_z = \frac{\partial v}{\partial x} - \frac{\partial u}{\partial y} \tag{4.3}$$

where u and v are the velocity component in the x and y directions of the flow.

Figure 4.16 shows the flow evolution within one cycle. A small vortex appears at the end of plates as the flow starts to flow into the channel at $\phi 1$. The vortex becomes weaker as it moves into the channel and disappears completely before $\phi 8$. A similar feature appears at the other end of the channel when the flow changes direction at $\phi 11$. The laminar model is shown to capture well the features of the oscillatory flow at 0.3% drive ratio.

4.5.3. The effect of the presence of wall temperature on flow and heat transfer

Figure 4.17 shows the velocity profiles for a flow at a location 10 mm from the joint above the cold plate with an imposed temperature profile similar to the experiment. The slight differences in magnitude between experimental and numerical result may be caused by the thermophoresis effect that affects the PIV measurement (thermophoresis is a phenomenon of particle motion due to the thermal gradient). In the experimental measurement, oil droplets are used as seeding particles (Shi et al., 2010b). The heat exchangers are set close to each other with a very large temperature gradient occurring at the joint and the nearby area. The large temperature gradient created a thermopherotic force causing the seeding particle to move into the direction opposite to the temperature gradient. This is also observed by Talbot et al. (1980) whereby the particle-free-zone is observed within the boundary layer of their experimental study. Hence the velocity profile near the wall within a nearby area of the joint obtained from the experiment of Shi et al. (2010b) is less reliable. The particle motion due to thermophoretic force is estimated with an uncertainty of ± 0.02 m/s near the wall and ± 0.005 near the centreline. This estimation is carried out using steady flow correlation proposed by Talbot et al. (1980). The effect of the thermophoretic force on oscillatory flow may be amplified.

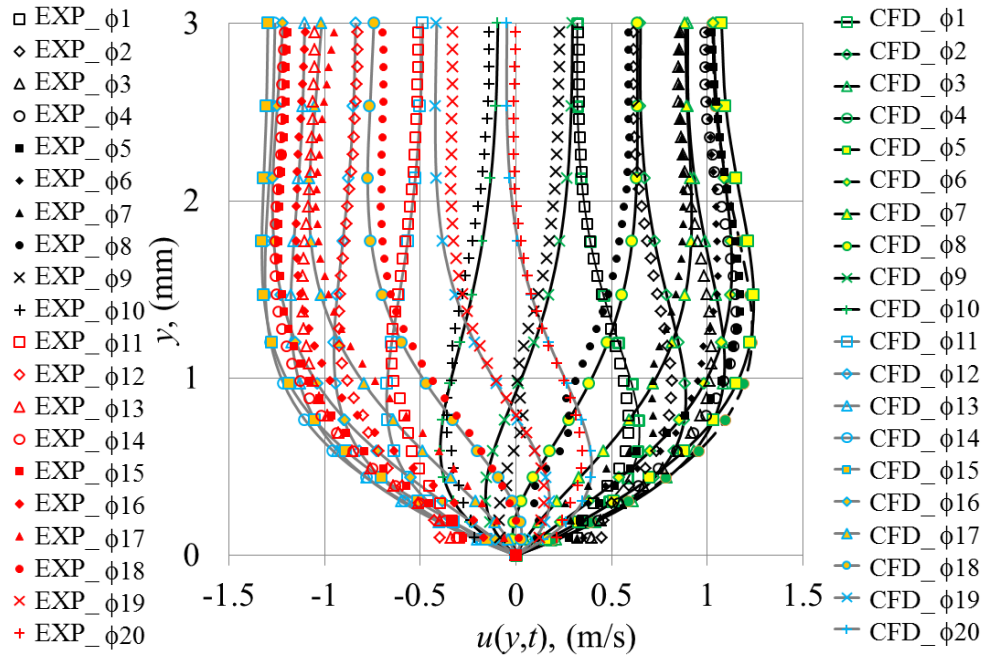

Figure 4.17: Velocity profiles from CFD (black and grey lines) and experiment (red and black symbol) for 20 phases of a flow cycle with influence from heat exchanger walls temperature.

Temperature induces changes to the property of the flow and creates an effect that is sometimes unexpected. As shown in Figure 4.13(a), a buoyancy effect is observed in the experimental result. The heat supplied by the hot heat exchanger reduced the density of the fluid. This creates buoyancy driven flow at the open area next to the hot end of the heat exchanger assembly and the force convection as well as thermal expansion within the channel due to the change of temperature field within the area. These temperature effects are then suggested as the possible reasons that contribute to the asymmetry observed in Figure 4.5(b). The effect is seen through a comparison of velocity profiles between the models with and without the temperature imposed on the heat exchanger's wall as can be seen by comparing Figure 4.15 with Figure 4.17.

The temperature effects result in different velocity profiles. This agreed with experimental findings (Shi et al., 2010b). The model developed captures the essence of oscillatory flow quite well. As with experimental data, the flow symmetry is broken due to temperature effects. This distortion is observed in two ways.

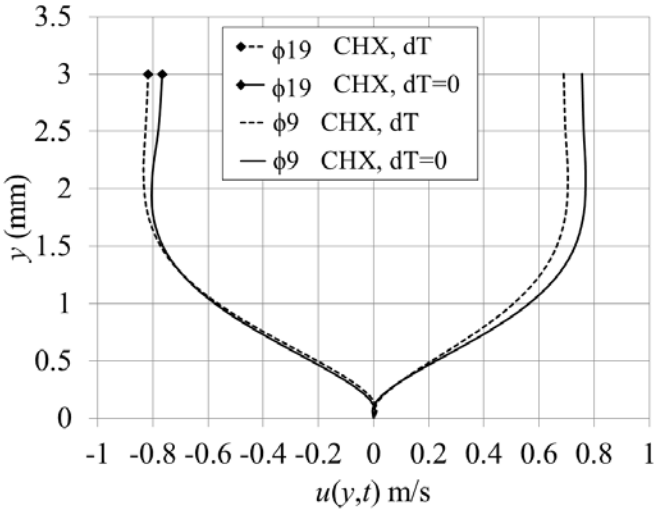

Figure 4.18: The effect of temperature to the velocity profile.

Firstly, the whole structure of the velocity profile plotted in Figure 4.17 seems to be "leaning" to the left in comparison to Figure 4.15. This is clearly illustrated in Figure 4.18, where the presence of temperature makes the velocity profile of ϕ9 and its reverse order, ϕ19, "lean" to the left. The variation of velocity corresponds to the variation of gas displacement in the presence of temperature efcts. This results in asymmetry between the first and the second part of the cycle and hence the asymmetrical velocity profile.

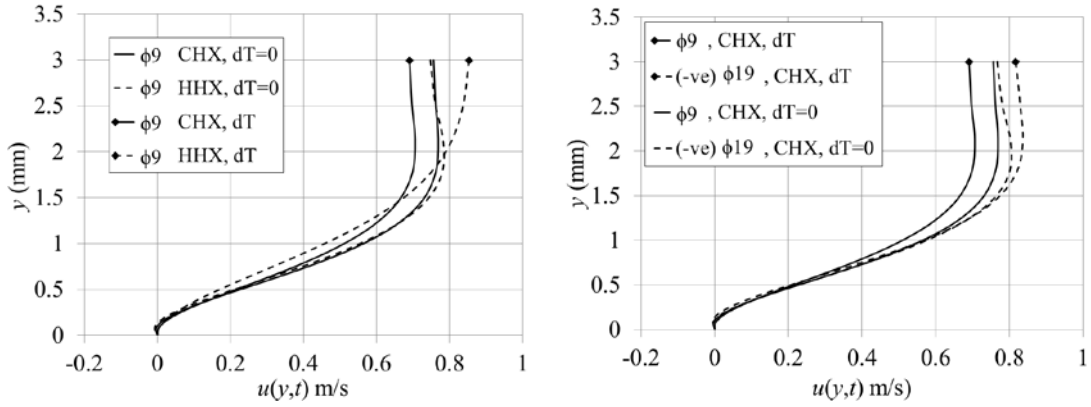

(a) (b)

Figure 4.19: Velocity profile; (a) for ϕ9 at cold heat exchanger (CHX) and hot heat exchanger (HHX), both at a location 15 mm away from the joint; (b) at CHX only at different flow direction.

Secondly, the maximum magnitude of velocity fluctuation extends further to the centreline when temperature effects are included in the model as seen in Figure 4.19(a). In the absence of temperature effects (adiabatic wall), the velocity profile is similar at both cold and hot heat exchangers. When the temperature effect is considered, the velocity profile at the hot heat exchanger seems shifted up towards the centreline (y = 3 mm) and the magnitude of velocity (corresponding to the gas displacement) is larger compared to an equidistant location at the cold heat exchanger. On the other hand, focusing at one location, Figure 4.19(b) shows that the velocity at the selected point of the cold heat exchanger at a similar but reverse phase value (ϕ9 and ϕ19), is also affected by the presence of temperature effects. For ease of comparison, the axial velocity of ϕ19 in Figure 4.19(b) is presented as a negative (-ve) value. The presence of temperature effects results in a lower centreline velocity at ϕ9 but bigger magnitudes in the reverse flow direction at ϕ19. The results indicate a possible change in the viscous boundary layer due to the presence of temperature.

The asymmetry of the flow structure can be further illustrated through the vorticity contour at the open area next to the heat exchanger. The vorticity is plotted for two phases. Comparisons between three different conditions of the walls of the heat exchangers are shown in Figure 4.20 to Figure 4.22. Two phases are selected to represent each half of a cycle for each case. Phase one is when the flow is moving in the direction from hot to cold heat exchangers while phase eleven is when the flow is moving in the opposite direction. For each phase, the contour is shown with two views at the end of each heat exchanger. The designation of phase is shown on top of the plots of the two ends.

Ideally, as shown in the previous section, the magnitude of the velocity in a scenario whereby temperature is not imposed at the wall should be the same for both phases. Hence the resulting vorticity should also be symmetrical. Figure 4.20 shows the vorticity contour of flow in the absence of temperature. As expected, the vorticity contour shows that the structure at the end of plates between one half of a cycle (presented by phase ϕ1) is the same at the other half of the cycle (ϕ11).

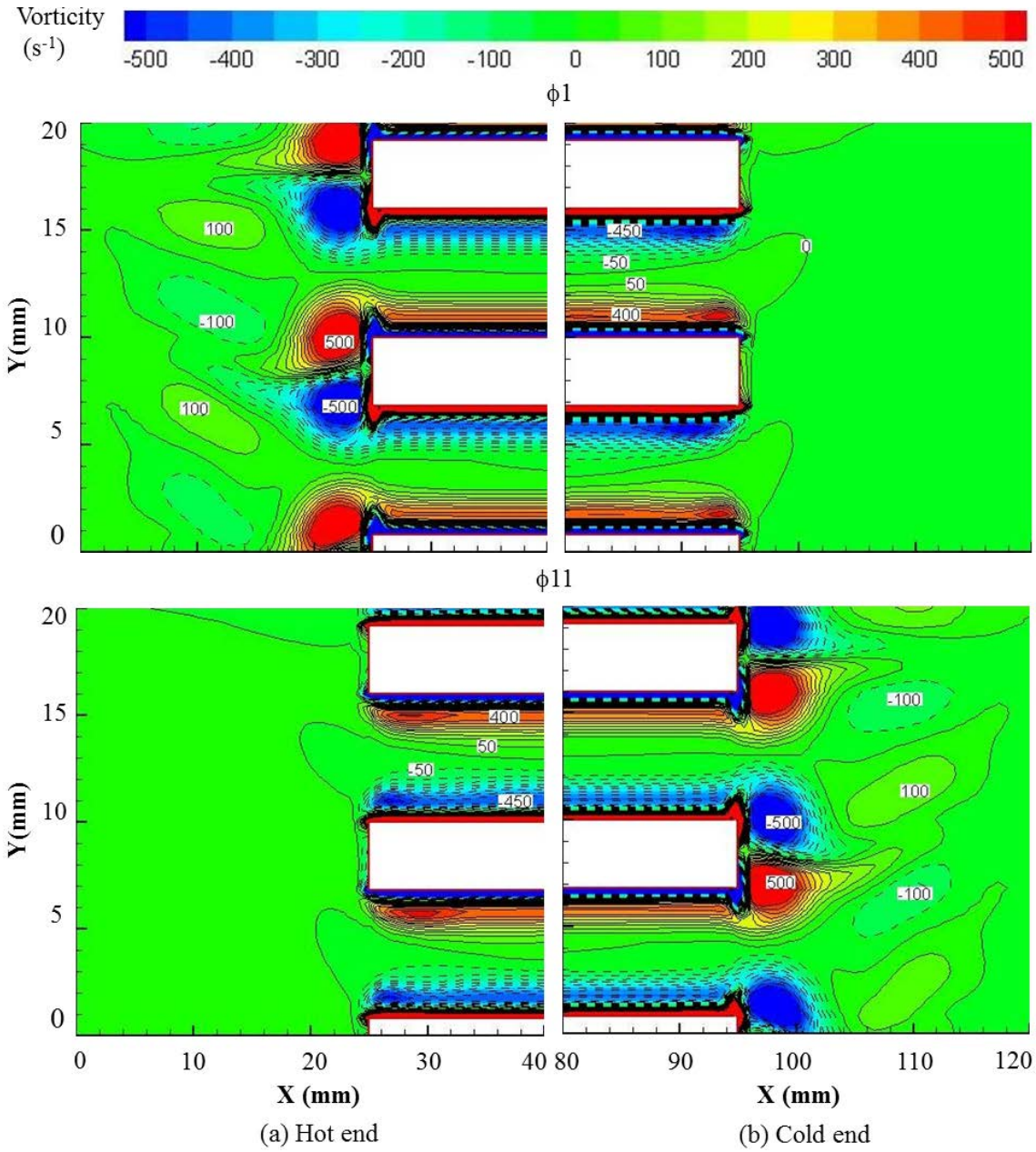

Figure 4.20: Vorticity contour for case of heat exchanger set as adiabatic wall at the (a) hot and (b) cold plates. (1 bar in nitrogen gas, 0.3% drive ratio, 13.1Hz).

Figure 4.21 shows the structure of the vorticity when there is a temperature difference imposed at the plates of the heat exchanger. The symmetry of the flow is broken. Temperature-driven flow at the open area at the left end of the heat exchanger assembly, seen at phase ϕ1, is the result of the hot plume observed within the same area as shown in Figure 4.13.

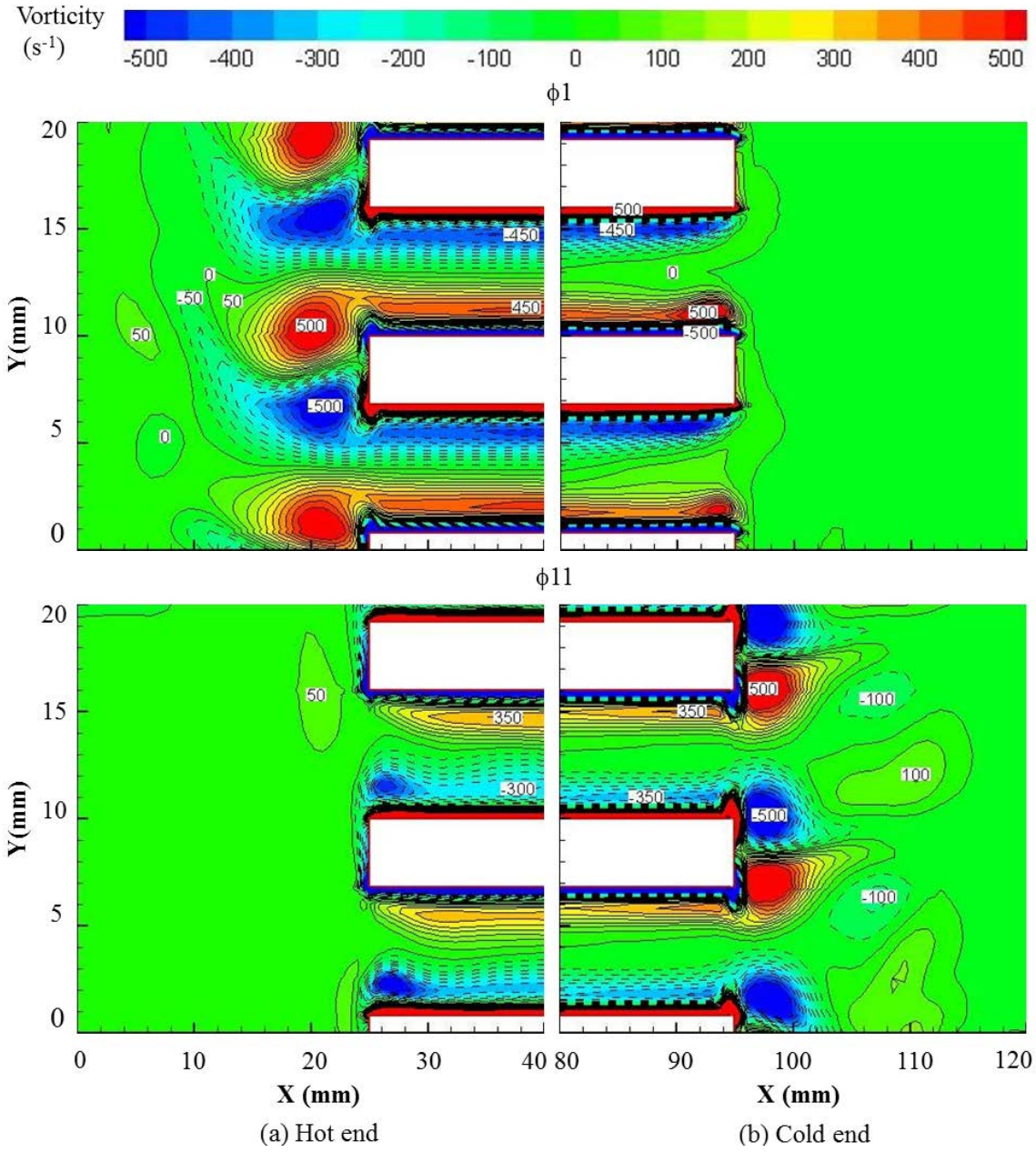

Figure 4.21: Vorticity contour for case of heat exchanger set at 200 °C at the (a) hot and 30 °C at the (b) cold plates. (1 bar in nitrogen gas, 0.3% drive ratio, 13.1Hz).

The temperature-driven flow at the hot end may create resistance on the main flow as the fluid flows in a positive direction from ϕ1 to ϕ10. As the main flow reverses, the temperature-driven flow may provide assistance to the flow within the plates. This again suggests that the asymmetry of the flow between the two halves of the cycle as observed in Figure 4.5(b) is an artefact of nonlinear behaviour partly due to the temperature-driven flow. Further increase in the temperature of the hot plate leads to a higher

strength of temperature-driven flow at the open end next to the hot heat exchanger as shown in Figure 4.22.

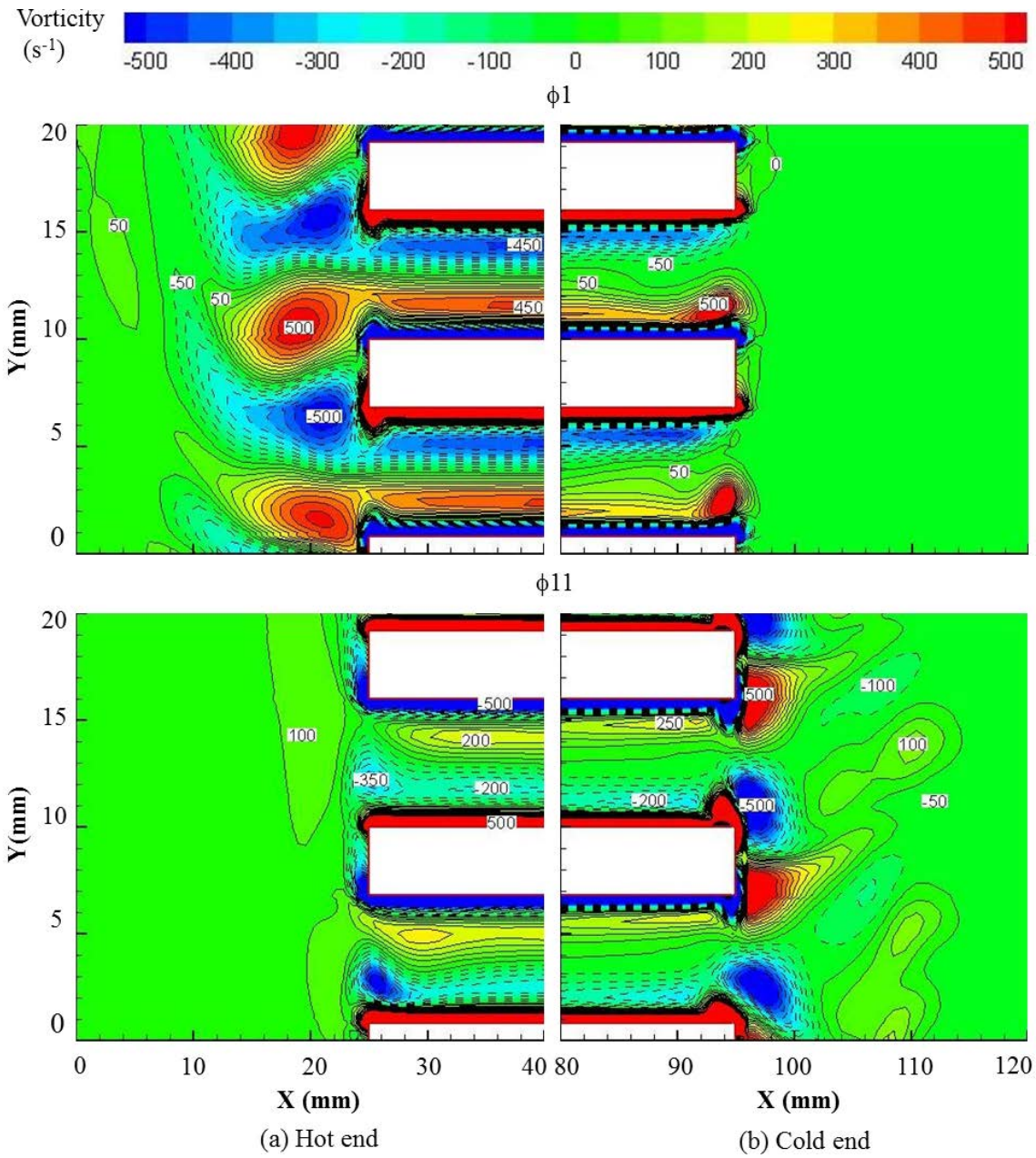

Figure 4.22: Vorticity contour for case with heat exchanger set at 300 °C at the (a) hot and 30 °C at the (b) cold plates. (1 bar in nitrogen gas, 0.3% drive ratio, 13.1Hz).

The temperature also changes the flow structure between the plates. Figures 4.21 and 4.22 show that the vortex lines at the hot channel expand towards the centre of the channel. The vortex lines at the cold channel are more attached to the wall. This is not seen in the adiabatic flow condition shown in Figure 4.20. The expansion of the vortex

lines indicates the changes in the thickness of the shear layer. This agrees with the shifted velocity profiles at a hot heat exchanger as shown in Figure 4.19(a). The expansion of the shear layer corresponds to the change of viscous penetration depth near the wall. Consequently the adiabatic velocity also changes. In the analytical solution, the adiabatic velocity is represented by the first term of equation (2.17). When the density becomes smaller the adiabatic velocity becomes bigger. Hence the amplitude of velocity at the core between the plates of the hot heat exchanger becomes bigger if compared to a similar location above the cold plate. The high viscous penetration depth results to the "shifted" velocity gradient as shown in Figure 4.19(a).

The change in amplitude of velocity corresponds to the change of gas displacement. Temperature causes asymmetry to the flow, which also means that the gas particle travels to a different length back and forth during its reciprocating movement. This may alter the efficiency of heat transfer between fluid and the heat exchangers. The entrance effect may change as well.

The wall temperature of the heat exchanger is varied to allow more temperature difference across the heat exchanger as described in Table 4.2. All the cases are still operating at a drive ratio of 0.3%, a mean pressure of 0.1 MPa with nitrogen as the working medium. For simplicity, the wall temperatures are all set at constant value. The results of the centreline axial velocity along the heat exchangers are plotted in Figure 4.23.

Figure 4.23 shows the values of velocity amplitude across the whole length of the area of the heat exchangers. The velocity is for the location midway between the plates of the heat exchangers ($D/2$). Two selected phases, $\phi 9$ and $\phi 19$, representing the first half and the second half of the cycle are chosen. The description of the wall temperature of the heat exchanger is given in the legend on top of the figure. The vertical dashed-line serves as an eye-guide separating the hot heat exchanger on the left and the cold heat exchanger on the right side of the line.

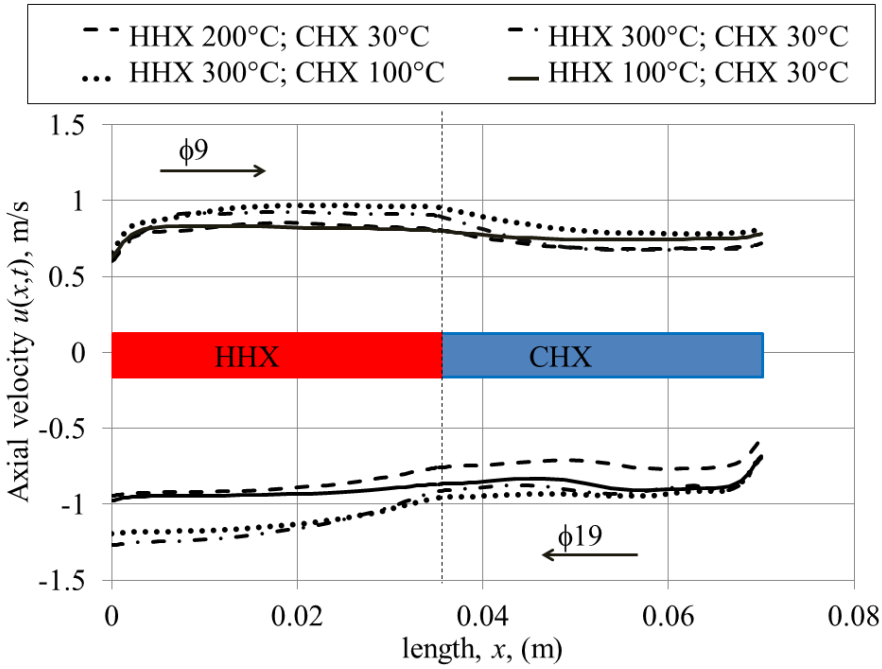

Figure 4.23: Axial velocity at the middle of the channel along the hot (HHX) and cold (CHX) heat exchangers.

At ϕ9, the flow is moving in the direction from the hot heat exchanger towards the cold heat exchanger. The velocity at the hot heat exchanger is generally bigger than that at the cold heat exchanger because the fluid density is lower within the hot channel.

The solid line represents the case with the lowest temperature difference between the hot and cold heat exchanger (100 °C vs. 30 °C). When the wall temperature of the hot heat exchanger increases to 200 °C the velocity at the cold area drops slightly. Meanwhile the magnitude of velocity at the hot area remains approximately the same as for the case of hot plates at 100 °C. This indicates the existence of at least one missing factor other than the density change which influences the magnitude of velocity at the core. The increase of hot wall temperature to 200 °C creates a bigger temperature difference between hot and cold areas, which may encourage natural convection "cells" both within the channel and in the surrounding area. This effect results in a buoyancy-driven flow that is opposing or helping the mean oscillatory flow. On the other hand, changes in velocity amplitude are also due to density changes (because of the imposed wall temperatures). The combined influence of these two effects will create differences in profiles shown in Figure 4.23.

The sharp increases of velocity amplitude at the first few millimetres from the left end of the heat exchanger assembly, for all the cases, represent the entrance effects as the flow starts entering the channel from that direction. The amplitude then saturated at a different value depending on the combined effect of temperature-dependent density and buoyancy-driven flow. A drop in magnitude of velocity is also seen at the joint when the wall temperature drops from hot temperature to the cold temperature.

When the flow reverses (ϕ19), the entrance effects appear at the opposite end of the heat exchangers. For the lowest temperature difference case, shown by the solid straight-line, the velocity amplitude exhibits an almost constant magnitude throughout the length. The effect of density and buoyancy flow are expected lowest at 100 °C for the hot plate and 30 °C for the cold plate. As the hot plate temperature increases, the combined effect of temperature-dependent density and the buoyancy flow starts influencing the velocity. The magnitude of velocity of the model with 200 °C hot plates and 30 °C cold plates remains the lowest throughout the channel. This may be related to the balance between the effect of temperature-dependent density and the buoyancy flow.

For all cases, the maximum amplitudes of velocity at the second half of the cycle, for all cases, are relatively higher than the first half of the cycle. The flow becomes more asymmetrical as the temperature gradient increases.

4.6 The effect of gravity and device orientation on flow and heat transfer

The orientations investigated in this study are illustrated in Figure 4.24. The three pairs of heat exchanger plates in Figure 4.24 are only an illustration, representing a total of 10 pairs of plates in the real model. Gravity is modelled accordingly following the orientation illustrated.

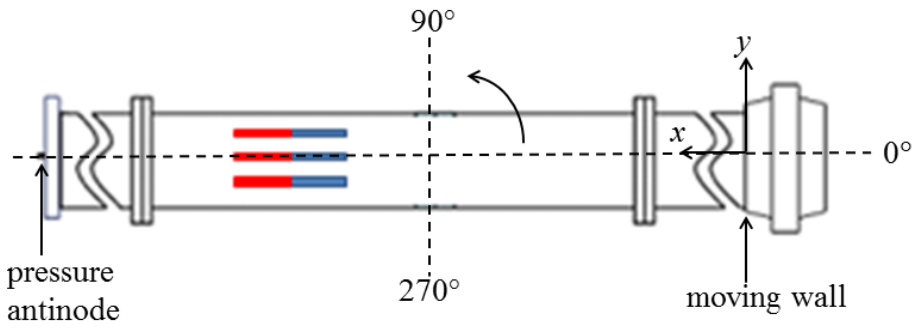

Figure 4.24: Illustration of thermoacoustic device orientation.

Figure 4.25 shows the effect of gravity and device orientation (tilt angle 0°, 90° and 270°) on the velocity profile plotted 15 mm from the joint above the cold and hot plates. In order to differentiate data between cold and hot channels, the lines for velocity profiles at the hot channel are assigned a “diamond” symbol at the top end of the lines. The effect of gravity can be seen by comparing cases assigned as “g,0°” (presented by solid-lines) and “g=0” (presented by a dashed-lines). For phase ϕ9 (Figure 4.25(b)), the comparison shows that gravity has little effect on the flow structure in the horizontal orientation. However, the effect of gravity is seen bigger at ϕ19. Comparison between the magnitude of velocity between ϕ9 and ϕ19 for both “g,0°” and “g=0” shows that the temperature-driven buoyancy flow seems to make the asymmetry between the first and second parts of the flow cycle stronger. The temperature-driven flow due to gravity seems significantly assisting the flow at ϕ19 and slightly resisting the flow at ϕ9.

For orientation other than horizontal, the gravity effect affects the flow depending on the direction of flow and the relative locations of the hot/cold heat exchangers. At an orientation of 90° (presented by the dashed-dotted lines), the cold plate is located above the hot plate resulting in a reduced velocity magnitude during ϕ9 of the flow cycle, because the buoyancy effects are resisting the flow. As the flow reverses (shown as ϕ19), the buoyancy effect is helping the flow. As a result the velocity magnitude becomes bigger than that at the first half of the cycle.

Conversely, when the device is oriented at 270° (presented by the dotted-lines), the temperature-driven buoyancy effect assists the flow at ϕ9 (Figure 4.25(b)), resulting in a higher velocity amplitude and hence a greater fluid displacement between the plates. At ϕ19 (Figure 4.25(a)), the flow reverses and the temperature-driven buoyancy effect is resisting the flow. Consequently, the velocity amplitude within the channel is lower than the first part of the cycle.

For all device orientations, the velocity amplitude within the hot channel is always bigger than that at the cold channel. This is a logical consequence of the temperature-dependent density.

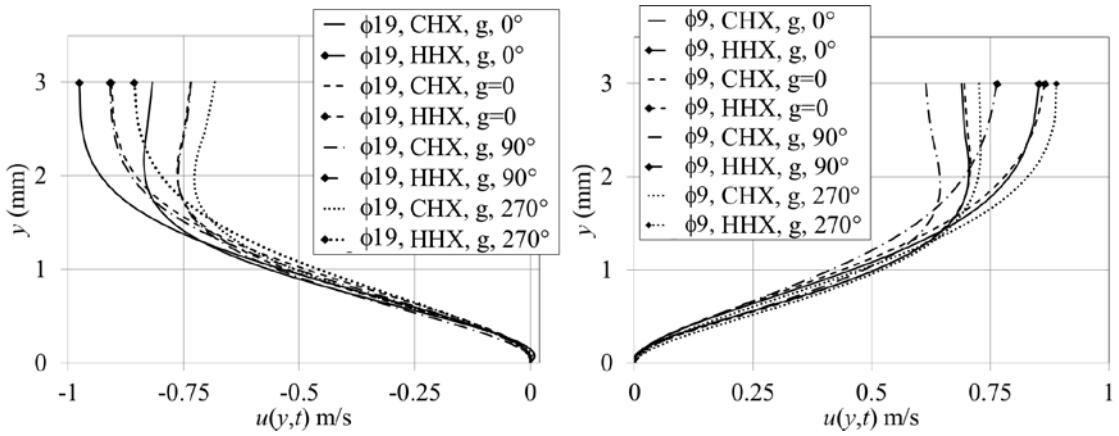

(a) (b)

Figure 4.25: The effect of gravity and device orientation on the velocity profiles for phases (a) ϕ19 and (b) ϕ9.

The effect of gravity and device orientation on the wall heat transfer is shown in Figure 4.26. The heat flux is averaged over the length of the heat exchanger and calculated using equation (4.2). The effect of gravity is less pronounced in the cold heat exchanger compared to the hot heat exchanger. This is in accordance with the effect of buoyancy-driven flow, which is more pronounced at the hot heat exchanger compared to the cold heat exchanger. Figure 4.27 shows that gravity does not significantly influence the temperature between the plates. However, the orientation changes the temperature field depending on the location of the hot heat exchanger, the direction of flow and the resulting temperature-driven buoyancy effect.

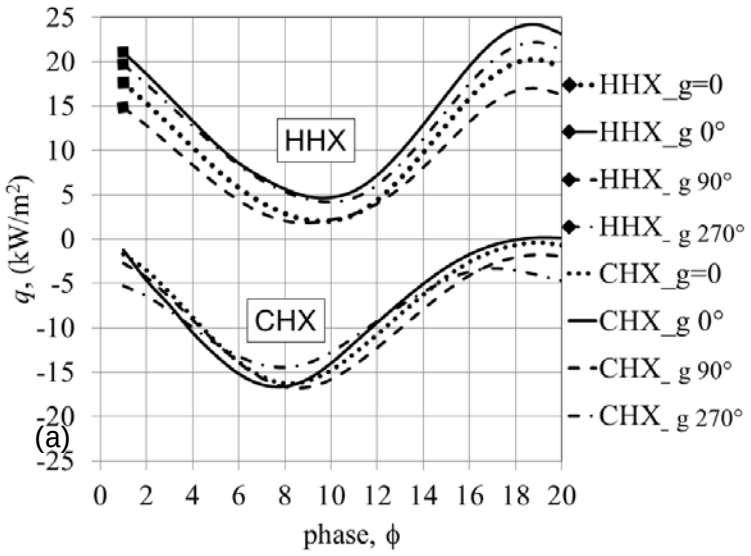

(a)

Figure 4.26: The effect of gravity and device orientation on the wall heat flux.

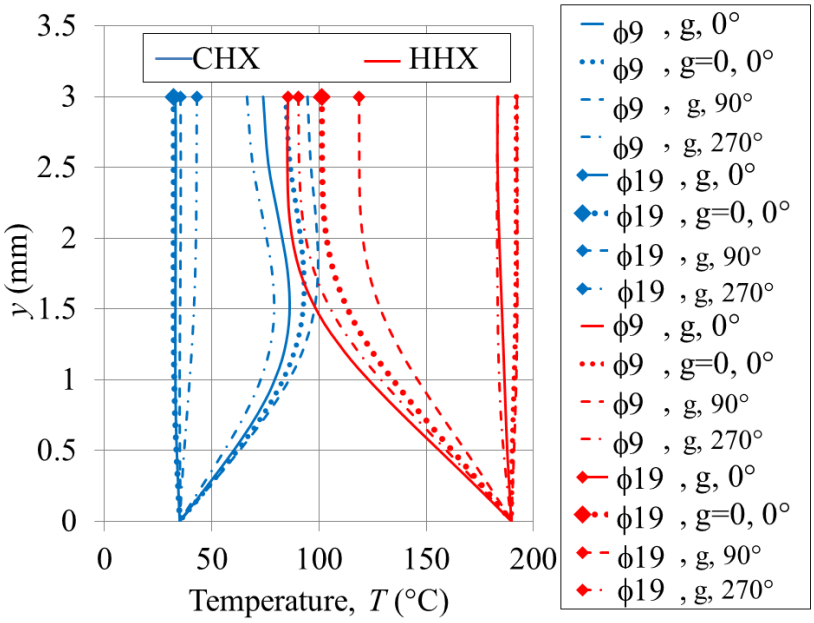

Figure 4.27: Temperature profiles for two selected phases, when there is no gravity (g=0) and with gravity, g, at different tilt angles; 0°, 90°, 270°.

When the flow is moving in the positive direction (ϕ9), the effect of device orientation to the temperature profiles is more pronounced at the cold heat exchanger. When the flow reverses (ϕ19), the effect appears to be more obvious at the location of hot heat exchanger. Of course, at orientation 90° (dashed line), when the hot heat exchanger is located below the cold heat exchanger, the temperature between both hot and cold heat exchangers increases due to the temperature-driven buoyancy effect. At orientation 270°, presented by a dashed-dotted line, the temperature between the plates and hence the wall heat flux is lower because heat is driven away from the plates of the heat exchanger by the buoyancy effect.

4.7 Dimensional Analysis

It is often found that presenting results using proper dimensionless groups of variables provides meaningful explanation and comparison for different experimental circumstances. In the following chapters, the investigation involves a range of parametric investigations. A selection of the appropriate dimensionless parameters is required to make comparisons between the cases investigated. One way of identifying the appropriate dimensionless number is to consider similarity analysis to the transport equation that governs the flow. Dimensional analysis should lead to the dimensionless

groups on which fluid flow and heat transfer solution may depend. The analysis is carried out using a two-dimensional Navier-Stokes equation for compressible flow as follows:

$$\frac{\partial \rho}{\partial t} + \nabla \cdot (\rho \vec{v}) = 0 \tag{4.4}$$

$$\frac{\partial(\rho u)}{\partial t} + \nabla \cdot (\rho \vec{v} u) = -\frac{\partial p}{\partial x} + \frac{\partial}{\partial x}\left(-\frac{2}{3}\mu(\nabla \cdot \vec{v}) + 2\mu\frac{\partial u}{\partial x}\right) + \frac{\partial}{\partial y}\left(\mu\left(\frac{\partial v}{\partial x} + \frac{\partial u}{\partial y}\right)\right) + \rho g_x \beta(T - T_c) \tag{4.5}$$

$$\frac{\partial(\rho v)}{\partial t} + \nabla \cdot (\rho \vec{v} v) = -\frac{\partial p}{\partial y} + \frac{\partial}{\partial x}\left(\mu\left(\frac{\partial v}{\partial x} + \frac{\partial u}{\partial y}\right)\right) + \frac{\partial}{\partial y}\left(-\frac{2}{3}\mu(\nabla \cdot \vec{v}) + 2\mu\frac{\partial v}{\partial y}\right) + \rho g_y \beta(T - T_c) \tag{4.6}$$

$$\rho c_p \frac{DT}{Dt} = \frac{\partial}{\partial x}\left(k\frac{\partial T}{\partial x}\right) + \frac{\partial}{\partial y}\left(k\frac{\partial T}{\partial y}\right) + \frac{Dp}{Dt} + \mu\Phi \tag{4.7}$$

where;

$$\frac{D}{Dt} = \frac{\partial}{\partial t} + u\frac{\partial}{\partial x} + v\frac{\partial}{\partial y} \tag{4.8}$$

$$\nabla = \frac{\partial}{\partial x} + \frac{\partial}{\partial y} \tag{4.9}$$

$$\Phi = 2\left\{\left(\frac{\partial u}{\partial x}\right)^2 + \left(\frac{\partial v}{\partial y}\right)^2\right\} + \left(\frac{\partial v}{\partial x} + \frac{\partial u}{\partial y}\right)^2 - \frac{2}{3}\left(\frac{\partial u}{\partial x} + \frac{\partial v}{\partial y}\right)^2 \tag{4.10}$$

The last term on the right-hand-side of equations (4.5) and (4.6) is the gravitational force as defined in Schlichting (1987). The terms g, ρ, β, c_p, $\vec{v}$ and Φ are the gravity, density gas thermal expansion coefficient, gas heat capacity, velocity vector and viscous dissipation, respectively. In this study, the normalisation parameters are introduced as:

$$u^* = \frac{u}{\sigma u_c};\quad v^* = \frac{v}{\sigma u_c};\quad x^* = \frac{x}{d_c};\quad y^* = \frac{y}{d_c};\quad t^* = t\omega;\quad p^* = \frac{p}{\rho_c \sigma^2 u_c^2}$$

$$\rho^* = \frac{\rho}{\rho_c};\ g^* = \frac{g}{g_c};\ \beta^* = \frac{\beta}{\beta_c}\ \mu^* = \frac{\mu}{\mu_c};\ T^* = \frac{T - T_c}{T_H - T_c};\ c_p^* = \frac{c_p}{c_{p,c}};\ k^* = \frac{k}{k_c} \tag{4.11}$$

The superscript * describes the dimensionless variable. The subscript *c* refers to a reference value, preferably selected in the open area distance away from the stack/regenerator where the property and behaviour of fluid are not much affected by the presence of the object. The velocity is normalised by the velocity at reference point multiplied by the porosity, σ. The change of flow structure due to the presence of solid object was considered by Mao and Jaworski (2010b) by including the ratio of gap, *D*, and plate thickness, *d*. In this study, porosity is used instead as the representation of the changes in the velocity within the area affected by the object. Porosity is defined as the fraction of area wetted by the fluid within the total area of the structure. In the parallel-plate arrangement, the porosity can be represented as, $\sigma = D/(d + D)$. Clearly, porosity is also a representation of plate thickness and spacing. Equations (4.4) to (4.7) are also valid in the region outside the structure (i.e in the open area other than heat exchanger), where the thickness of the plate is zero leaving the porosity value to be equal to unity. This selection is believed to match the porous medium treatment for transport equations in ANSYS FLUENT 13.0 (2010) where porosity is introduced into the system for similar structures if modelled as a porous medium.

In some papers, pressure is normalised by a product of density, porosity, velocity and sound speed. This is also the approached used by Mao and Jaworski (2010a). In this study, the sound speed is replaced by a product of porosity and velocity. This is achieved based on the argument that flows within thermoacoustic systems, although compressible never reaches a situation where a Mach number may become important. Considering the low Mach number encountered within the investigated flow field, it is suggested that the normalisation of pressure be done with the product of density and a square product of velocity and porosity, as shown above.

The dimensions *x* and *y* are both normalised by the characteristic dimension, d_c. The selection of characteristic dimension depends on the condition of flow investigated. For instance, the characteristic length in an internal flow can take the diameter of a tube, or a gap between plates. For flow across an object with a short length, the axial length of the object may be selected as the characteristic length. The effect of different characteristic dimensions can be seen in the resulting definitions of Reynolds number, Re_d. Re_d can be interpreted as hydraulic Reynolds number (usually used for flow in a

pipe) or length based Reynolds number (commonly seen for flow affected by the length).

It is found that the porosity appears at all dimensionless numbers containing velocity. This is consistent with the fact that the velocity considered in the dimensionless number depends on whether it is a free stream velocity, or the physical velocity (or also known as Darcy velocity in porous medium community). For example, the velocity involved in the Reynolds number will be the Darcy velocity when the equation is being solved within the stack of plates.

The temperatures T_h and T_c selected represent the hot and cold fluid temperatures, respectively. It is important to distinguish between these and the T_H and T_C used later in describing the heat exchanger temperatures. The small letter used in the subscript of T, as seen here, is a characteristic of hot and cold parts of the fluid area investigated. The values may change as it moves into different parts of a system investigated and depends on the condition of the domain. This general approach gives freedom for the equation and is not restricted to any particular situation or domain.

The resulting dimensionless equations for the two-dimensional Navier-Stokes equations are:

Continuity equation

$$\mathrm{Re}_\omega \frac{\partial \rho^*}{\partial t^*} + \sigma \mathrm{Re}_d \frac{\partial\left(\rho^* u^*\right)}{\partial x^*} + \sigma \mathrm{Re}_d \frac{\partial\left(\rho^* v^*\right)}{\partial y^*} = 0 \tag{4.12}$$

x-momentum equation

$$\begin{aligned} &\mathrm{Re}_\omega \frac{\partial}{\partial t^*}\left(\rho^* u^*\right) + \sigma \mathrm{Re}_d \frac{\partial}{\partial x^*}\left(\rho^* u^{*2}\right) + \sigma \mathrm{Re}_d \frac{\partial}{\partial y^*}\left(\rho^* u^* v^*\right) + \sigma \mathrm{Re}_d \frac{\partial p^*}{\partial x^*} \\ &= \frac{Gr}{\sigma \mathrm{Re}_d} \rho^* g^* \beta^* T^* + \frac{\partial}{\partial x^*}\left[2\mu^* \frac{\partial u^*}{\partial x^*} - \frac{2}{3}\mu^*\left(\frac{\partial u^*}{\partial x^*} + \frac{\partial v^*}{\partial y^*}\right)\right] + \frac{\partial}{\partial y^*}\left[\mu^*\left(\frac{\partial v^*}{\partial x^*} + \frac{\partial u^*}{\partial y^*}\right)\right] \end{aligned} \tag{4.13}$$

y-momentum equation

$$\begin{aligned}&\mathrm{Re}_\omega \frac{\partial}{\partial t^*}\left(\rho^* v^*\right)+\sigma \mathrm{Re}_d \frac{\partial}{\partial x^*}\left(\rho^* u^* v^*\right)+\sigma \mathrm{Re}_d \frac{\partial}{\partial y^*}\left(\rho^* v^{*2}\right)+\sigma \mathrm{Re}_d \frac{\partial p^*}{\partial y^*}\\&=\frac{Gr}{\sigma \mathrm{Re}_d}\rho^* g^* \beta^* T^*+\frac{\partial}{\partial x^*}\left[\mu^*\left(\frac{\partial v^*}{\partial x^*}+\frac{\partial u^*}{\partial y^*}\right)\right]+\frac{\partial}{\partial y^*}\left[2\mu^*\frac{\partial v^*}{\partial y^*}-\frac{2}{3}\mu^*\left(\frac{\partial u^*}{\partial x^*}+\frac{\partial v^*}{\partial y^*}\right)\right]\end{aligned} \tag{4.14}$$

Energy equation

$$\begin{aligned}&\mathrm{Re}_\omega \theta \frac{\partial}{\partial t^*}\left(\rho^* c_p^* T^*\right)+\sigma \mathrm{Re}_d \theta\left[\frac{\partial}{\partial x^*}\left(\rho^* c_p^* u^* T^*\right)+\frac{\partial}{\partial y^*}\left(\rho^* c_p^* v^* T^*\right)\right]\\&=\frac{\theta}{\mathrm{Pr}}\left[\frac{\partial}{\partial x^*}\left(k^*\frac{\partial T^*}{\partial x^*}\right)+\frac{\partial}{\partial y^*}\left(k^*\frac{\partial T^*}{\partial y^*}\right)\right]\\&+\sigma^2 Ec\left[\mathrm{Re}_\omega \frac{\partial p^*}{\partial t^*}+\sigma \mathrm{Re}_d\left(\frac{\partial}{\partial x^*}\left(p^* u^*\right)+\frac{\partial}{\partial y^*}\left(p^* v^*\right)\right)\right]+\sigma^2 Ec\left(\mu^* \Phi^*\right)\end{aligned} \tag{4.15}$$

The term Φ^* is defined as:

$$\Phi^* = 2\left\{\left(\frac{\partial u^*}{\partial x^*}\right)^2+\left(\frac{\partial v^*}{\partial y^*}\right)^2\right\}+\left(\frac{\partial v^*}{\partial x^*}+\frac{\partial u^*}{\partial y^*}\right)^2-\frac{2}{3}\left(\frac{\partial u^*}{\partial x^*}+\frac{\partial v^*}{\partial y^*}\right)^2 \tag{4.16}$$

The dimensionless parameters discovered through this practice are:

$$\mathrm{Re}_\omega = \frac{\omega {d_c}^2}{\nu_c}\ ;\ \mathrm{Re}_d = \frac{u_c d_c}{\nu_c}\ ;\ Gr = \frac{g_c \beta_c (T_H - T_c) d_c^3}{\upsilon_c^2};\ \theta = \frac{T_h - T_c}{T_c}\ ;$$

$$Ec = \frac{u_c^2}{c_{p,c} T_c}\ ;\ \mathrm{Pr} = \frac{\mu_c c_{p,c}}{k_c} \tag{4.17}$$

The kinetic Reynolds number, Re_ω, describes the influence of frequency on the flow. The hydraulic Reynolds number, Re_d, gives description of the flow based on the amplitude of velocity, u_c. The combined effect of frequency and flow amplitude can be shown related to a dimensionless number known as Keulegen-Carpenter number, $KC=\mathrm{Re}_d/\mathrm{Re}_\omega$. The temperature-driven characteristic is represented by the Grashof number, *Gr*. The dimensionless temperature, θ, represents the effect of temperature on the flow. Depending on the definition of reference temperature used, this dimensionless

number may represent the effect of heat accumulation within the investigated area. The effect can be seen in the transient and convection part of energy equation. This indicates that heat accumulation changes over time and is very much dependent on the amplitude of flow. The Eckert number, *Ec*, expresses the relationship between the flow kinetic energy and enthalpy, and is used to characterise dissipation. It may be argued that the viscous dissipation effect may be small and negligible for a low speed flow. However, the contribution of viscous dissipation due to the existence of internal structures within the investigated domain may be significant and hence is considered in the current study. The Prandtl number describes the property of fluids, which is useful when comparing cases with different fluid medium. The dimensionless number introduced will be used appropriately for the presentation of results in this chapter and the subsequent chapters.

4.8 Viscous dissipation

In a viscous flow, the energy of the fluid motion (kinetic energy) is transformed into internal energy of the fluid through the existence of viscous dissipation. Viscous dissipation for a two-dimensional model is defined in equation (4.9). A dimensional analysis, as presented earlier, has been used for the presentation of the effect of viscous dissipation in this study.

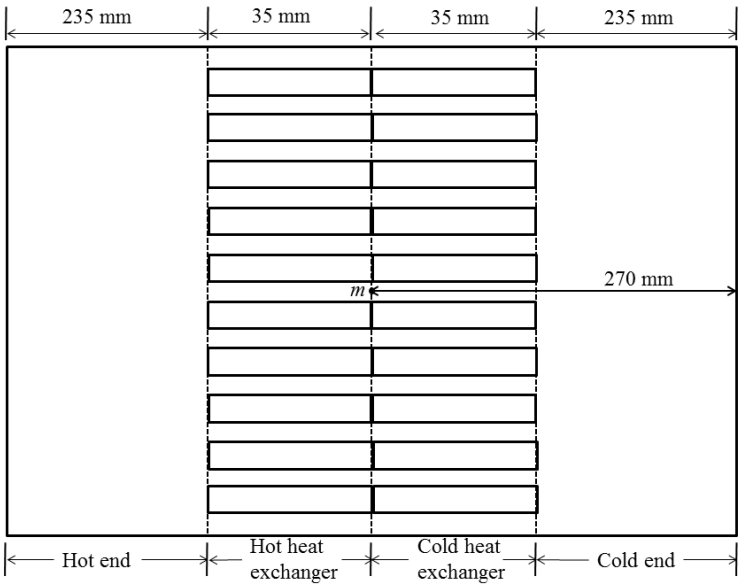

Figure 4.28: Illustration of the region defined for analysis of viscous dissipation.

The computational domain is divided into four regions as defined in Figure 4.28. This definition of regions applies to analysis of viscous dissipations for all models to be

presented in this chapter and chapters onwards. Note that the illustration in Figure 4.28 resembles the heat exchanger assembly currently used in this chapter. The number of heat exchangers plates may vary for later investigations in chapter six but the definition of regions remains unchanged.

The normalised viscous dissipation is averaged over cycle and space, *A*, corresponding to each region and calculated as:

$$\langle \Phi^* \rangle = \frac{1}{2\pi A} \int_0^A \int_0^{2\pi} (\mu^* \Phi^*) d\phi dA \tag{4.18}$$

The term in the bracket on the right-hand-side of equation (4.18) is calculated as follows:

$$\mu^* \Phi^* = \frac{1}{\mu_c} \left(\frac{d_c}{u_c \sigma} \right)^2 \mu \left[2 \left\{ \left(\frac{\partial u}{\partial x} \right)^2 + \left(\frac{\partial v}{\partial y} \right)^2 \right\} + \left(\frac{\partial v}{\partial x} + \frac{\partial u}{\partial y} \right)^2 - \frac{2}{3} \left(\frac{\partial u}{\partial x} + \frac{\partial v}{\partial y} \right)^2 \right] \tag{4.19}$$

Following dimensional analysis, the weighted-average value is further multiplied by the dimensionless parameters identified as porosity, σ, and Eckert number, *Ec*:

$$\langle \Phi \rangle = \sigma^2 Ec \langle \Phi^* \rangle \tag{4.20}$$

The reference velocity is taken at a certain distance away from the heat exchangers. For consistency reasons with later chapters the location is chosen to be at 270 mm from the joint (labelled as *m* in Figure 4.7) towards the right end of the figure within the region called “cold end”. The reference location is selected as such to avoid the influence of temperature on the open area next to the hot heat exchanger, where a hot plume is observed as a result of gravity.

A value of porosity, σ, is appropriately used when calculating dissipation for the open area and the area of the heat exchanger following the discussion earlier. For the open area the porosity is set to one while an appropriate value of porosity (equal 0.65 for the

geometry presented in this chapter) is used for heat exchangers. Figure 4.29 shows the effect of the heat exchanger wall temperature on the dimensionless viscous dissipation.

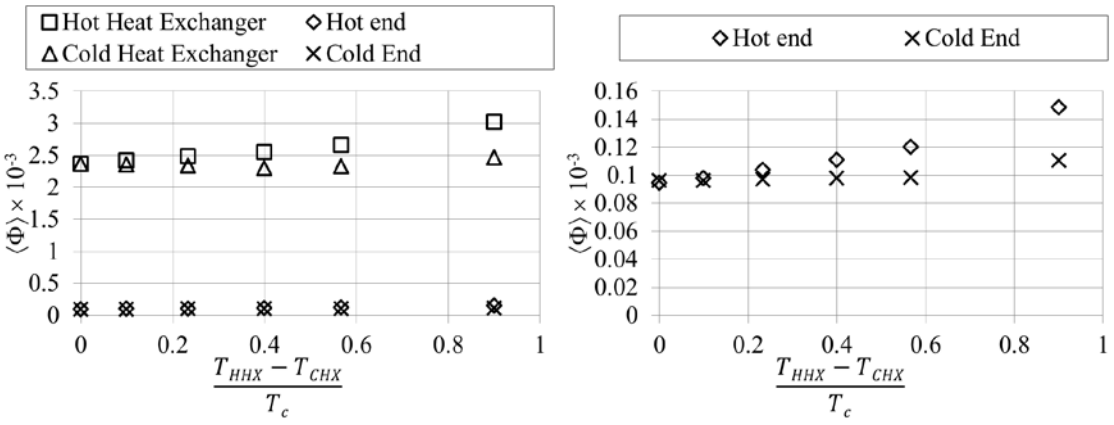

(a) (b)

Figure 4.29: (a) The effect of the heat exchanger wall temperature on viscous dissipation and (b) the enlarged view for dissipations at the open area next to heat exchangers.

The viscous dissipations at the open area at both ends of the heat exchangers are one order of magnitude lower than the dissipations at the area between the plates. This is consistent with the fact that the working medium interacts with more wall surfaces within the area of the heat exchanger where viscous resistance is significant, hence causing more energy dissipation. When the hot heat exchanger becomes hotter, the dissipation becomes bigger. This is a consequence of gas viscosity that becomes bigger as the temperature increases. Figure 4.29(b) is an enlarged view of the dissipations for open area at the ends of heat exchanger assembly. It shows that the dissipation of energy at the open area next to the hot end is bigger than that next to the cold end presumably due to the buoyancy flow at the hot end. The dissipation increases with an increase of temperature of the hot heat exchanger. This is likely related to the combined effect of bigger gas viscosity at higher temperature and the more pronounced gravity-driven flow as seen by the development of the hot plume at that end.

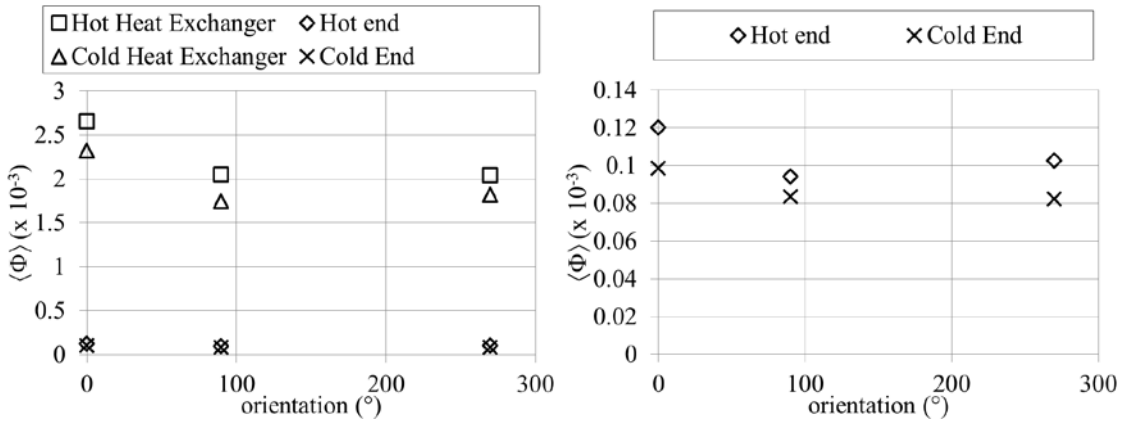

(a) (b)

Figure 4.30: (a) The effect of the device's orientation on viscous dissipation and (b) the enlarged view for viscous dissipation at the open area next to heat exchangers.

Figure 4.30 shows that viscous dissipation is lower in all areas when the device is set at a vertical orientation. Gravity determines the flow direction of the hot plume. For vertical arrangements (90° and 270°), the temperature-driven flow is in line with the direction of flow. The temperature-driven flow can either assist or obstruct the flow depending on the device orientation and the direction of flow within a flow cycle. This may affect the magnitude of velocity as the fluid flows back and forth within the heat exchanger, but the gradients of velocity near the wall are approximately the same, as seen in Figure 4.25. However, the low dissipation of the device arranged at vertical orientation indicates that the combined effect of temperature-driven flow and the mean flow may help reduce the viscous dissipation that may relate to the circulation of flow. The horizontal arrangement (0°) results in a temperature-driven flow perpendicular to the direction of flow. Hence, circulation tends to be bigger in comparison to the vertical arrangement.

4.9 Summary

The developed two-dimensional model has the potential to model the oscillatory flow across the parallel-plate heat exchanger at the investigated low amplitude of flow with a drive ratio of 0.3%. The flow as represented by the velocity profiles is well predicted by the model. The differences noted in the temperature profiles and the resulting heat fluxes are likely to be the result of the real flow being three-dimensional as well as possible heat accumulation in the system. However, since the model is already reaching a steady state oscillatory condition, the pattern of flow and heat transfer shows a good

qualitative match to the experiment. The current model under-predicts the space-time-averaged wall heat transfer by 30% in comparison to experimental values. The investigation of the effect of initial temperature on the flow and heat transfer helps explain the selection of appropriate initial temperature that best suit the model.

Temperature-dependent gravity effects influence the magnitudes of velocity profiles and temperature profiles between the plates depending on the direction of the flow and the locations of the cold/hot heat exchangers. Consequently, the heat fluxes also change. The presence of the imposed temperature field is shown to influence the velocity profile and gas displacement across the plates, hence breaking the symmetry of the flow. The vortex structure at the end of the plates and the shear layer within the area bounded by the plates changes with temperature. Device orientation influences the flow and heat transfer due to temperature-driven buoyancy effects. The vertical arrangement is shown to provide a lower viscous dissipation but care should also be taken when dealing with this kind of arrangement because the temperature-driven flow changes the temperature and velocity field within the channel.

Chapter Five: Heat exchanger: Flow and heat transfer at higher amplitude oscillatory flow

The models in chapter four were for an oscillatory flow driven at low amplitude with a drive ratio (defined as maximum pressure amplitude to mean pressure) of 0.3%. In this chapter, investigations are carried out at higher flow amplitudes (higher drive ratios). Attention is given to develop a model that can explain the physics of phenomena observed in the experimental work. The general description of the computational models is given in section 5.1. Section 5.2 presents the results obtained from laminar model. The suitability of turbulence models for predicting the flow phenomena at varied drive ratios has been tested and is discussed in section 5.3. The effect of drive ratio on dimensionless mean-flow viscous dissipation is shown in section 5.4 followed by discussions related to heat transfer condition in section 5.5. Section 5.6 sums up the findings related to flow and heat transfer at higher amplitude oscillatory flow within the parallel-plate heat exchanger.

5.1 Computational Model

The computational domain used in this chapter is still based on the experimental setup presented by Shi et al. (2010b). In the previous chapter, a two-dimensional 'long model' covering the full length and height of the experimental setup was presented. The model gives good predictions of flow structures for a drive ratio of 0.3%, in agreement with experiment reported by Shi et al. (2010a, b). The 'long model' allows the verification of the phase differences between pressure and velocity from the computational model to follow the definition from the experiment. It is found that the pressure and velocity in the flow far away from the heat exchanger can be estimated fairly well by the linear thermoacoustic theory. This indicates that the use of a shorter model is also acceptable provided that the boundary is far enough for the incoming/outgoing oscillatory flow not to interfere with the plate structure (Worlikar and Knio, 1996, Versteeg and Malalasekera, 2007). In this chapter, the computational domain is developed based on a 'short model' to cover a shorter length of 270 mm either way from location *m* of the joint, as shown in Figure 5.1.

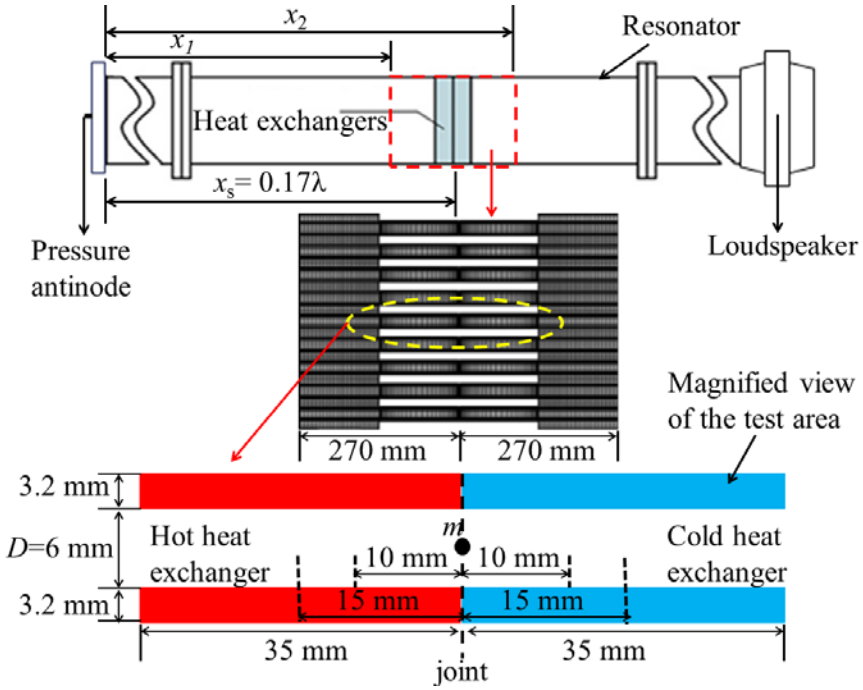

Figure 5.1: A "short model" shown as a "red-dashed box" on the schematic diagram (top); computational domain (middle); and area of investigation (bottom).

Due to flow asymmetry caused by natural convection as observed in the experiment, the full height that covers all the 10 parallel-plates used in the experiment is selected for this 'short model'. The 'short model' is favorable because it is computationally less expensive than the first model that covers the full length of the two-dimensional area. The temperatures imposed on hot and cold heat exchangers are as in Figure 4.2.

The laminar model is solved using the Navier-Stokes equation. The Reynolds-averaged Navier-Stokes (RANS) equation is used for the turbulence model. The Navier-Stokes equations have previously been described in chapter two.

ANSYS FLUENT 13.0 (2010) provides a comprehensive selection of turbulence models to choose from. The basic model uses the Reynolds-averaging technique, where variables in the instantaneous (exact) Navier-Stokes equations are decomposed into the mean (ensemble-averaged or time-averaged) and fluctuating components. Hence, the variable components are written in the form of:

$$\varphi = \overline{\varphi} + \varphi' \tag{5.1}$$

where $\overline{\varphi}$ and φ' are the mean and fluctuating components of the scalar variable. The scalar variable can be velocity, pressure or any other scalar transport quantities.

Substituting expressions of this form into the instantaneous continuity and momentum equation, with the introduction of stress-tensor for the fluctuating component in a manner similar to laminar flow, give equations for turbulence flow known as Reynolds-averaged Navier-Stokes (RANS) equation shown here in index notation as:

$$\frac{\partial \rho}{\partial t} + \frac{\partial}{\partial x_j}(\rho u_i) = 0 \tag{5.2}$$

$$\begin{aligned}\frac{\partial(\rho u_i)}{\partial t} + \frac{\partial}{\partial x_j}(\rho u_i u_j) &= -\frac{\partial p}{\partial x_i} + F_i + \frac{\partial}{\partial x_j}[\tau_{ij}] \\ &+ \frac{\partial}{\partial x_j}\left(-\rho\overline{u'_i u'}_j\right) + \frac{\partial}{\partial x_i}\left(-\rho\overline{u_i'^2}\right) + S_m\end{aligned} \tag{5.3}$$

$$\frac{\partial}{\partial t}(\rho E) + \frac{\partial}{\partial x_i}[u_i(\rho E + p)] = \frac{\partial}{\partial x_j}\left((k)_{eff}\frac{\partial T}{\partial x_j} + u_i(\tau_{ij})_{eff}\right) + S_h, \tag{5.4}$$

where

$$(\tau_{ij})_{eff} = \mu\left(\frac{\partial u_j}{\partial x_i} + \frac{\partial u_i}{\partial x_j}\right) - \frac{2}{3}\mu_{eff}\frac{\partial u_k}{\partial x_k}\delta_{ij}. \tag{5.5}$$

These equations have a form similar to the laminar model of Navier-Stokes equation presented in equation (2.1) to equation (2.3). Velocities and other solution variables now represent the ensemble-averaged (or time-averaged) values. The new terms which appear at the end of the Reynolds-averaged momentum equation (5.3) are the Reynolds stresses representing the turbulence effect. For compressible flow, the fluctuation of density may affect the turbulence. In this case the transport equation can be interpreted as Favre-averaged Navier-Stokes equations, with velocities representing the mass-averaged values (Schlichting and Gersten, 2001).

The effective stress tensor $(\tau_{ij})_{eff}$ represents the stress tensor under the influence of turbulence with effective viscosity, $\mu_{eff} = \mu + \mu_t$, defined as a sum of laminar

viscosity, μ ,and turbulent viscosity, μ_t . Similarly, the effective thermal conductivity, $k_{eff}=k+k_t$, is the sum of mean thermal conductivity, k, and turbulent conductivity, k_t. The turbulent thermal conductivity is calculated as, $k_t=\mu_t c_p/\mathrm{Pr}_t$ and turbulent Prandtl number, Pr_t, has a constant value of 0.85. The eddy viscosity, μ_t, is calculated using turbulence model. The terms S_m and S_h are the user-defined features available in ANSYS FLUENT 13.0 (2010).

The Reynolds stresses are solved through additional equations provided by the turbulence model. In this chapter, turbulence is assumed isotropic so that the Boussinesq hypothesis is applicable to relate the Reynolds stresses to the mean velocity gradient as follows:

$$-\rho\overline{u'_i\,u'_j}=\mu_t\left(\frac{\partial u_i}{\partial x_j}+\frac{\partial u_j}{\partial x_i}\right)-\frac{2}{3}\left(\rho k+\mu_t\frac{\partial u_k}{\partial x_k}\right)\delta_{ij} \qquad (5.6)$$

The subscript i, j, and k refers to the component of x, y and z coordinates, respectively. The term, $k=(u_1'^2+u_2'^2+u_3'^3)/2$, is known as the turbulent kinetic energy. The Kronecker delta, ($\delta_{ij}=1$ if $i=j$ and $\delta_{ij}=0$ if $i\neq j$) is introduced to correctly model the normal component of the Reynolds Stress (Versteeg and Malalasekera, 2007).

ANSYS FLUENT 13.0 (2010) provides algorithms for several turbulence model including Reynolds-Averaged Navier-Stokes (RANS) model, a full Reynolds stress model (RSM) and Large Eddy Simulation (LES). The last two options are computationally very expensive but might be important for high-speed flow or highly anisotopic turbulence cases. RANS model is most widely used and has been vastly verified to suit many conditions of practical flow.

Several RANS turbulence models are tested in this study. The models used additional equations provided by the RANS models to solve for turbulent viscosity, μ_t, and turbulent kinetic energy, k, to obtain the Reynolds-stresses using equation (5.6). The Reynolds stresses are then used by the software to correctly model momentum equation for the turbulence-affected flow through equation (5.3).

A pressure-based solver is used for all models with the application of Pressure-Implicit with Splitting Operators (PISO) algorithm for the pressure-velocity coupling. Second order discretisation is selected for discretisation of time, transport equation and turbulent equations. The boundary conditions are calculated from the lossless equation described in chapter two and given as:

$$P_1 = P_a \cos(k_w x_1)\cos(2\pi f t) \tag{5.7}$$

$$m'_2 = \frac{P_a}{a}\sin(k_w x_2)\cos(2\pi f t + \theta) \tag{5.8}$$

$$\left.\frac{\partial T}{\partial x}\right|_{x_1 . x_2} = 0 \tag{5.9}$$

Oscillating pressure, P_1, and mass flux, m'_2, are assigned at locations x_1 and x_2, respectively. These are shown in Figure 5.1. The wave number, $k_w=2\mu f/a$, is constant because frequency, f, is fixed at 13.1 Hz. The terms a and P_a refer to speed of sound and oscillating pressure measured at pressure antinode, respectively. The phase, θ, is set to follow the standing-wave criterion where pressure and velocity are 90° out of phase. Condition (5.9) is set at boundaries x_1 and x_2 so that when the flow reverses, the temperature of the reversed flow is equal to the temperature of the cells next to the boundary. The condition of the wall boundary and the gas properties are the same as described in chapter four. The influence of gravity is modeled with gravitational acceleration set to 9.81 m/s^2.

Additional equations are used to solve Reynolds stresses appearing on the right hand side of the RANS equation (5.3). The equations depend on the type of turbulence model solved. In general, additional boundary conditions are needed to solve additional equations used to model turbulence. For all turbulence models tested, additional boundary conditions for turbulence model are set at the boundaries, x_1 and x_2, by assigning a value of turbulence intensity, I, and turbulence length scale, ℓ, defined as:

$$I \equiv \frac{u'}{u_{average}} = 0.16(\mathrm{Re})^{-1/8} \tag{5.10}$$

$$\ell = 0.07D \tag{5.11}$$

The Reynolds number, $\mathrm{Re}=\rho u_m D/\mu$, is calculated using velocity at location m, u_m, obtained from Shi et al. (2010) and the gap between plates, D = 6 mm, as shown in Figure 5.1. The density, ρ, and viscosity, μ, used in calculating equation (5.10) are taken at 300 K. ANSYS FLUENT 13.0 (2010) use the inputs defined in equation (5.10) and (5.11) to estimate the inlet distributions of turbulence kinetic energy, k, and turbulence dissipation, ε, by means of the following equations (ANSYS FLUENT 13.0 (2010), Versteeg and Malalasekera, 2007):

$$k = \frac{2}{3}\left(u_{avg} I\right)^2 \tag{5.12}$$

$$\varepsilon = C_\mu^{3/4} \frac{k^{3/2}}{\ell} \tag{5.13}$$

where u_{avg} is the mean flow velocity and C_μ is an empirical constant that varies depending on the turbulence model used (approximately 0.09). The sensitivity of the results to these inlet conditions is tested by changing the value of turbulence intensity, I, to be the value calculated using velocity at the boundaries. The velocity at the boundaries is calculated using the equation from lossless theory. It is found that the solution is insensitive to the turbulence boundary conditions. This shows that the computational domain is sufficiently long to avoid the interaction between the flow around the plates and the inlet/outlet flows into/out of the domain. Default values are retained for all constants of all turbulence models used (ANSYS FLUENT 13.0, 2010).

5.2 Laminar flow model

Increasing drive ratio will result in an increase of gas displacement. Consequently, the corresponding Reynolds number also increases. According to Merkli and Thomann (1975), an oscillatory flow is considered laminar as long as the critical Stokes Reynolds number is less than 400. The Stokes Reynolds number is defined as $\mathrm{Re}_c=2u/(\upsilon\omega)^{1/2}$ with u, υ and ω representing the velocity, viscosity and angular velocity, respectively. The Stokes Reynolds number for all the drive ratios investigated in the experiment of Shi et al. (2010) is calculated and shown in Table 5.1. The Stokes Reynolds number involved in this study is shown lower than the transition point suggested by Merkli and Thomann (1975). Thus, at first, a laminar model is used to model the flow and heat transfer for the drive ratios of 0.45%, 0.65% and 0.83%.

Table 5.1: Stokes Reynolds number based on experimental results of Shi et al. (2010).

Drive ratio, (%)	Stokes Reynolds number, Re_c
0.3	58.76
0.45	75
0.65	118.61
0.83	168.26

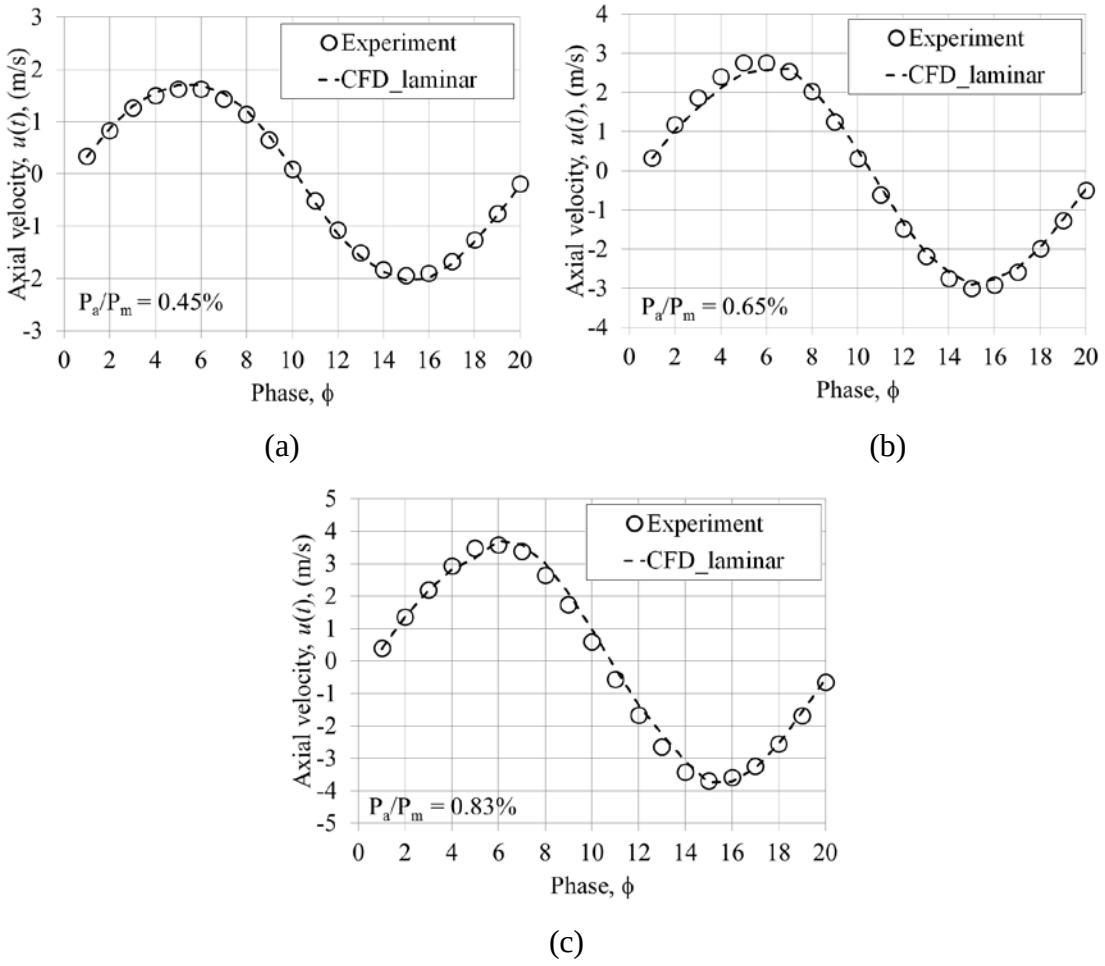

Figure 5.2: Axial velocity in the middle of the channel at location 10 mm away from the joint above the cold plate for a drive ratio of (a) 0.45%, (b) 0.65% and (c) 0.83%.

Figure 5.2 shows the velocity magnitude at location 10 mm from the joint at the central area between the cold plates for different drive ratios modelled as laminar. At a drive ratio of 0.45%, the oscillating velocity predicted by the laminar model agrees reasonably well with the experiment. As the drive ratio increases, slight discrepancies are spotted at some phases of a flow cycle.

A closer look at the velocity profiles allows the comparison be made throughout the flow area including boundary layer. This should reveal whether the laminar model is indeed suitable to model the flow under investigation. The profiles of velocity are plotted at 10 mm away from the joint above the cold plates as shown in Figures 5.3a to 5.3c. The profiles show the variation of axial velocity over the vertical direction y starting from the wall up to the location in the middle of the channel, y = 3 mm, for all the 20 phases of a flow cycle. The magnitudes of velocity at y = 3 mm are not all the time matched to the experimental results. Even if they match, say at ϕ1, the profiles still show discrepancies at other locations especially near the wall. The over prediction of velocity profiles near the wall as calculated by the laminar model suggests a possibility of turbulence (Schlichting and Gersten, 2001). Often, smaller amplitude of velocity profile within the boundary layer area is related to the occurrence of turbulence, this being strictly true for steady flows.

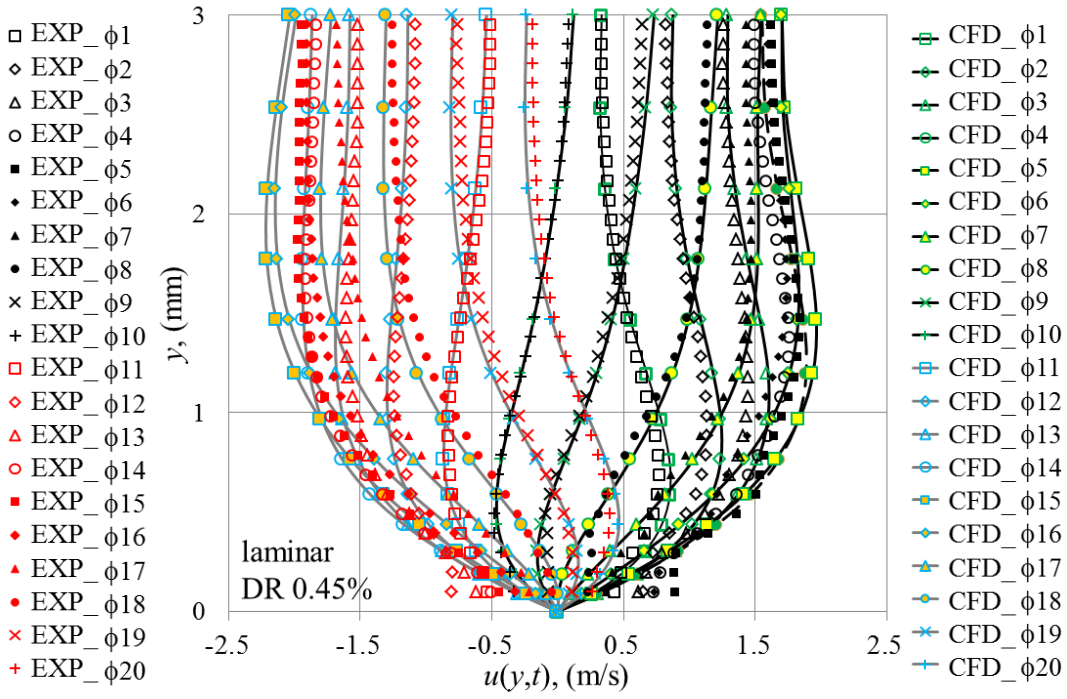

Figure 5.3a: Velocity profiles within the cold channel for 0.45% drive ratio.

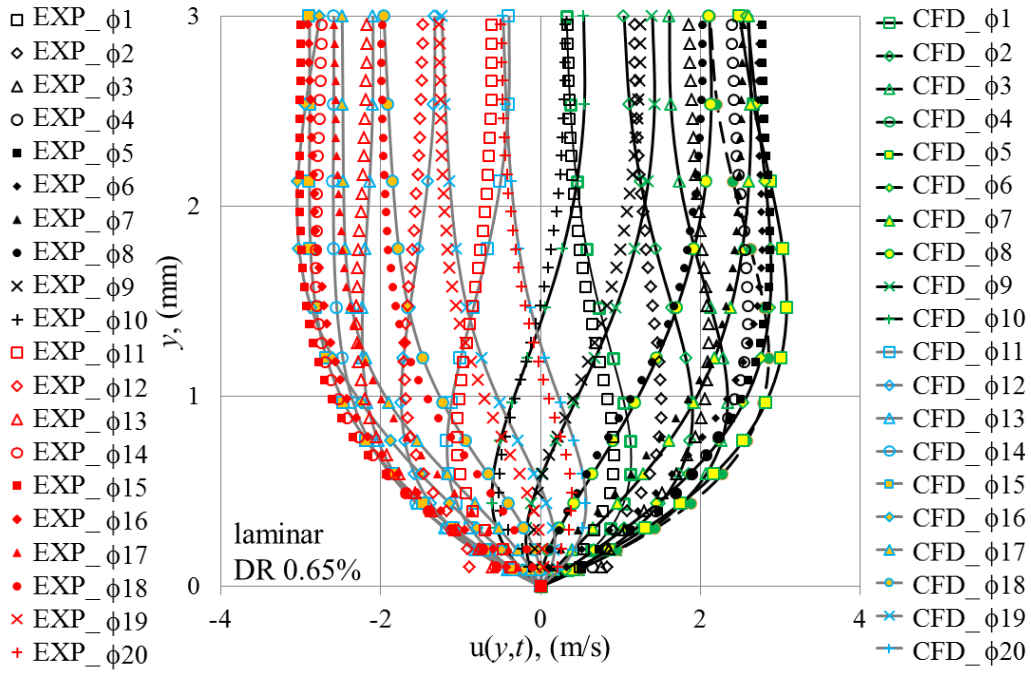

Figure 5.3b: Velocity profiles within the cold channel for 0.65% drive ratio.

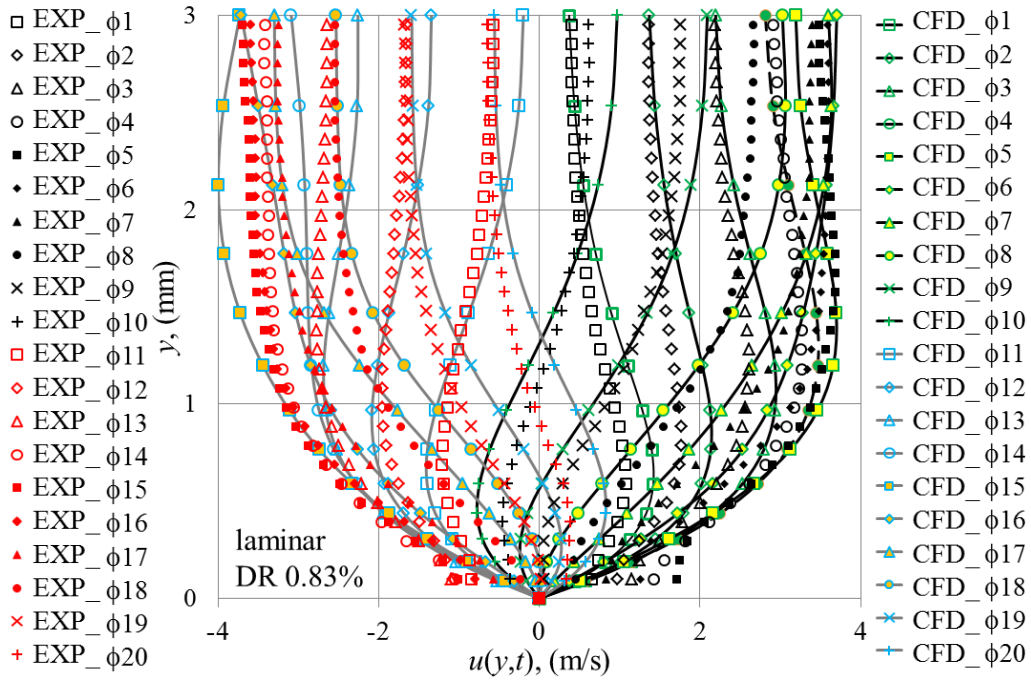

Figure 5.3c: Velocity profiles within the cold channel for 0.83% drive ratio.

As the drive ratio becomes higher, the disparity between the velocity profiles from the laminar model and the experiment become bigger. The laminar model does not seem to provide velocity profiles that have reasonable agreement to the experimental results.

The differences in velocity profile between experiment and numerical result can also be illustrated in the vorticity contours (Figure 5.4). Here, in the numerical solutions, there appear structures (disturbances) not present in the reality.

Figure 5.4 covers the area within a channel of a heat exchanger and is for drive ratio of 0.83%. The experimental data at low drive ratios is unavailable due to the thermophoresis effect, as mentioned earlier in section 4.5.3.

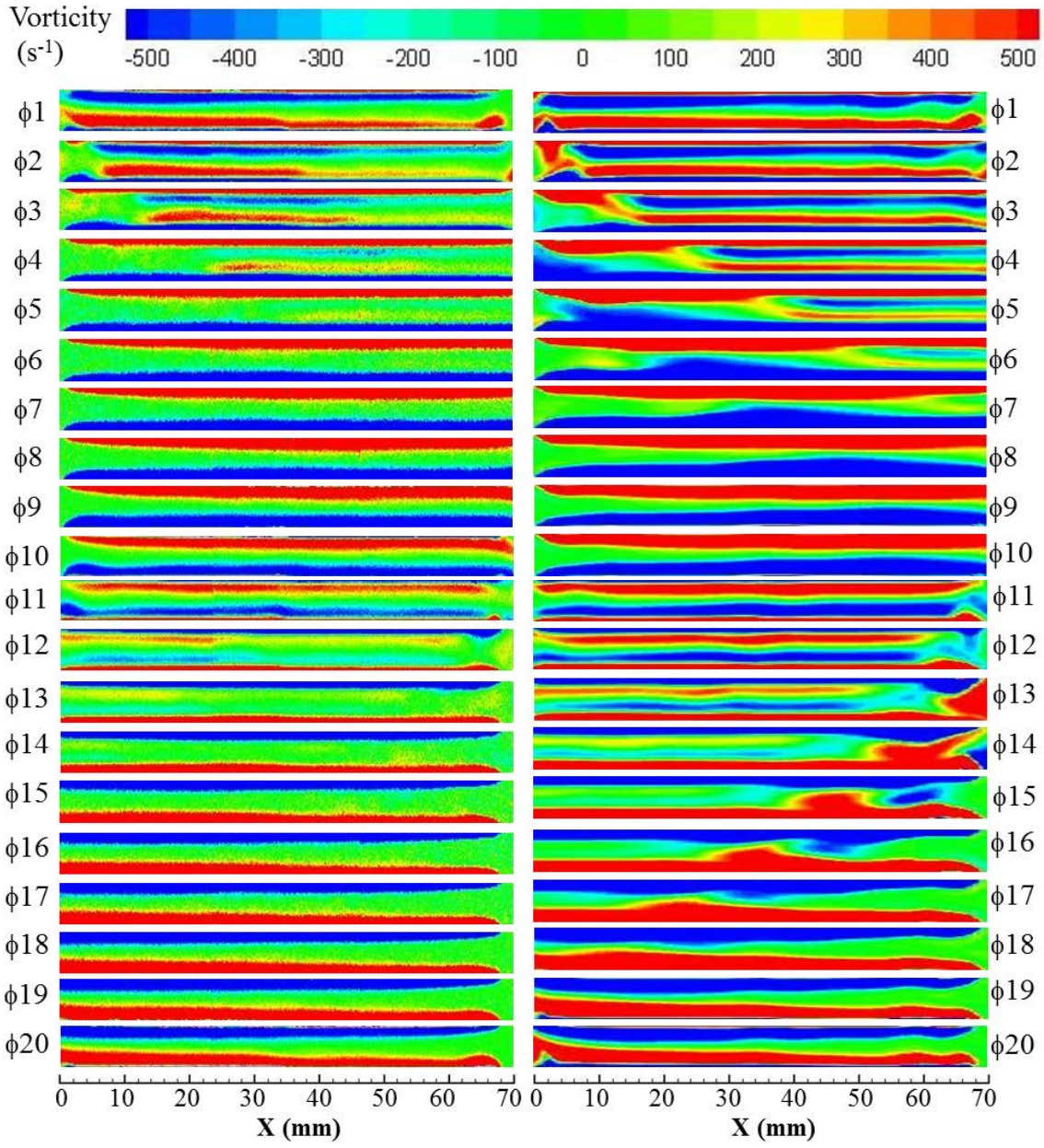

(a) (b)

Figure 5.4: Comparison between vorticity contour from (a) experiment and (b) CFD laminar model. The drive ratio is 0.83%. The ratio of *x*:*y* is 1:1.

Comparing $\phi 3$ for experimental and numerical results, it seems that the second shear layer within the channel, predicted by the numerical model, appears stronger than in the experimental results. Furthermore, the laminar model also produce a "blob" of vorticity that travels within the channel between phases $\phi 13$ to $\phi 17$ and that is not seen in the experimental results.

Many investigations (c.f. Mao and Jaworski, (2010a), Mao and Jaworski (2010b), Worlikar and Knio (1996)) have shown that oscillatory flow past parallel plate structures creates strong vortex structures at the end of plates. The remains of these structures tend to be re-entrained into the channel as the flow changes direction. This suggests that there may be sufficient instabilities present in the flow to trigger turbulent transition. Furthermore, the critical Reynolds number defined by Merkli and Thomann (1975) was strictly for a flow within a long channel (infinite length). Therefore it seems plausible that that turbulent transition may be triggered for much lower Re_c when fluid flows past relatively short plates. This is why it is worthwhile to test a range of turbulent models presented in the following section.

5.3 Turbulence flow model

Figure 5.5 shows the vorticity contours for the drive ratio of 0.83% obtained using two turbulence models: k-ε and k-ω. The results in Figure 5.5 are best discussed in comparison with Figure 5.4. The vorticity between the plates predicted by the k-ω model exhibit a lower level of "disturbance" compared to the results obtained from the laminar model. However, there is still a suspect "disturbance" that travels within the channel that is not seen in the experimental visualisations. A much better vorticity contours are produced by the k-ε model. However, the second shear layer is slightly under predicted as can be seen by comparing phases $\phi 1$ and $\phi 3$ of Figures 5.4(a) and 5.5(a).

The results of Figures 5.4(b) and 5.5(b) suggest that the disturbances originate from the open area at the end of plates. A comparison of vortex structures at the end of the plates is then carried out to help decide the best turbulence model that describes the flow. The results are presented in Figures 5.6 to 5.8.

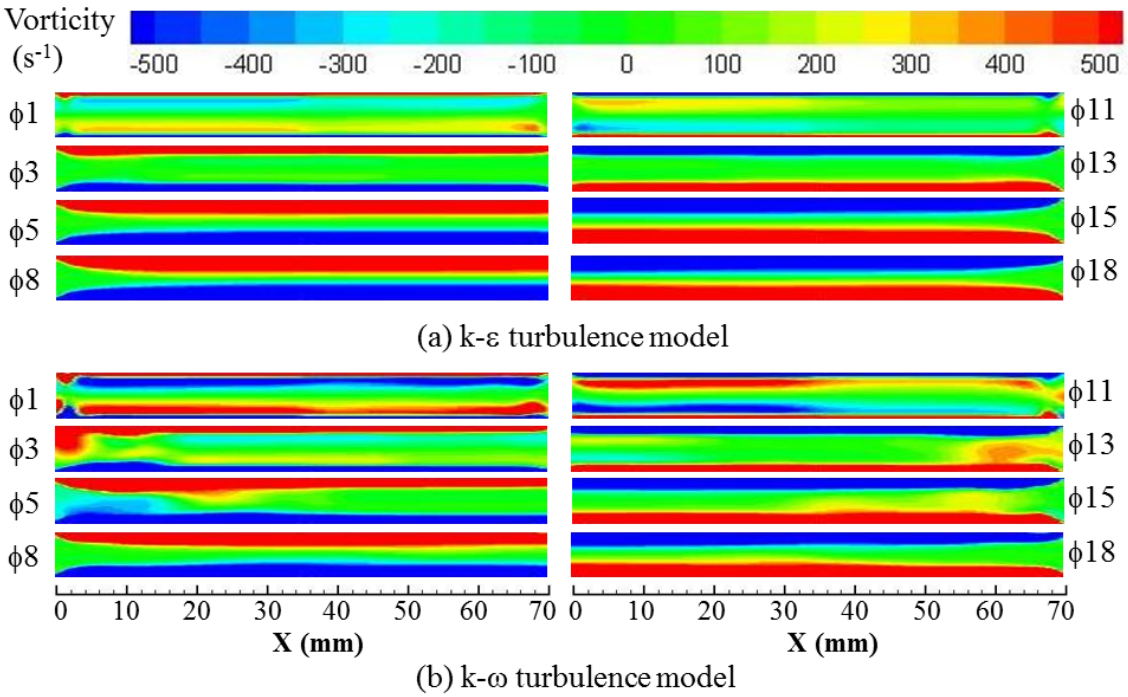

Figure 5.5: Comparison between vorticity contours from (a) k-ε; and (b) k-ω turbulence models. The drive ratio is 0.83%. The ratio of *x*:*y* equals 1:1.

Figure 5.6 shows that the flow enters the left end of the heat exchanger assembly at phase ϕ1 and reaches the maximum amplitude at ϕ5. During these phases, a weak vortex structure from the open area next to the left end of the hot heat exchanger moves into the channel. The vortex structure at the right end of the heat exchanger assembly elongates as the velocity increases but stays attached to the solid ends until the maximum velocity is reached at ϕ5. When the flow decelerates, the vortex structures at the right end of the plates start shedding as seen at ϕ8. Similar trends are observed for the second half of the cycle as the flow reverses from phases ϕ11 to ϕ20 although not exactly the same due to asymmetry of the flow (the effect of temperature).

Figure 5.7 shows vorticity contours at the ends of the heat exchanger assembly calculated by the k-ε turbulence model. A very different pattern to the experiment is observed. The vortex structures at the right end of the plate for ϕ3 appear more “stable” than in the experiment. This is consistent with the prediction of a very weak second shear layer within the channel as seen in Figure 5.7. The pair of vortex structures at the end of plates elongates until the flow reaches maximum velocity at ϕ5. In the

experimental results, the vortex structures at this phase starts to “wiggle”. This is not seen from the results calculated from the k-ε model. As the flow decelerates, the elongated structures predicted by k-ε model retain their shapes but start to lose their strengths. The strength of the attached vortex structures fades until the flow completely reverses at ϕ11. The second half of the cycle takes place and a similar trend is observed. Vortex shedding phenomena are not seen from the results of k-ε turbulence model.

Figure 5.8 shows vorticity contours at the left and right ends of the heat exchanger assembly calculated by the k-ω turbulence model. The vortex structures have a closer resemblance to the experimental result than those from k-ε model. The vortex shedding process starts at the right end for ϕ1 and the left end at ϕ11. The vortex strengths seem slightly over predicted, as the corresponding structures appear somewhat “weaker” in the experimental results. The differences may be related to the consequence of “stitching” and “averaging” of the experimental results as explained in the original papers by Shi et al., (2010b) and Mao and Jaworski (2010b) . It may also be the result of two-dimensional assumptions used in the current turbulence model. Nevertheless, the resemblances of the flow structures to the experimental ones is quite compelling.

The results show that the flow structures at the end of plates are best predicted by the k-ω turbulence model. The slight disparity observed for the vorticity plots within the area bounded by the plates of the heat exchangers between the k-ω model and experimental results may require a more refined investigation. This will be discussed in the next paragraph.

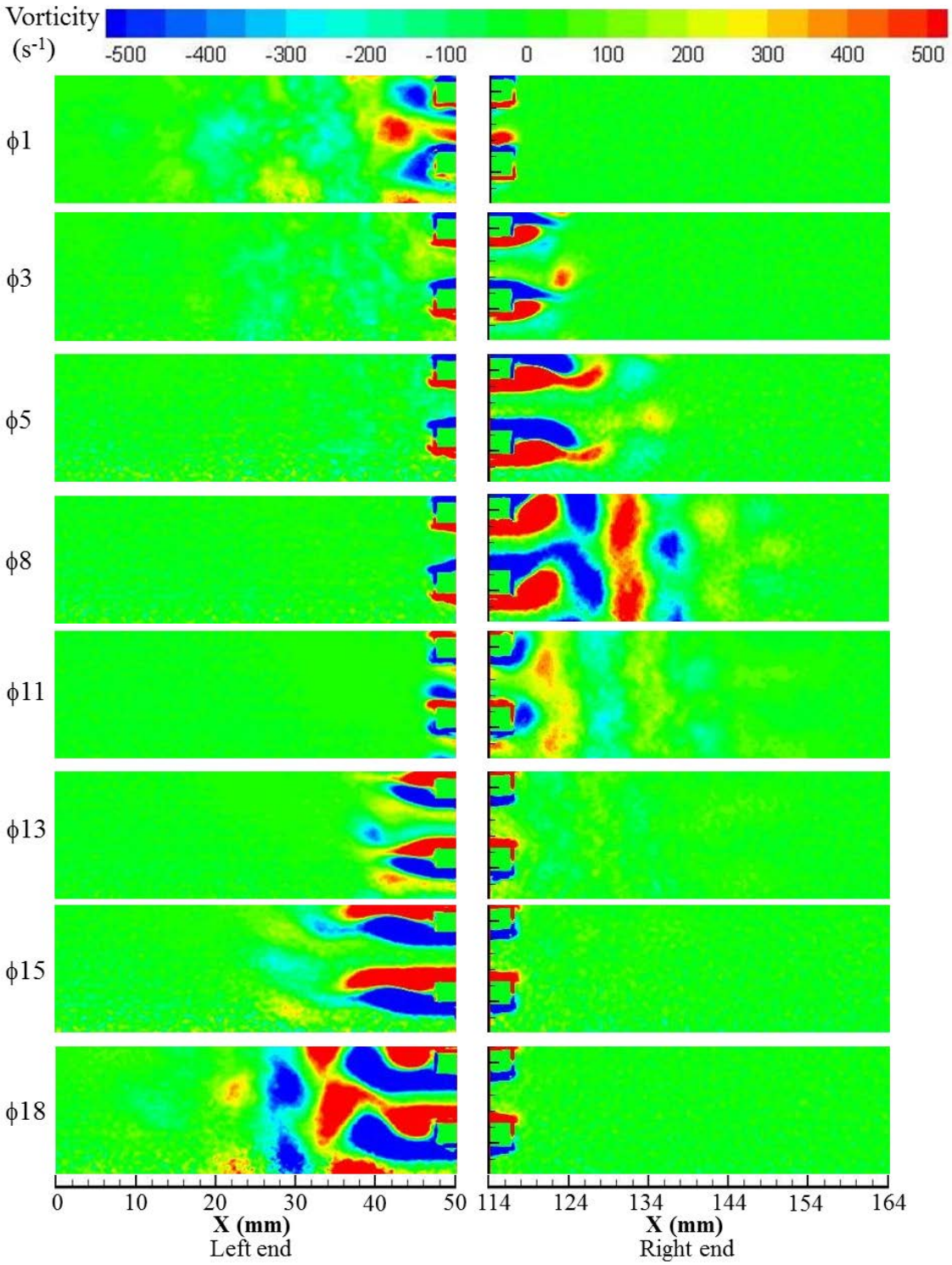

Figure 5.6: Vorticity contours at the left and right ends of the heat exchanger assembly calculated from the experimental results of Shi et al. (2010). The ratio of *x*:*y* equals 1:1.

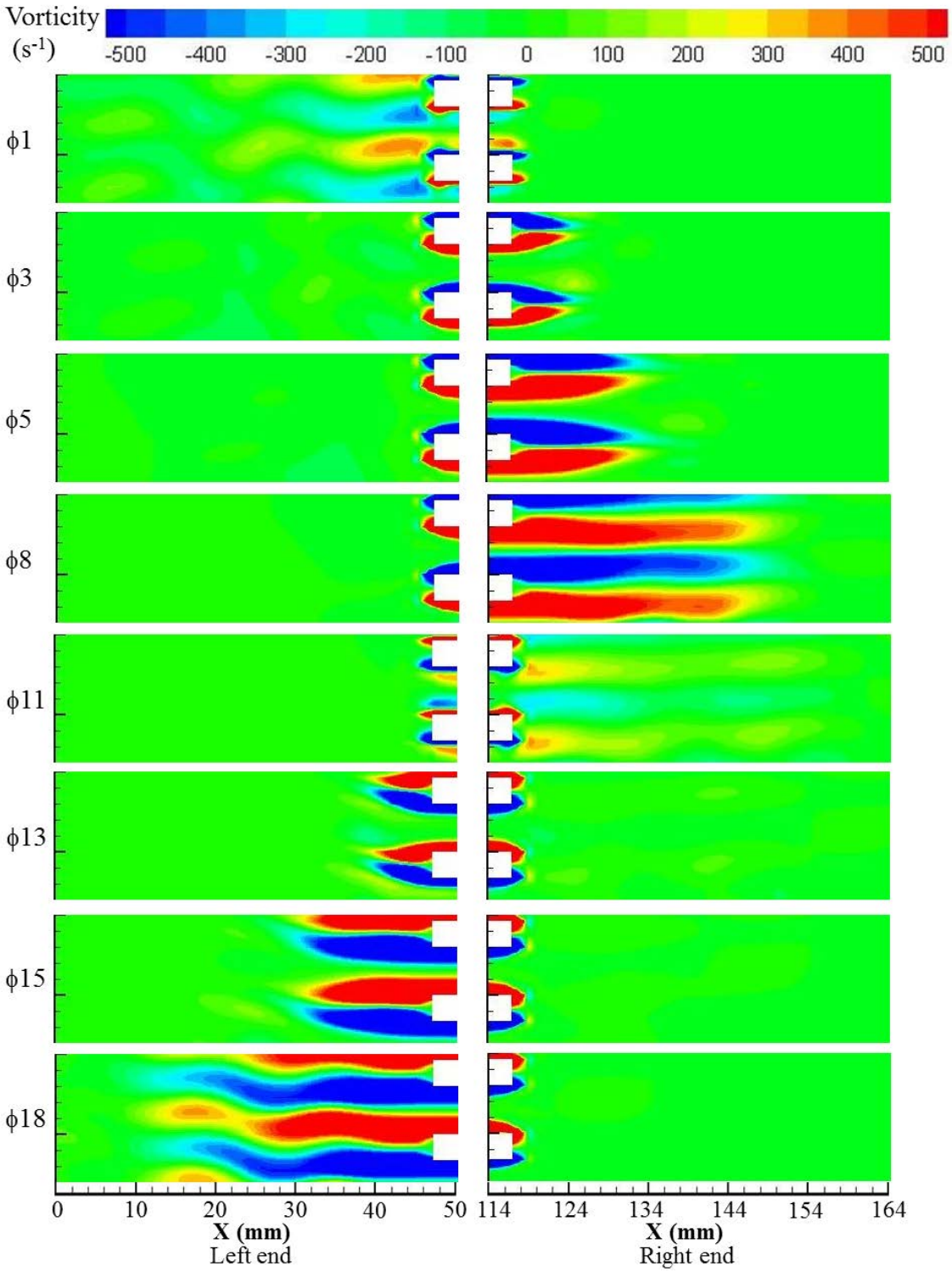

Figure 5.7: Vorticity contours at the left and right ends of the heat exchanger assembly calculated from results of k-ε turbulence model. The ratio of *x*:*y* equals 1:1.

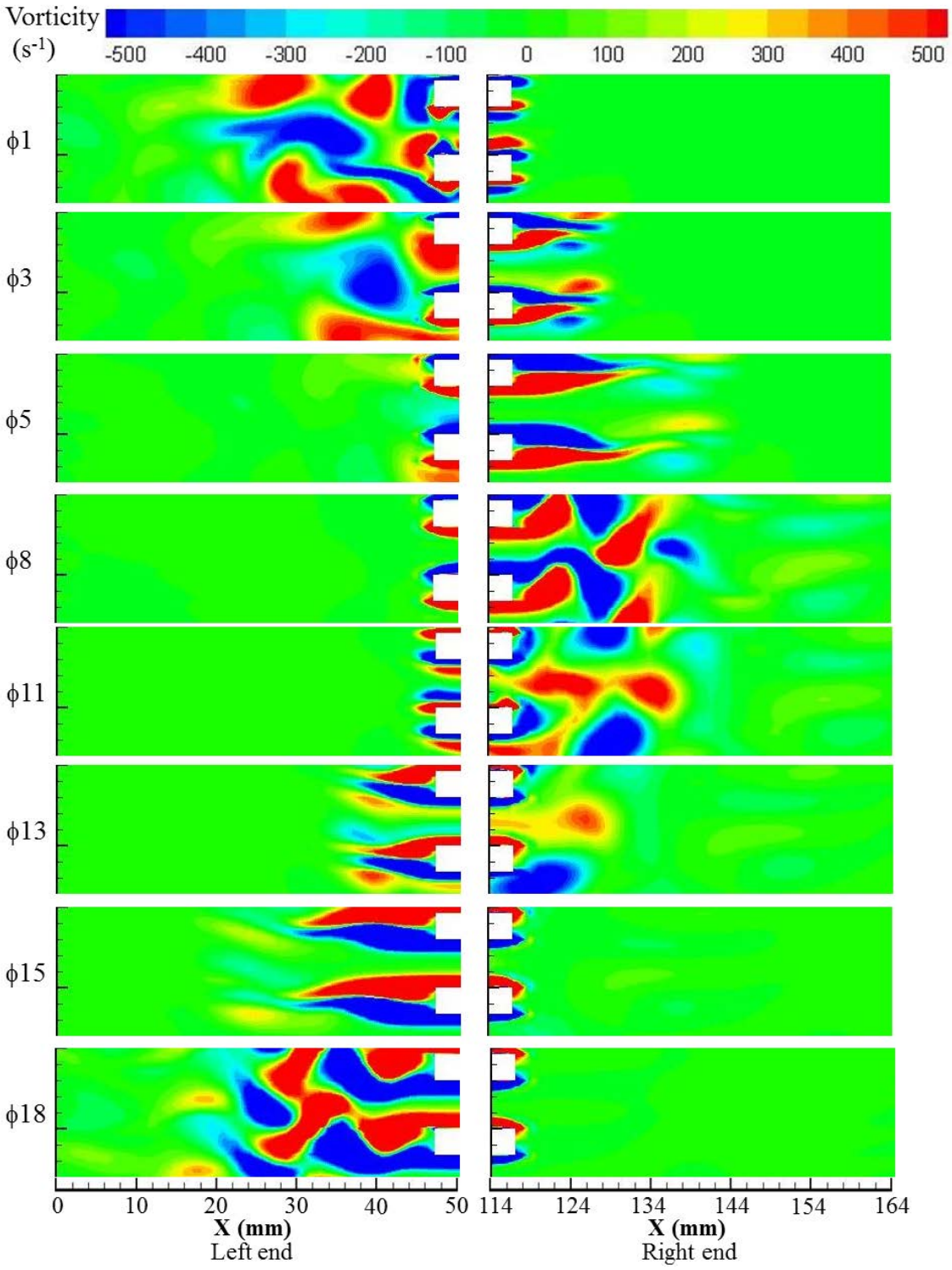

Figure 5.8: Vorticity contours at the left and right ends of the heat exchanger assembly calculated from results of k-ω turbulence model. The ratio of *x*:*y* equals 1:1.

Menter (1994) proposed a modified two equations model called shear-stress-transport (SST) k-ω model. It was proposed based on the observations of performance of the conventional k-ε and k-ω models. The k-ε model is reported to perform best in the wake and free stream region while k-ω model best models a flow in a bounded area. Based on this observation, Menter developed the SST k-ω model, which used both the k-ε and k-ω models appropriately. This is implemented through an introduction of a control parameter that applies the appropriate model depending on the distance to the nearest wall. The model is suggested to cater for flows that involve both inviscid and viscosity affected regions. The SST k-ω model was used in this study in an attempt to get a better prediction of the flow considered in this chapter. The comparison between velocity profiles from the experimental results and the numerical models is shown in Figure 5.9 for selected phases of the flow cycle.

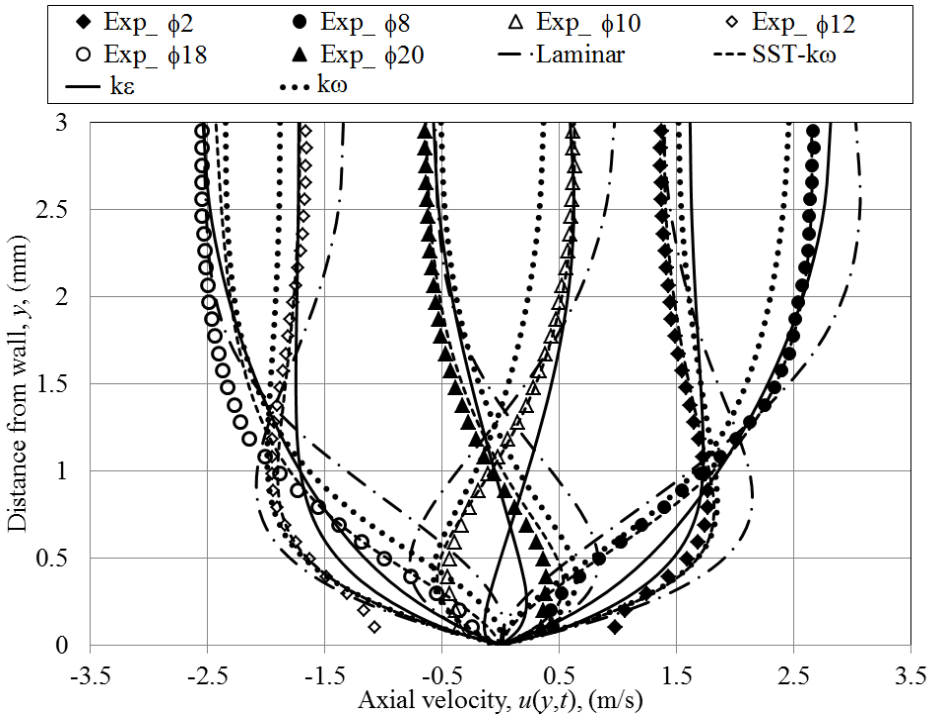

Figure 5.9: Comparison between velocity profiles from experimental and numerical results. The drive ratio is 0.83% in nitrogen at 1 bar and 13.1 Hz.

The velocity profiles are plotted at a location 10 mm away from the joint above the cold plate. As was shown earlier, the laminar model over predicts the profiles especially at locations near the wall. The predictions from k-ε and k-ω models miscalculate the magnitude of velocity both near the wall and within the core away from the wall.

Taking ϕ1 as an example, the k-ε model gives good predictions at the core but under predicts the velocity magnitude near the wall. On the other hand, the k-ω model gives a better prediction near the wall but under predicts the magnitude of velocity at the core. The profiles are better predicted by the SST k-ω model. A good match is found between the results from the SST k-ω model and the experimental results for almost all the phases of a flow cycle as shown in Figure 5.10.

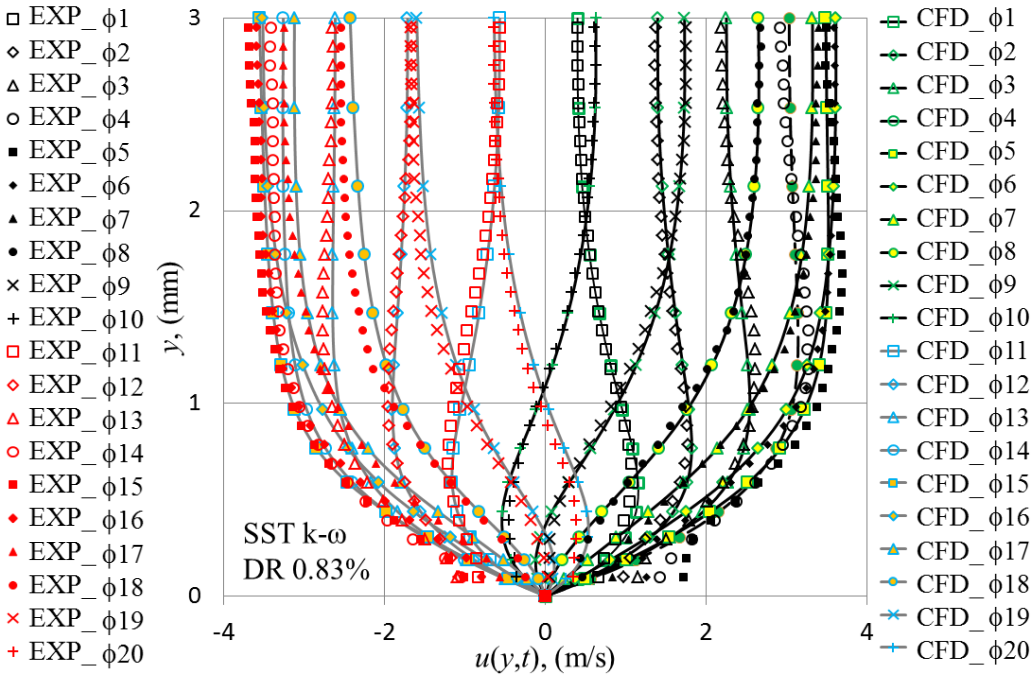

Figure 5.10: Comparison between velocity profiles from SST turbulence model (black and grey lines) and experiment (red and black symbol). (N_2, 1 bar, 13.1 Hz, 0.83% drive ratio).

The resulting vorticity contours within the channel are shown in Figure 5.11. Overall, Figure 5.11 shows that a good match to experimental results is obtained through the use of the SST k-ω model. A slight disagreement on the strength of the secondary shear layer is still visible during the first few phases that represent the acceleration stages of a flow cycle (ϕ2 to ϕ4 and ϕ12 to ϕ14). This may be related to the uncertainty of the measurement as well as the two-dimensional assumptions of the numerical model used in modelling the three-dimensional flow features. Nevertheless, the SST k-ω model has provided the best solution for the drive ratio of 0.83% with the closest match of flow field to experiment. The vorticity contours at the ends of the heat exchanger assembly,

calculated by this model also agree well with experiment. The results are shown in Figure 5.12.

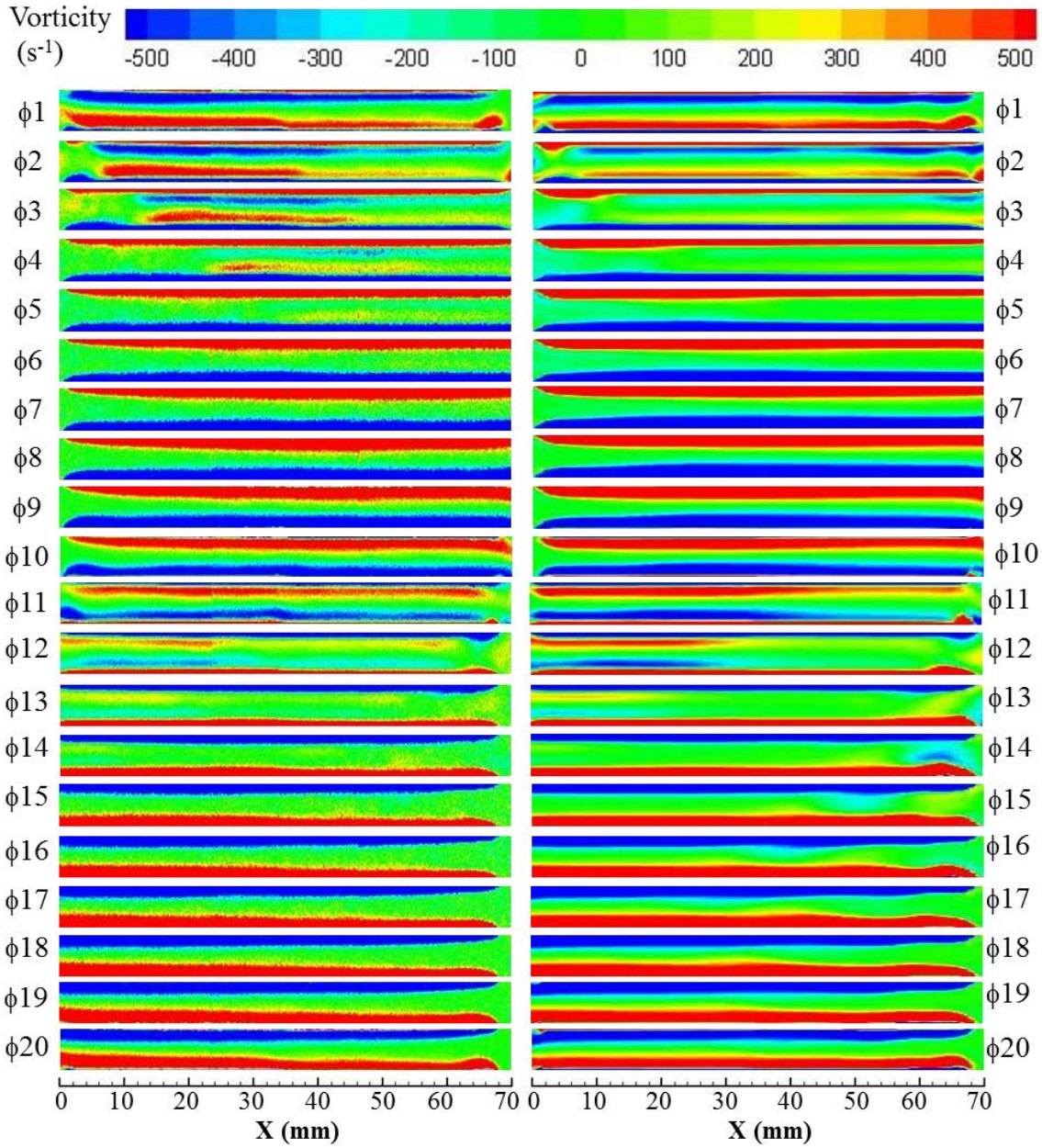

Figure 5.11: Comparison between vorticity contours from (a) experiment of Shi et al. (2010) and (b) SST k-ω model. The drive ratio is 0.83%.

The vorticity contours in Figure 5.12 are similar to the results obtained from the k-ω model. This indicates that the vortex structures at the end of the plates are strongly influenced by the movement of the shear layer near the wall of the channel. The correctly defined flow condition within the channel results in a better prediction of flow

structures at the end of plate. Clearly, the SST k-ω model with its excellent control parameter has given an improved prediction of the flow field in both the areas within the channel and the open area next to it.

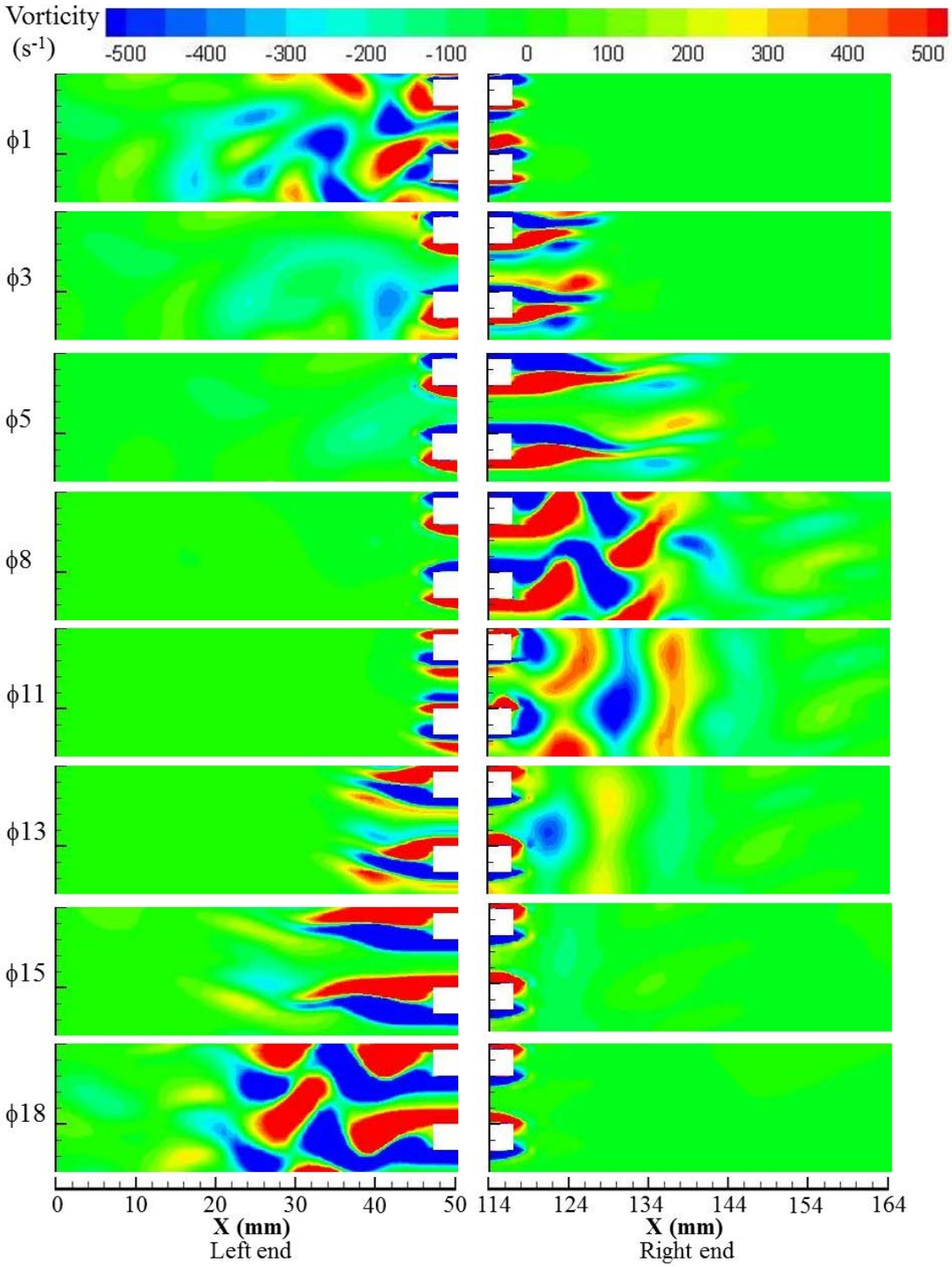

Figure 5.12: Vorticity contours at the ends of heat exchanger assembly calculated from SST k-ω model. The drive ratio is 0.83%.

Following the successful application of the SST k-ω to modelling the flow field within the heat exchanger at 0.83% drive ratio, the model was subsequently applied to the other two drive ratios of 0.45% and 0.65%. The resulting velocity profiles for all 20 phases, together with their experimental counterparts, are shown in Figure 5.13.

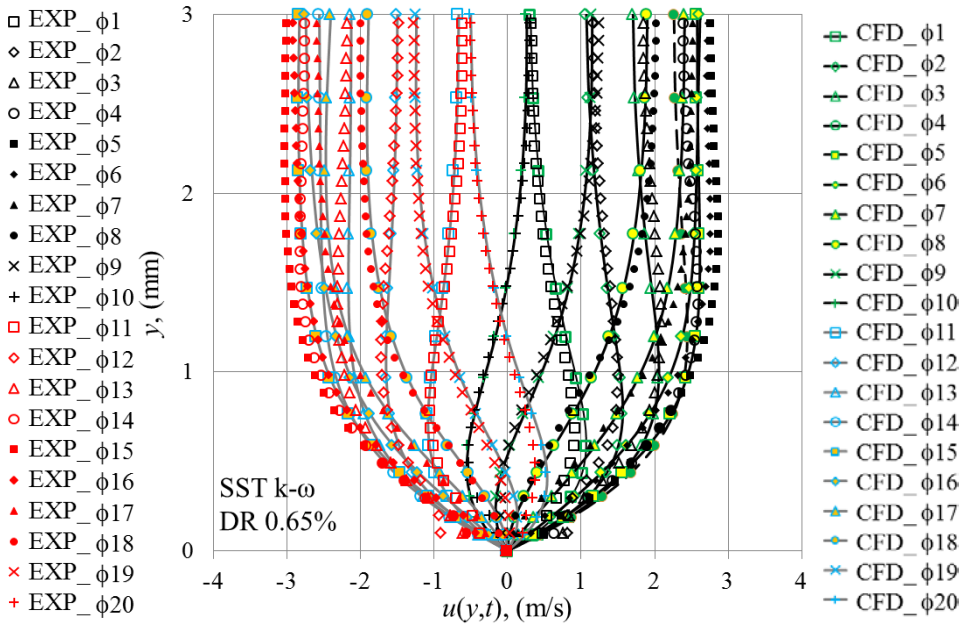

(a)

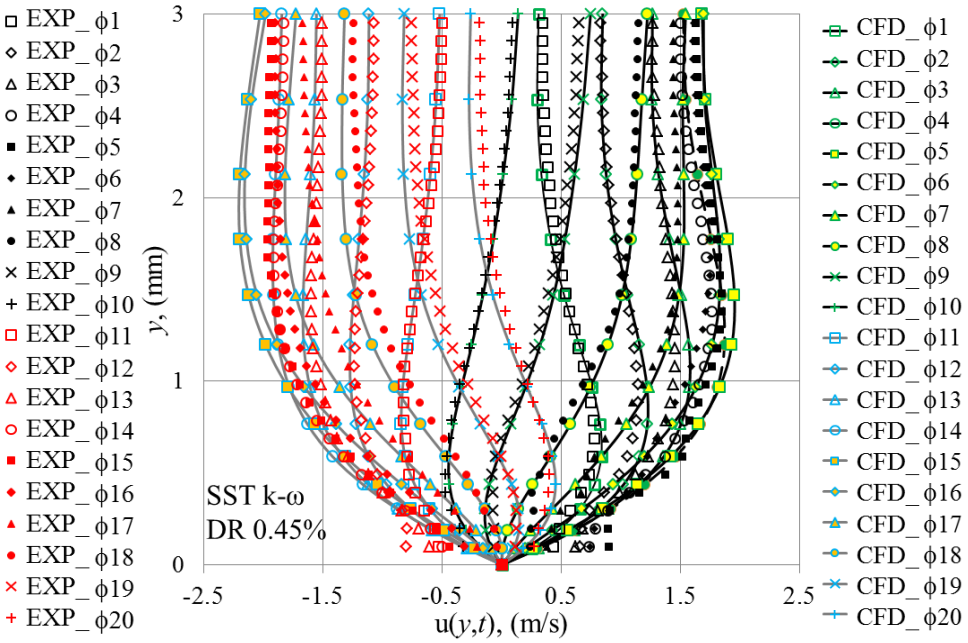

(b)

Figure 5.13: Velocity profiles from SST k-ω model for drive ratio of (a) 0.65% and (b) 0.45%.

For drive ratio of 0.65%, a better match to experiment is obtained if it is compared to prediction from the laminar model as shown earlier in Figure 5.3b. However, the match is not as good as predicted for the drive ratio of 0.83%. For 0.45% drive ratio, the turbulence model provides no improvement on the velocity profiles when compared to that of laminar model. This indicates that the flow at a drive ratio of 0.45% has not yet reached a state suitable for turbulence model. The laminar model does not seem to provide a satisfactory solution either. Observations between the flow of two extreme conditions, the 0.3% and 0.83% drive ratios, suggest that there may be a transitional phenomenon involved within this intermediate range of drive ratios. Therefore, the four equation transition model known as Transition-SST (Menter et al., 2006) is used and the resulting velocity profiles are shown in Figure 5.14.

Figure 5.14 shows the resulting velocity profile calculated by the Transition-SST model for cases with drive ratio of 0.45% and 0.65%. The velocity profiles corresponding to 0.65% drive ratio predicted through the transition model are not any better than the profile shown in Figure 5.13(a). Hence, the turbulence model seems to be a better model for predicting the flow at this drive ratio. The difference in amplitude of velocity between experimental and numerical results at $\phi 5$ and $\phi 15$ may be due to moderation constant not varied in this study.

The transition SST model is shown to provide velocity profiles for 0.45% drive ratio that agree well with experiment. This may indicate that the flow at this drive ratio is transitional in its nature. In oscillatory flow, turbulent transition is a much more complex process. Swift (2002) summarizes that the transitional region exists between “weakly turbulent region” (flow with turbulent burst at the centre of pipe with the boundary layer remaining laminar) and “conditionally turbulent region” (the flow changes between “weakly turbulent” and “fully-turbulent” flow within a cycle). Furthermore, an oscillatory flow may also experience “relaminarization” where a “turbulent-like” flow is followed by a “laminar-like” flow in one cycle (c.f. Narasimha and Sreenivasan, 1979 and Akhavan et al., 1991).

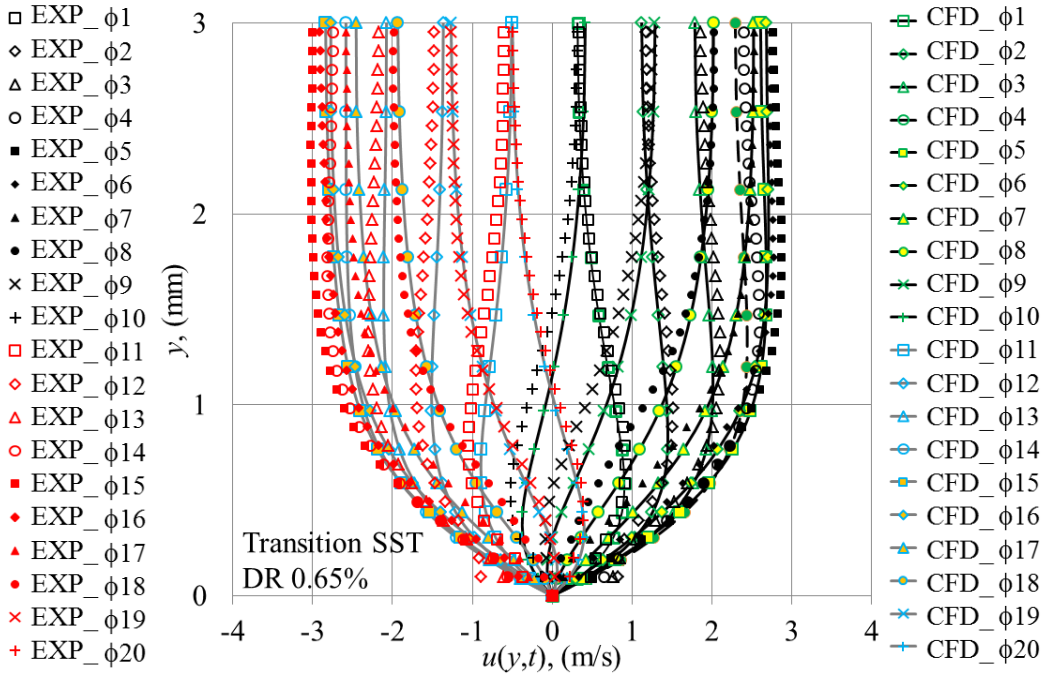

(a)

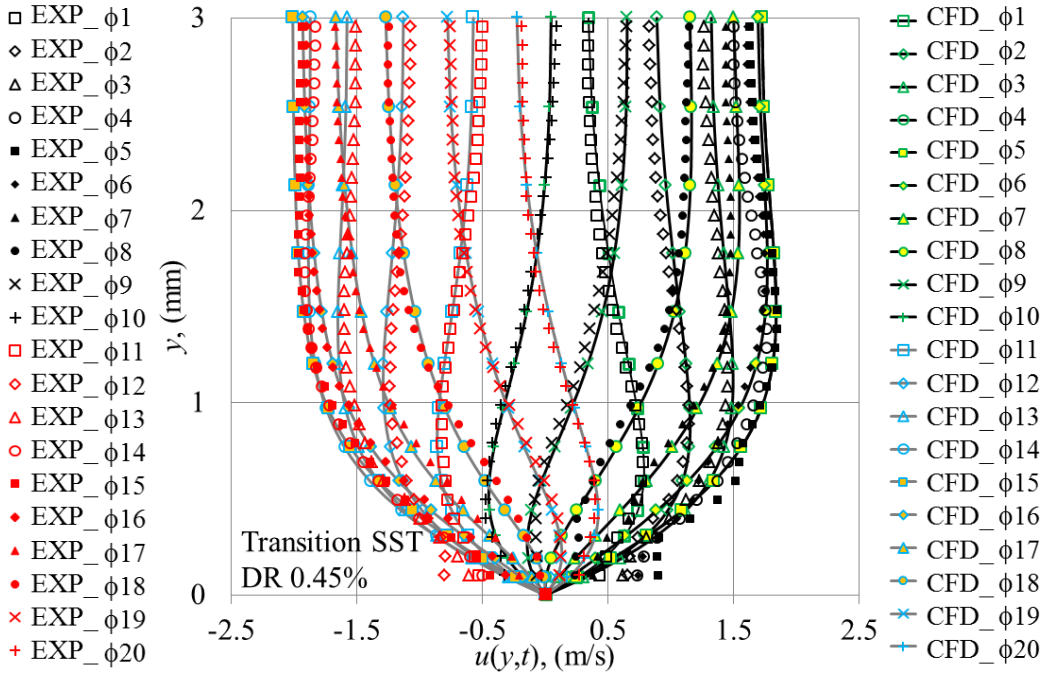

(b)

Figure 5.14: Velocity profiles from Transition SST model for a drive ratio of (a) 0.65% and (b) 0.45%.

As mentioned earlier, all the drive ratios investigated in this study correspond to a critical Reynolds number, Re_c, less than 400. It is worth noting that the critical Reynolds number was defined based on an oscillatory flow within an infinite pipe (Merkli and

Thomann, 1975). The heat exchanger assembly in the current study has a short length. The disturbances from the edge of plates and the shed vortices as shown in Figure 5.12 may act as "seeds" for turbulent transition. This may explain the need for turbulence/transition model even though the drive ratios are relatively low (Re_c<400). The resulting velocity magnitudes at location *m* for all the drive ratios investigated are tabulated in Table 5.2. It is shown that the laminar model is sufficient to model the flow at 0.3% drive ratio. Transition model give better predictions for 0.45% drive ratio, but the difference in magnitude is not much improved. The turbulent model gives a very good comparison to experiment for 0.83% drive ratio. The profiles of velocity for drive ratio 0.65% are well estimated by the turbulent model, but the difference in magnitude is quite significant.

Table 5.2: Velocity amplitude comparison between numerical models.

Drive ratio (%)	Velocity amplitude at point *m*, (m/s)			
	Experiment	Laminar	Transition SST	SST k-ω
0.3	1.30	1.32	1.32	1.32
0.45	1.90	1.99	1.98	2.00
0.65	2.97	3.07	2.86	2.84
0.83	3.84	4.40	-	3.73

The velocity magnitudes tabulated in Table 5.2 can also be used to represent the gas displacement, $\delta=u_m/2\mu f$. It follows that the drive ratios of 0.3%, 0.45%, 0.65% and 0.83% correspond to the gas displacement of 16, 23, 36 and 47 mm, respectively. Clearly, the gas particle in the flow with drive ratio higher than 0.65% moves more than half of the total length of the heat exchanger channel (70 mm). Then the flow reverses and moves over an approximately similar distance. The forward and backward movements of the gas particle convey the energy of the vortex structures at the end of plates into the channel. Vortex structures of a selected phase, $\phi 8$, are shown in Figure 5.15 for drive ratios of 0.3% and 0.83%.

Evidently, the vortex strength for the wake appearing at the end of plates for 0.83% drive ratio can create a strong disturbance when it is pushed back into the channel. This could be a possible explanation for the appearance (and the need for) turbulence in this drive ratio as a means of dissipating the flow energy.

The disturbance that occurs between the plates of the heat exchanger is also complicated by the effect of thermal expansion that causes the gas particles to move at a different magnitude for two halves of one cycle as suggested in chapter four. Note that the critical Reynolds number, Re_c, suggested in literature is obtained for a fully developed flow in a relatively long pipe. The short length of the plates investigated in this study prohibits the flow of high drive ratios to reach a fully developed state. Most heat exchangers are short and a practical system works with high drive ratio. This study suggests that turbulence is likely to occur within heat exchangers of high performance systems working in oscillatory flow condition.

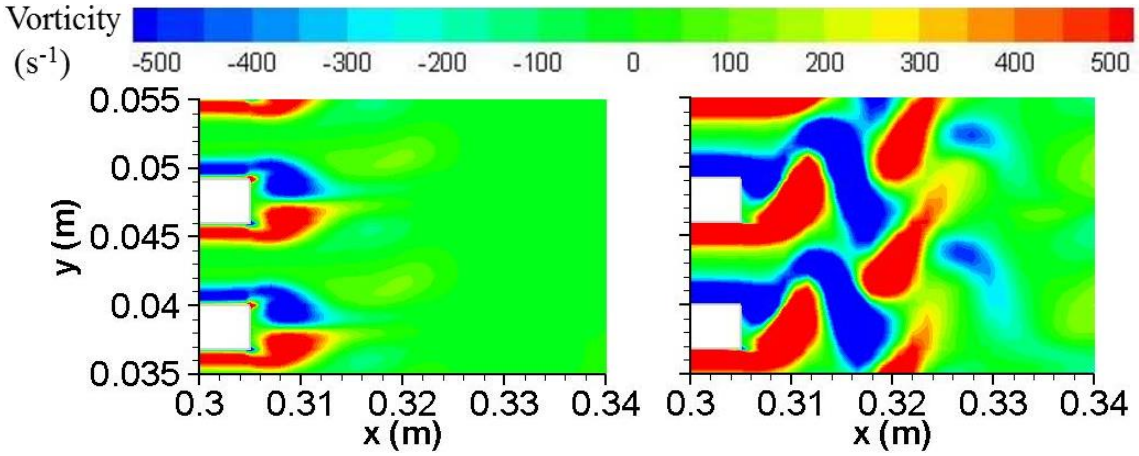

(a) Drive ratio = 0.3% (b) Drive ratio = 0.83%

Figure 5.15: Vorticity contour of ϕ8 plotted at the end of cold heat exchanger at a drive ratio of (a) 0.3% and (b) 0.83%.

5.4 Viscous dissipation

The dimensionless viscous dissipation for all the drive ratios investigated in this chapter is shown in Figure 5.16. This dissipation is based on the mean flow velocity as defined in equation (4.20). This is also known as “direct dissipation”, not to be confused with turbulent dissipation (Schlichting and Gersten, 2001). As with the laminar model, the direct dissipation represents the transfer of mechanical energy to internal energy through viscosity. The turbulent dissipation (which is a transfer of energy from the mean motion into the turbulence fluctuation and then into the internal energy) is indirectly affecting the mean flow when turbulence model is used. The effect on the internal energy of the flow is reflected in the final velocity of the mean flow used in

equation (4.20). As seen in Figure 5.16, the viscous dissipation increases as the drive ratio increases. The increment occurs in both the areas within the channel and at the end of the channel. These areas have higher viscous dissipation compared to cold area presumably due to higher gas viscosity as temperature increases. Thermal expansion at the area bounded by the wall of the hot heat exchanger and the temperature-driven effect particularly prominent at the hot end may as well be responsible for the higher viscous dissipation within the area. As the drive ratio increases, the amplitude of flow increases and the viscous dissipation becomes bigger.

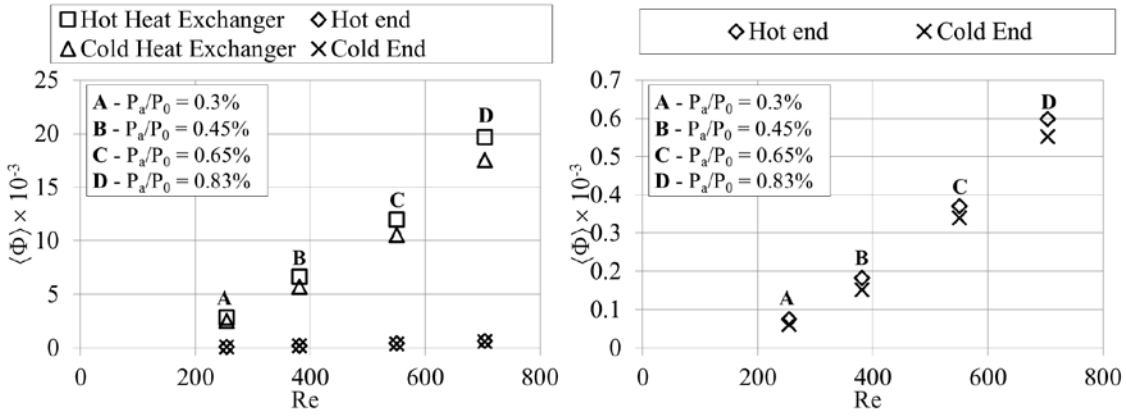

(a) (b)

Figure 5.16: (a) The effect of drive ratio on dimensionless mean flow viscous dissipation and (b) the enlarged view of the viscous dissipation at the end of plates.

5.5 Heat transfer condition within the heat exchanger plates

Finally, the wall heat transfer calculated from the model is compared to the experimental data. Heat flux, *q*, for all models is averaged over one cycle and the length of the heat exchanger, *l*, and calculated as:

$$q_{H,C} = \frac{1}{2\pi l}\int_0^{2\pi}\int_0^{l} -k\frac{dT}{dy}\bigg|_{wall} dx d\phi \qquad (5.14)$$

The subscripts *C* and *H* refer to cold and hot heat exchanger, respectively. Here, the mean thermal conductivity, *k*, is used to calculate the heat flux obtained from laminar, Transition SST and SST k-ω model (Schlichting and Gersten, 2001). The Reynolds number is calculated with hydraulic radius defined as twice the size of the gap between

the plates, 2*D*.

Figure 5.17 shows that the heat flux predicted from the numerical models and experiments increases with an increase of drive ratio. The Reynolds number calculated from the turbulent model is consistently closer to experiment with a good match of velocity discussed earlier.

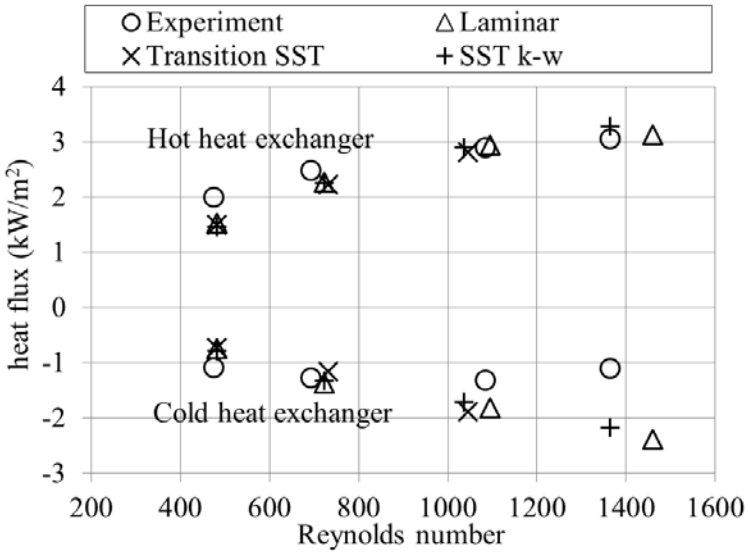

Figure 5.17: Heat fluxes at cold and hot heat exchangers-comparison between numerical and experimental results.

The turbulent model brings the magnitude of heat flux slightly closer to experiment. The large difference between numerically and experimentally calculated heat fluxes of cold heat exchanger at higher drive ratios might be the result of losses occurring in the experiment due to the non-insulated resonator wall. The heat supplied by the hot heat exchanger is transferred to the fluid on the left and right side of the hot plate during the first and second part of the cycle. Part of the heat may be accumulated at the open area next to the hot heat exchanger and the rest is absorbed by the cold plate. As the drive ratio increases the gas particles travel to a larger distance away from the hot heat exchanger. This may encourage more heat losses to the surroundings especially when the resonator wall is not insulated. Hence, the losses may become bigger at higher amplitude of flow. There is also a possibility that the disparity is the result of three-dimensional features not captured by the two-dimensional model applied in this study. Nonetheless, the heat flux estimated by the numerical model has the same increasing trend as the experimental results.

5.6 Summary

Whilst the turbulent model is shown to predict the velocity profiles for a flow with drive ratio higher than 0.45% better, the prediction of heat transfer is not satisfactory, particularly at the cold heat exchanger working at a drive ratio of 0.65% and 0.83%. This investigation gives an insight of possible future research directions to improve the turbulence heat transfer model. It is noted that modeling heat accumulation through proper initialization procedures, as discussed in chapter four, may be a precondition for achieving more accurate solutions. Nevertheless, all trends qualitatively agree with the experiment.

Chapter Six: Heat Exchanger: The effect of operating condition on flow and heat transfer within the heat exchangers

The model developed in chapters four and five is used for further investigations of the flow and heat transfer within the parallel-plate heat exchanger. Sections 6.1, 6.2 and 6.3 are devoted to investigating the influence of the operating frequency, mean pressure and geometrical dimensions, respectively. A description of the computational model, which applies to all topics in this chapter, is given at the beginning of section 6.1. Specific descriptions of the various operating conditions tested will be given separately when covering each topic. An 'adiabatic model', where the heat exchanger walls were treated as adiabatic, was used to validate the model with the available theoretical prediction. The validation of cases with varied frequencies is shown and described in section 6.1.1. Validation for all other operating conditions is shown in Appendix One. Sections other than 6.1.1 are all related to results and discussions for cases with heat exchanger walls with a temperature profile. Two drive ratios (0.3% and 0.83%) were tested for each operating condition. Discussions on velocity profiles, temperature profiles and heat transfer conditions were all based on the low amplitude drive ratio of 0.3%. The effect of velocity amplitude was already described in chapter five. In the current chapter, the effect of increasing drive ratios is illustrated through vorticity plots. Finally, comparison between the heat transfer model used in this study and earlier works is shown in section 6.4 followed by a summary in section 6.5.

6.1 The effect of frequency

The investigation on the effect of frequency was carried out at atmospheric pressure. The 'short model', similar to that used in chapter five, was used with heat exchanger assembly fixed at the same location of 0.17λ from the pressure antinode, P_a, of a quarter-wavelength setup. The computational domain was shown in Figure 5.1.

Unlike in chapters four and five, the wavelength, λ, changes when the frequency changes following equation (2.5). The boundary conditions were selected so that the location of the heat exchanger assembly, x_s, corresponding to point *m* used before, was fixed at 0.17λ. The length of the computational domain was also fixed to 540 mm. The heat exchanger was located at the middle of the computational domain with inlet and

exit boundary conditions located 270 mm away to the left and right of the location of heat exchanger assembly, x_s, respectively.

Table 6.1: Details of cases of frequency studies with nitrogen as working medium.

Working medium : nitrogen								
P_m (bar)	f (Hz)	Distance from location of P_a (m)			Oscillating pressure, p_1 (Pa)	Oscillating mass flux, m_2' (kg.m/s)	P_a (Pa)	Drive Ratio (%)
		x_s	x_1	x_2				
1	13.1	4.6	4.33	4.87	159.6728	0.7705	300	0.3
	25	2.4	2.13	2.67	175.0567	0.7883		
	50	1.2	0.93	1.47	202.9931	0.8206		
	75	0.8	0.53	1.07	228.0034	0.8412		
1	13.1	4.6	4.33	4.87	441.7613	2.1318	830	0.83
	25	2.4	2.13	2.67	484.3235	2.1809		
	50	1.2	0.93	1.47	561.6144	2.2704		
	75	0.8	0.53	1.07	630.8094	2.3272		

Oscillating pressure of equation (5.7) was assigned at location x_1 while location x_2 was given an oscillatory mass flux following equation (5.8). The working medium was nitrogen. The oscillatory pressure and mass flux were estimated using the lossless equation as presented in equations (2.15) and (2.16). The mass flux was obtained by multiplying equation (2.16) by the mean density of the flow. The corresponding values obtained from the calculation are tabulated in Table 6.1.

The walls of the heat exchanger were treated firstly as adiabatic, to compare the results with theoretical solutions, and secondly with an imposed temperature profile as defined in chapters four and five (c.f. Figure 4.2) for the cold and hot heat exchangers. Considering the experimental work of Shi et al. (2010b), it was thought that there was heat conduction loss between the plates of the cold and hot heat exchangers which resulted in this kind of temperature distribution.

Walls other than the heat exchangers were treated as adiabatic. The thermal conductivity and viscosity of nitrogen was temperature-dependent as described in chapters four and five. The same solver settings as discussed in chapters four and five were used for the investigation in this chapter with time step size increased from 1200 steps per cycle to 1000 steps per cycle to get a convergence similar to the model reported in previous chapters.

Two drive ratios were investigated; 0.3% and 0.83%. Following the findings of chapters four and five, a laminar model was used for 0.3% drive ratio while a SST k-ω turbulence model was used for 0.83% drive ratio. In the current study the frequency is varied. The consequence of increasing the frequency is a more rapid fluid acceleration and deceleration. It is possible that turbulence may become important at lower amplitude of flow than that identified in chapter five. However, the effect is assumed to be very small (if there is any) for the smallest flow amplitude of 0.3% drive ratio and therefore neglected in this part of study. Using the cases with frequency of 13.1 Hz and nitrogen as working medium as already validated in chapter four and five as a benchmark, the extended studies presented in this chapter will then use the same solver and be validated against the established theoretical predictions found in literature (Swift, 2002).

6.1.1. Model validation

Although the theoretical predictions are based on one dimensional harmonic assumption, it was shown in chapter four that fairly good qualitative agreements between theoretical, experimental and numerical findings were achieved for cases with adiabatic boundary conditions at the wall of heat exchangers plates. Therefore the same process of validation was used here. However in chapter four the case with temperature profiles for the wall of heat exchangers plates can be validated against experiment while there was no experiment for higher frequencies.

Figure 6.1 shows the comparison between numerical and theoretical values of magnitude of axial velocity plotted in the middle of the channel for the location of 15 mm away from the joint above the location of cold plates treated as adiabatic. A good match was found as with previous results presented in chapter four.

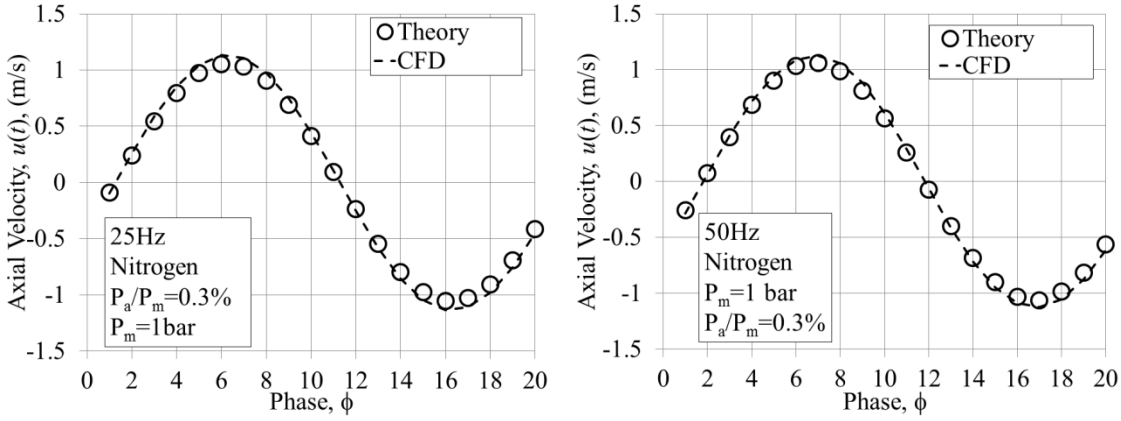

(a) (b)

Figure 6.1: Theoretically and numerically calculated axial velocity for the location at the centre of the space between plates, 15mm away from the joint, for frequencies of (a) 25 and (b) 50 Hz. Both cases use adiabatic conditions at the heat exchangers walls.

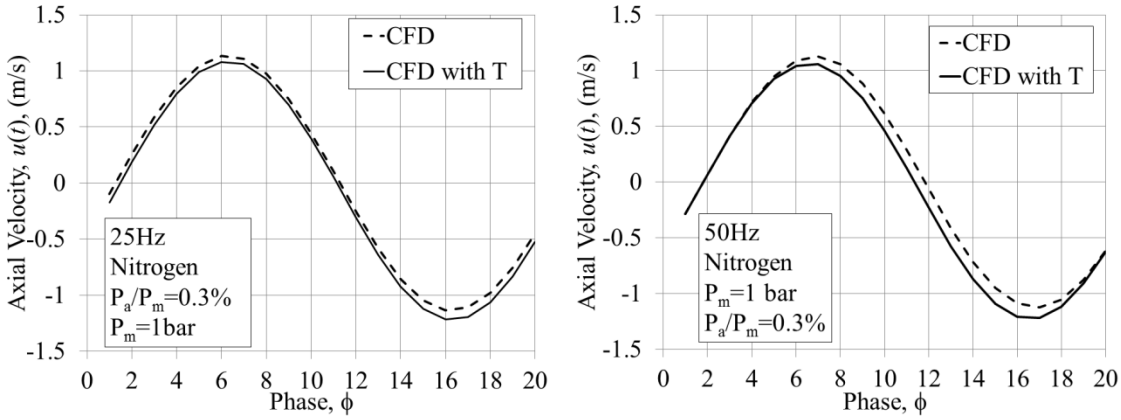

(a) (b)

Figure 6.2: Axial velocity at the centre of the gap between plates – comparison between cases with adiabatic boundary condition and temperature profile, T, along the wall of the heat exchanger. Two frequencies shown: (a) 25 and (b) 50 Hz.

Figure 6.2 shows the comparison of axial velocity obtained from adiabatic models and models with temperature profiles along the heat exchangers plates. As expected, the variation of temperature along the surface of the heat exchangers plates influences the velocity. During the first half of the cycle (from ϕ1 to ϕ10), the amplitude of the velocity for cases with temperature profile is smaller than the cases of plates treated as adiabatic. In the second half of the cycle, the magnitude of velocity is higher when there is a temperature profile at the heat exchanger plates. This is consistent with the discussions of asymmetric flow features in chapter four.

6.1.2. Velocity profiles

Figure 6.3 shows the axial velocity at the core between the plates at location 15 mm from the joint for four of the frequencies investigated. Here and onwards all results are for cases with temperature profiles along the surface.

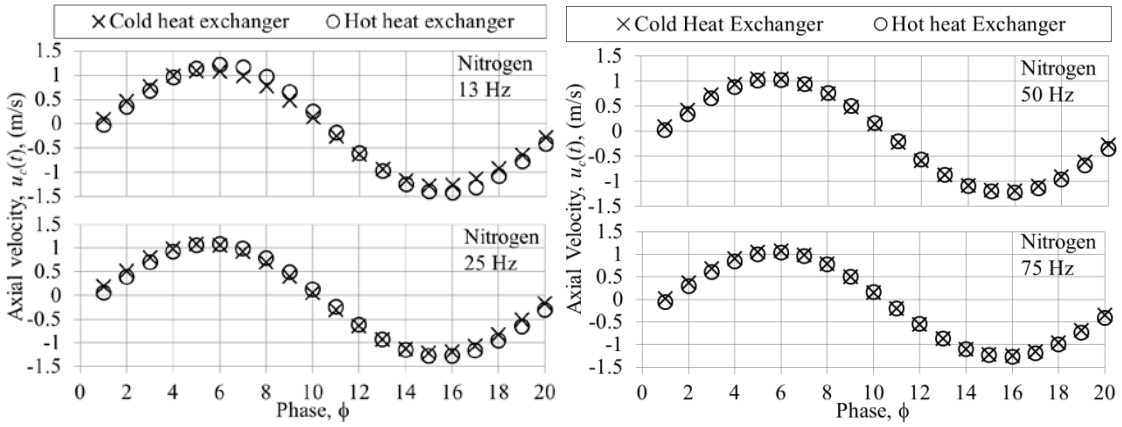

Figure 6.3: Axial velocity at the core between plates with location 15mm from the joint either way – comparison between cold heat exchanger and hot heat exchanger.

At 13 Hz, the velocity magnitude between the plates of the cold channel is lower than that at the hot channel. As the frequency increases the magnitude of velocity at cold channel matches more closely the magnitude of velocity at the hot channel. This indicates that the gas particles, at the core of both cold and hot channels, move at similar amplitudes of displacement as the frequency increases regardless of the big gradient of temperature along the heat exchangers plates. This may be related to the thermal penetration depth which becomes thinner at higher frequency hence limiting the effect of temperature on the flow at the core. This point will becomes clearer with discussions on temperature field in later section of 6.1.3. The asymmetry of the velocity profiles can still be observed with the maximum magnitude at the second half of the cycle (ϕ16) slightly bigger than in the first half (ϕ6). Consequently, the gas particles move slower during the first half of the cycle and returning faster in the second half.

Figure 6.4 shows comparison of the velocity profiles for four frequencies: 13, 25, 50 and 75 Hz. The profiles are all plotted at the same location of 15 mm away from the joint above the cold plate. The plots start from the surface of the plate up to the centre of the gap, *D*/2 (definition of location is as shown in Figure 5.1). When the frequency increases from 13 to 25 Hz, the boundary layer at the bottom of the "bell-like" shape of

the velocity profiles are “squashed” towards the wall. This indicates that the viscous penetration depth becomes smaller. The reduction of the viscous penetration depth can be observed by looking at the crossing between velocity profiles that belong to the first half of the cycle to its pair in the second half of the cycle. The pair was defined as the two phases that, ideally, had a similar magnitude but correspond to the flow in opposite directions. For example, the pair for phase ϕ10 was phase ϕ20. Hence, looking at the crossing point between phase ϕ10 and phase ϕ20 for all the four frequencies shown in Figure 6.4, one can observe that the crossing point is closer to the wall as the frequency increases.

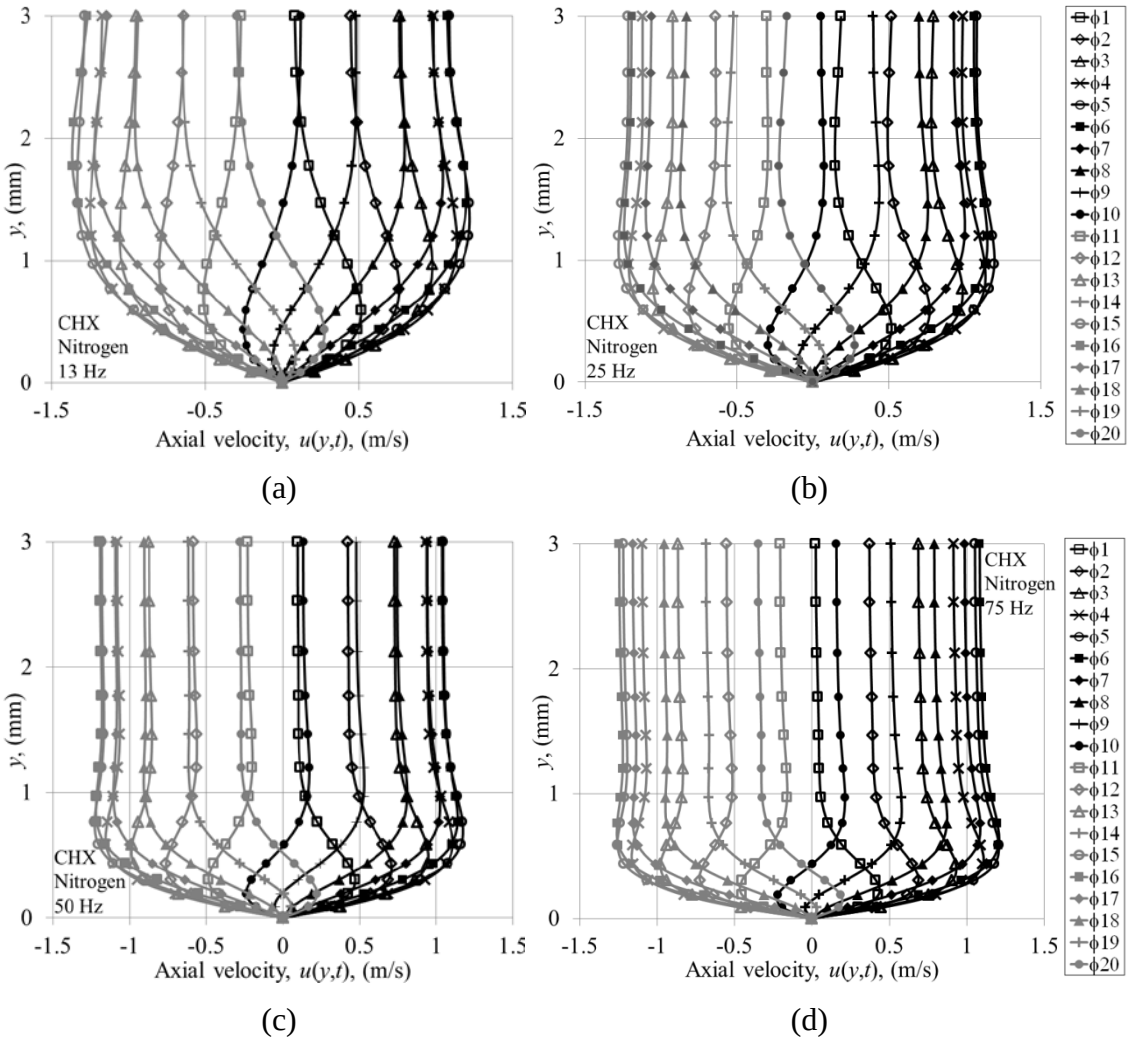

(a) (b)

(c) (d)

Figure 6.4: Velocity profiles for all 20 phases of a flow cycle for cases with a frequency of (a) 13, (b) 25, (c) 50 and (d) 75 Hz.

The change in the character of velocity profiles due to the change of frequency can be elaborated with the aid of the solution from linear thermoacoustic theory presented in equation (2.17). Equation (2.17) shows the oscillating velocity as a sum of two terms. The first term on the right hand side of the equation represents the adiabatic velocity magnitude at the core of the channel. The second term represents the decay of the magnitude due to the interaction with the solid boundary within the viscous boundary layer. A similar foundation of a solution given for oscillatory flow through channel can be found in Schlichting and Gersten (2002). Schlichting and Gersten (2002) described the two terms as Stokes-layer (near the wall) and inviscid layer (at the core). The findings suggest that the flow condition within the structure of thermoacoustic device resemble the condition reported for fundamental study of an oscillatory flow.

Figure 6.4 shows that when the frequency increases, the velocity profiles change from a "parabolic-like" profile to a profile encompassing two regions comprising of the region near the wall, also known as Stokes-layer (Schlichting and Gersten, 2007) and the region away from the wall known as the inviscid layer. The inviscid layer was shown as a "slug-like" profile.

In Figure 6.5 the profiles of all the four frequencies are superimposed in one plot and presented for selected phases of a flow cycle. The phases were selected to represent the changes during the first and the second half of the cycle. At low mean velocity of phases $\phi 1$, $\phi 3$, $\phi 11$ and $\phi 13$, the maximum velocity occurs at location near the wall. This is the feature of oscillatory flow reported elsewhere as "annular effect" (Zhao and Cheng, 1998). The "annular effect" is a phenomenon where maximum velocity occurs at location near the wall rather than at the core (Zhao and Cheng, 1998). This can be clearly seen from the plots of Figure 6.5. It is shown that the distance from the maxima to the wall reduces with an increase of frequency.

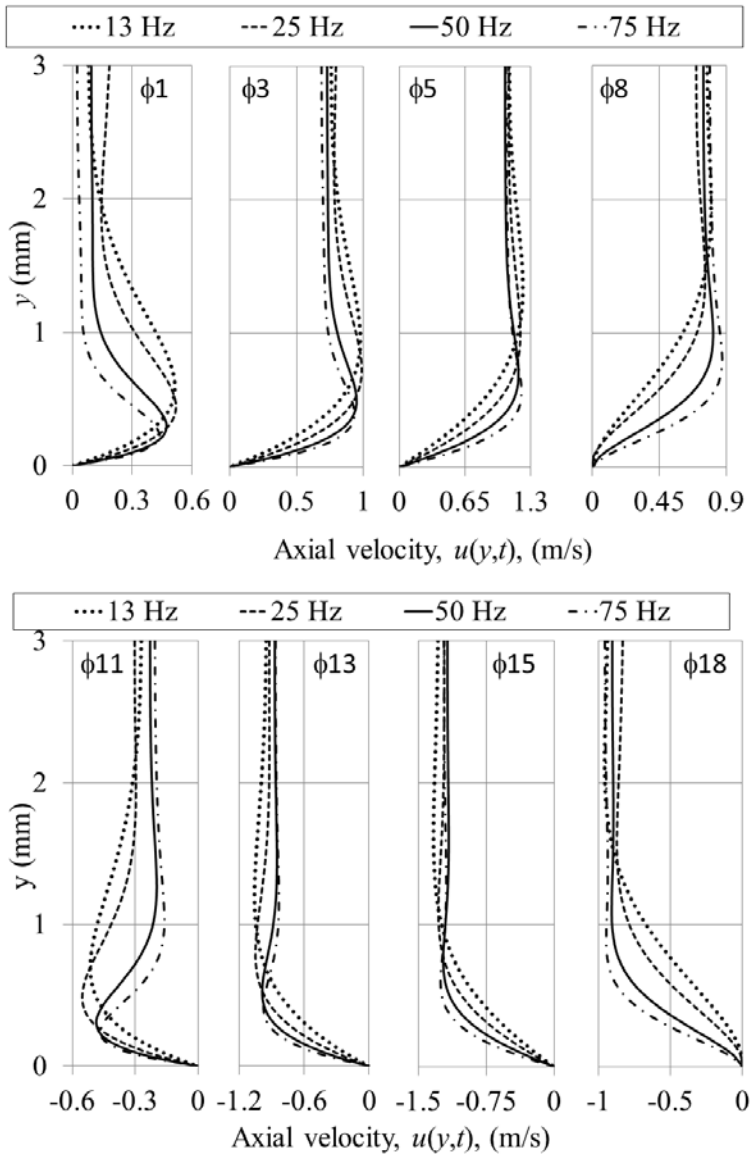

Figure 6.5: Velocity profiles for the range of frequencies investigated during the first (top) and second (bottom) half of the cycle.

The "annular effect" was explained in literature as a feature of the oscillatory flow that could influence the heat transfer provided by the flow especially when the effect was also seen in the temperature profiles (Zhao and Cheng, 1998). It is debatable whether this condition enhances or degrades the heat transfer of a system. However it may be possible to investigate this by looking at the temperature profiles.

6.1.3. Temperature profiles

Figure 6.6 shows the temperature profiles for selected phases for flow frequencies of 13 and 50 Hz. They are plotted for locations 1, 5, and 10 mm away from the joint above the

cold plates. The temperature profiles represent the value of temperatures from the wall towards the core (middle of the channel).

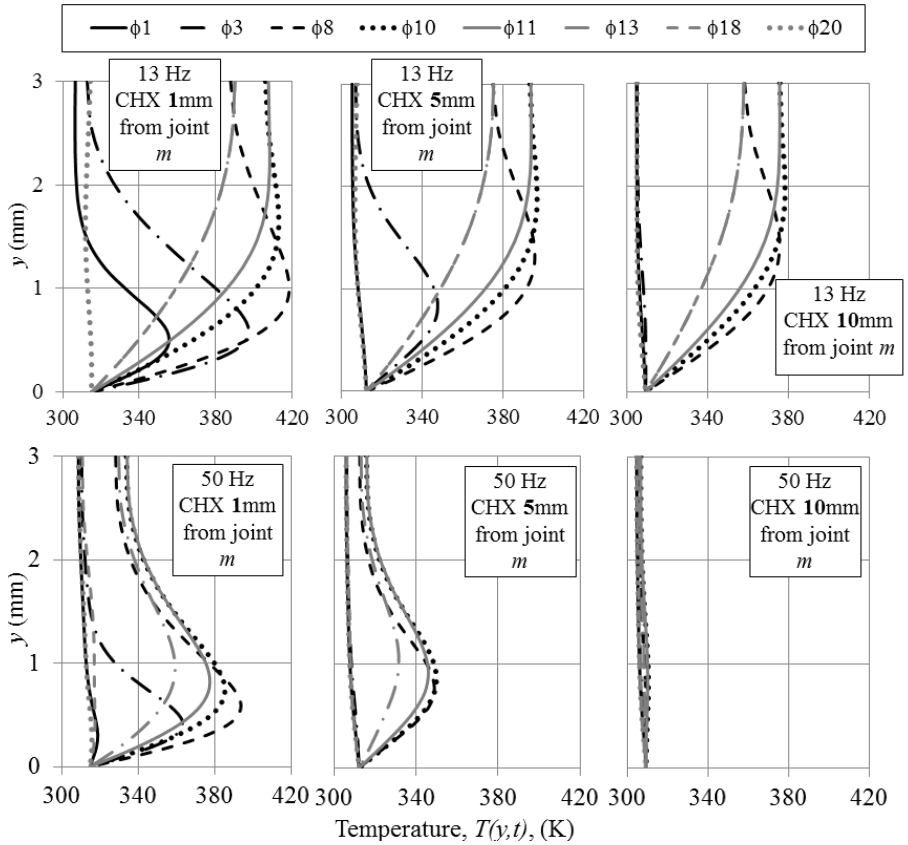

Figure 6.6: Temperature profiles within the cold channel for locations 1, 5 and 10 mm from the joint *m* (*m* is defined in Figure 5.1). Two frequencies are shown: 13 Hz (top) and 50 Hz (bottom).

Maximum values of temperature profiles within the cold channel with 13 Hz flow frequency are generally bigger than those at 50 Hz for the three locations shown. At 50 Hz, the temperatures at locations further away from the joint become very small and eventually almost collapse into a single line as seen in the bottom plots of Figure 6.6. This indicates that the fluid within the cold channel further away from the joint is not very much affected by the nearby hot fluid that flows into and out of the cold channel. This is a logical consequence of the reduced displacement amplitude at a higher frequency (as the velocity amplitude is almost fixed on account of fixed drive ratio).

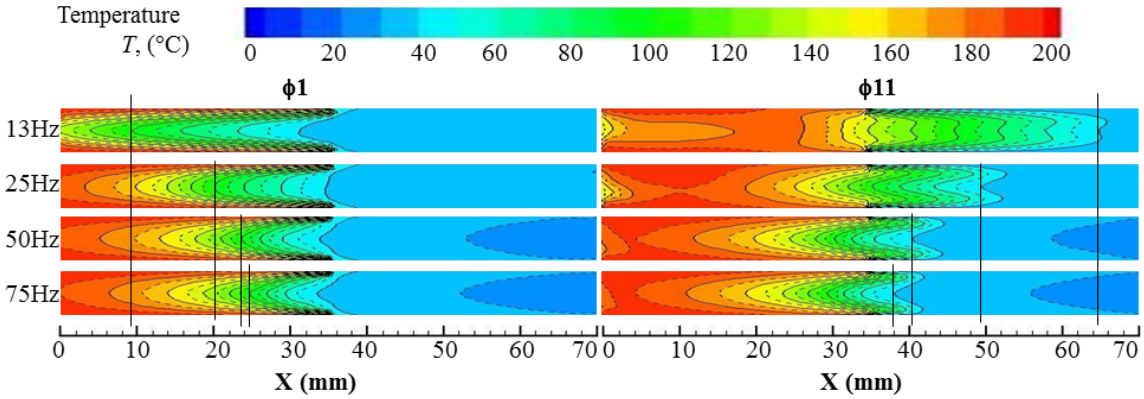

Figure 6.7: Comparison between temperature contours at phases ϕ1 and ϕ11 for 13, 25, 50 and 75Hz. Hot channel is on the left (0 to 35 mm) and cold channel is on the right (35 to 70 mm).

Figure 6.7 shows the temperature contours for 13, 25, 50 and 75 Hz at selected phases ϕ1 and ϕ11. At ϕ1, the temperatures within the hot channel are generally assuming minimum values. The hot channel is very much affected by the fluid which is just about to leave the channel. For 13 Hz, the change of fluid temperature is shown to propagate through the hot channel and into the open area next to the hot end (not shown in the figure). This propagation becomes less and less pronounced as the frequency increases. This is shown by the vertical lines which are introduced to help the reader. The illustration of the travel distance by the fluid within the hot channel at ϕ1 is done by comparing the contour line corresponding to temperature of 100 °C (which touches the vertical markers).

Similarly, at ϕ11 the hot fluid which is about to leave the cold channel has a maximum length of temperature propagation at 13 Hz. The length of temperature propagation reduces with an increase of frequency. The “guide” line was set to touch the isotherm corresponding to 40°C (313.15 K).The visualisation of temperature contour confirms that the size of the temperature affected area within the hot and cold channel reduces with an increase of frequency. This is a consequence of smaller gas displacement as the frequency increases.

The isotherms within the hot channel at ϕ1 have a different trend to that of cold channel at ϕ11. At ϕ1, fluid from cold channel flows into the hot channel and change the temperature of fluid away from the wall. The minimums occur at the core and seen as a

peak of isotherms that touch the vertical marker. At ϕ11, fluid from hot channel flows within the boundary layer into the cold channel. Fluids near the wall have higher temperatures than that at the core. The core temperatures are smaller with amplitude shown by the isotherms that touch the vertical marker. The temperature profiles within the two channels are asymmetrical. This is a consequence of temperature boundary condition at the wall and the corresponding behaviour of temperature propagation into the flowing fluid.

The isotherms within the hot channel also seem to propagate further towards the open area next to the hot end of the heat exchanger assembly. The propagation seems shorter within the cold channel. The lower fluid density at the hot end seems to be the reason for this behaviour. In addition, the natural convection effect at the hot area next to the heat exchanger may also provoke the fluid within the hot channel to flows further.

As mentioned, as frequency increases the gas displacement becomes smaller. The estimated length of the gas displacement for each frequency is calculated based on the velocity amplitude at the joint, *m*, and tabulated in Table 6.2. Theoretically, when frequency is varied and other flow conditions are fixed, the flow will have similar velocity amplitude within the channel. The slight difference in velocity amplitude of increasing flow frequency shown in Table 6.2 may be due to the differences in the character of the temperature fields developing within the channel.

Table 6.2: Velocity amplitudes and gas displacements for flow at different frequencies.

Frequency *f* (Hz)	Velocity amplitude at the joint, *m*, (m/s)	Gas displacement δ (mm)	Location equivalent to half of gas displacement, x_p, (mm)
13	1.32	16.2	8.1
25	1.22	7.8	3.9
50	1.17	3.7	1.85
75	1.18	2.7	1.35

Smaller gas displacement has also the effect of reducing the effective area of energy transfer between cold and hot plates (c.f. Figure 6.7). Thus, in order to fairly investigate the influence of frequency, comparison between temperature profiles was done at a location "x_p" corresponding to half of the displacement of the gas particle (c.f. Table 6.2). The resulting temperature profiles are shown in Figure 6.8.

At phase ϕ1, the fluid temperature away from the wall is lower than the cold plate. As the velocity increases during the cycle, the hot fluid starts flowing into the cold channel. At ϕ3, an "annular effect" of temperature for 13, 25, 50 and 75 Hz starts developing at locations near the wall. The "annular effect" is defined by the occurrence of the maximum value of temperature near (but not at) the wall. It is associated with the flow of the fluid near the wall within the boundary layer regions where the heat upstream affects the temperature within the boundary layer of the cold plates (Schlichting and Gersten, 2001).

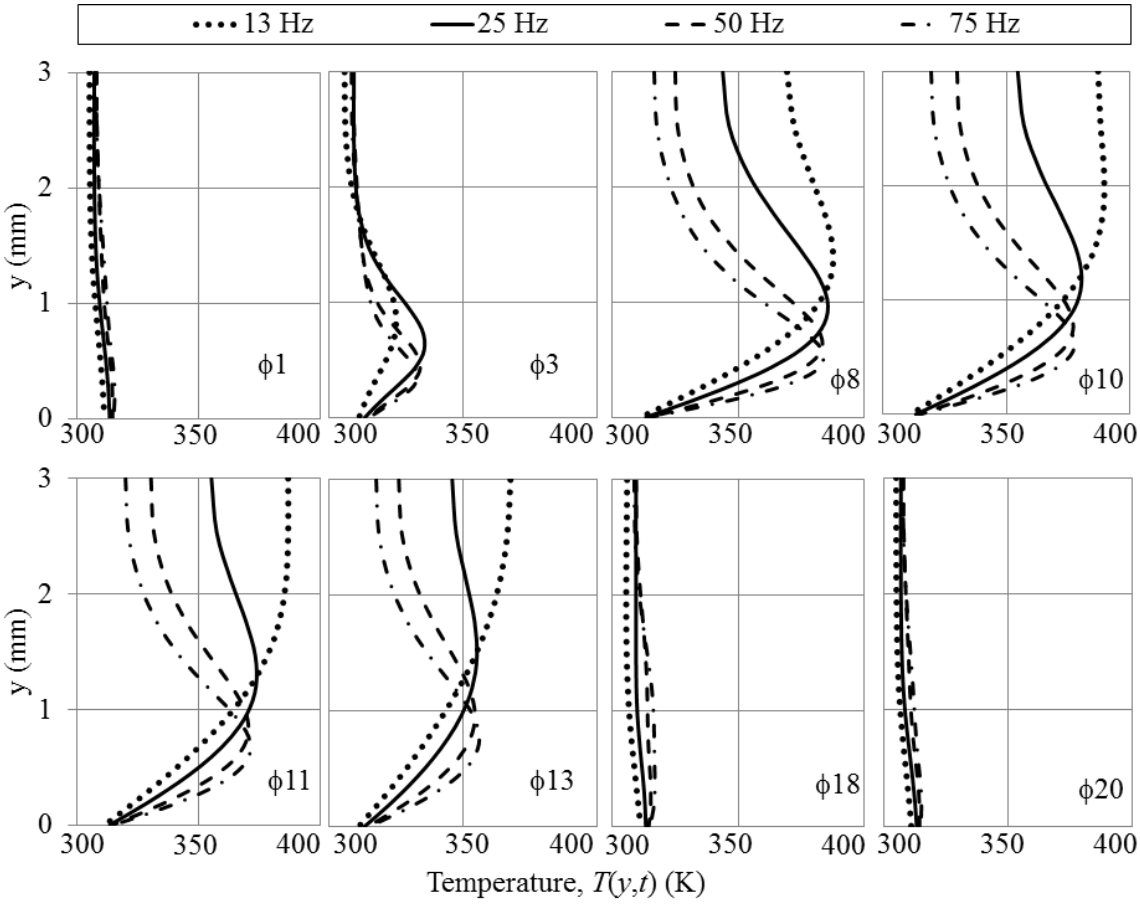

Figure 6.8: Temperature profiles within the cold channel for frequencies of 13, 25, 50 and 75 Hz for locations 8.1, 3.9, 1.85 and 1.35 mm, respectively, from the joint during the first (top) and the second (bottom) half of the cycle.

As the velocity increases further, the values of temperature within the cold channel increase. For 13 Hz, the increase of temperature starts within the boundary layer at ϕ3 and then propagates further into the core of the channel (y = 3mm) as the flow reaches

ϕ10. At ϕ11, the flow starts reversing and the fluid starts leaving the cold channel. Consequently, the temperature starts dropping until ϕ20 before the flow changes its direction again.

At higher frequencies, the temperature profiles tend to reach maximum values nearer the wall, but the temperature field propagation into the core is weaker (i.e. heating up the fluid at the core). As a consequence, the temperature away from the wall is smaller as the frequency increases. These behaviours of the temperature profiles are a consequence of reducing the thermal penetration depth with frequency increase.

For the particular location, x_p, within the cold channel, the maximum temperatures for 13, 25, 50 and 75 Hz are reached at locations 2.13, 0.97, 0.59, 0.44 mm, respectively, from the wall. For 13 Hz, the maximum temperature is reached at ϕ10. The biggest thermal penetration depth of 13 Hz brings the maximum temperature of the fluid at location furthest away from the wall. It also lends more time for the fluid to reach the maximum temperature. After ϕ10, the fluid starts leaving the cold channel and the temperature of fluid within the channel starts dropping. Flows at other frequencies reach the maximum temperature at an earlier phase of ϕ8 with locations nearer to the wall. This confirms that the wall temperature has a smaller effect on the fluid away from the wall as the frequency increases.

Table 6.3: Selected characteristic values of temperature for location x_p corresponding to various operating frequencies.

Frequency f, (Hz)	Location x_p (mm)	Maximum Temperature, (K)	Location of maximum temperature from the wall, y (mm)	Phase ϕ
13	8.1	389.437	2.13	10
25	3.9	385.487	0.97	8
50	1.85	382.954	0.59	8
75	1.35	382.934	0.44	8

The theoretical support for the temperature profiles can be represented by the solution form linear thermoacoustic theory given in equation (2.19). According to this equation, oscillating temperature may be related to three contributing factors. The first factor described by the first term on the right hand side of equation (2.19), is the adiabatic temperature oscillation, $T_1 = (1/\rho_m c_p)p_1$ (Swift, 2002). The adiabatic temperature is the

feature of temperature away from the wall. As the gas particles gets closer to the wall, the second term starts influencing the temperature. The adiabatic temperature changes with respect to the increase of thermal contact with a solid surface. The third contributing factor is represented by the last term which describes the change in temperature due to the gas motion along the temperature gradient in the direction of the gas motion. Equation (2.19) theoretically describes the value of fluid temperature which changes with distance from the solid wall. The averaged solution, equation (2.20), gives the average value of mean temperature within the channel.

Referring to equations (2.20) and (2.21), the changes of frequency can be attributed to the changes of averaged shape factor, f_κ, that are related to the second and third terms of equation (2.20). If the mean density within a channel is assumed to be constant, as frequency becomes higher the thermal penetration depth becomes smaller. Accordingly, as can be seen in Figure 2.4, f_κ decreases. As a result, the mean temperature of the fluid within the channel becomes less influenced by the wall temperature as the frequency increases. This explains the small amplitude of fluid temperature profiles within the channel when fluid flows at higher frequencies of 25, 50 and 75 Hz as shown in Figure 6.8. The change of temperature from the wall to the middle of the channel can be explained through solution (2.19). Away from the wall (y in equation (2.18) sets to zero), the fluid temperature is mostly the adiabatic temperature of the flow. As the location gets closer to the wall the shape factor, h_υ, becomes bigger. The oscillating temperature reaches the wall temperature. However, as hot fluid flows into the cold channel, axial temperature gradient change with flow. The third term of equation (2.19) starts dominating over the first and second term. The fluid temperature near the wall changes from adiabatic temperature to hotter temperature from the hot fluid. However, the wall temperature was fixed to a constant temperature of approximately 300 K. As a result, heat transfer occurs between fluid adjacent to the wall and the solid surface of the wall. This explains the “annular effect” occurring near the wall of the cold plate. The effect was shown occurring at certain phases only, when hot fluid travels within the boundary layer of the cold channel. At other phases when the mean adiabatic temperature is lower than the wall temperature, the “annular effect” is not seen and an adverse temperature gradient is observed due to fluid temperature being slightly lower than the wall. This may be related to the fluid being initialised at 300K. As describe in the beginning of this chapter, the cold plate temperature at locations near the hot

channel is higher than the fluid initial temperature due to conduction losses between the hot and cold plate. Although the model has reached a steady oscillatory state (where, pressure, velocity and temperature do not change much from one cycle to another), the change in temperature may still continue, as illustrated in chapter four. However, this change progress in a very small magnitude from one cycle to another and steady-oscillatory state suitable for analysis is assumed reached. The adverse temperature-gradient seen in Figure 6.8 is small and negligible.

For the hot channel, the temperature profiles for location x_p (as given in Table 6.3) from the joint above the hot plate are shown in Figure 6.9. At ϕ1, the fluid temperature away from the wall is lower than the hot plate. As the phase increases, the fluid starts leaving the hot channel. The temperature away from the wall starts rising. The rise is quicker for 13 Hz and slowest at 75 Hz. At ϕ10, temperature at the core is at a maximum value. The maximum core temperature is biggest for 13 Hz and becomes lower as the frequency increases. This is a consequent of low thermal penetration depth of higher frequencies. At ϕ11, the cold fluid starts entering the hot channel. The temperature away from the hot plate starts dropping again.

The temperature profiles at the hot channel are all having a negative gradient (heat transfer into the channel) throughout the phases of a cycle. The “annular effect” observed at the cold channel is not seen at the hot channel. The cold fluid entering the hot channel results in drops of temperatures of the fluid away from the wall in a consistent manner. The temperatures are lower at the core and increase linearly from the location of thermal layer towards the wall. Flow at the core becomes less affected by the wall temperature as the frequency increases, as seen in phases ϕ1 and ϕ20, due the lower thermal penetration depth with the increase of frequency.

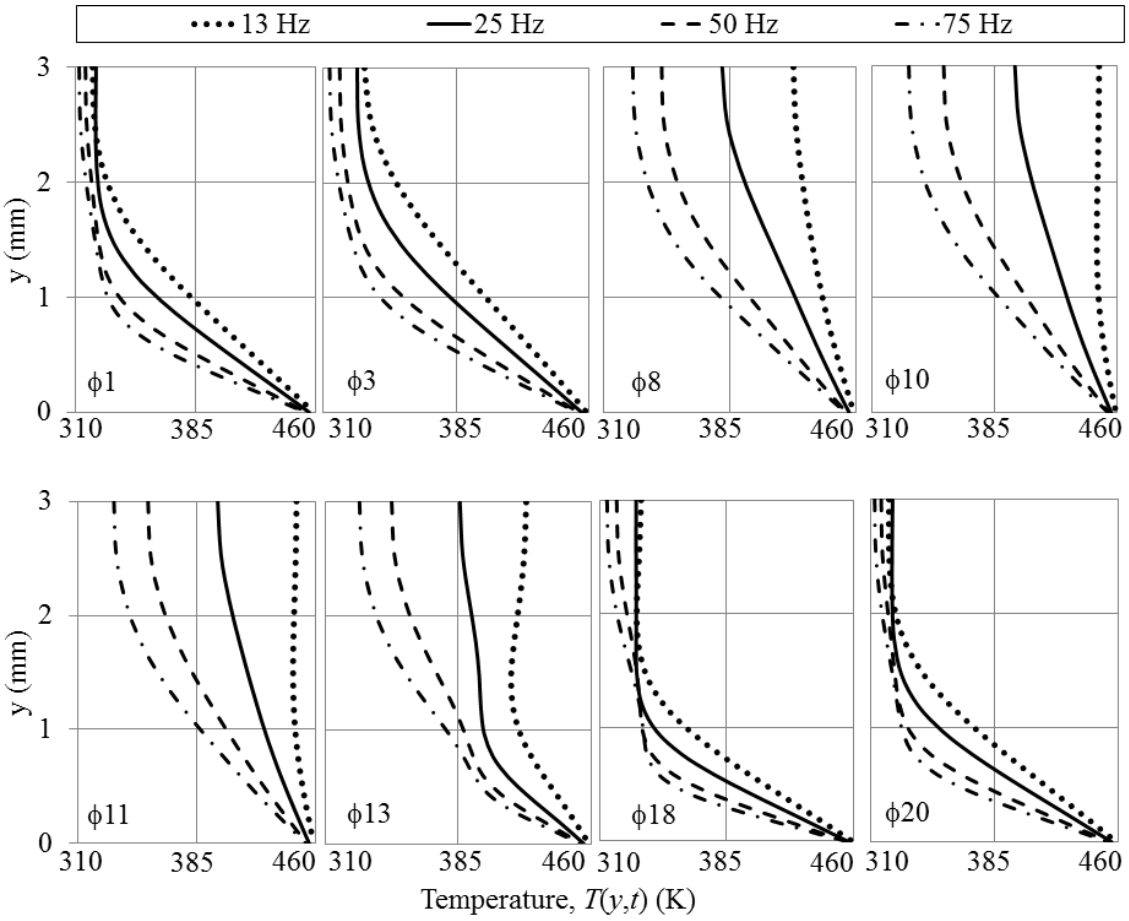

Figure 6.9: Temperature profiles within the hot channel for frequencies of 13, 25, 50 and 75 Hz for locations of 8.1, 3.9, 1.85 and 1.35 mm, respectively, from the joint during the first (top) and the second (bottom) half of the cycle.

6.1.4. Heat transfer condition

Figure 6.10 shows a space-phase-averaged heat flux defined as:

$$q_L = \frac{1}{2\pi L}\int_0^{2\pi}\int_0^{L} -k\left.\frac{dT}{dy}\right|_{wall} dx d\phi \qquad (6.1)$$

The heat flux was averaged over time (equivalent to a cycle) and length of the heat exchanger, L. The terms k, T and y refer to the thermal conductivity of the fluid, temperature and vertical position, respectively.

The heat flux is plotted against the kinetic Reynolds number defined as $\mathrm{Re}_\omega = \omega D^2/\upsilon$ with ω, D and υ representing the angular velocity, the spacing of the

plates and kinematic viscosity of the fluid, respectively. All properties were calculated at a reference temperature of 300 K. The results for both cold and hot heat exchangers are as shown in Figure 6.10.

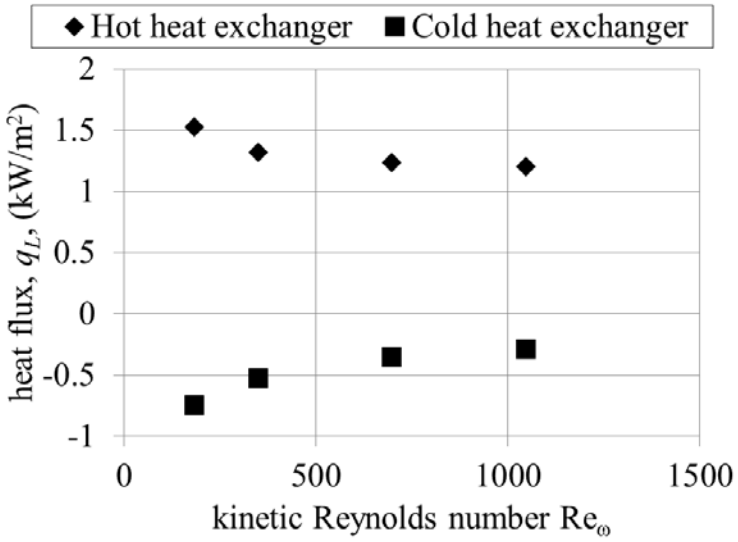

Figure 6.10: Space-phased-averaged heat flux over the length of the heat exchangers wall for all the frequencies investigated.

The space-phase-averaged wall heat flux is highest at lowest frequency. The heat flux reduces as the frequency increases up to 50 Hz and then it becomes practically constant. According to equations (2.6) and (2.7), higher frequency corresponds to thinner viscous and thermal boundary layers. Zhao and Cheng (1998) suggested that thinner thermal boundary layer implies that the heat will be quickly transferred to the fluid and consequently the heat transfer improves as the frequency increases. This is not reflected by the results shown in Figure 6.10. The contradiction of results shown in Figure 6.10 to those of Zhao and Cheng (1998) is likely due to the fixed dimension of the current heat exchanger. However increasing the frequency reduces the effective area of heat transfer between hot and cold channels due to the reduced gas displacement.

For a fair comparison the heat flux was averaged over the wall with length equivalent to the size of the gas displacement, δ (c.f. Table 6.2), and results are shown in Figure 6.11. The heat flux was calculated as:

$$q_\delta = \frac{1}{2\pi\delta}\int_0^{2\pi}\int_0^{\delta} -k\left.\frac{dT}{dy}\right|_{wall} dx d\phi \qquad (6.2)$$

Once the heat-flux is averaged over the length equivalent to the gas displacement, the heat flux shows an increasing trend with respect to frequency. The decreasing pattern shown in Figure 6.10 is likely to be the result of the big influence of the remaining "passive" area of heat transfer on the space-phase-averaged heat flux defined in equation (6.1). The "passive" area becomes bigger with frequency.

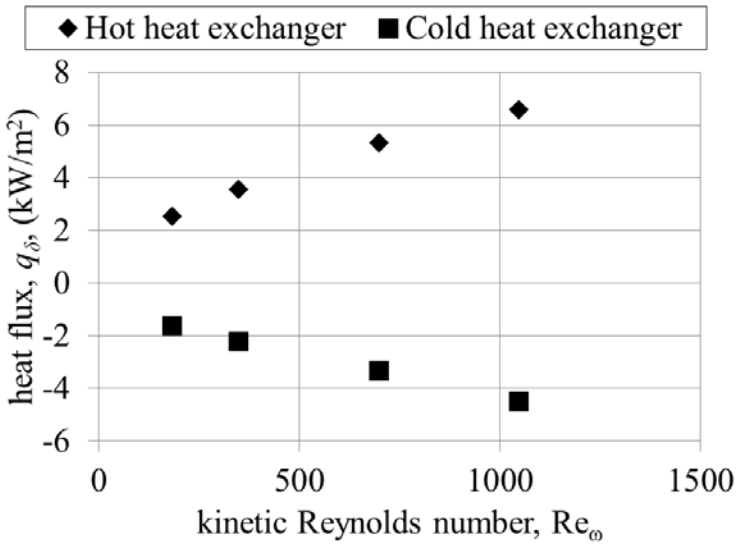

Figure 6.11: Space-phased-averaged heat flux over the length equivalent to the size of the particle displacement corresponding to the frequency investigated.

The space-phase-averaged heat flux at the cold heat exchanger remains negative for all the frequencies investigated indicating that the heat is taken out of the fluid. However, for all the frequencies investigated, the magnitude of heat absorbed by the cold heat exchanger is always smaller than the amount of heat supplied by the hot heat exchanger. This is clearly seen in Figure 6.10. This can be a result of how the model is set up. Here the temperature of the fluid in the system is allowed to rise with time and so there will be energy accumulation within the fluid surrounding the heat exchangers. On the other hand the heat transfer direction within the cold channel is not always "from fluid to plate". This is seen in $\phi 1$ and $\phi 20$ of Figure 6.8 when the "annular effect" is absent and the temperature away from the wall is smaller than the plate. This may also affect the

balance between the heat transfer in hot and cold channel. The influence from "adverse" temperature gradient of ϕ1 and ϕ20 is however small and considered negligible. The heat accumulation shown as natural convection at the open area next to hot heat exchanger, as shown earlier in Figure 4.12, may be the reason for the loss of heat between hot and cold channel.

Another way of increasing the capability of heat transfer is to change the working medium. Helium has been one of the favourable working media due to its high heat capacity. The numerical model was set following the boundary conditions stated in Table 6.4.

Table 6.4: Details of cases of frequency studies with helium as working medium

Working medium : helium								
P_m (bar)	f (Hz)	Distance from location of P_a			Oscillating pressure, p_1 (Pa)	Oscillating mass flux, m_2' (kg.m/s)	P_a (Pa)	Drive Ratio (%)
		x_s	x_1	x_2				
1	13.1	13.2	12.96	13.5	150.1452	0.2610	300	0.3
	50	3.5	3.19	3.74	165.9014	0.2688		
	75	2.3	2.04	2.58	176.1560	0.2736		
	100	1.7	1.46	1.97	186.4680	0.2759		
1	50	3.46	3.20	3.74	458.9342	0.7438	830	0.83
	100	1.73	1.46	1.96	515.0927	0.7683		

The thermal conductivity and viscosity of helium were modelled as follows (Swift, 2002):

$$\mu(T) = 1.99 \times 10^{-5} (T/T_C)^{0.68} \tag{6.3}$$

$$k(T) = 0.152 (T/T_C)^{0.72} \tag{6.4}$$

The model was also validated and the results are shown in Appendix One to avoid repeating the discussion. The resulting heat fluxes, calculated using equation (6.1), are plotted in Figure 6.12.

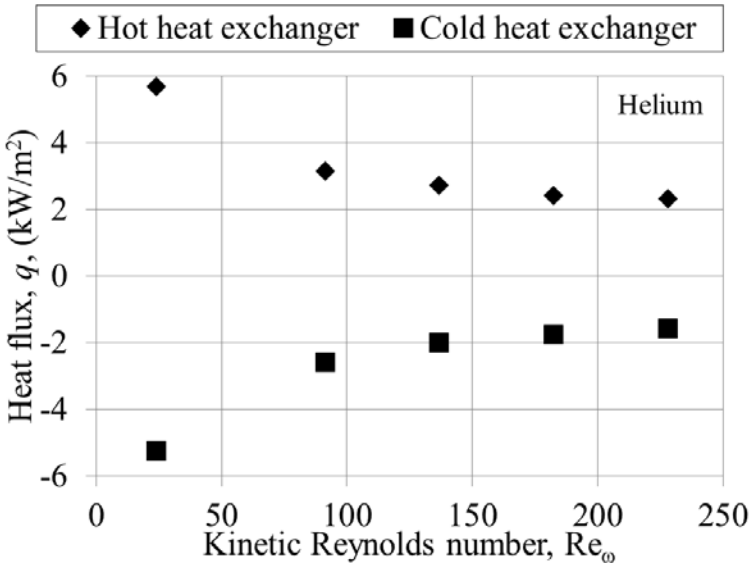

Figure 6.12: Space-phased-averaged wall heat flux for all investigated frequencies in helium.

As seen in Figure 6.12, the magnitude of the heat fluxes are significantly larger compared to the heat fluxes obtained with nitrogen (c.f. Figure 6.10). This is likely due to the change in thermal penetration depths within the channel. In helium the depths corresponding to the range of frequencies investigated are bigger than that for nitrogen. Furthermore the heat capacity of helium is much bigger than nitrogen. Hence, the adiabatic temperature away from the wall becomes smaller. The combination of low core temperature and high thermal penetration depth allow a bigger range of temperature change which result in higher heat transfer between the plates and the fluid.

A similar trend to nitrogen is observed for helium where the heat fluxes decrease with an increase of frequency. This is due to the already discussed big “passive” heat transfer area at higher frequency. The difference in magnitude of heat flux between cold and hot heat exchangers is smaller compared to cases with nitrogen as the working medium. This indicates that the heat loss is significantly smaller when helium is used as the working medium. The result is expected due to the decreasing influence of natural convection as the flow in helium involves higher range of velocity (c.f. Figure A1.2 in Appendix One). Higher velocity means that the axial convection is significantly larger than the transverse flow of natural convection. Hence the loss due to natural convection becomes smaller and negligible.

6.1.5. Flow structure

Figure 6.13 shows the flow structures in the form of vorticity plots for the investigation of frequency affects at a drive ratio of 0.3% in nitrogen at 1 bar. It is clear that as the viscous penetration depth reduces with frequency the shear layer near the wall becomes thinner. The gas displacement decreases with an increase of frequency. As a consequence, the vortex structure developed at the end of the plates becomes weaker.

Figure 6.14 shows the vorticity contours of flow at 0.83% drive ratio with three different frequencies. At the end of plates the flow structure becomes weaker as the frequency increases. This is possibly due to the shorter gas displacement at higher frequencies. In the area between the plates, a second shear layer with opposite vorticity sign to the layer adjacent to the heat exchangers wall starts developing as the flow moves from $\phi 1$ to $\phi 5$. The second layer is more apparent as the frequency increases.

The appearance of second shear layer agrees with the “annular effect” on the velocity profiles that becomes prominent with an increase of frequency. The second layer disappears completely at $\phi 8$ of 13 Hz. The layer becomes disturbed and thinner as the frequency increases as can be seen by comparing $\phi 8$ for the three frequencies shown. At 50 Hz the second layer remains within the plates for all phases of a flow cycle, appearing weak at some phases and stronger at other.

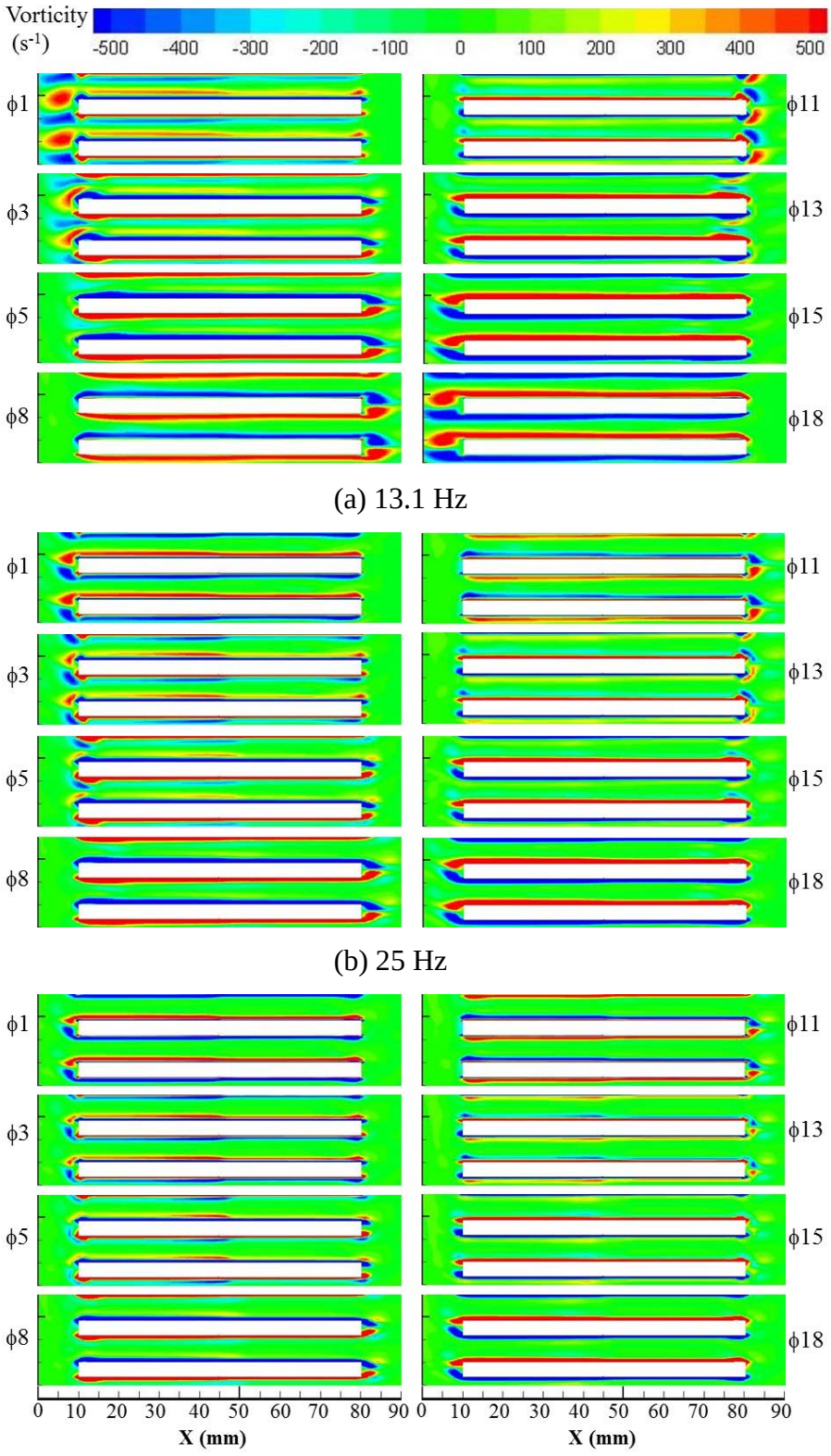

(a) 13.1 Hz

(b) 25 Hz

(c) 50 Hz

Figure 6.13: Vorticity contours for frequencies (a) 13, (b) 25 and (c) 50 Hz. The working medium is nitrogen at 1 bar and a drive ratio of 0.3%.

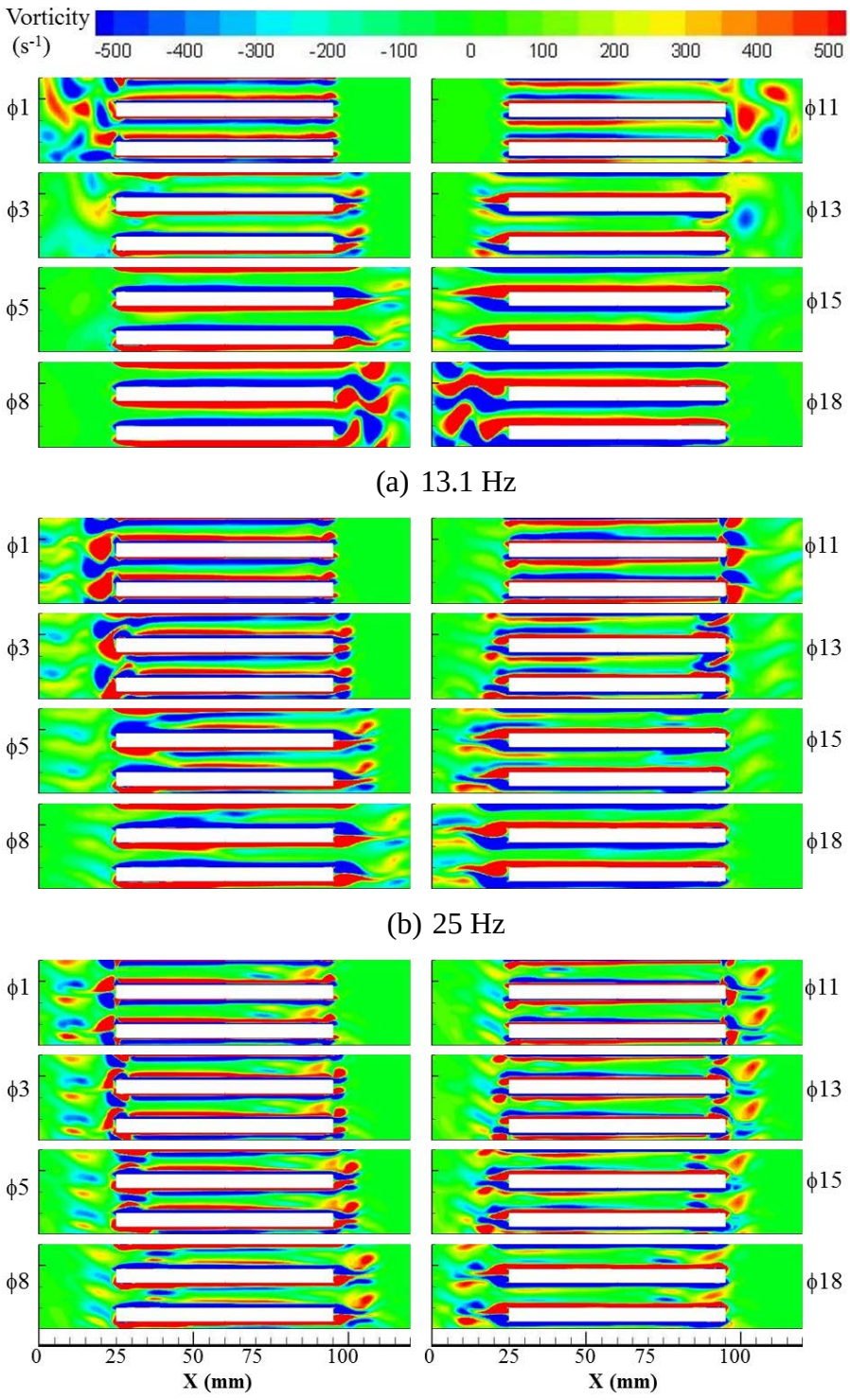

(a) 13.1 Hz

(b) 25 Hz

(c) 50 Hz

Figure 6.14: Vorticity contour for frequencies (a) 13 (b) 25 and (c) 50Hz. The working medium is nitrogen at 1 bar and a drive ratio of 0.83%.

6.1.6. Viscous dissipation

The effect of frequency on the dimensionless viscous dissipation defined in equation (4.20) is shown in Figure 6.15. The viscous dissipation at area between the plates and

area at the end of plates increases with frequency. Thinner boundary layers due to frequency increase result in higher velocity gradients. Consequently, the viscous dissipation becomes higher. At the open area next to both ends of the heat exchanger assembly, the viscous dissipation is also increasing with an increase of frequency. However, at lower frequency the dissipation at area next to the hot end is higher than that next to the cold end. As described in chapter four, this may be related to the temperature-driven flow which distorts the flow at that end. Furthermore, the gas viscosity is also higher at the hot area compared to the cold area. As the frequency increases the difference between the dissipations at the two areas becomes smaller and eventually for 75 Hz the dissipation at cold end becomes higher than that at the hot end. This indicates that the rapid flow of fluid at high frequency results in a flow which is more distorted at cold end compared to the hot end. The reason for this is not clear. However, it is possible that, at high frequency, the combined effect of rapid movement of the gas and the natural convection at the hot end results in a less circulation at the hot end compared to the cold end. The vorticity contours of Figures 6.13 and 6.14 also show that as the frequency increases the vortex structure at the cold end is shown to be more disturbed compared to the hot end.

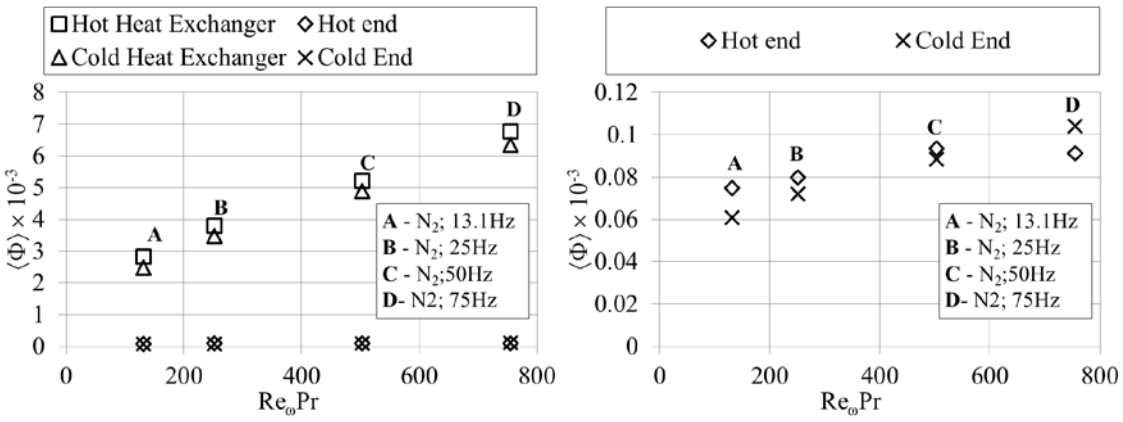

Figure 6.15: (a) The effect of frequency on viscous dissipation and (b) the enlarged view of viscous dissipation at the end of plates.

The effect of flow with different working media on viscous dissipation is shown in Figure 6.16. Helium has a density much lower than nitrogen. Change of density changes the velocity within the flow following equation (2.16). For a fair comparison using dimensionless representation, equation (4.20) was divided by a dimensionless Reynolds

number to rule out the effect of density on the dimensionless equation so that misleading result may be avoided. Figure 6.16 shows that helium causes higher viscous dissipation compared to nitrogen. The high velocity amplitude of flow in helium (c.f. Figure A1.2 in Appendix One) causes high velocity gradients within the flow and the viscous dissipation becomes higher. Helium gas particles move with higher displacements than nitrogen. Therefore more dissipation is anticipated in helium as gas particles make more contact with the solid wall. Similar trend of viscous dissipation is observed at the open areas next to the cold and hot ends of the plates but with a smaller magnitude. The high velocity of flow in helium tends to create more disturbances at the open area next to the heat exchanger assembly.

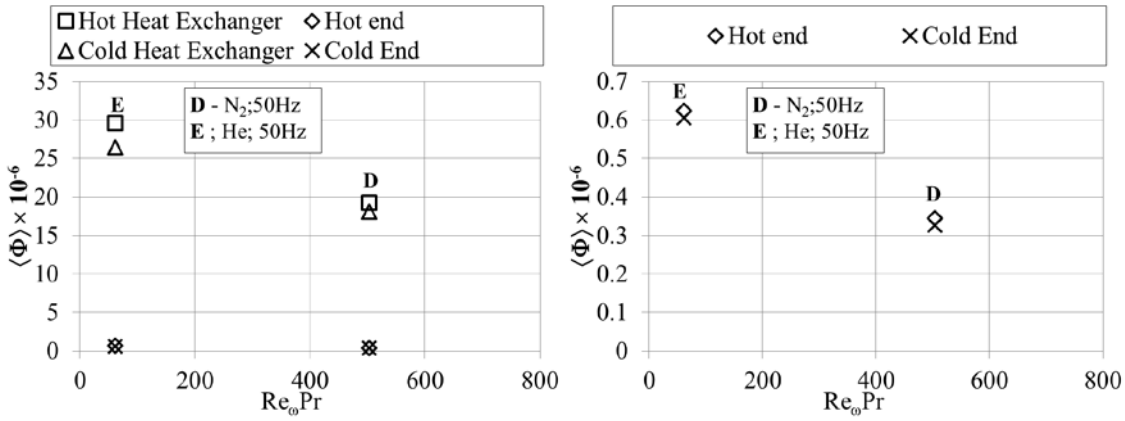

Figure 6.16: (a) The effect of gas medium on viscous dissipation and (b) the enlarged view of viscous dissipation at the end of plates.

6.2 The effect of geometrical dimensions

A particular operating condition was chosen for the study of the effect of geometrical dimensions on flow and heat transfer within the heat exchangers.

Table 6.5: Investigation of the effect of plates dimensions

Case	Plate thickness, *d*, (mm)	Plate spacing , *D*, (mm)	Porosity, σ, (%)
T3G3	3	3	50
T3G4	3	4	57
T3G6	3	6	67
T1G3	1	3	75

The working medium was helium at a frequency of 100 Hz, a mean pressure of 0.1 MPa and a drive ratio of 0.3%. Two plate thicknesses and three sizes of gap between plates were tested as shown in Table 6.5. The length of the heat exchanger was maintained at 35 mm each.

6.2.1 Velocity profiles

The resulting velocity profiles for the investigation of geometrical dimensions are shown in Figure 6.17.

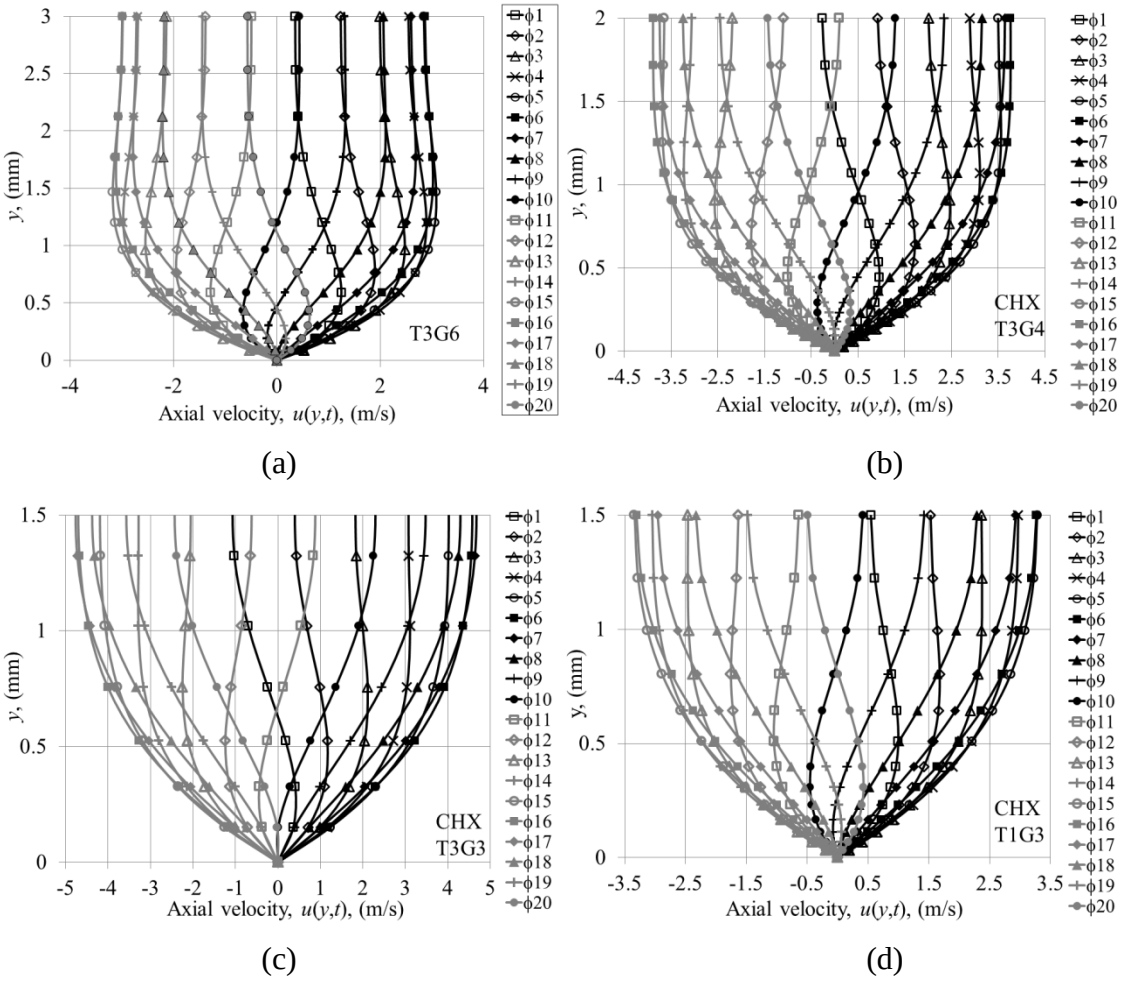

Figure 6.17: Velocity profiles for location of 15 mm away from the joint above cold heat exchanger (CHX) for (a) T3G6, (b) T3G4, (c) T3G3 and (d) T1G3. Description of each case is given in Table 6.5.

The first three plots, (a), (b) and (c) in Figure 6.17, correspond to the investigation of the effect of the spacing between the plates. The spacing between the plates is varied from 3 mm to 6 mm with a constant plate thickness of 3 mm. The investigation of the

effect of plate thickness is done by comparing plot (c) and (d) of the same figure. Here, the plate spacing for both cases was 3 mm while the thicknesses of the plate were set to 1 mm and 3 mm.

When the space between plates is smaller the velocity profiles change from a “bell-like” shape to a “parabolic-like” shape. This means that the “slug-like” feature at the core as seen in plot (a) becomes narrower in plot (b) and disappears from the flow as the gap between the plates decreases to 3 mm as seen in plot (c). As mentioned in the previous section, the “slug-like” feature represents the existence of an inviscid region within the channel. The study shows that as the gap becomes smaller the inviscid region fades. The frictional wall layer develops neat to the two opposite walls and dominates the space. Furthermore, the “annular effect” is less pronounced and the velocity maxima occur at location closer to the core.

Figures 6.17 (a), (b) and (c) also show that as the gap between the plates becomes smaller the magnitude of the velocity increases due to the effect of porosity, σ. With the thickness of the plates fixed, smaller gap results in smaller porosity. For a fixed magnitude of incoming flow, say u_{x1}, the velocity of flow between the plates, u_m, becomes $u_m=u_{x1}/\sigma$; the magnitude of velocity becomes bigger when the porosity is smaller. The same reasoning applies to the results obtained when the thickness of plates is reduced to 1 mm. Comparison between plots (c) and (d) of Figure 6.17 shows that the magnitude of velocity becomes smaller as the thickness of plates reduces. This will of course affect the heat transfer conditions within the channel due to a change of gas displacement as will be shown in section 6.2.3

6.2.2 Temperature profiles

Figure 6.18 shows the temperature profiles within the cold channel for selected phases for cases with different sizes of plate spacing, 3 (T3G3), 4 (T3G4) and 6 (T3G6) mm. As described earlier, as the drive ratio for each case was fixed to 0.3%, the resulting velocity amplitude within the channels varies from one case to another. Hence, the effective area of heat transfer was also affected. For a fair comparison, the temperature profiles were taken at a location half the distance of the gas displacement, x_p. For T3G3, T3G4 and T3G6, x_p corresponds to 9.7, 6.7 and 6 mm, respectively.

From phases ϕ1 to ϕ10, the hot fluid flows into the cold channel. The temperature within the channel starts rising. As it reaches ϕ10, the maximum temperature is reached at the core of each channel. This happens at y = 1.5 mm for T3G3, y = 2 mm for T3G4, and y = 3 mm for T3G6. The maximum gradient near the wall is approximately the same. This indicates that increasing the gap between plates does not lead to an increase in heat transfer rate. It is a consequence of already having $D/\delta_\kappa \approx 3.9$ which is reaching the optimum range (2-4 according to Tijani (2002)). Therefore further increases in the gap should not lead to an improvement of heat transfer. However, there is an exception in this overall picture which is the gap for ϕ8 in Figure 6.18. Clearly the temperature "annular effects" play a role locally in changing the local temperature gradients.

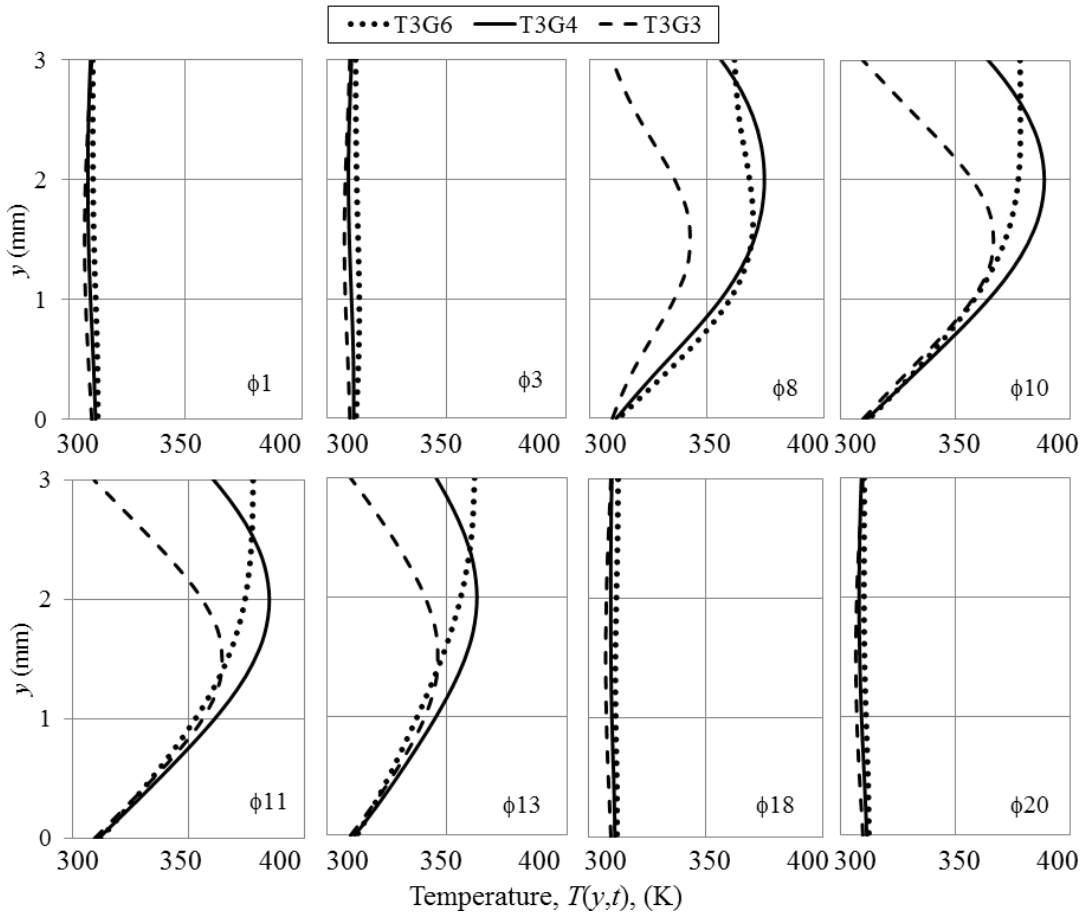

Figure 6.18: Temperature profiles within the cold channel for T3G3, T3G4 and T3G6 for locations 9.7, 6.7 and 6mm, respectively, from the joint during the first (top) and the second (bottom) half of the cycle.

The adiabatic feature of temperature (fluid away enough from the wall and "less" affected by the wall temperature) can only be seen at T3G6 where fluid at the core of the channel has an approximately uniform value of temperature at ϕ10. This is also the reason for a small "annular effect" seen for T3G6 at ϕ8 because there is a clear boundary separating the adiabatic flow and the thermal boundary layer. Flow within smaller channels is dominated by the thermal layer hence does not seem to exhibit the "annular effect" feature.

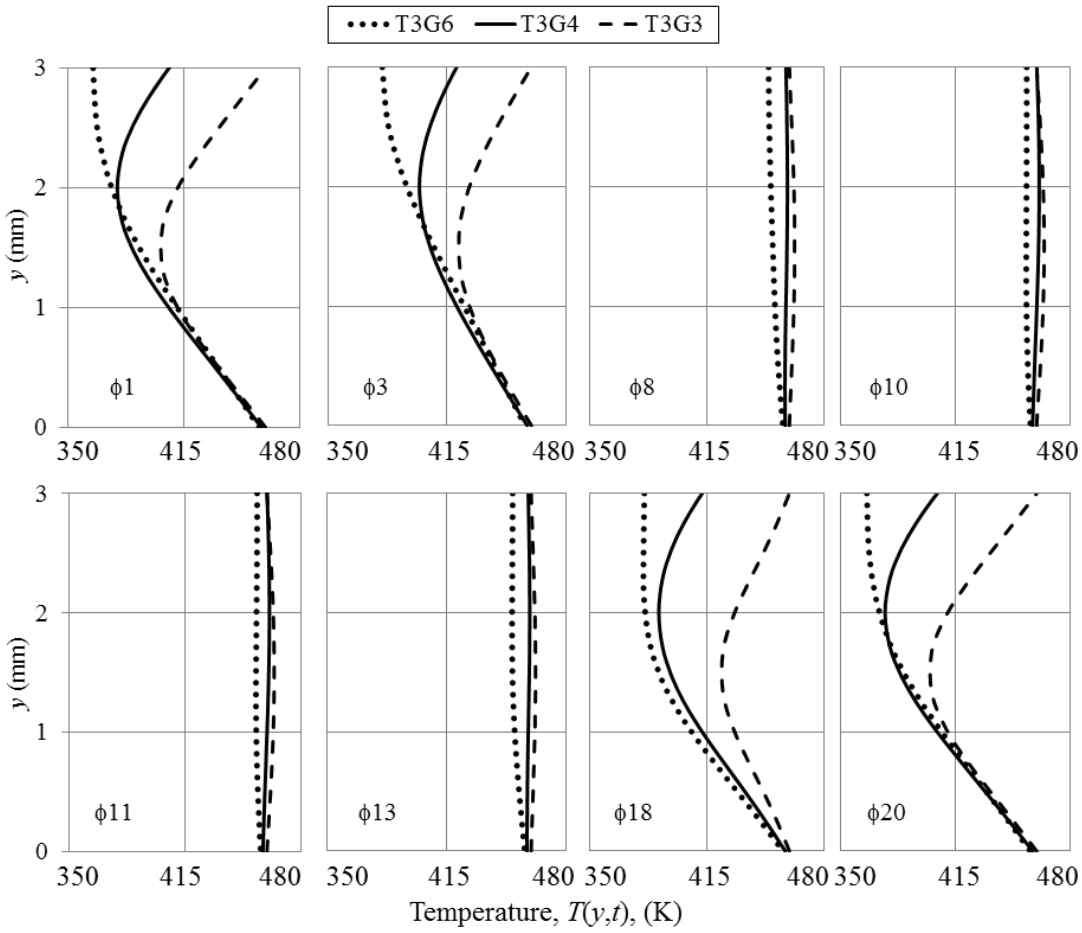

Figure 6.19: Temperature profiles within the hot channel for T3G3, T3G4 and T3G6 for locations 9.7, 6.7 and 6mm, respectively, from the joint during the first (top) and the second (bottom) half of the cycle.

Figure 6.19 shows the temperature field for locations similar to Figure 6.18 but within the hot channel. From ϕ11 to ϕ20, colder fluid from cold channel flows into the hot channel. The temperature away from the wall starts dropping. The thermal penetration depths for all cases are the same. A big difference of temperature between the core and

the wall as seen for T3G6 is due to the fluid away from the wall being less “affected” by the hot wall. As the direction of flow changes (ϕ1 to ϕ10), the fluid starts leaving the hot channel and the fluid temperature becomes higher again.

As the channel becomes smaller, the fluid within the hot channel becomes dominated by the thermal boundary layer. The temperature of the hot plate “penetrates” through to the core of the hot channel. As the channel size increases the magnitude of temperature at the core is less affected by the hot wall due to the limitation of thermal penetration depth. For all cases the maximum gradients of temperature within the boundary layer near the wall are approximately the same. However there is an exception in ϕ18 of Figure 6.19 which may be related to a specific interplay between the velocity and temperature fields.

6.2.3 Heat transfer condition

Figure 6.20 shows the effect of geometrical dimensions on the heat flux calculated following equation (6.1).

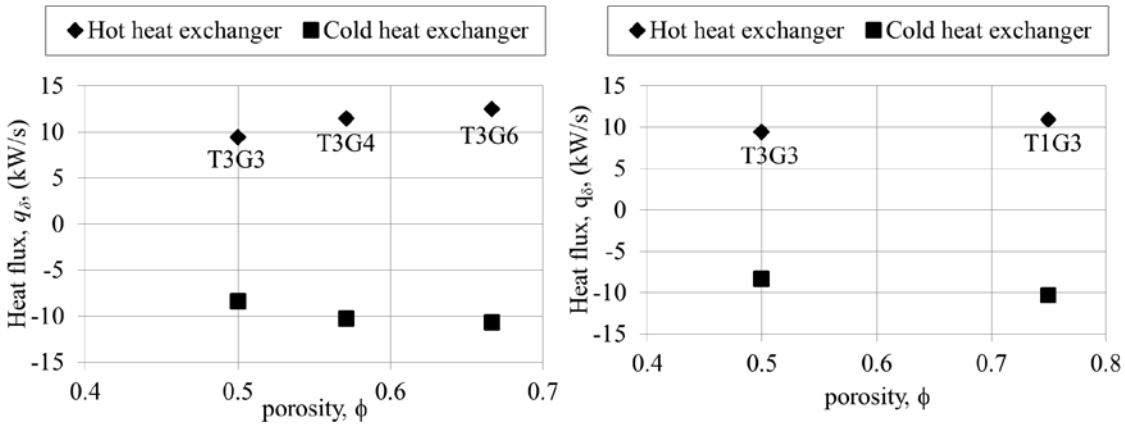

Figure 6.20: The heat flux averaged over one cycle and length equivalent to the gas displacement: (a) the effect of spacing of the plates and (b) the effect of thickness of the plates.

The heat flux represents the heat transfer within the effective area only. As expected, the effective heat flux for T3G3, T3G4, T3G6 and T1G3 is approximately the same. For a fixed flow frequency, mean pressure and gas medium, changing the channel space does not affect the heat transfer within the “effective” area. The slight variation of heat flux from one case to another may be due to the estimated area of integration which was

based on the gas displacement calculated from velocity at location *m*. The exact "effective" area of heat transfer may vary following the dynamics of the flow.

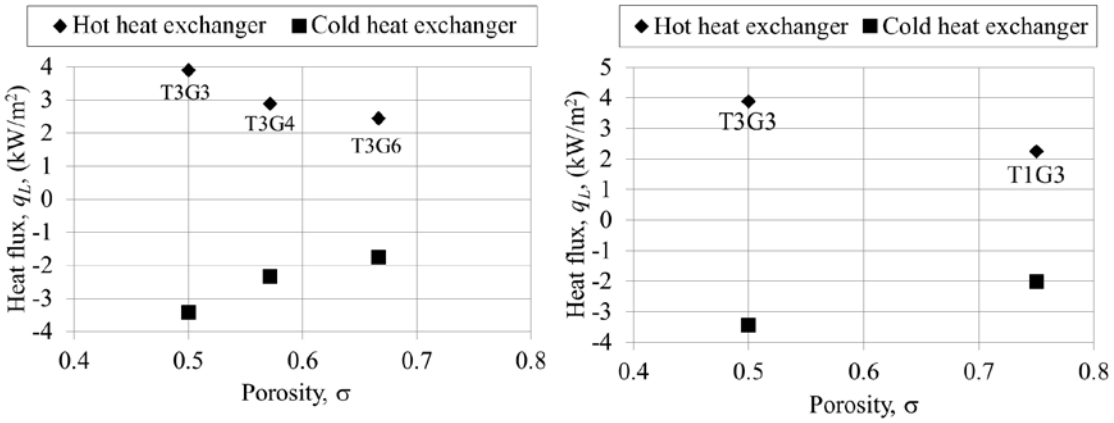

(a) (b)

Figure 6.21: The total heat flux averaged over one cycle and the plate length: (a) the effect of spacing of the plates and (b) the effect of thickness of the plates.

Figure 6.21 shows the total heat flux integrated over the whole length of the heat exchanger following equation (6.2). The total heat flux decreases with an increase of porosity. In the current study, the velocity of the flow between the plates increases as the porosity decreases. Hence, the gas displacement becomes bigger. Therefore the fluid moves to a larger distance that covers a larger area of the heat exchanger. Therefore, the effective heat transfer area to the total fin area is bigger hence the heat flux is bigger.

6.2.4 Flow structure

Vorticity contours were plotted to investigate the flow structures for different geometrical dimensions. Reducing the gaps makes the shear layer from the top and bottom surfaces become closer to each other as shown in Figures 6.22 (a) and (b).

As the gap reduces the frictional layer fills the area between the plates. Reducing the gap between the plates reduce the porosity as seen by comparing plots (a) and (b) which are plotted on identical scales. Thinner plates with the same spacing result in an increase of porosity (c.f. (b) and (c)). The vortex structures at the end of the plates stay attached to the plate for all cases.

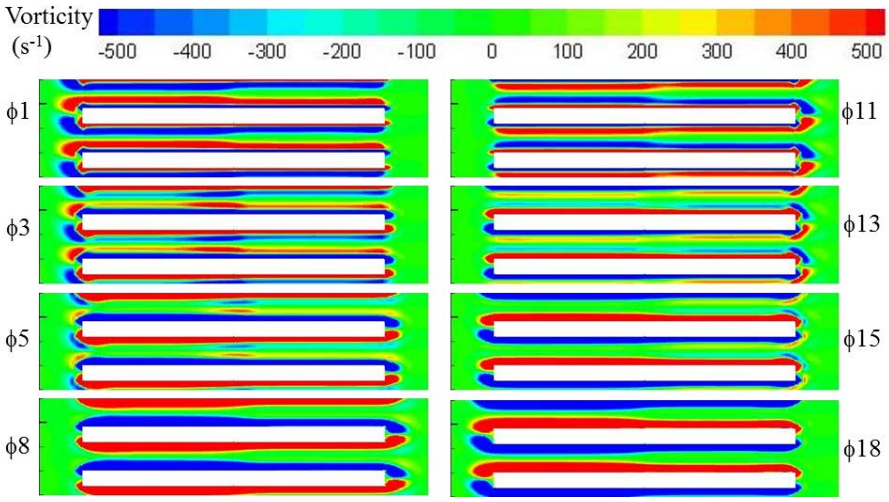

(a) T3G6

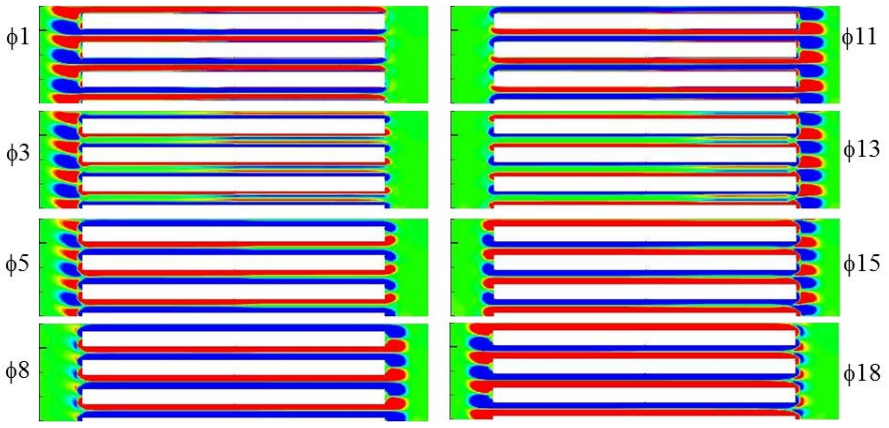

(b) T3G3

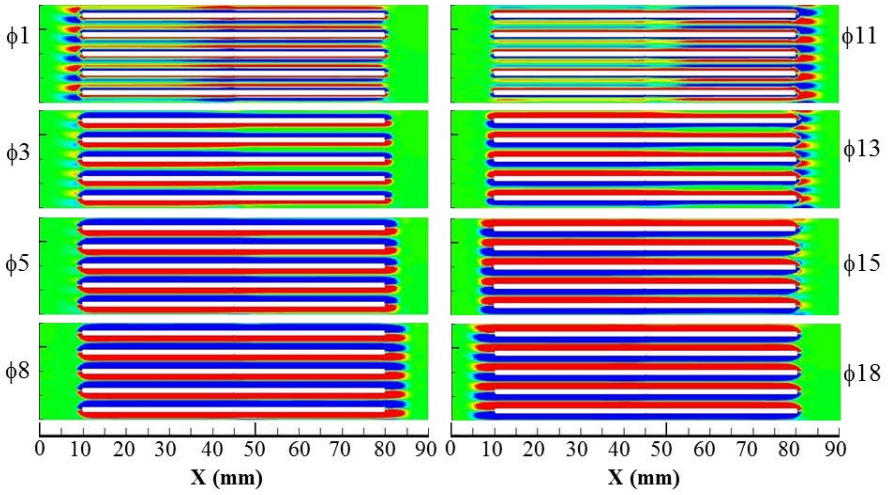

(c) T1G3

Figure 6.22: Vorticity contours for cases with: (a) plates of 3mm thickness and 6 mm gap (T3G6), (b) plates of 3 mm thickness and 3 mm gap (T3G3), and (c) plates with 1 mm thickness and 3 mm gap (T1G6). Drive ratio is 0.3%.

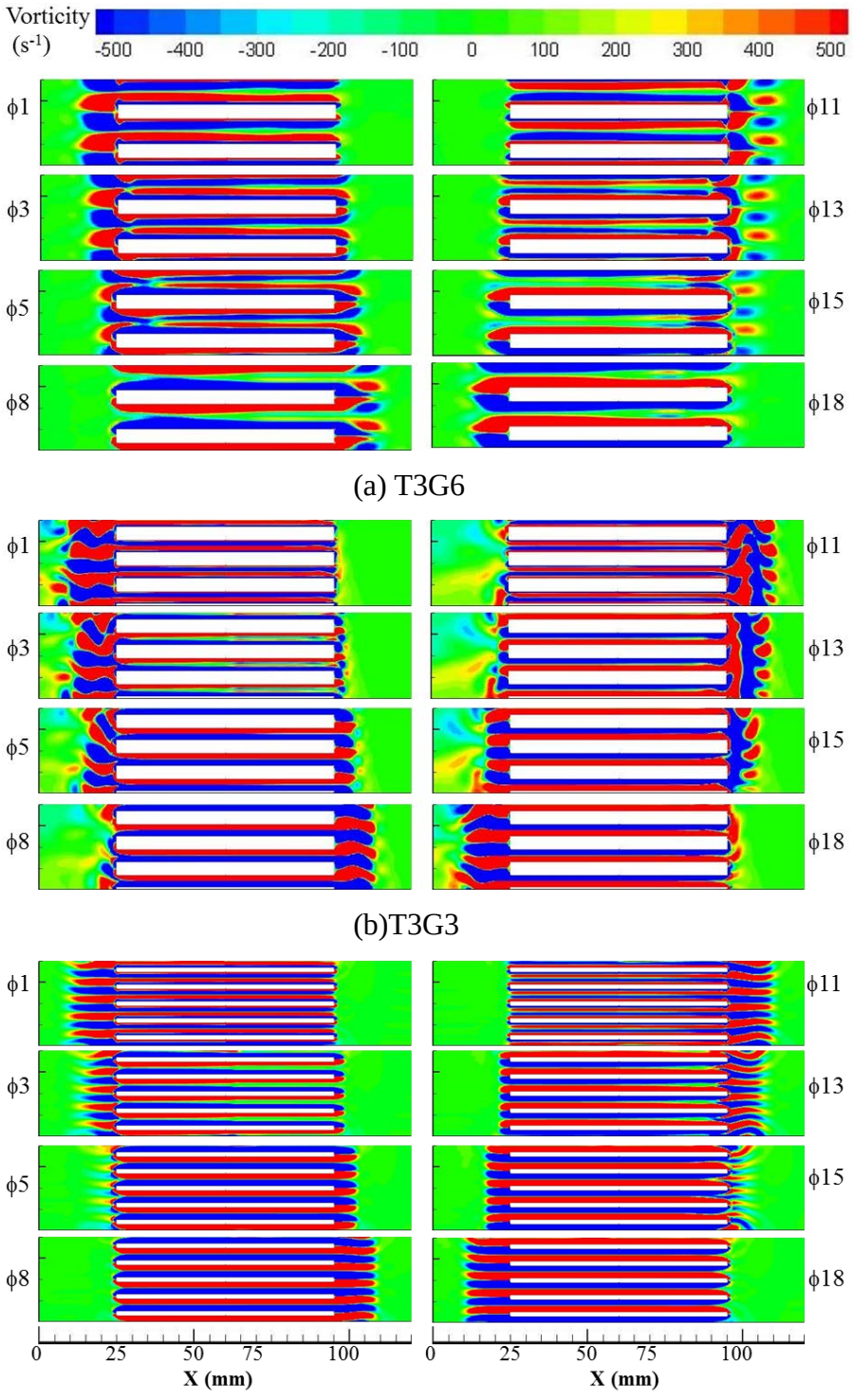

(a) T3G6

(b)T3G3

(c) T1G3

Figure 6.23: Vorticity contours for three cases with: (a) 3mm plates thickness and 6 mm plates spacing (T3G6), (b) 3mm plates thickness and 3 mm plates spacing (T3G3), and (c) 1 mm plate thickness and 3 mm plates spacing (T1G3). Drive ratio is 0.83%.

As the drive ratio increases, the vortex structures are shed from the end of the plates and propagate further into the open area next to the heat exchanger as shown in Figure 6.23.

At the right end of the heat exchanger assembly (cold end) shown in plots (a) and (b) clear vortex shedding appears. As the flow reverses, no vortex shedding is observed at the left end of the heat exchanger assembly (hot end) of plot (a) and the vortex structures stay attached to the plates. This is possibly the influence of viscosity which is higher at higher temperature. Hence flow at hot end is more difficult to shed.

As the spacing between plates is reduced to 3 mm, plot (b), vortex shedding at the left end of the assembly appears with a more distorted structure than that at the right end. The shedding phenomenon is not seen on plot (c).

Apparently when the plate thickness is reduced to 1 mm, the vortex structures at both ends of the heat exchanger assembly elongate but never shed. The high porosity of thinner plate arrangement has a less “violent” cross-sectional change and consequently the flow is less “disturbed”. Similar observation was also reported in the experimental work of Mao et al. (2008).

6.2.5 Viscous dissipation

Figure 6.24 shows the dimensionless viscous dissipation for plates with different thicknesses. As discussed earlier, the arrangement of size of plate thickness and spacing used in current study affects the velocity of the flow. The velocity within a channel bounded by thin plates was shown to be lower due to the change of porosity. Hence the velocity gradient within the heat exchanger with thin plates becomes smaller. Thinner plates introduce less obstruction to the flow. Hence less disturbances is expected to travel within the channel as the flow moves in its cyclical manner.

For both plate thicknesses, the viscous dissipation within the hot channel is bigger compared to the cold channel. This is due to the higher gradient of velocity and bigger fluid viscosity at the hot channel as the fluid within the channel is heated by the hot wall. The low viscous dissipation at the end of the heat exchanger assembly with thinner plates is due to a smaller obstruction to the flow by the structure itself.

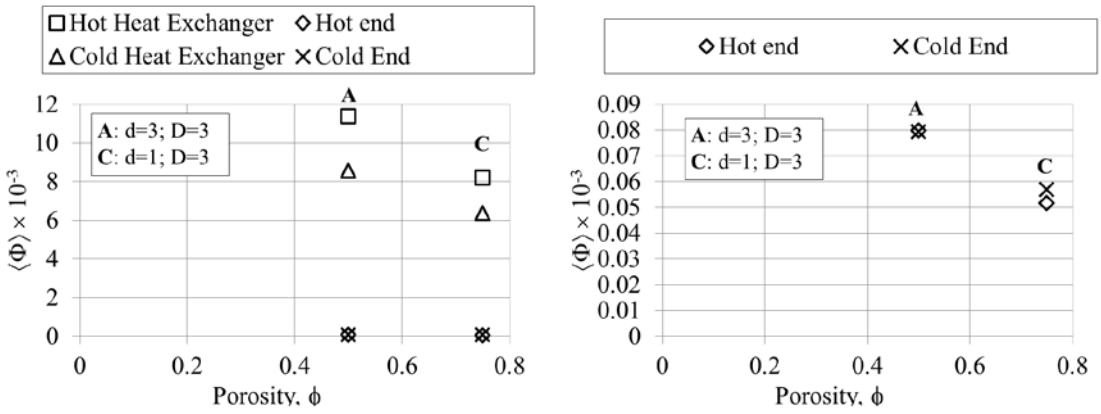

(a) (b)

Figure 6.24: (a) The effect of plate thickness, *d*, on viscous dissipation and (b) the enlarged view of viscous dissipation at the end of plates.

Figure 6.25 shows the effect of the size of gap between plates on the viscous dissipation. In the current study, as the space becomes bigger the porosity increases. Hence the resulting lower velocity amplitude results in the lower viscous dissipation. In addition, wall surface area becomes smaller due to the reduction of the number of plates to allow for the flow area. This also reduces viscous dissipation.

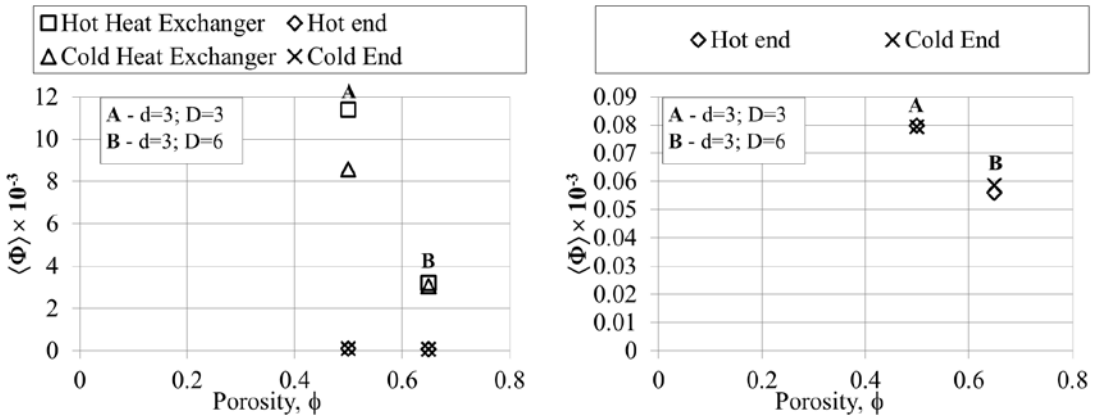

(a) (b)

Figure 6.25: (a) The effect of size of gap between plates, *D*, on viscous dissipation and (b) the enlarged view of viscous dissipation at the end of plates.

A similar trend of decreasing viscous dissipation between cases A and B is observed at the open area next to the hot and cold end of the plates. The high dissipation at areas next to the cold and hot ends of the plates with a smaller spacing d = 3 mm may be

related to the elongated vortex structure that propagates further into the open area as shown in Figure 6.22(b) (in comparison to 6.22(a)).

6.3 The effect of mean pressure

Thus far, the investigation has been carried out at atmospheric pressure. In this section, further investigation is carried out at a higher mean pressure with helium as the working medium and the frequency set to 100 Hz. The baseline plate thickness of 3 mm and plate spacing of 6 mm were selected for the heat exchanger. The flows were investigated for drive ratios of 0.3% and 0.83%. The description of the cases investigated is given in Table 6.6.

Table 6.6: Description of boundary conditions for the study of operating mean pressure.

Working medium : helium								
P_m (bar)	f (Hz)	Distance from location of P_a			Oscillating pressure, p_1 (Pa)	Oscillating mass flux, m_2' (kg.m/s)	P_a (Pa)	Drive Ratio (%)
		x_s	x_1	x_2				
1	100	1.7	1.46	2.0	186.468	0.2777	300	0.3
10					1864.7	2.7771	3000	
20					3729.4	5.5542	6000	
1	100	1.7	1.46	2	515.89	0.7683	830	0.83
10					5158.9	7.6833	8300	
20					10318	15.3667	16600	

6.3.1 Velocity profiles

Figure 6.26 shows the comparison between the resulting velocity profiles for the mean pressures investigated. The profiles were plotted for the location of 15 mm away from the joint, above the cold plate, for selected phases of a flow cycle.

It is observed that the viscous penetration depth becomes smaller with the increased mean pressure. Consequently, the "annular effect" appears closer to the wall as the mean pressure becomes higher. The inviscid region at the core grows with the increasing mean pressure. This is shown by the "slug-like" velocity profiles produced at the core particularly at 10 and 20 bar. The amplitude of velocity at the core for 1 bar is slightly bigger especially at phases $\phi 5$ and $\phi 8$. This is due to the bigger penetration depth which leads to a "less" pronounced "annular effect". Apart from these phases, the

resulting velocity amplitudes for all the three mean pressures investigated are very much the same.

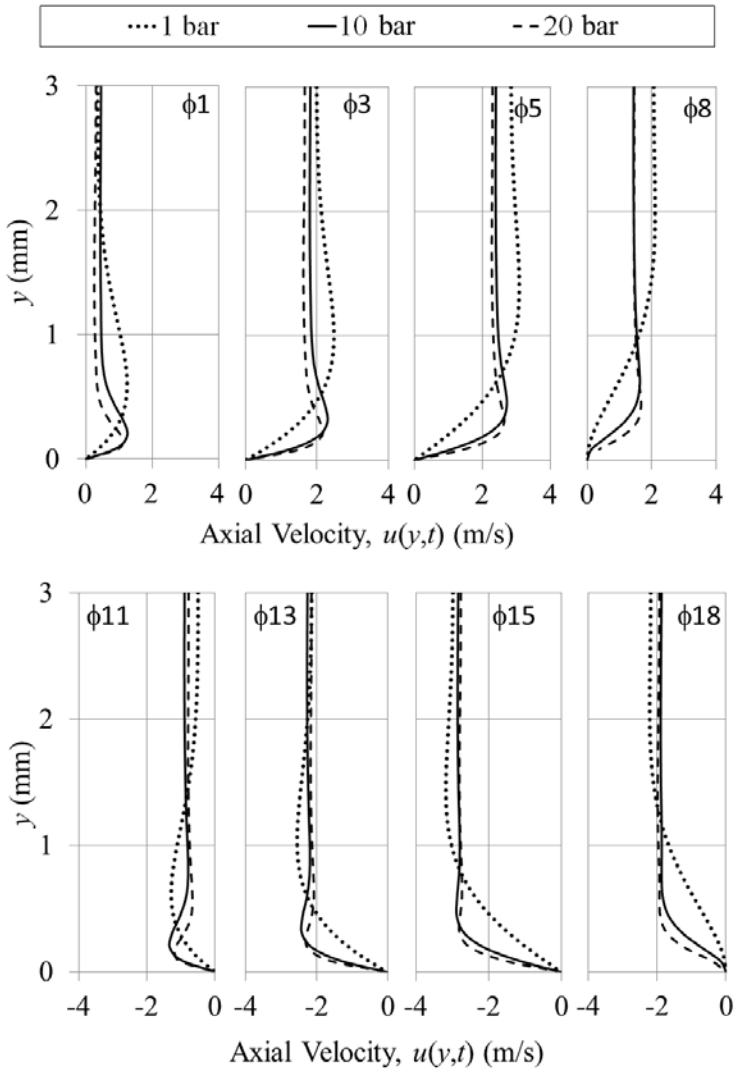

Figure 6.26: Velocity profiles for selected phases over the first (top) and the second (bottom) half of the cycle.

6.3.2 Temperature profiles

Figure 6.27 shows the development of temperature profiles over a flow cycle for a location of 8 mm away from the joint above the cold plate. Since the drive ratio, frequency and plate dimensions are fixed, the gas displacements for all the investigated mean pressures are the same. At high mean pressures of 10 and 20 bar, the temperature at the core is lower than at the cold plate. The core temperature stays that way throughout the flow cycle as it changes from phase ϕ1 to ϕ20.

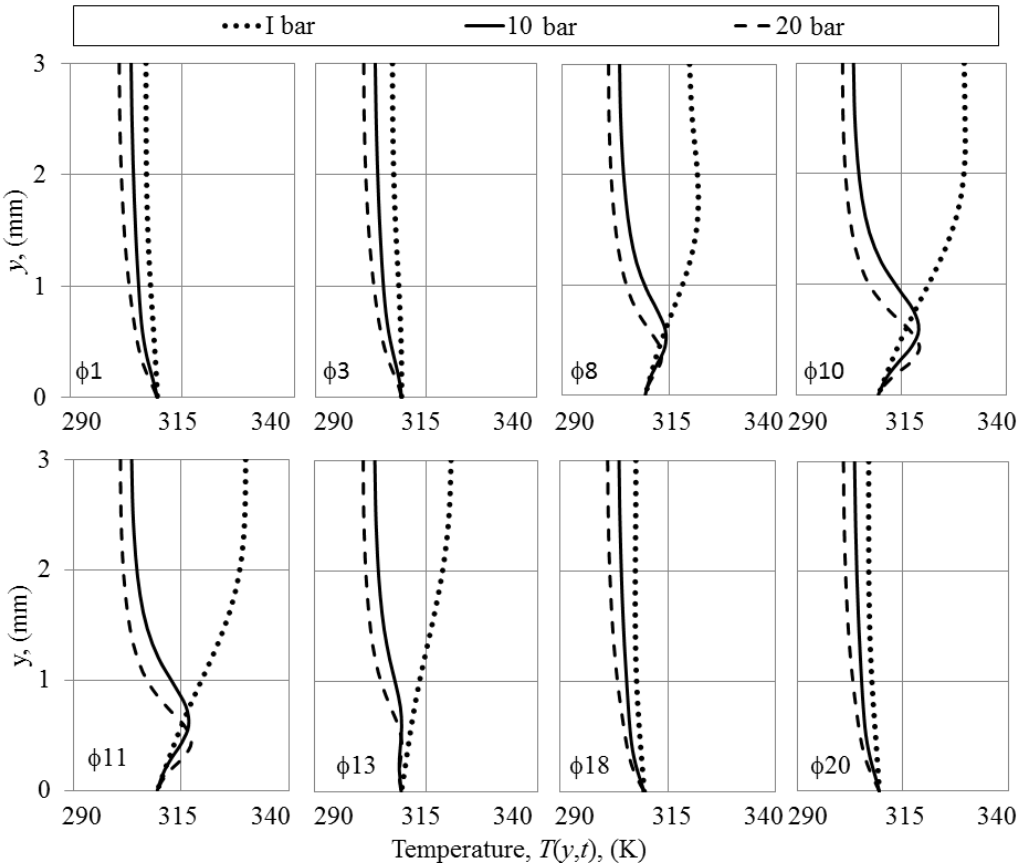

Figure 6.27: Temperature profiles at cold heat exchanger for selected phases during the first half (top) and second half (bottom) of the cycle.

For all cases, the temperature gradient becomes negative at certain parts of the cycle, the examples being phases ϕ1, ϕ3, ϕ18 and ϕ20. This means that there are instances when heat is transferred into the fluid from the cold plate (opposite to the expected overall heat transfer direction). The amount of this "adverse" heat transfer is bigger at higher mean pressures. This is due to the fact that the fluid away from the wall is "less" affected by the wall temperature and therefore the increase of fluid temperature from the initial temperature may takes longer as the mean pressure increases.

Similar to the findings from the frequency investigations, there are instances when the maximum temperature occurs near the wall (c.f. ϕ8, ϕ10, ϕ11, ϕ13). This "annular effect" of temperature, where heat from the hot channel travels into the cold channel within the boundary layer, is best seen for pressures of 10 and 20 bar. At 1 bar, the "annular effect" is not seen because the thermal penetration depth is thickest and therefore the temperature gradient develops further into the core.

Figure 6.28 shows that temperature profiles at the hot channel have negative temperature gradients for all phases in the flow cycle. The heat is being transferred from the hot wall to the fluid for most of the times. Few exceptions are spotted from the enlarged view of profiles for 1 bar shown as an inset in the figure. A small positive wall temperature gradient occurs at phase ϕ8, ϕ10, and ϕ11. This "annular effect" of temperature is due to the flow of cold fluid into the hot channel which becomes significant due to the high thermal penetration depth of 1 bar mean pressure. However, the amounts are too small and the effect on the total averaged heat flux is insignificant

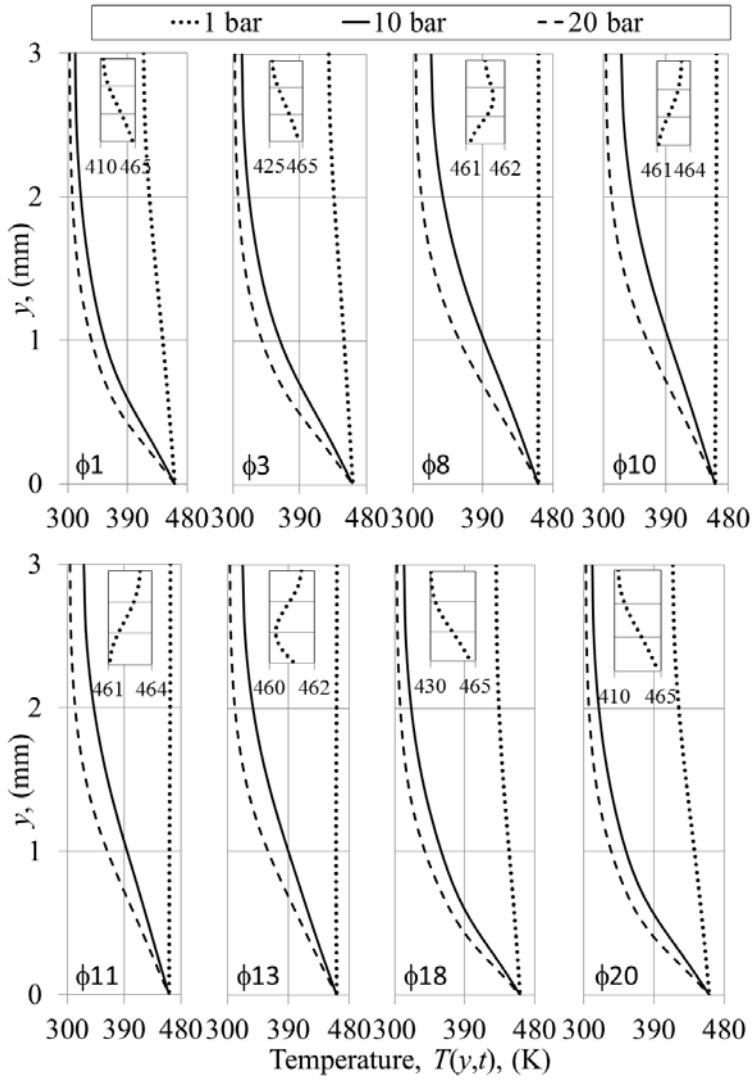

Figure 6.28: Temperature profiles at hot heat exchanger during the first (top) and second (bottom) half of the cycle.

6.3.3 Heat transfer condition

Figure 6.29 shows the effect of various mean pressures on the heat flux as defined in equation (6.1). As the mean pressure increases, the heat fluxes at both cold and hot exchangers increase. Thermal penetration depth becomes smaller with an increase of mean pressure. Consequently, the temperature gradient becomes bigger and heat transfer is improved. Meanwhile density increases with mean pressure as indicated by the value calculated for mass flux at boundary condition x_2 as tabulated in Table 6.6. The dense fluid is able to absorb/release more heat within the thermal layer.

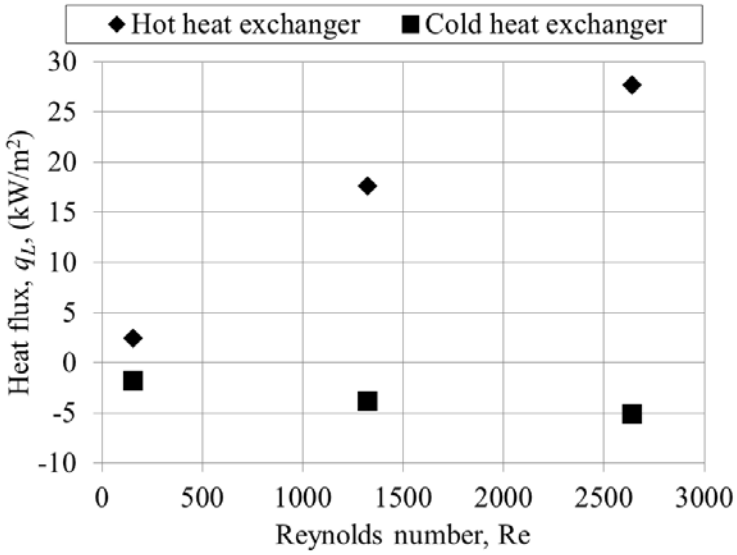

Figure 6.29: Heat fluxes at cold and hot heat exchangers at various operating mean pressure.

The increasing trend of heat flux at the hot heat exchanger is significantly bigger compared to a slow increase taking place at the cold heat exchanger. This means that the heat supplied by the hot heat exchanger is not fully removed by the cold heat exchanger. This phenomenon may be related to the heat accumulation inside the hot plume of gas as seen in Figure 6.30. Heat from the hot heat exchanger interacts with cold fluids at both ends of the hot plate. Some amount of heat is accumulated at the left end of the heat exchanger assembly. The accumulation becomes bigger as the mass flux increases with mean pressure. This results in less heat being transferred to the cold plate.

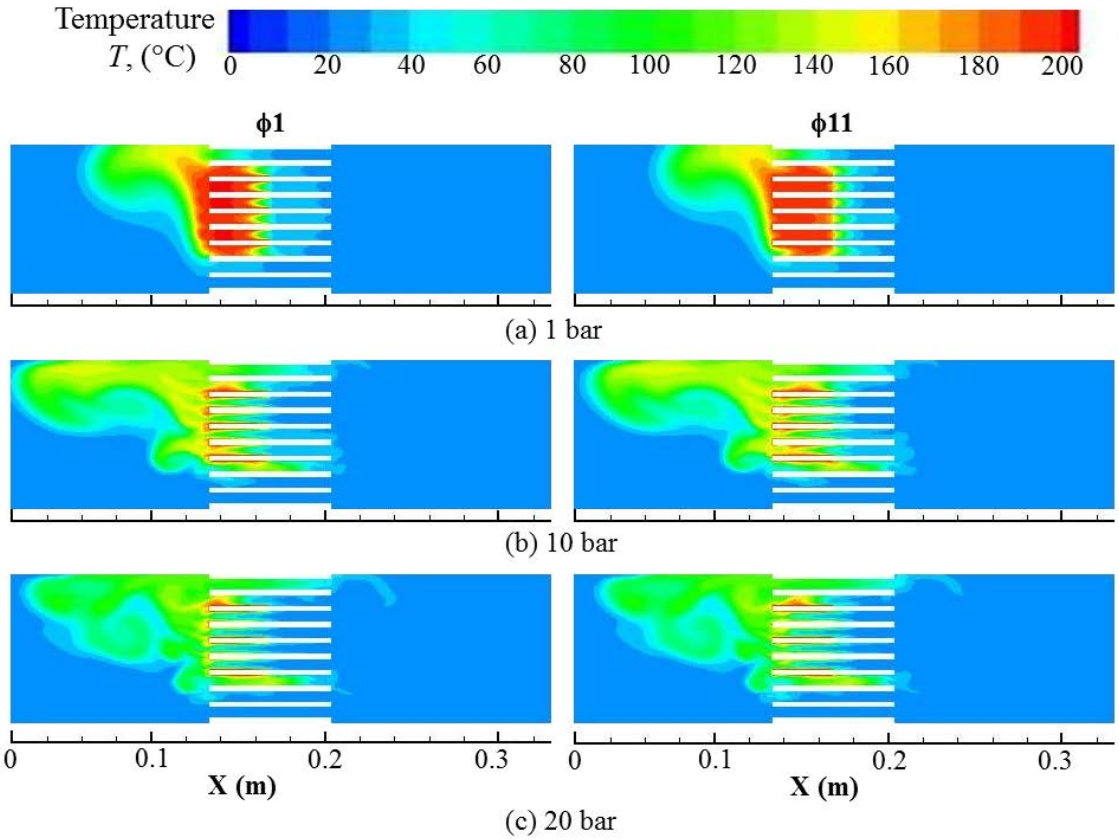

Figure 6.30: Visualisation of heat accumulation at the open area next to hot end of the heat exchanger assembly through temperature contours at (a) 1; (b) 10; and (c) 20 bar operating mean pressures.

Although there is no control point at which the temperature is monitored with time as the solution progresses, this effect was already illustrated in Figure 4.10 for nitrogen at atmospheric pressure. Here the gas is helium and the mean pressure increases, which makes the accumulation more pronounced.

6.3.4 The effect of temperature on velocity profiles

Figure 6.31 shows that the velocity profiles between the plates are significantly affected by the density changes due to the variation of mean pressure.

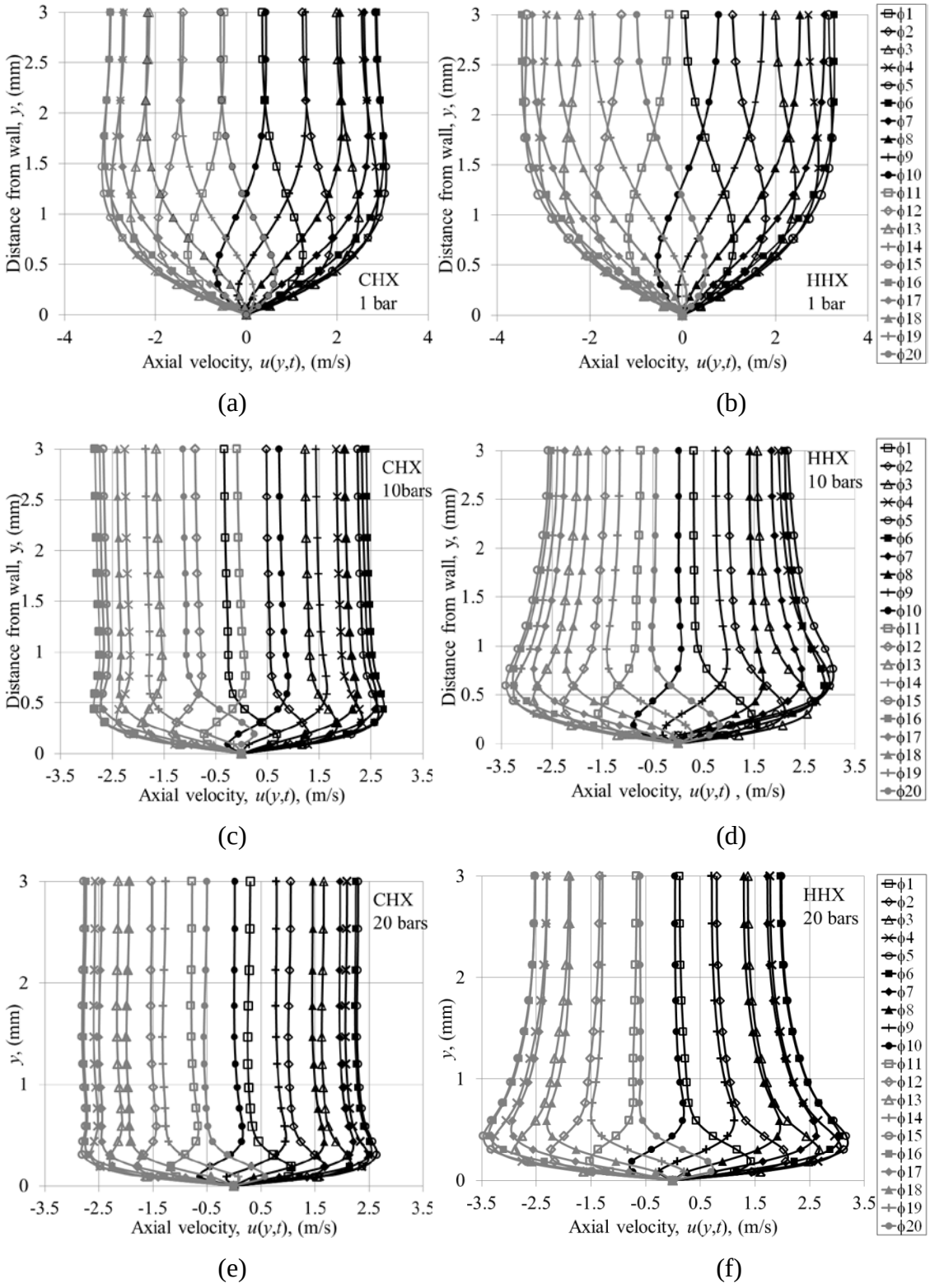

Figure 6.31: Velocity profiles at cold (left) and hot (right) heat exchangers with mean pressure increasing from top to bottom.

As the mean pressure increases, the velocity profiles within the viscous layer of the hot channel swell and thicken compared to those at the cold channel. The “slug-like” profiles at the core of the hot heat exchanger “contract” and this is especially prominent at high mean pressure. At 10 and 20 bar, the temperature in the bulk is practically constant (c.f. Figures 6.27 and 6.28). However, the temperatures within the thermal layer near the hot wall are high. This leads to a “swelling” of the velocity profiles and their “contraction” at the core so that the mass flux in the channel is preserved. This is why the “annular effect” of velocity becomes more pronounced. The slight “tilt” of velocity profiles within the cold channel may be related to the temperature-driven-flow as also seen in the results from investigations presented in chapter four.

Figure 6.32 shows velocity profiles plotted at six different locations along the heat exchanger assembly. These profiles are for 20 bar. Four phases that represent the maximum (ϕ5 and ϕ15) and minimum (ϕ1, and ϕ11) amplitude of velocity over a flow cycle were chosen for three locations of 1, 15 and 34 mm from the joint above hot and cold plates. The definition of locations used in plotting the velocity profiles is shown on top of the figure.

For clarity, each velocity plot has been labelled with letter C or H followed by a number 1, 15 or 34. The letters C and H represent cold and hot heat exchangers, respectively. The number was used to indicate the axial distance in millimetres from the joint, *m*. For instance, C1 means that the plots were taken at the cold heat exchanger at a point 1 mm from the joint. The three plots at the top of the figure are for hot channel and the bottom plots are for cold channel.

Phases ϕ1 and ϕ5 represent the first half of the cycle when the flow is moving in the direction from hot to cold heat exchangers. Phases ϕ11 and ϕ15 represent the second half of the cycle when the flow reverses. This is also illustrated using the “arrow” shown on the schematic diagram at the top of the figure.

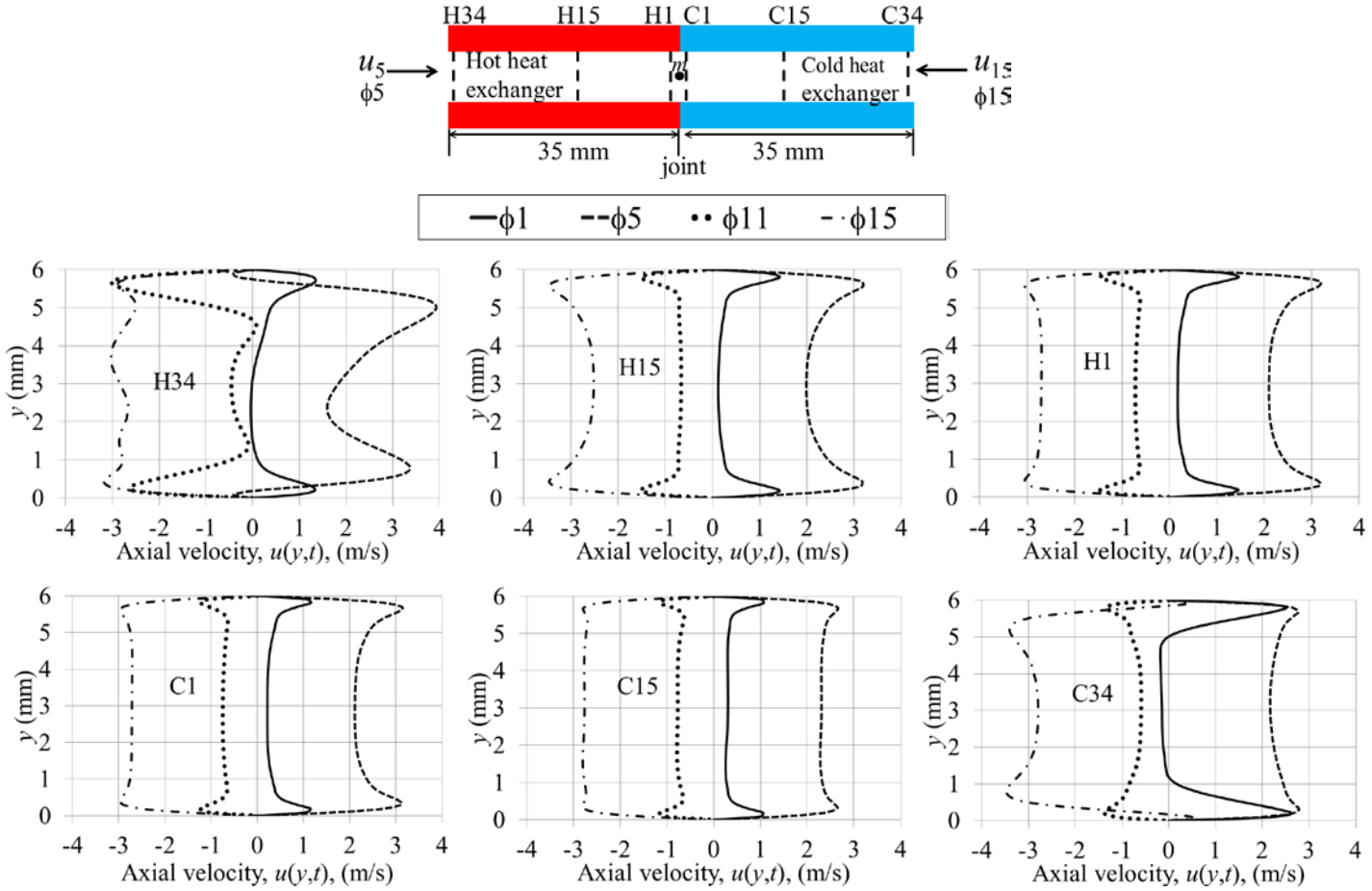

Figure 6.32: Velocity profiles for phases ϕ1, ϕ5, ϕ10,ϕ15 along the length of the heat exchangers at 20 bar. Schematic diagram of locations H34, H15, H1, C1, C15 and C34 is shown at the top.

The discussions based on Figure 6.32 will concentrate on the “contraction” of velocity profiles and “entrance/exit effect”. The “contraction” phenomenon within the core of the channel is seen prominent within the hot channel especially at location in the middle of the channel (shown as H15). At location closer to the cold channel, (shown as H1), the “contraction” is bigger during the first half of the cycle (shown as ϕ1 and ϕ5) compared to the second half of the cycle (shown as ϕ11 and ϕ15).

The bigger “contraction” at ϕ1 and ϕ5 is due to the strong influence of hot fluid within the channel. As the flow reverses the nearby cold fluid flows into location H1 and the “contraction” becomes smaller. Similar condition is observed at the cold channel 1 mm from the joint, C1, but with smaller amplitude of velocity. In the middle of cold channel (shown as C14) the “contraction” phenomenon is not seen. A normal “slug-like” feature of inviscid flow at the core is observed.

The “contraction” phenomenon should not be confused with the “entrance/exit effect” occurring at both ends of the channel (shown as C34 and H34). The “entrance/exit effect” is due to the incoming/outgoing flow following the cyclical manner of the flow. The effect of temperature-driven-flow due to a natural convection can be seen at ϕ5 of H34 when the fluid flows into the hot channel. This is represented by an asymmetry within the “annular effect”. The annular profile at the top wall of the channel has a bigger magnitude than that at the bottom. This is not seen at C34, presumably due to the absence of temperature-driven-flow at the cold end.

Furthermore, the asymmetry of the flow with respect to time (by comparing phases of a flow) becomes more pronounced at cold and hot ends of the heat exchanger compared to other locations within the channel. This can be seen by comparing the profiles for phases ϕ5 and ϕ15 for the two locations of C34 and H34. When the fluid is flowing at maximum velocity in the direction from the hot to the cold channel (represented by ϕ5), the profile at location C34 has the typical feature of “slug-like” flow at the core (with a slight “contraction”) and frictional flow near the wall. The velocity profile of H34 at ϕ15 has a very disturbed profile which is possibly due to the effect of natural convection occurring at the open area near that end.

6.3.5 Flow structure

Figure 6.33 shows a vorticity contour within the area of heat exchanger at a drive ratio of 0.3%. The increase in mean pressure results in thinner shear layers that form at the walls of the heat exchangers within the area between the plates. The shear layer is thicker at hot channel than at the cold channel. This is related to the expansion of the viscous layer near the hot plate as a result of the change in the temperature-dependent-density.

At 1 bar, the vortex structures remain attached to the plates at both ends. For 10 and 20 bar, a clear detached vortex structure constantly appears at the left end of the heat exchanger assembly for all phases.

At ϕ15 of 10 bar, the shear layer starts shedding at the left end of the heat exchanger assembly. It moves back into the channels as the flow changes the direction at ϕ1. However, there still is a pair of structures remaining within the open area which do not seem to be affected by the direction of flow. This clear structure may be related to the natural convection which introduces a "current" perpendicular to the main flow. As a result a small vortex structure remains almost stationary at the hot end. This phenomenon is more pronounced as the mean pressure increases. This may be related to "jet-like" profiles of velocity next to the wall as the fluid is ejected into open areas. This layer of fluid with high momentum will encourage separation and resulting vortex structures may be more disturbed.

At the right end, the second shear layer moves out into the open area at ϕ1 and shed at ϕ8 (c.f Figure 6.33(b)). The lower viscosity of fluid within the cold channel encourages shedding of the shear layer in that area. Hence the shedding of the shear layer at the right end of the heat exchanger assembly seems more prominent than that occurring at the left end (when viscosity is higher). This becomes more pronounced when mean pressure increases. This may be due to the inflection of the velocity profiles due to the "annular effect" which becomes steeper with an increase of mean pressure. Therefore, the shear layer is easily distorted as the flow leaves the plate and reaches the open area.

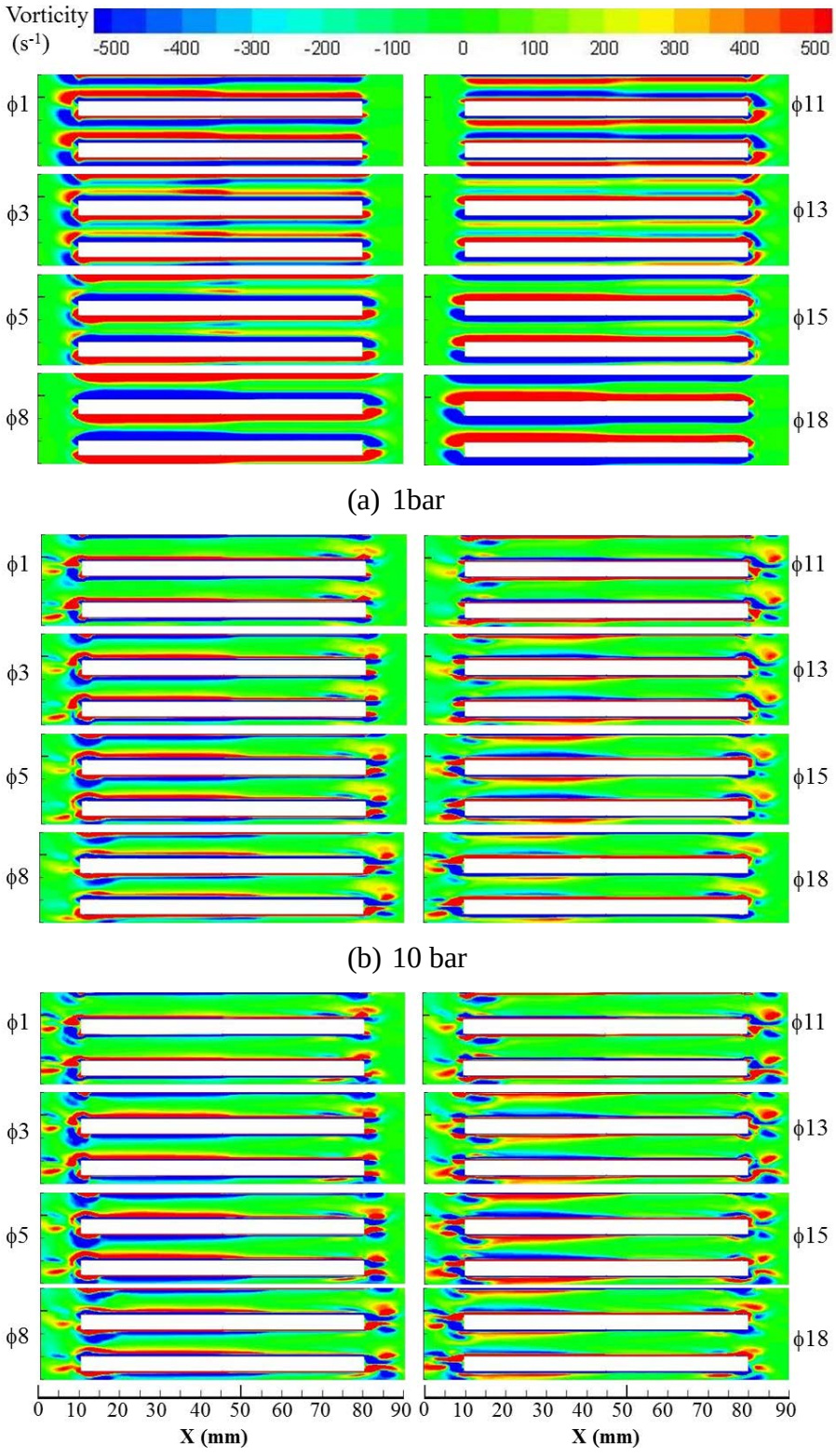

(a) 1bar

(b) 10 bar

(c) 20 bar

Figure 6.33: Vorticity contour for cases with operating mean pressures of (a) 1, (b) 10 and (c) 20 bars in helium at 100 Hz and a drive ratio of 0.3%.

The possibility of influence of the natural convection on the flowfield at the open area next to the hot end of the heat exchanger assembly is investigated further by looking at the development of the vortex structures in time. Figure 6.34 shows the results for operating mean pressures of 1 and 20 bar and a drive ratio of 0.3%. Earlier, in Figure 6.33, the vorticity contours have been shown for different phases of one cycle only. Here, the vorticity contour is shown for a selected phase (ϕ1 only) of different cycles in order to see the change of vortex structures with time (i.e. from cycle 70 to cycle 94). The results are plotted for several cycles which are equivalent to a real time between 0.7s to 0.94s. The plot covers an extended area towards the left end of the computational domain. The area that has been shown in Figure 6.33 is given the same definition of scale (shown in Figure 6.34 as a positive scale of 0 to 15 mm). The extended area is marked with negative scale. The vertical pink dashed-line is introduced to help the reader. For ease of discussion, the vorticity contours are shown by both colours and iso-lines.

At 1 bar, the vortex structure remains similar as time increases from 0.7 s to 0.94 s. The natural convection effect does not seem strong enough to change the vortex structures that remain attached to the plate. For 20 bar, the vortex structures at the end of plate change with time. The vortex structures that cross the vertical line at 0.7 s seem to be moving away from the plate (towards the left of the vertical mark) in the upward direction as the time increases. It is quite easy to track a relatively large structure visible at the bottom half of “0.7 s” graph. The structure becomes weaker as it moves from 0.7 s and disappears from the plot at 0.82 s. At the same time, another vortex structure starts separating from the vortex shedding near the end of the plate and moves away from the plate – this can be seen by monitoring the area at the right side of the vertical mark. Natural convection seems to encourage the fluid within the vortex shedding area to separate and flow upward following the buoyancy flow. This confirms that the pair of vortex structure, which seems to cling to the left end of Figure 6.33(c) for all phases of the flow cycle is achieved as a result of the combined effect of oscillatory flow condition and the natural convection within the area.

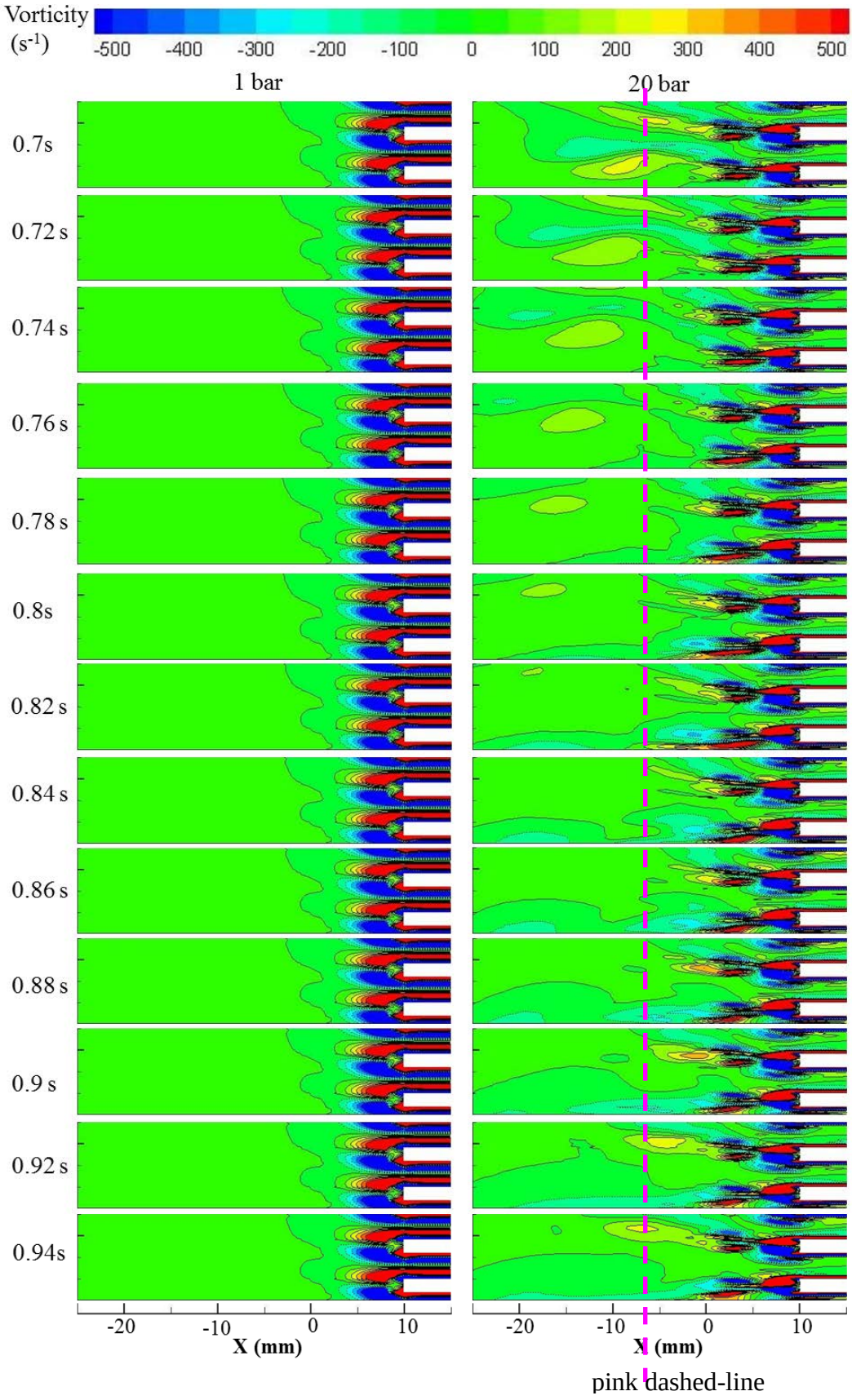

Figure 6.34: Vorticity contours at ϕ1 for operating mean pressures of 1 (left) and 20 (right) bar. The vorticity is recorded for every 0.02 second. Drive ratio is 0.3%.

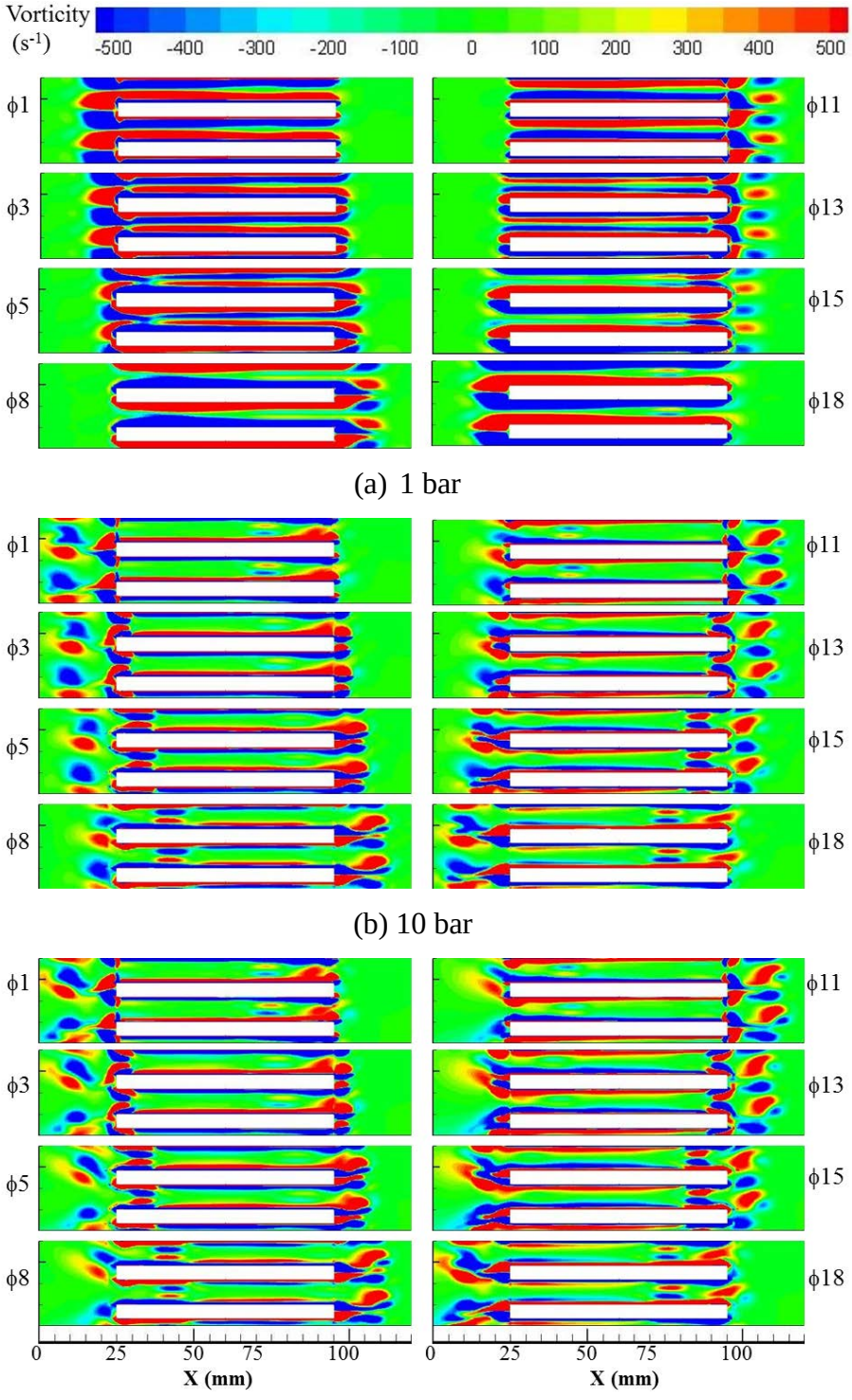

(a) 1 bar

(b) 10 bar

(c) 20 bar

Figure 6.35: Vorticity contour for cases with operating mean pressures of (a) 1 (b) 10 and (c) 20 bars working in helium at 100 Hz and 0.83% drive ratio.

Figure 6.35 shows the vorticity contours for three cases with different operating mean pressures in helium at 100 Hz and a drive ratio of 0.83%. Again, the shear layer at the wall of the heat exchangers becomes thinner with an increase of mean pressures.

For 1 bar, the vortex structures at the left and right ends of the heat exchanger assembly exhibit a different trend. At the left end, the vortex structure elongates into the open area and remains attached to the plate. This is likely to be the result of high viscosity of fluid within the hot channel which can withstand bigger amount of shear. At the right end, the viscosity is smaller hence vortices start shedding at $\phi 8$ and then propagate into the open area until the flow reverses at $\phi 11$.

As the operating mean pressure increases, vortex shedding is seen at both ends of the heat exchanger assembly. The influence of natural convection can be seen in vortex structures rising. However, unlike in the case for 0.3% drive ratio, the vortex structures do not “float” outside the heat exchanger but are sucked back into the shear layer at the channel walls. In this sense, the high drive ratio is likely to dwarf the natural convection effect. The shedding of the shear layer also moves further out of the channel due to higher drive ratio before it comes back as the flow reverses. The vortex shedding becomes more distorted at the left end of the heat exchanger with an increase of mean pressure. At phases $\phi 5$, $\phi 8$, $\phi 15$, and $\phi 18$ of 10 and 20 bar, a small “patch” of vorticity travels within the heat exchanger plates to a distance almost 15 mm into the channels before it gets pushed out of the channels by the reversed flow.

6.3.6 Viscous dissipation

The viscous dissipation increases with an increase of mean pressures. This is shown in Figure 6.36. The viscous dissipation at hot channels is generally bigger than the cold. This may be related to the increase of viscosity with temperature. Furthermore, a pronounced “annular effect” and “contraction” phenomenon as the mean pressure increases introduces additional contribution to viscous dissipation due to bigger gradients formed by the inflection of velocity profiles. Consequently, the viscous dissipation within the hot channels is bigger than that at the cold channels when mean pressure increases.

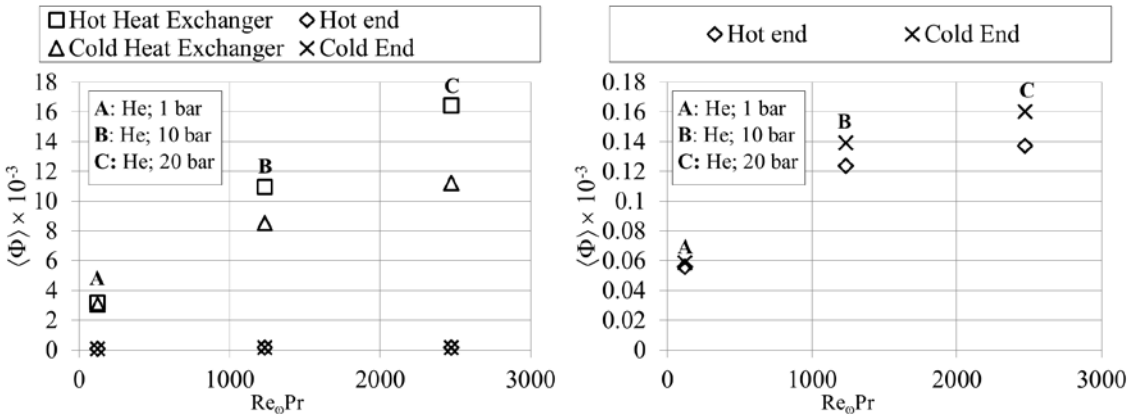

Figure 6.36: (a) The effect of mean pressure on viscous dissipation and (b) the enlarged view for the open area near the cold and hot ends of the heat exchanger assembly.

For the three mean pressures investigated, the viscous dissipation at the open area near the cold end is always bigger than at the area next to the hot end. The difference in value of viscous dissipations between the two areas becomes bigger when mean pressure increases. The reason for this is not clear but it may be related to the vortex shedding which is more prominent at the open area next to the cold end (right end of the heat exchanger assembly of Figure 6.33). The viscosity of flow is lower at the cold area. Hence the shear layer at the cold end is easily shed compared to that at the hot end. The combined effect of stronger natural convection and thinner shear layer as the mean pressure increases seems to result in a lower viscous dissipation at the hot end.

6.4 Comparison between heat transfer from current model and other studies

The results of heat transfer condition from the current model are compared to results from previously published studies to strengthen the validity of the model in line with previous investigations as shown in Figures 6.37 and 6.38.

Figures 6.37 and 6.38 show a Colburn j-factor, j_c, plotted against the hydraulic Reynolds number, Re, for all the cases investigated in this study with comparison to results obtained from various studies found in literature.

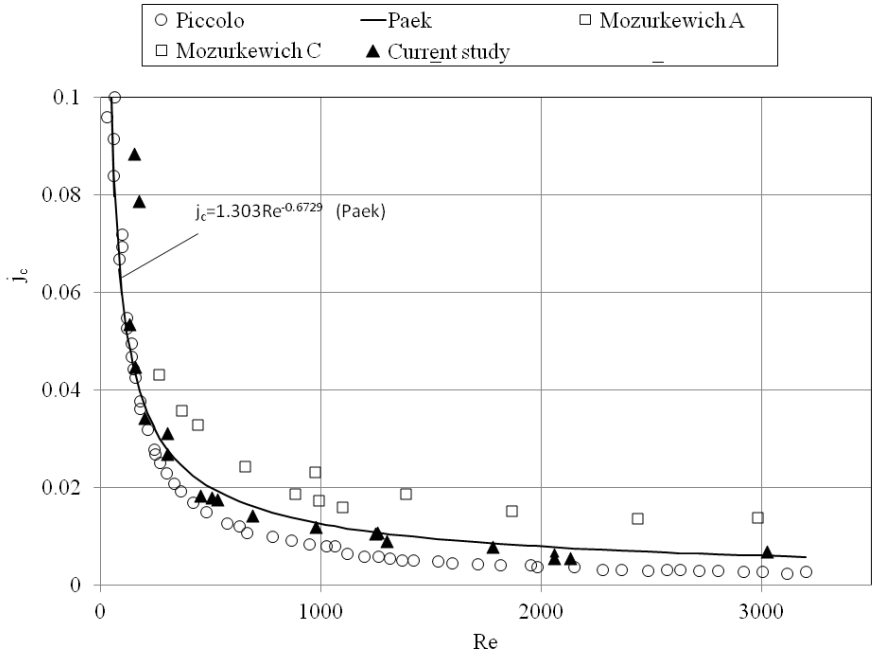

Figure 6.37: Heat transfer condition from results of current study (calculated at hot heat exchanger) presented as Colburn j-factor, j_c, in comparison with results from earlier works.

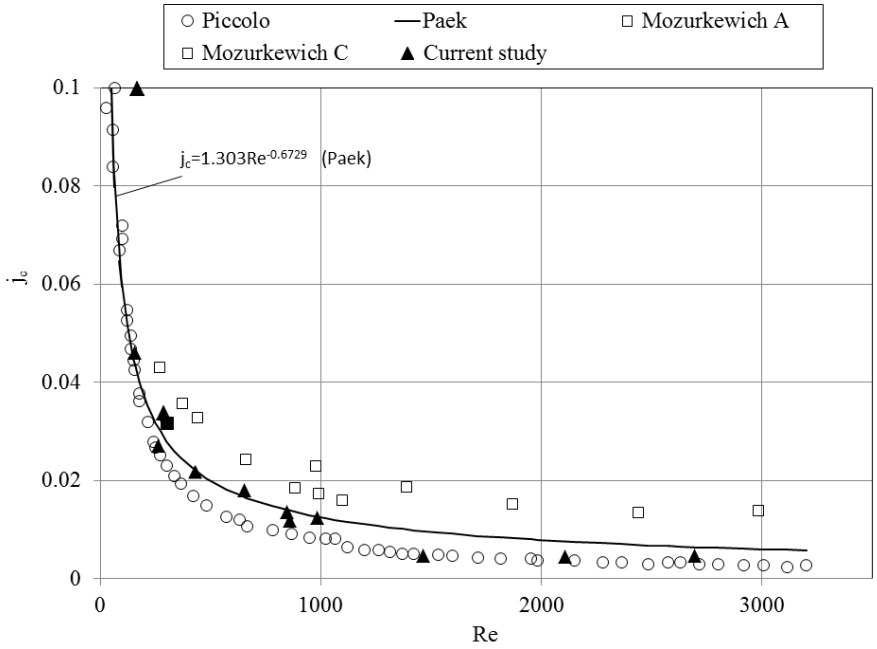

Figure 6.38: Heat transfer condition from results of current study (calculated at cold heat exchanger) presented as Colburn j-factor, j_c, in comparison to results from earlier work.

The Colburn j-factor relates the Nusselt number to the product of Reynolds number, $\mathrm{Re} = \rho u_m D_h / \mu$, and Prandtl number, $\mathrm{Pr} = \mu c_p / k$, as follows (Piccolo, 2011):

$$Nu = j_c \,\mathrm{Re}\,\mathrm{Pr}^{1/3} \tag{6.5}$$

The Nusselt number was calculated as follows:

$$Nu = \frac{hD_h}{k} \tag{6.6}$$

The term D_h refers to the hydraulic diameter defined as two times the size of plates spacing and k is the fluid thermal conductivity. The heat transfer coefficient was calculated as follows:

$$h = \left(\frac{q}{T_{wall} - T_{x_p}}\right) \tag{6.7}$$

The terms q and T_{wall} in equation (6.7) are the wall heat flux and heat exchanger wall temperature, respectively. The term T_{x_p} refers to temperature at the location corresponding to half of the gas displacement. The reference temperature was selected based on understanding of the effective area of heat transfer corresponding to the size of the gas displacement. For ease of comparison with the published data, the Nusselt number was calculated in a similar way as reported by Piccolo (2011). The hydraulic diameter of the pore (D_h=2D) was used in calculating the Nusselt number and Reynolds number. All fluid properties were calculated at a reference temperature of 300 K.

The heat fluxes from cases investigated in this study were compared to the experimental results of Mozurkewich (2001), Paek et al. (2005) and numerical results of Piccolo (2011). These experimental and numerical results had a heat exchanger with closest arrangement to the parallel-plate heat exchanger investigated in this study. Heat fluxes from two arrangements of heat exchangers labelled as ‘Mozurkewich A’ and ‘Mozurkewich C’ were selected from the study of Mozurkewich (2001). ‘Mozurkewich

A' involves 12 evenly spaced parallel copper tubes heat exchanger while 'Mozurkewich C' was a copper screen soldered to four parallel tubes. The copper tubes of 'Mozurkewich A' were arranged with gap, *D*, of 5 mm from one to another while the copper screen of 'Mozukewich C' had a pore which provide gaps of 1.23 mm. Paek et al. (2005) used a fin-and-tube micro heat exchanger. The Nusselt and Reynolds number from all these studies were re-scaled by the same length parameters (2*D*). The root-mean-square velocity used in calculating Reynolds number reported in Paek et al. (2005) have been "corrected" by the factor $\sqrt{2}$ and by the porosity, σ. The correlation proposed by Paek et al. (2005) based on their experimental results was also used for estimating data for low Reynolds number not covered in their experiment.

The values of Colburn j-factor, j_c, in the current investigation (Figure 6.37) were calculated based on data gained at the hot heat exchanger. They were obtained from all the cases investigated from chapters four to six. The results were shown to fall within the range of j_c reported in the literature.

Figure 6.38 shows that the Colburn j-factors, j_c, obtained for cold heat exchanger also fall within the range reported in other studies. It is noteworthy to point out that a proper selection of reference temperature using location x_p seems to work well for the representation of heat transfer condition at both the hot and the cold heat exchanger. The findings show that the heat transfer obtained from the model is congruent with prior studies in this area.

6.5 Summary

The models developed in this chapter were validated by comparing the axial velocity of flow with an adiabatic heat exchanger wall condition to the available theoretical solution. Good agreements were found. The effects of frequency, geometrical dimensions and mean pressure on the instantaneous velocity and temperature profiles were discussed. The "annular effect" which is a unique feature of oscillatory flow was shown occurring for velocity as well as temperature profiles at certain phases of a flow cycle. The effect becomes prominent when the viscous and thermal layers become thinner relative to the height of the channel.

The effective heat transfer between the fluid and the heat exchanger plates depends on the size of the gas displacement. The study suggests that the length of the heat exchanger should be made comparable to the size of the gas displacement so that the heat is effectively transferred between the fluid and the heat exchanger. Part of the heat supplied by the hot heat exchanger is transferred to the fluid at the open area next to the hot end of the heat exchanger assembly. A heat accumulation is observed at that end. Consequently heat is not fully removed by the cold heat exchanger. This condition becomes more pronounced with an increase of mass flux as mean pressure increases. The Colburn j-factor obtained from current model is in good agreement with other works when bulk fluid temperature at location x_p (half the size of gas displacement) is used as the reference temperature for calculating the Nusselt number. This strengthens the validity of the models.

The vortex structures changes with the change of operating conditions. Generally, the shear layer at the cold channel is easily shed compared to that at the hot channel as the flow progresses. This relates to the viscosity which increases with temperature. Consequently, the flow from the first half of the cycle is asymmetrical compares to the second half of the cycle. The combined effect of the jet-like velocity profiles near the wall and the natural convection at the open area next to the hot end which becomes pronounced as mean pressure increases is believed to cause the constant appearance of vortex structure next to the hot end of the heat exchanger assembly at 0.3% drive ratio. This is not seen so much at 0.83% drive ratio presumably due to the negligible influence of natural convection as the mean velocity of the oscillatory flow increases. The vortex shedding observed for most cases at a drive ratio of 0.83% disappears when the thickness of plates is reduced to 1mm. This may be related to a lower obstruction to the flow by the structure itself.

Generally, the dimensionless viscous dissipation is higher at the hot channel compared to the cold channel because the viscosity is bigger at higher temperature. The inflection of velocity profiles due to “annular effect” and “contraction” particularly at high mean pressure may also contribute to the high viscous dissipation within the hot channel. At high frequency, the viscous dissipation at the open area next to the cold end is higher than that next to the hot end. As frequency increases the viscous layer becomes thinner. The thinner layer causes high velocity gradient which will encourage the separation and

a roll-up of the vortex structures at the end of plates. The combined effect of boundary layer expansion and natural convection at area within and near the hot channel seems to reduce the dissipation at the open area next to the hot end of the heat exchanger assembly.

Chapter Seven: Conclusions and future work

7.1 Conclusions

As outlined previously in section 1.3, the overall aim of the current study has been to investigate (predominantly numerically) the flow and heat transfer processes in two types of internal structures commonly encountered within thermoacoustic systems, namely a regenerator and a parallel-plate heat exchanger.

Referring to the original objectives listed in section 1.3, objectives (i) and (ii) have been achieved through the study presented in chapter three. A two-dimensional model has been developed for the regenerator working in a travelling-wave setting. The pressure drop of the porous tortuous structure of the regenerator has been modelled and validated by the results obtained from experiment carried out in an apparatus where a control could be achieved over the phase angle between velocity and pressure thus enabling a travelling-wave condition to be imposed. The values of computationally determined permeability coefficient, K, that represents the hydrodynamic loss of the regenerator investigated, are shown in Table 3.3. Friction factor correlation has been developed based on a porous medium model. A simplification offered by Darcy's law has been used for the low speed condition studied. The results from this correlation appear to match the results calculated through the correlation proposed by Swift and Ward (1996). This indicates that steady flow assumptions, used by Swift and Ward (1996) when developing his correlation, apply to the travelling-wave conditions investigated here.

Unfortunately, the results obtained from the experiment are somewhat limited because of the design of the apparatus. Flow within samples made of fine mesh screen was limited to low Reynolds number, while the flow within samples made of coarse mesh screen was at a relatively high Reynolds number (otherwise a sufficient pressure drop could not be recorded). Phase shift was observed between pressure and velocity within the regenerator made of coarse mesh screen (#94 and #30). The phase shifting phenomenon may be related to the inertial effect described by the Forchheimer model. This may be the reason for the discrepancy between numerical and experimental results at Reynolds number higher than 60. As illustrated in section 3.6, apart from pressure

drop that reduces the performance of the regenerator a heat transfer condition within the regenerator should also be considered (suggested as future work).

The second structure is a parallel-plate heat exchanger of a standing wave system presented in chapters four through to six. Chapter four corresponds to the original objectives (iii) – (v) listed in section 1.3. To this end, a two-dimensional model (referred to as the 'long model') has been developed and validated against the experimental results of Shi et al. (2010). The model is shown to provide velocity profiles and temperature profiles with qualitatively good agreement to the experiment suggesting that the model has successfully captured important features of the thermofluid processes within the investigated heat exchanger structures. Discrepancies in the magnitude of temperature, velocity and heat flux between the experimental results and the results from simulations are shown to be partly due to the heat accumulation that occurs in the experiment, although a number of other reasons are possible as given in sections 4.4 and 4.5.3. However, the qualitative disagreement of temperature profiles falls within the range of the experimental uncertainties.

The current approaches of prescribing the initial temperature fields showed that the initialisation procedure influences both the magnitude of heat flux and velocity profiles within the structures. The investigation of initial temperature suggests that the current model is best initialised at 300 K. The model initialised with a temperature field defined more closely to the experimental conditions resulted in a change of the flow character, incongruent with the real flow behaviour. It can only be speculated that the possible reason for this is the type of boundary conditions imposed on the model, which could not fully represent the reality of experiment with its long time-history (hours), far beyond the capabilities of the current CFD model.

The imposed temperature boundary conditions (on the heat exchanger plates) is shown to cause asymmetry to the flow seemingly related to the nonlinearity caused by the combined effects of temperature-dependent density and temperature-driven flow (buoyancy). The change in fluid density with respect to temperature results in lower velocity amplitudes during the first part of the cycle and relatively higher magnitudes of velocity for the second part of the cycle. Here, an "asymmetrical boundary" creates asymmetries in the temperature and velocity fields. In addition, the temperature-driven

buoyancy flow creates further “distortions” to the already asymmetrical features of velocity and temperature fields. The results indicate that there are “net flows” through channels (or in other words “streaming”). These effects are well illustrated through changing the orientation of the device relative to gravity field. The viscous dissipation is also affected.

Objective (vi) has been achieved through the investigation presented in chapter five using the so-called ‘short model’. Several numerical models have been tested to obtain a model that best represents the flow and heat transfer from the point of view of the earlier experimental findings. The need for a turbulence model for higher drive ratios investigated in chapter five has been demonstrated. The investigation of the differences observed between the velocity profiles from the experiment and laminar numerical model led to a hypothesis that turbulence may have influence on the flow, despite the commonly accepted criterion for transition proposed by Merkli and Thomann (1975). This was concluded to be the effect of the finite length of the channel and the presence of the flow disturbances re-entrained after the vortex shedding cycle. Some validity to this description of the flow has been given by showing that the turbulent model gives a good match between the results obtained from the experiment and the simulation, particularly at the drive ratio of 0.83% (the highest investigated). The SST k-ω model developed by Menter (1994) is shown to best capture the essence of the flow at that drive ratio. Transition is expected to occur at a drive ratio as low as 0.45%. This finding is important in that it contributes to a new understanding that the turbulent flow features may appear at lower flow amplitudes within structures of thermoacoustic systems. Of course the nature of turbulence and transition in the oscillatory flows is not the same as in relatively better understood steady flows. It is known that there are quite a few different turbulent flow regimes in oscillatory flows and these may appear at different parts of the cycle with a possibility of relaminarization. Therefore, in the context of the current study, it may well be necessary to refine any future CFD models from the point of view of the possible turbulence regimes in the oscillatory flows.

Following objective (vii), studies of the operating conditions culminate in an investigation driven by the needs of the more practical working conditions than those investigated experimentally by Shi et al. (2010). Of particular interest here were the resulting velocity and temperature field features at different operating mean pressures,

frequencies, working medium and geometrical dimensions. The characteristics of the parallel-plate heat exchangers were investigated from the point of view of the so-called “annular effect”, adiabatic velocity (shown as a “slug-like” profile) and adiabatic temperature.

For all conditions tested, the heat flux at the cold heat exchanger has always been lower than the hot heat exchanger. This indicates that the heat supplied by the hot heat exchanger is not fully removed by the cold heat exchanger. The differences become significant as the mean pressure increases as it also corresponds to an increased mass flux. This phenomenon is likely to be related to the heat accumulation and natural convection at the open area next to the hot heat exchanger.

The length of heat exchanger is an important feature to consider when designing a system for high operating frequency. For a fixed drive ratio, changing the operating conditions (c.f. frequency and geometrical dimensions), may change the gas displacement. If the gas displacement becomes smaller and the length of the heat exchanger is fixed, the “passive area” of the heat exchanger becomes bigger. Thus the total wall heat transfer is significantly affected and the heat exchanger becomes less effective. Based on this observation, a “fair comparison” was made between cases with different size of gas displacement where analysis of temperature profiles was done at a location equivalent to half the distance of the gas displacement. The effective heat transfer between working medium and the solid wall of the heat exchanger plates was shown to be determined by the size of the gas displacement.

The viscous dissipation and vortex structures within and around the heat exchanger assembly are also discussed and shown to change with operating conditions. For instance, when helium is used as a working medium, the resulting heat transfer is better than that which can be achieved with nitrogen. However, the viscous dissipation is also shown to be higher. The dissipation becomes bigger with an increase of operating frequency and mean pressure. The influence of natural convection at the open area at the end of the hot heat exchanger becomes stronger if the drive ratio remains small but the operating mean pressure increases. These conditions need to be fully understood when designing heat exchangers in thermoacoustic devices.

Finally, a good agreement is found when the heat transfer values from the current model are compared to other studies. The heat transfer represented by the values of the Colburn *j*-factor calculated at the heat exchangers is within the range of heat transfer reported elsewhere.

The numerical parametric investigations such as these presented in this thesis have certain advantages over the experimental approaches in that they can potentially avoid significant time and financial penalties. However a significant further research effort would be required to ensure that the CFD predictions could be confidently used for designing practical thermoacoustic systems.

7.2 The contribution to the body of knowledge

In a nutshell, and to summarise the detailed conclusions given in Section 7.1, the current study succeeded in improving the understanding of the important characteristics of flow and heat transfer within the structures investigated. For the regenerator, the pressure drop within the regenerator of a thermoacoustic cooler was found to be estimated fairly well by the steady flow correlations as long as the pressure and velocity within the regenerator are in-phase. For the heat exchanger, turbulence has been found to occur at a lower drive ratio than suggested in the literatures. Furthermore, the phenomenon of heat accumulation and the combined effect of natural convection and temperature-dependent density were found to affect significantly the flow and heat transfer within the heat exchanger, particularly at higher operating mean pressures. These issues need to be properly addressed in the future for a better design of thermoacoustic systems.

7.3 Future works

The general aim of this study was to perform numerical investigations in order to gain a better understanding of the flow physics observed in the experiment. While it is a step forward in gaining such an understanding, the outcomes of this study also suggest that future works should concentrate on a more involved and well defined numerical and experimental work that would focus more on the essence of thermoacoustic processes. These include:

(i) Improvement of CFD model for regenerators to include non-thermal-equilibrium and inertial effect to better predict the pressure drop especially for the flow with a higher Reynolds number and regenerators with higher temperature gradients. This

may involve a development of a travelling-wave experimental rig that is able to operate to a higher Reynolds number to supply the required pressure drop data for the model.

(ii) Practical thermoacoustic systems often work at pressure-velocity time-phasing which is neither standing-wave nor travelling-wave. Therefore, it is interesting to carry out investigations regarding the effect of phase difference between pressure and velocity on the pressure drop of flow across the regenerator.

(iii) In the current study of the flow past parallel-plate heat exchangers, the plates have sharp edges. It is possible that the shape of the end of the plate may have an effect on the flow and heat transfer in the oscillatory flow investigated (Aben et al. 2009). It would be interesting to pursue a study in this direction. Investigation of different types of heat exchangers, such as finned-tube and shell-and-tube arrangements, should also be considered.

(iv) A development of a three-dimensional CFD model is also an interesting area to venture. It is expected that a three-dimensional model will reveal three-dimensional effects overlooked by the current investigation. A cost-effective model needs to be developed. This will include a good combination of initialisation procedures and a good selection of solver setting. The three-dimensional model may be proven useful especially in understanding high amplitude operating conditions where nonlinearities are expected to play an important role.

(v) Extension of the investigation of heat transfer conditions to heat exchangers working in a travelling-wave time-phasing would be also an interesting area to pursue. It is not clear if the phase angle between pressure and velocity would make significant changes to the resulting heat fluxes.

(vi) The investigation of the effect of the operating conditions may be extended to cases where the gas displacement is kept constant. This may provide a better understanding of the heat transfer condition within the internal structures of thermoacoustic systems.

The model developed in this study is ready for further development in order to simulate flows within two internal structures of thermoacoustic systems: the regenerator and heat exchanger. Numerous experimental and numerical works may be continued from this point onwards towards creating a database for the benefit of the future developments in the area of sustainable thermoacoustic technologies.

References

Aben P. C. H., Bloemen P. R., and Zeegers J. C. H., 2009. 2-D PIV measurements of oscillatory flow around parallel plates. Experimental Fluid. Vol. 46, pp. 631-641.

Abramenko T. N., Aleinikova V. I., Golovicher L. E., and Kuz'mina N. E., 1992. Generalization of experimental data on thermal conductivity of nitrogen, oxygen, and air at atmospheric pressure. J. Eng. Phys. Thermophys. Vol. 63, pp. 892-897.

Akhavan R., Kamm R. D., and Shapiro A. H., 1991. An investigation of transition to turbulence in bounded oscillatory Stokes flows Part1. Experiments, J. Fluid Mech. Vol. 225, pp. 395-422.

ANSYS FLUENT 13.0, (2010), User Manual, ANSYS Inc.

Arnott W. P., Bass H. E., and Respet R., 1991. General formulation of thermoacosutic for stacks having arbitrarily shaped pore cross sections. Journal of the Acoustical Society of America. Vol. 90, iss. 6, pp. 3228-3237.

Backhaus S., and Swift G. W., 2002. New Varieties of Thermoacoustic Engines. 9th International Congress on Sound and Vibration. July 2002.

Brewster J. R., Raspet R., and Bass H. E., 1997. Temperature discontinuities between elements of thermoacoustic devices. J. Acoust. Soc. Am. Vol 102, iss. 6,pp. 3355-3360.

Bejan A., Dincer I., Lorente S., Miguel A. F., and Reis A. H., 2004. Porous and complex flow structures in modern technologies. Springer. USA. Pg 9.

Besnoin E., and Knio O. M., 2001. Numerical Study of thermoacoustic heat exchangers in the thin plate limit. Numerical Heat Transfer. Part A, 40,pp. 445-471.

Besnoin E., and Knio O. M., 2004. Numerical study of thermoacoustic heat exchangers. Acta Acustica United With Acustica. 90,pp. 432-444.

Ceperley P. H., 1979. A pistonless Stirling engine—The travelling wave heat engine. The Journal of the Acoustical Society of America. 66(5) pp. 1508-1513.

Ceperley P. H., 1985. Gain and efficiency of a short travelling wave heat engine. The Journal of the Acoustical Society of America. 77(3) pp. 1239-1244.

Cha J. S., Ghiaasiaan S. M., Kirkconnell C. S., 2008. Oscillatory flow in microporous media applied in pulse-tube and Stirling-cycle cryocooler regenerators. Experimental Thermal and Fluid Science. Vol. 32,pp. 1264-1278

Choi S., Nam K., and Jeong S., 2004. Investigation on the pressure drop characteristic of cryoocooler regenerators under oscillating flow and pulsating pressure conditions. Cryogenics, Vol. 44, pp. 203-210.

Clearman W. M., Cha J. S., Ghiaasiaan S. M. and Kirkconnell, 2008. Anisotropy steady-flow hydrodynamic parameters of microporous media applied to pulse tube and Stirling cryocooler regenerators. Cryogenics. Vol. 48, pp. 112-21.

Feldman K. T., 1986. Review of the literature on Rijke thermoacoustic phenomena. Journal of Sound and Vibration. 7(1), pp. 83-89.

Feldman K. T., 1986. Review of the literature on Sondhauss thermoacoustic phenomena. Journal of Sound and Vibration. 7(1), pp. 71-82.

Gedeon D., and Wood J. G., 1996. Oscillating-Flow Regenerator Test Rig: Hardware and Theory with Derived Correlations for Screens and Felts. NASA Contractor Report 198442. NASA Lewis Grantt NAG3-1269.

Gifford, W. E. and Longsworth, R. C., 1966. Surface Heat Pumping." Advances in Cryogenic Engineering. Vol. 11, pp. 171-179.

Guillaume D. W., and LaRue J. C., 2001, Comparison of the vortex shedding behaviour of a single plate and plate array. Experiments in Fluids. Vol. 30, pp. 22-26.

Guillaume D. W., and LaRue J. C., 2002, Comparison of the numerical and experimental flow field downstream of a plate array. Journal of Fluids Engineering. Vol. 124, pp. 184-186.

Hoftler, T. J., Wheatley, J. C., Swift, G. W. and Migliori, A., 1988. Acoustic cooling engine. US Patent 4,722,201.

Hsu C., 2005. Dynamic Modeling of Convective Heat Transfer in Porous Media, In: Vafai K, *Handbook of Porous Media* 2nd ed, Boca Raton, Taylor and Francis Group, pp. 39-80.

Hsu C. T., Cheng P., 1990. Thermal dispersion in a porous medium. International Journal of Heat and Mass Transfer. Vol. 33, pp. 1587-1597.

Hsu C., Fu H., Cheng P., 1999. On Pressure-Velocity Correlation of Steady and Oscillating Flows in Regenerators Made of Wire Screens. Journal of Fluid Engineering Vol. 121, pp. 52-56.

Incropera F. P., and DeWitt D. P., 1996. Introduction to heat transfer third edition. John Wiley & Sons. Canada.

Jaworski A. J., and Piccolo A., 2012. Heat transfer processes in parallel-plate heat exchangers of thermoacoustic devices-numerical and experimental approaches. Applied Thermal Engineering. Vol. 42, pp. 145-153.

Ju Y., Jiang Y., and Zhuo Y., 1998. Experimental study of the oscillating flow characteristics for a regenerator in a pulse tube cryocooler. Cryogenics. Vol. 38, pp. 649-656.

Kays W. M., and London A. L., 1964. Compact Heat Exchangers. New York: McGraw-Hill.

Landrum E. C., Conrad T. J., Ghiaasiaan S. M., Kirkconnell C. S., 2010. Hydrodynamic parameters of mesh fillers relevant to miniature regenerative cryocoolers. Cryogenics. Vol. 50, pp. 373-380.

Mao X., and Jaworski A. J., 2007. Measurement of thermal boundary layer in a channel of parallel-plate thermoacoustic stack. International Congress of Refrigeration. Beijing.

Mao X., Yu Z., Jaworski A. J., and Marx D., 2008. PIV studies of coherent structures generated at the end of a stack of parallel plates in a standing wave acoustic field. Experimental Fluids. Vol. 45, pp. 833-846.

Mao X., and Jaworski A. J., 2010a. Oscillatory flow at the end of parallel-plate stacks: phenomenological and similarity analysis. Fluid Dyn. Res. Vol. 42, pp 055504.

Mao X., and Jaworski A. J., 2010b. Application of particle image velocimetry measurement techniques to study turbulence characteristics of oscillatory flows around parallel-plate structures in thermoacoustic devices. Meas. Sci. Tech. Vol. 21, pp. 035403.

Matveev K., Backhaus S., and Swift G., 2006. On Some Nonlinear Effects of Heat Transport in Thermal Buffer Tubes. Proceedings of the 17th International Symposium on Nonlinear Acoustics. Pennsylvania, 18-22 July.

Menter F. R., 1994. Two-equation eddy-viscosity turbulence models for engineering application. AIAA Journal. Vol. 32, No. 8, pp. 1598-1605.

Menter F. R., Langtry R., Volker S., 2006. Transition modeling for general purpose CFD codes. Flow turbulence combust. Vol. 77, pp. 277-303.

Merkli P., and Thomann H., 1975. Transition in oscillating pipe flow. J. Fluid Mech. Vol. 68, part3, pp. 567-575.

Mozurkewich G., 1995. Heat transfer from a cylinder in an acoustic standing wave. Journal of Acoustical Society of America.Vol. 98, iss. 4, pp. 2209-2216.

Mozurkewich G., 2001. Heat transfer from transverse tubes adjacent to a thermoacosutic stack. Journal of Acoustical Society of Americ. Vol. 110, iss. 2, pp. 841-847.

Nam K., and Jeong S., 2005. Novel flow analysis of regenerator under oscillating flow with pulsating pressure. Cryogenics. Vol. 45, pp. 368-379.

Nam K., and Jeong S., 2006. Investigation of oscillating flow friction factor for cryocooler regenerator considering cryogenic temperature effect. Cryogenics. Vol. 45, pp. 733-738.

Narasimha R., and Sreenivasan K. R., 1979. Relaminarization of Fluid Flows. Advances in Applied Mechanics. Academic Press, Burlington, MA. pp 221-309.

Nsofor E. C., Celik S., and Wang X., 2007. Experimental study on the heat transfer at the heat exchanger of the thermoacoutic refrigerating system. Applied Thermal Engineering. Vol. 27, pp. 2435-2442.

Ohmi M., Iguchi M., Kakehashi K., and Masuda T., 1982. Transition to turbulence and velocity distribution in an oscillating pipe flow. JSME, Vol. 25, no. 201, pp. 365-371.

Olson J. R., and Swift G. W., 1994. Similitude in thermoacoustics. Journal of Acoustical Society of America. Vol. 95, iss. 3, pp. 1405-1412.

Paek I., Braun J. E., and Mongeau L., 2005. Characterizing heat transfer coefficeints for heat exchangers in standing wave thermoacoustic coolers. Journal of Acoustical Society of America. Vol. 118, iss. 4, pp. 2271-2280.

Piccolo A., 2011. Numerical computation for parallel plate thermoacoustic heat exchangers in standing wave oscillatory flow, International Journal of Heat and Mass Transfer. Vol. 54, pp. 4518-4530.

Putnam A. A., and Dennis W. R., 1956. Survey of Organ-Pipe Oscillations in Combustion Systems. The Journal of the Acoustical Society of America. 28(2), pp. 246-259.

Rott N., 1980. Thermoacoustics, Advances in Applied Mechanics. Vol. 20, pp. 135-175.

Schlichting H., 1987. Boundary layer theory. McGraw-Hill. New York. Pg 44-64,252-255,258-263,300-304,438-442,656-660.

Schlichting H., and Gersten K., 2001. Boundary layer theory, 8th revised and enlarged edition. India: Springer-Verlag. pp 76,416-507.

Shen C., He Y., Li Y., Ke H., Zhang D., and Liu Y, 2009. Performance of solar powered thermoacoustic engine at different tilted angles. Applied Thermal Engineering. Vol. 29, pp. 2745-2756.

Shi L., Yu Z., and Jaworski A. J., 2010a. Application of laser-based instrumentation for measurement of time-resolved temperature and velocity fields in the thermoacoustic system. International Journal of Thermal Sciences. Vol. 49, pp. 1688-1701.

Shi L., Mao X., and Jaworski A. J., 2010b. Application of planar laser-induced fluorescence measurement techniques to study the heat transfer characteristics of parallel-plate heat exchangers in thermoacoustic devices. Meas. Sci. Technol. Vol. 21, pp. 115405.

Song B. H., and Bolton J. S., 2000. A transfer-matrix approach for estimating the characteristic impedance and wave number of limp and rigid porous materials. Journal of Acoustical Society of America. Vol. 167, iss. 3, pp. 1131-1152.

Spoor P. S. and Swift, G. W., 2000. "Thermoacoustic Separation of a He-Ar Mixture." Physical Review Letters, 85(8): 1646-1649.

Swift G. W., 1997. Thermoacoustic natural gas liquefier. U.S. Dept. of Energy's Natural Gas Conference, Houston, Houston, TX, March 24-27.

Swift G. W., 2004. What is thermoacoustics? A brief description, with technical details and citations, Technical Report LA-UR 04-2298, Condensed Matter and Thermal Physics Group, Los Alamos National Laboratory, Los Alamos, New Mexico 87545.

Swift G. W., and Ward W. C., 1996. Simple Harmonic Analysis of Regenerators. Journal of Thermophysics and Heat Transfer. Vol 10, no.4, pp.652-662.

Swift G. W., 2002. Thermoacoustics: a unifying perspective for some engines and refrigerators. Sewickley (PA): Acoustical Society of America Publications.

Talbot L., Cheng R. K., Schefer R. W., and Willis D. R., 1980. Thermophoresis of particles in a heated boundary layer. J. Fluid Mech.. Vol. 101, part 4, pp 737-758.

Tao Y. B., Liu Y. W., Gao F., Chen X. Y., and He Y. L., 2009. Numerical analysis on pressure drop and heat transfer performance of mesh regenerators used in cryocoolers. Cryogenics. Vol. 49, pp.497-503.

Tijani M. E. H., Zeegers J. C. H., de Waele A. T. A. M., 2001. Design of thermoacoustic refrigerators. Cryogenics. Vol. 42, iss. 1, pp. 49-57.

Ueda Y, Kato T, and Kato C., 2009. Experimental evaluation of the acoustic properties of stacked-screen regenerators. J. Acoust. Soc. Am. Vol. 125, iss. 2, pp. 780-786.

Urieli, I. and Berchowitz, D. M.,1984. Stirling Cycle Engine Analysi, CRC Press.

Versteeg H. K., and Malalasekera W., 2007. An introduction to computational fluid dynamics the finite volume method, 2nd edition. England. Pearson Education Limited. Ch 3.

Wakeland R. S., and Keolian R. M., 2004a. Effectiveness of parallel-plate heat exchangers in thermoacoustic devices. J. Acoust. Soc. Am. Vol. 115, iss. 6, pp. 2873-2886.

Wakeland R. S., and Keolian R. M., 2004b. Calculated effects of pressure-driven temperature oscillations on heat exchangers in thermoacoustic devices with and without a stack. J. Acoust. Soc. Am. Vol. 116, iss. 1, pp. 294-302.

Ward W. C., Swift G. W., 1994. Design environment for low-amplitude thermoacoustic engines. J Acoust Soc Am. Vol. 95, pp. 3671-3672.

Worlikar A. S., and Knio O. M., 1996. Numerical simulation of a thermoacoustic refrigerator I. Unsteady adiabatic flow around the stack. Journal of Computational Physics. Vol. 127, pp. 424-451.

Worlikar A. S., Knio O. M, and Klein R., 1998. Numerical simulation of thermoacoustic refrigerator II. Stratified flow around the stack. Journal Of Computational Physics. Vol. 144, pp. 299-324.

Yu Z., Jaworski A. J., 2010. Impact of acoustic impedance and flow resistance on the power output capacity of the regenerators in travelling-wave thermoacoustic engines. Energy Conversion and Management. Vol. 51, pp. 350-359.

Zhao T. S., and Cheng P., 1996. Oscillatory pressure drops through a woven-screen packed column subjected to a cyclic flow. Cryogenics. Vol. 36, pp. 333-341.

Zhao T. S., and Cheng P., 1998. Heat transfer in oscillatory flows, in Tien, C.L., Annual Review of Heat Transfer. Vol. IX (Chapter 7).

Appendices

Appendix One	Validation of model for chapter six
Appendix Two	User-Defined-Code developed for used in ANSYS FLUENT 13.0
Appendix Three	List of publications

Appendix One: Validation of model for chapter six

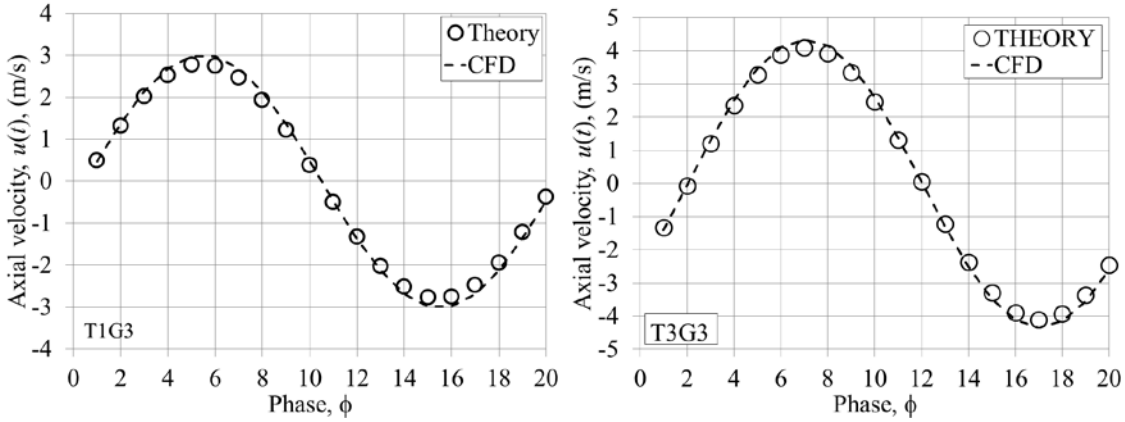

Figure A1.1: Comparison of axial velocity for T1G3 (left) and T3G3 (right)

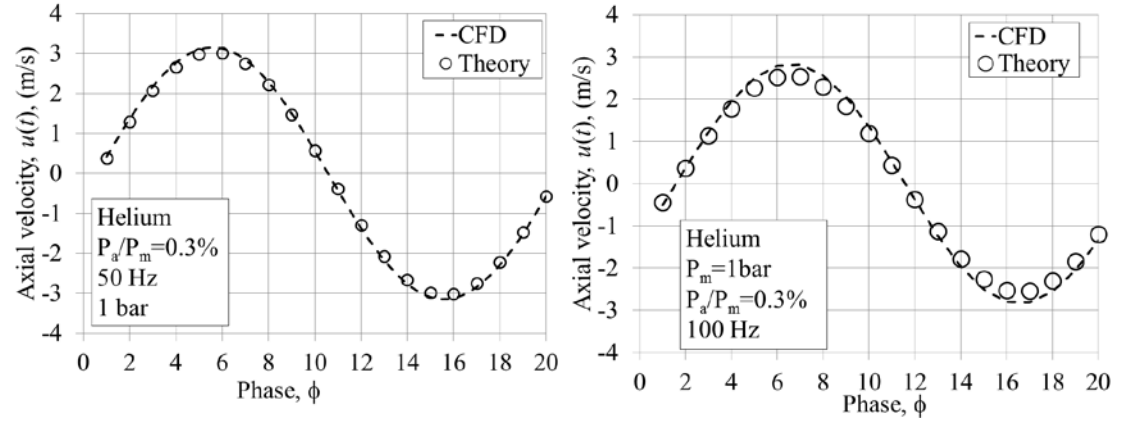

Figure A1.2: Comparison of axial velocity for investigation of frequency of 50Hz (left) and 100 Hz (right) both in helium at 1 bar.

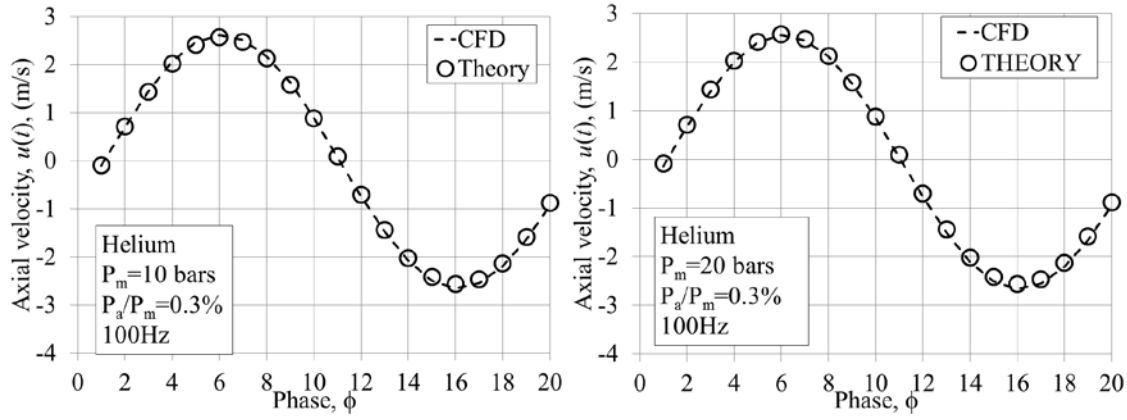

Figure A1.3: Comparison of axial velocity for investigation of mean pressure of 10 bars (left) and 20 bars (right).

Appendix Two: User-Defined-Code developed for used in ANSYS FLUENT 13.0

/*Moving wall for model with full length as indicated in Figure 4.1:*/

```
#include "udf.h"

DEFINE_CG_MOTION(vel_comp9, dt, vel, omega, time, dtime)
{
real freq=13.1;                  /*define frequency*/
real w=2.0*M_PI*freq;            /*define angular velocity*/
real Xcomp=0.009;                /*define displacement*/
NV_S(vel,=,0.0);                 /*reset velocities*/
NV_S(omega,=,0.0);
vel[0]=w*Xcomp*cos(w*time);      /*define axial velocity*/
}
```

/*Heat exchanger wall temperature with result shown in Figure 4.2:*/

```
#include "udf.h"
DEFINE_PROFILE(chx, thread, index)
{
real x[ND_ND];
real y;
face_t f;

begin_f_loop(f,thread)
{
F_CENTROID(x,f,thread);
y=x[0];
if ((y>=2.765) && (y<=2.8))
{
F_PROFILE(f,thread,index)=10939.*y*y-60529.*y+84036;
}
}
end_f_loop(f,thread)
}

DEFINE_PROFILE(hhx, thread, index)
{
real x[ND_ND];
real y;
face_t f;

begin_f_loop(f,thread)
{
F_CENTROID(x,f,thread);
y=x[0];
if ((y>=2.8) && (y<=2.835))
{
F_PROFILE(f,thread,index)=-8129.2*y*y+46376.*y-65668.;
}
}
end_f_loop(f,thread)
```

/*Initial temperature to be hooked at initial panel within ANSYS FLUENT 13.0 (2010)*/

```
#include "udf.h"

DEFINE_INIT(my_init_func,d)
{
      cell_t c;
      Thread *t;
      real x[ND_ND];

      thread_loop_c(t,d)
      {
            begin_c_loop_all(c,t)
            {
                  C_CENTROID(x,c,t);
                  if ((x[0]>=2.8) && (x[0]<=6.4))
                        C_T(c,t)=2239.9*x[1]+282.15;
                  else if ((x[0]>=1) && (x[0]<=2.8))

      C_T(c,t)=19040*x[1]*x[1]+153.81*x[1]+282.15;
                  else
                        C_T(c,t)=282.15;
            }
            end_c_loop_all(c,t)
      }
}
```

/***Gas Property for helium in equation (6.3) and (6.4)***/

```
#include "udf.h"
DEFINE_PROPERTY(muHe,c,t)
{
      real mu_lam;
      real temp=C_T(c,t);
      real tc=300;
      real b1=1.99e-05;
      real b2=0.68;
      mu_lam=b1*pow(temp/tc,b2);
return mu_lam;
}

DEFINE_PROPERTY(kHe,c,t)
{
      real kct_lam;
      real temp=C_T(c,t);
      real tc=300;
      real b1=0.152;
      real b2=0.72;
      kct_lam=b1*pow(temp/tc,b2);
return kct_lam;
}
```

/*Condition of temperature at the boundary of short model (equation (5.9))*/

```
#include "udf.h"

DEFINE_PROFILE(xT,t,j)
{
      cell_t c0, c;
      face_t f;
      Thread *t0;

      c0=F_C0(f,t);          /*define the cell c0*/
      t0=F_C0_THREAD(f,t);  /*define the thread t0*/
      begin_c_loop(c,t)
      {
            C_PROFILE(c,t,j)=C_T(c0,t0);     /*define temperature
at the boundary to follow cell c0*/
      }
      end_c_loop(c,t)
}
```

/*Pressure boundary condition for x1 on Figure 5.1*/

```
#include "udf.h"


DEFINE_PROFILE(pressure13Hz,thread,position)
{
face_t f;
real t=CURRENT_TIME;

      begin_f_loop(f,thread)
            {

      F_PROFILE(f,thread,position)=159.6728*cos(82.30972752*t);

            }

      end_f_loop(f,thread)
}
```

/*Mass flux boundary condition for x2 on Figure 5.1*/

```
DEFINE_PROFILE(mass,thread,position)
{
face_t f;
real t=CURRENT_TIME;

      begin_f_loop(f,thread)
            {

      F_PROFILE(f,thread,position)=1.1233*0.6437*cos(82.30972752
*t+1.57);       /*define the oscillatory mass flux equation*/

            }
```

```
      end_f_loop(f,thread)
}
```

/*Calculating and storing vorticity (equation (4.3)) and viscous dissipation (equation (4.20)) in a defined memory within ANSYS FLUENT 13.0 (2010)*/

```
#include "udf.h"

DEFINE_ON_DEMAND(store_hdd)
{
      Domain *d;
      cell_t c;
      Thread *t;
      real f1,f2,f3,f4,fa,fb,fc,fd,dissipation;
      real temp_gradient_x,temp_gradient_y,vorticity;
      d=Get_Domain(1);

      thread_loop_c(t,d)
      {
            begin_c_loop(c,t)
            {
                  temp_gradient_x=C_T_G(c,t)[0];   /*dT/dx*/
                  temp_gradient_y=C_T_G(c,t)[1];   /*dT/dy*/
                  C_UDMI(c,t,0)=temp_gradient_x;
                  C_UDMI(c,t,1)=temp_gradient_y;

                  f1=C_U_G(c,t)[0];     /*du/dx*/
                  f2=C_V_G(c,t)[1];     /*dv/dy*/
                  f3=C_V_G(c,t)[0];     /*dv/dx*'
                  f4=C_U_G(c,t)[1];     /*du/dy*/
                  fa=f1*f1;
                  fb=f2*f2;
                  fc=(f3+f4)*(f3+f4);
                  fd=(f1+f2)*(f1+f2);
                  dissipation=(2*(fa+fb))+fc-(2/3*fd);
                  C_UDMI(c,t,2)=dissipation; /*store in memory2*/

                  vorticity=f3-f4;
                  C_UDMI(c,t,3)=vorticity;   /*store in memory3*/

            }

      end_c_loop(c,thread)
      }
}
```

Appendix Three: List of publications

Saat F. A. Z., Yu Z., and Jaworski A. J., 2011. CFD-assisted regenerator analysis: application to thermoacoustic system. Proc. 23rd IIR International Congress of Refrigeration. Paper ID 580 – keynote, 21-26 August, Prague, Czech Republic.

Mohd Saat F. A. Z., Jaworski A. J., Mao X., and Yu Z., 2012. CFD modelling of flow and heat transfer within the parallel plate heat exchanger in standing wave thermoacoustic system. Proc. 19th International Congress on Sound and Vibration, 8-12 July, Vilnius, Lithuania.

Mohd Saat F. A. Z., and Jaworski A. J., 2013. Oscillatory flow and heat transfer within parallel-plate heat exchangers f thermoacoustic systems. International Conference of Mechanical Engineers, 3-5 July, London, United Kingdom.